POLITECNICO DI TORINO

Master's Degree in Mechanical Engineering

Master's Degree Thesis

Electric powertrain transmission design including NVH performance using specialized software

Supervisors

Prof. Enrico Galvagno

Prof. Gianmario Pellegrino

Candidate

Luca Ciravegna

Academic Year 2022-2023

Abstract

In recent years, due to the sadly well-known environmental problems concerning air pollution, the automotive field is moving towards greener solutions: the electrification of vehicles is becoming more and more important, even exceeding most forecasts.
The electrification of vehicles is spreading worldwide only recently, and the NVH (Noise, Vibration, Harshness) problem should be completely reconsidered, since the main noise and vibrations sources are changed with respect to conventional ICE (Internal Combustion Engine) vehicles. Furthermore, many noises that were totally inaudible in ICE vehicles, moving to electric vehicles can become really annoying since the masking effect of the engine is missing.
Therefore, the aim of this thesis is to propose a method to investigate in depth all the aspects concerning the NVH of electric powertrains, by exploiting the features of a commercial specialized software, Romax.
Before performing any dynamic analysis, static analyses are required, to understand if the system can bear the required loads of the duty cycle. Different versions of the model are evaluated, focusing on macro and micro-geometry modifications of the gears of the transmission system. It has been proved that the life of the components remarkably increases moving from spur gears to helical. Moreover, adding the proper microgeometry modifications it possible to even enhance the static performance, also centring the contact patch, which is another important goal of static evaluation.
Then, the dynamic analysis can be done, considering as excitation source the transmission error (TE) of both gear sets composing the transmission system, the unbalance of the rotor and the electromagnetic excitation coming from the electric motor. Considering the model with spur gears, it has been verified the supremacy of the vibration response due to TE excitation, rather than due to the other sources. Moving to helical gears, it is possible to strongly reduce the vibration response and the emitted noise caused by the TE excitation. Only adding proper microgeometry modifications, the response to electromagnetic excitation becomes the only relevant one, leading to almost negligible vibrations and noises produced by TE. Finally, a sensitivity analysis on the electric motor is performed, too, mainly considering modifications of the parameters of the motor, modifying the number of poles and slots.
As regards the dynamic analyses, not only results in terms of amplitude of forces and acceleration response are available, but also results directly related to sound and acoustic are obtainable, which are particularly important to gain information about the directivity of the sound.

The last considered aspect concerns the efficiency: it is indeed possible to compute the losses of both the mechanical and the electric components of the powertrain. It is demonstrated that microgeometry can also strongly help in enhancing the performance of gears even from the efficiency viewpoint.
This thesis represents a starting point useful to understand how to use the features of this commercial software to study in a pretty complete way all relevant aspects of the design of an electric powertrain. Future steps could require moving beyond just the simulation world, trying to correlate the results obtained by the software with some experimental data coming from an existing model. Further optimizations of the transmission system and other methodologies to reduce the noises and vibrations caused by the electric motor can be studied, such as considering for instance skewed rotors.

Acknowledgments

First of all, I wish to express my gratitude to my primary supervisor, Professor Enrico Galvagno, who really has supported me producing this thesis work. He has always been present and available to solve any doubt, giving a precious contribution to my work. Moreover, he puts me in connection with many relevant academic figures, helping me improving from the professional viewpoint. I would also like to thank Professor Gianmario Pellegrino, for helping me completing the part of the thesis related to the electric motor. Furthermore, I appreciated the support given by Dr. Simone Ferrari and PhD student Giorgio De Donno, who give me valuable advices and aid during some relevant parts of this thesis work. Moreover, the assistance provided by Romax support, in particular by Mr. Daniele Catelani and Mr. Matteo Iannone was very helpful and genuinely appreciated.
Then, I would like also to show my appreciation to all important people in my private life. The biggest thanks goes to my girlfriend, Noemi. She has always been on my side, she has always been present, supporting and motivating me every day. She is the only one who really knows all the difficulties and challenges that I have faced during these years. She is always my greatest supporter, and, without her, nothing would have been possible.
An huge thank is reserved to my parents, who always supported me: they give me the possibility to study what I liked and they make all of this possible. I wish to extend my gratitude to my grandparents and to all my family, for always believing in me. In particular, a big thank goes to my grandfather, Nonno Meco. Unfortunately he didn't have the possibility to see me during this path, but I am sure that he always supported me and I hope that I made him proud of me.
A special thanks for sure goes to my best friend Ale, who has always been present for me since the high school: we lived together many important steps of our lives. Then, I want to extend my thanks to all my classmates of Politecnico, with whom I shared many important moments during this period, both funny ones and desperate ones, especially during the tough exam sessions.
Finally, my last but not least thanks go to anybody who helped me growing professionally during my five years at Politecnico, and during my internship, too. I met wonderful people who certainly helped me and had a strong influence on me.

Luca Ciravegna

Table of Contents

List of Tables

List of Figures

Chapter 1

Introduction to NVH

In the automotive field, customers can be very demanding: different aspects can have a critical importance, such as performance of vehicles, fuel consumption, comfort of driver and passengers. Especially in the last few years, with the improving of people's living standards, the comfort has become one of the most important aspect to be considered and lot of car makers decided to strongly focus on it.
In terms of comfort, the vibroacoustic behaviour of the vehicle is of vital importance. To fully understand this behaviour a new field of study has been developed, called *NVH*.

1.1 Definition of NVH

Noise, Vibration and Harshness, NVH, is a measurement of the comfort of passengers from the vibroacoustic point of view. This is a critical aspect to be considered in the automotive field, since there are plenty of different noise and vibration sources that can generate discomfort to passengers. Noise and vibrations can induce stress and fatigue on the passengers, motion sickness, and can also affect driver's concentration. The sound isolation of the cabin of the vehicle assumes a critical role in the noise perceived by driver and passengers.
Going more in details with the definition of NVH:

- Noise: any unpleasant sound created by a mechanical vibration of an object in an elastic medium.
- Vibration: repetitive motion of an object in which energy is continuously exchanged between two different forms.
- Harshness: human perception of diseases generated by noises and vibrations. It is qualitative and subjective.

1.1.1 Noise

Noise is usually defined as a sound that causes some unpleasant, and sometimes even painful, effects on humans.
Acoustic studies the sound propagation, in particular it studies the propagation of mechanical energy that propagates through elastic waves from the source to the receiver (i.e. humans' ears in this case). To be able to propagate, the elastic waves need an elastic medium to propagate in, that can be solid, liquid or gaseous. The speed of the sound, c, depends on the property of the medium, however it is possible to link the speed with the sound wavelength, λ, and the frequency, f.

$$c = \lambda \cdot f$$

Sound sources produces a certain amount of energy per time, i.e. sound power (unit of measure: W), which does not depend on the characteristic of the environment. On the other hand, from the receiver point of view, the sound intensity that is measured on a certain place depends also on the characteristic of the medium. In other words, sound intensity depends on the amount of sound energy that is absorbed by the environment: in fact, it is defined as the ratio between the power transmitted by the wave from the source and the receiving surface, the unit of measure is W/m^2. Moreover, the sound pressure, indicated as Δp, is the local pressure difference between the environmental pressure and the pressure produced by the sound wave, the unit of measure is Pa.
Since the pressure depends on time, and being periodic, with period $\tau = 1/f$, it is possible to define the effective pressure:

$$\Delta p_{eff} = \sqrt{\frac{1}{\tau} \int_0^\tau \Delta p^2(t)\, dt}$$

Generally, sound is not characterized by only one frequency, if so it would be a *pure tone*, but it is more common to have a continuous spectrum made of many frequencies.
Humans' ear is sensitive to a very wide range of pressure, considering a pure tone with frequency $f = 1000\, Hz$, typically the range of audibility is defined by two thresholds. The lower threshold is called *lower limit of audibility*, with value $\Delta p_{eff} = 2 \cdot 10^{-5} Pa$, while the upper threshold is the *pain threshold*, with value $\Delta p_{eff} = 20 Pa$.
Being the range of audibility so wide, it is common to prefer a logarithmic scale rather than a linear one, using decibels (dB).
As regards the important quantities defined above (sound intensity, pressure and power), it is usually preferred to consider relative quantities rather than absolute ones: for a generic quantity x, with respect to a reference value x_0, the *level*, measured in dB, is equal to $L_x = 10 \cdot log\,(x/x_0)$.

Therefore, it is possible to define:

- Sound pressure level, with $\Delta p_0 = 2 \cdot 10^{-5}\, Pa$

$$L_p = 10 \cdot log \frac{(\Delta p_{eff})^2}{(\Delta p_0)^2} = 20 \cdot log \frac{\Delta p_{eff}}{\Delta p_0}$$

- Sound power level, with $W_0 = 10^{-12}\, W$

$$L_W = 10 \cdot log \frac{W}{W_0}$$

- Sound intensity level, with $I_0 = 10^{-12}\, W/m^2$

$$L_I = 10 \cdot log \frac{I}{I_0}$$

Therefore, considering the sound pressure level, the range of audibility is defined in the range $0 \leq L_p \leq 120\, dB$.
One of the most important variable concerning noise, or sound in general, as already anticipated, is the frequency. Humans' ear is sensitive in a frequency range from 16 Hz to 16 kHz (other studies state that the frequency range is from 20 Hz to 20 kHz). Sounds with higher frequencies are called *ultrasounds*, while if lower frequencies they are called *infrasounds*.
To be more effective, noise and vibration signals are analysed in frequency bands, the most common are *one octave* and *one-third octave*. In both cases, each band is defined by a central frequency, i.e. f_C, and a lower and an upper limit, f_L and f_U respectively.
In the case of one octave band, the thresholds of the band are: $f_L = \frac{f_C}{\sqrt{2}}$ and $f_U = \sqrt{2}\, f_C$. On the other hand, in the case of one-third octave band, the boundaries of the band are: $f_L = \frac{f_C}{\sqrt[6]{2}}$ and $f_U = \sqrt[6]{2}\, f_C$.
The human's ear is not equally sensitive to any frequency. To better understand this statement, an experiment was carried out. Different sounds within a certain frequency range are compared to sound at a reference value of frequency, i.e. 1000 Hz, and evaluating for which values of effective mean pressure the same feeling in booth cases is obtained.
Thus is possible to obtain a diagram, reported in Figure 1.1, called *normal audiogram*, in which the abscissa indicates the frequency within the audible range, while the ordinate indicates the pressure level. The curves plotted in the graph represent the iso-phon curve, which are the curves with equal sound sensation. Hence, looking at a certain value of pressure, it is possible to understand how the human sensation changes by varying the frequency.

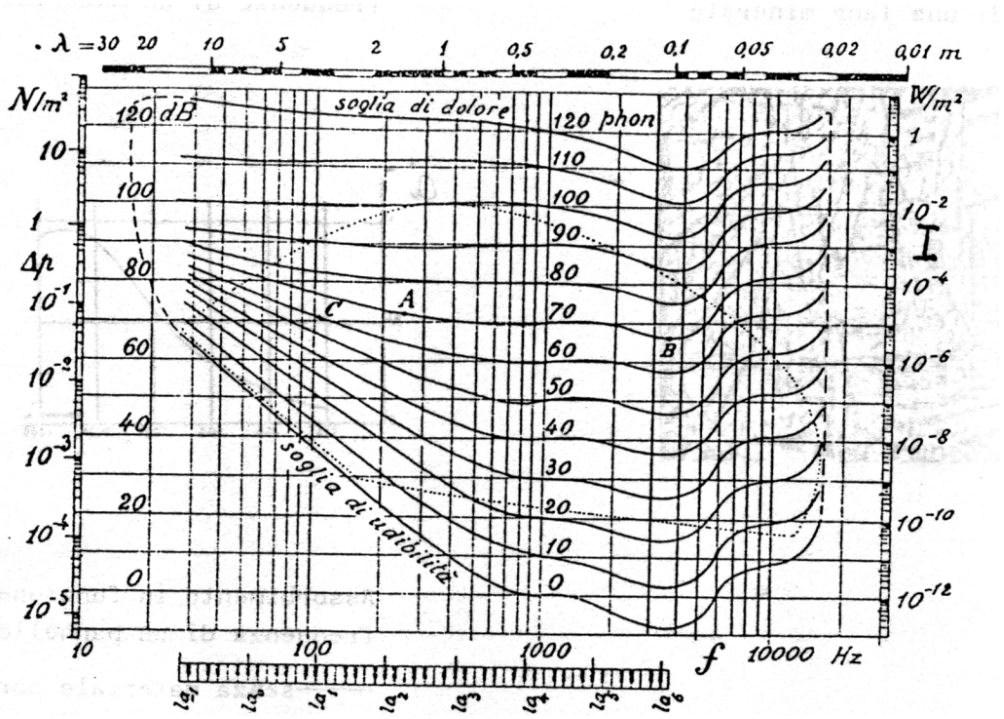

Figure 1.1: Normal audiogram [1]

From the graph, it is clear how, if the frequency is low, the iso-phon curves reach high values of pressure. This means that, to obtain the same acoustic feeling, if the frequency is lower, an higher pressure is required.
Moreover, it is shown that human's ear is more sensitive in a frequency range from 3000 Hz to 4000 Hz.
Notice that in the graph in Figure 1.1 the lower limit of audibility is indicated as *soglia di udibilità*, while the pain threshold is indicated as *soglia del dolore*.
Another aspect to consider when speaking about NVH is the so called sound quality, that can be analysed more in details focusing on psycho-acoustic. The most relevant psycho-acoustic auditory dimensions are the following:

- Loudness: it characterizes the auditory perception of the sound intensity or volume.
- Roughness: it quantifies the perception of amplitude fluctuations in the range from 20 Hz to 200 Hz.
- Sharpness: it describes the auditory perception of the sound density.
- Tonality: it extracts the tonal characteristic of a sound. It is related to the pitch of sounds.

1.1.2 Vibration

Vibration can be defined as repetitive motion of an object in which energy is continuously exchanged between two different forms.
Many studies have been carried out concerning people's discomfort due to vibrations and noise, some standards have been developed, too. Generally, it is possible to say that the level of discomfort caused by vibrations is linked to the root mean square value of the acceleration, to the frequency and to the time of exposure. The standard ISO 2631-1978 defines a plot, reported in Figure 1.2, that shows the vertical vibration exposure criteria curves. This plot indicates the time of exposure that a person can be subjected to in relation to a certain root mean square value of the acceleration, depending on the frequency. It can be clearly seen that the range between 4 Hz and 8 Hz is the one in which the impact on humans is the highest. The frequency axis ranges from 1 Hz to 80 Hz, since frequency below 1 Hz produce sensations similar to motion sickness, while, if frequency is higher than 80 Hz, the effect depends on the behaviour of the parts of the body. If frequency is not within the range from 1 Hz to 80 Hz, the effect is subjective, hence no general guidelines can be provided.

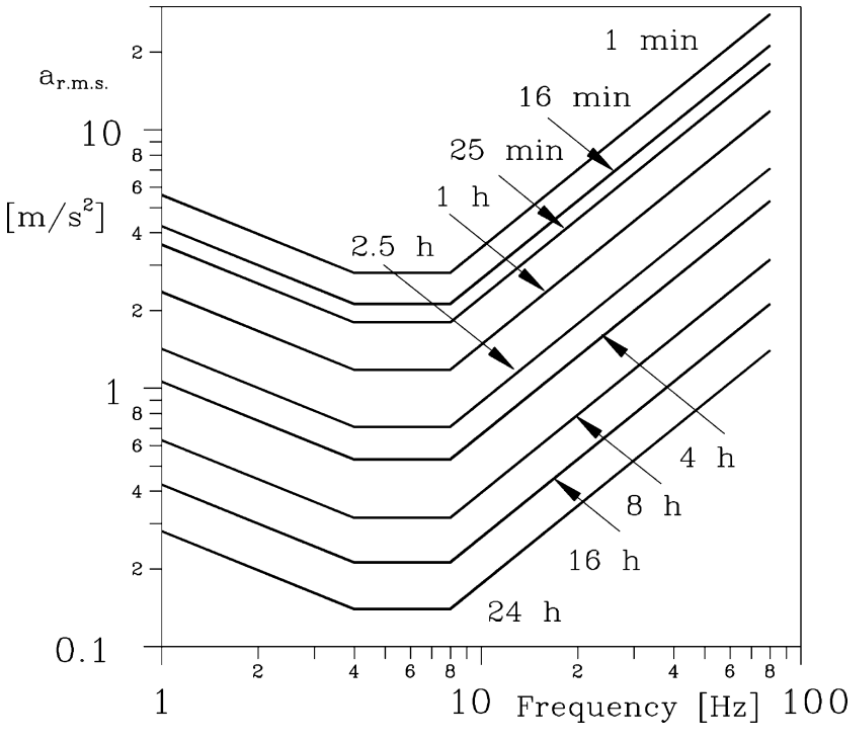

Figure 1.2: Vertical vibration exposure criteria curves, from ISO 2631-1978 [2]

Another important aspect to be considered is that external disturbances can interfere with the resonances of the human body organs, and, if so, the negative effects on comfort and on humans' health is even more remarkable. Some examples of resonances of human body organs are reported in the table below.

Thorax and abdomen	$3 \div 6\ Hz$
Head, neck and shoulders	$20 \div 30\ Hz$
Eyeball	$60 \div 90\ Hz$
Lower jaw and skull	$100 \div 200\ Hz$

In Figure 1.3 are represented the main effects of noise and vibration on the humans' body, depending on the frequency.

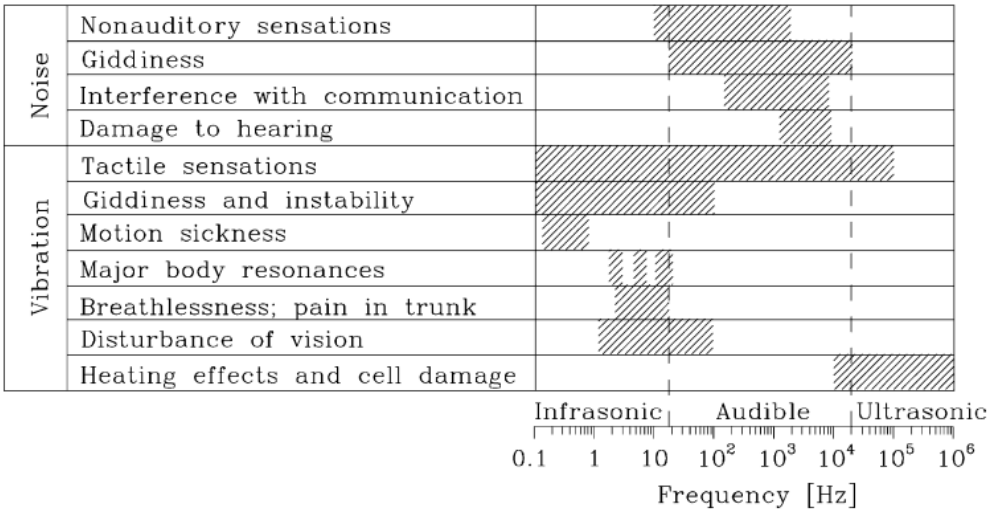

Figure 1.3: Effects of noise and vibration on humans' body [2]

1.2 New challenges of NVH

Nowadays, the environmental problems concerning air pollution are becoming more and more significant. Almost every field of any kind of industry is moving towards greener solutions, and no exception is made by the automotive world. Indeed, the rapid electrification of the vehicle sector is even exceeding most forecasts.
In figure 1.4, the sales forecasts by drive concept in Europe, USA, and China is shown.

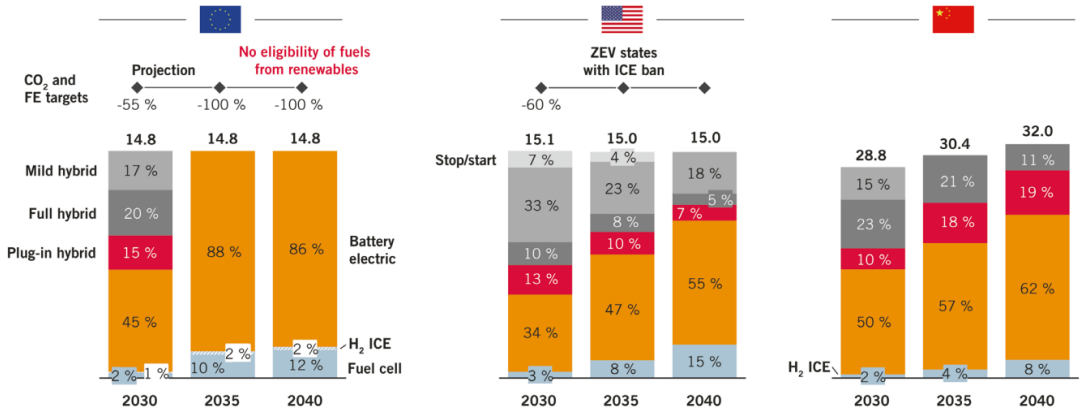

Figure 1.4: Sales forecasts in Europe, USA, China [3]

Hence, to reduce pollution produced by cars, the internal combustion engines (ICE) are being replaced mainly by two new solutions: hybrid electric vehicles (HEVs) and electric vehicles (EVs).
The main classification of these new drivetrains is the following:

- Electric Vehicle (EV)
  - Battery powered Electric Vehicle (BEV)
  - Hydrogen fuel cell Electric Vehicle (HyEV)
- Hybrid Electric Vehicle (HEV)
  - Micro and Mild HEV (MHEV)
  - Full-HEV (HEV)
  - Plug-in Hybrid Electric Vehicle (PHEV)

With the development of these new types of powertrains, a lot of new challenges must be faced. For instance, the problem of NVH should be completely revisited moving from ICE to HEVs and EVs.
In the development of this thesis work, the focus will be more on EVs, rather than on HEVs.
Changing the type of powertrain should lead, indeed, to a complete reconsideration of the NVH issue: the sources of noises and vibrations are completely different, since new components are now present. Moreover, also transmission paths can change.
The electrification of vehicles is spreading globally only in recent years: therefore, so far, the literature focused mainly on NVH issues related to ICE vehicles. However, since there are important differences in noises and vibrations between electric

powertrains and ICE, specific considerations must be performed and new studies should be carried out.
In this section, the main new challenges that should be overcome are briefly explained.
Typically, as can be also noticed thanks to Figure 1.5, electric drives are characterized by a comparatively low noise with respect to ICE, due to the relatively quiet electric motors.

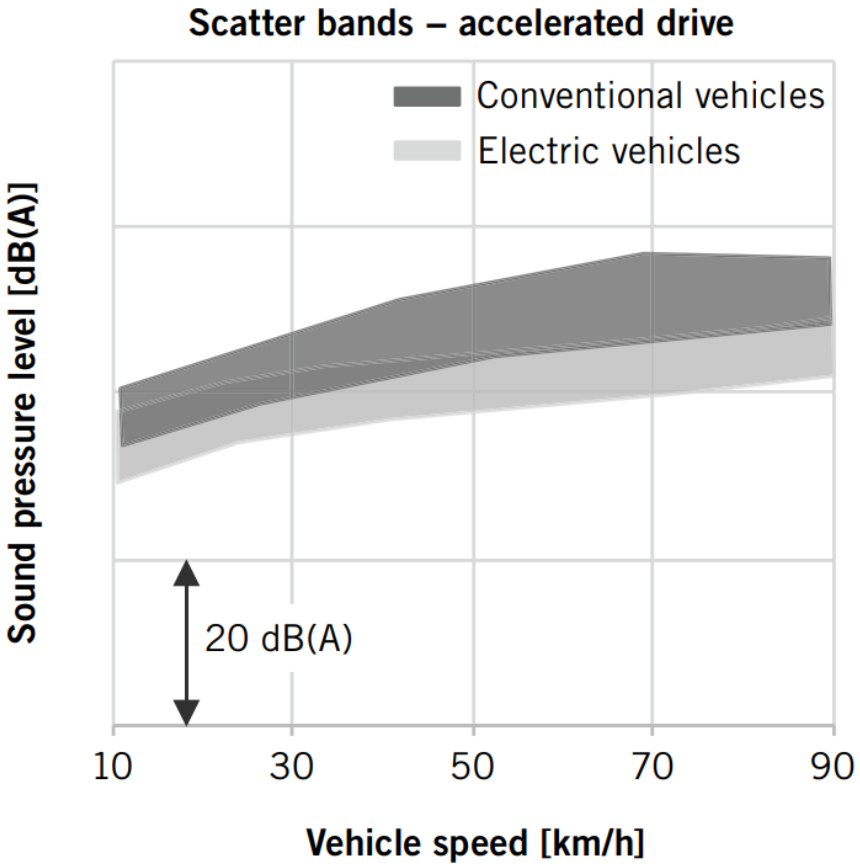

Figure 1.5: Interior vehicle noise, ICE vs EVs [4]

However, at the same time, the tonal noise typical of electric motors can be particularly disturbing. A tonal noise is obtained whenever a source emits noise that contains a very high amount of energy at a single value of frequency (similar to a pure tone). The problem is that tonal noise is generally more noticeable and more annoying than non-tonal noise of the same level. Tonal noise can become particularly disturbing if they are clearly identifiable in the overall noise. In order to mask tonal noises, it is more convenient to have masking sounds in the near frequency range, rather than using sounds with remarkably lower or higher

frequencies.
Masking is the phenomenon of a sound that interferes with the perception of another sound.
In Figure 1.6, the Campbell diagrams of the noise spectra of a battery electric vehicle is reported, both in the motor near field and at driver's ear position: the tonal orders are detectable, and effective masking should be performed.
Moreover, to effectively evaluate tonal sounds, the literature, and in particular FEV, developed a *tonality parameter*, which compares the energy content of a tonal noise to the energy of the corresponding one-third octave and to the overall energy. The values are a subjective evaluation from 1 (i.e. very bad) to 10 (i.e. not audible). Therefore, considering a certain tonality parameter target value, and a certain masking noise, then it is possible to evaluate the allowable level of tonal noise in each one-third octave band.

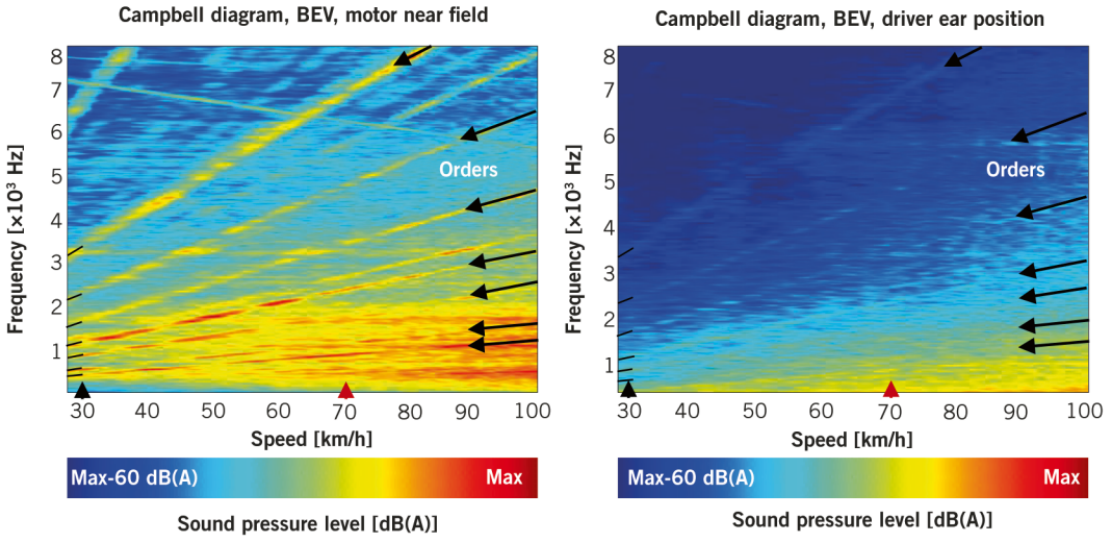

Figure 1.6: Tonal noise phenomena of an EV, in motor near field on the left, at driver's ear position on the right [3]

Another very important aspect to consider speaking about of NVH in EVs, as already anticipated, is that the masking effect of the ICE is totally missing. Therefore, a lot of noise contributions, that were negligible in vehicles equipped with ICE, in the case of EVs become significantly more important and they can potentially be a source of passengers discomfort.
In conclusion, the electrification of vehicles brings with itself a complete reconsideration of the NVH study of the whole vehicle.

1.3 Insights on the electric motor

In this section more details about the electric powertrain, and in particular about the electric motor, will be provided. As anticipated before, the main focus will be on EVs, rather than on HEVs.
The powertrain can be defined as the combination of all the components that generate power that will be transmitted to tyres in order to move the vehicle. The electric powertrain contains the inverter, the electric motor and the transmission system. Whereas, the electric motor drive is constituted by the electric motor, the inverter and the controllers.

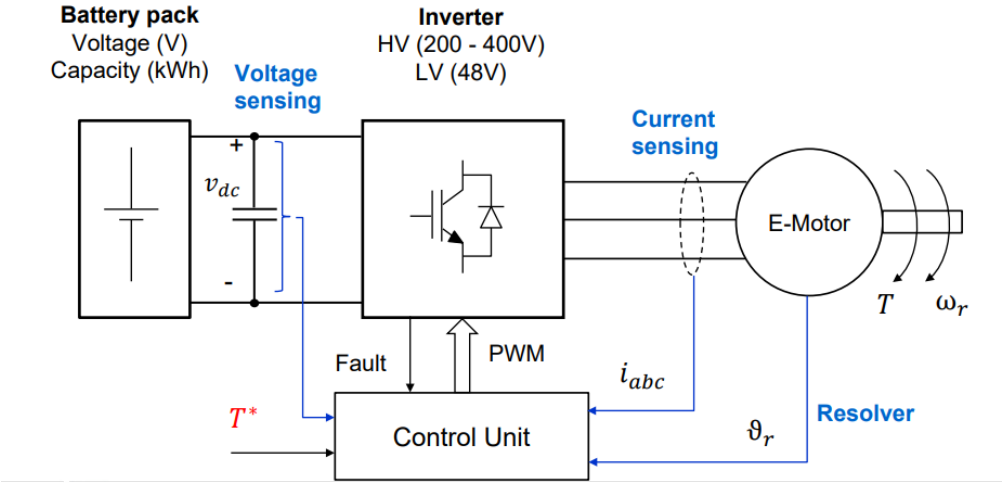

Figure 1.7: Scheme of an electric motor drive [5]

Focusing on the electric motor, different types are available:

- Brushed DC Motor
- Brushless DC Motor (BLDC)
- Permanent Magnet Synchronous Motor (PMSM)
- Induction Motor (IM)
- Switched Reluctance Motor (SRM)
- Synchronous Reluctance Motor
- Axial Flux Ironless Permanent Magnet Motor

Every type of motor has advantages and drawbacks, but it is possible to state that the majority of electric motors used in electric powertrains are Permanent Magnet

Synchronous Machines (PMSM). In order to better understand why PMSM is the most successful one, let's analyse more in detail its functioning and its main features.
PMSM is an example of PM brushless motor drive, but it is not the only one. Two different PM brushless motor drives can be selected, depending on the nature of the back-emf waveform:

- Trapezoidal or BLDC: this solution works as a DC machine but without brushes. A simple speed control is sufficient, hence the position sensor, required in order to ensure the synchronization of the current with the flux, can be a simple and low-cost Hall position sensor.
- Sinusoidal or PMSM: operates as synchronous machine. Sophisticated speed control are necessary, and therefore more complex and expensive position sensor, such as an encoder transducer of rotor angular position , is required.

The PM brushless machines become the most used for EVs due to their several advantages. Moreover, it is possible to say that, between the two different PM brushless motor, BLDC and PMSM, the latter is usually preferred for EVs, therefore the main focus from now on will be on PMSM. In fact, PMSM have traction characteristics, such as high power density and high efficiency. Moreover, PMSM are available for high power ratings, and they can operate in different speed ranges without using gear system, they are efficient, compact, eventually suitable for in-wheel applications, they can generate high torque even at low speeds. The main disadvantages are the costs and the iron loss at high speed during in-wheel operations.
Going more into details considering the structure of the motor, please refer to Figure 1.8.

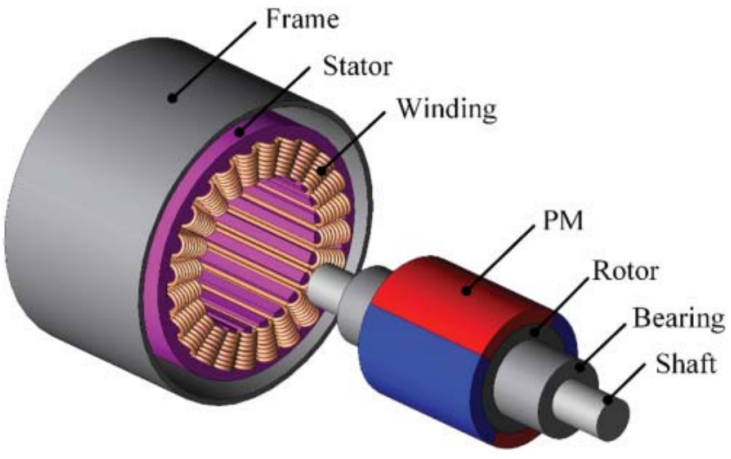

Figure 1.8: PM brushless motor exploded scheme [6]

The main components are the stator with the three-phase windings and a rotor which contains, in dedicated pockets, the permanent magnets.
Concerning the magnets, different materials can be selected. Their development started from the 1930s, as can be seen from Figure 1.9.

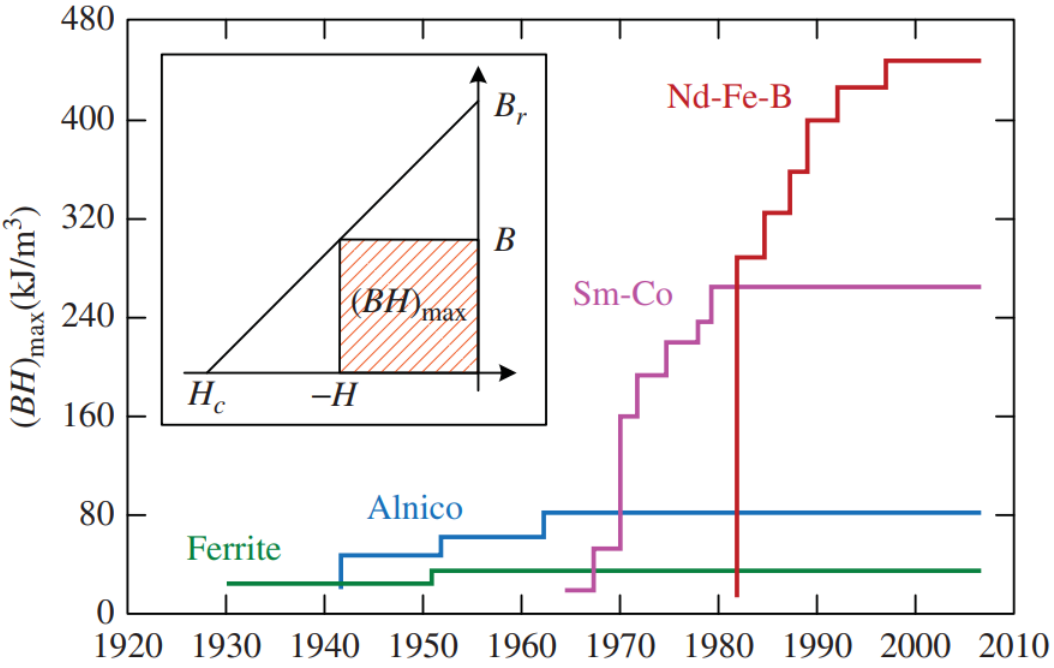

Figure 1.9: Development of most common PM materials over the years [6]

The main PM materials are the following:

- Ferrite: used since 1930. It is also used nowadays due of the abundance of raw material and low costs.
- Alnico: developed starting from 1940s, not very used nowadays since its coercivity is very low, hence it can be demagnetized easily.
- Sm-Co: rare-earth PM materials with lots of advantages, such as high remanence, coercivity, energy density, Curie temperature. The main drawback is the high cost.
- Nd-Fe-B: rare earth material with even better properties than Sm-Co. The only drawback is the not very high Curie temperature.

To better understand the properties just mentioned, recall that the remanence (B_r) indicates the strength of the produced magnetic field; the coercivity (H_c)

indicates the resistance to being demagnetized; the Curie temperature indicates the temperature above which the material loses its magnetization.
In Figure 1.9, the vertical axis (BH_{max}) indicates the maximum product of an operating point on the characteristic, that indicates the energy density.
As soon as the windings are fed with three-phase sinusoidal currents, a synchronously rotating sinusoidal air gap flux is created. Therefore, the rotor with the same number of poles as the rotating air gap flux rotates in synchronism, which depends on the applied frequency.
Depending on the placement of the PMs, two different configurations are possible:

- Surface Permanent Magnet (SPM)
- Interior Permanent Magnet (IPM)

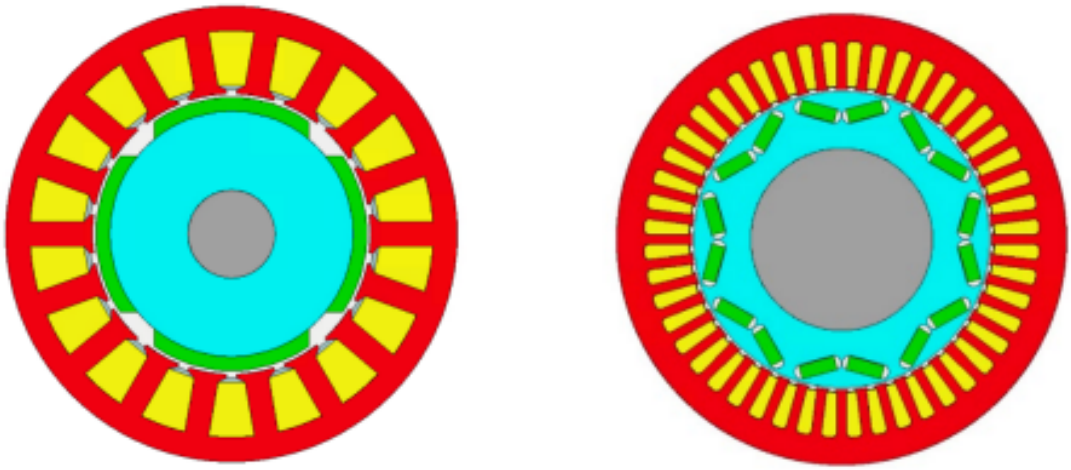

Figure 1.10: SPM on the left, IPM on the right [5]

Considering the windings, two different cases are possible:

- Distributed Windings (DW): the end turns connect non-consecutive slots. Moreover, end turns of phases do overlap. The overlapping leads to manufacturing complexity, lenghty ends result in additional losses and bigger size.
- Concentrated Windings (CW): each phase is made of coils wounded around a single tooth. Moreover, end turns of different phases do not overlap. Hence the manufacturing is easier, the losses are less and shorter ends cause longitudinal compactness.

Generally, BLDC motors have concentrated windings, whereas PMSM have distributed ones.

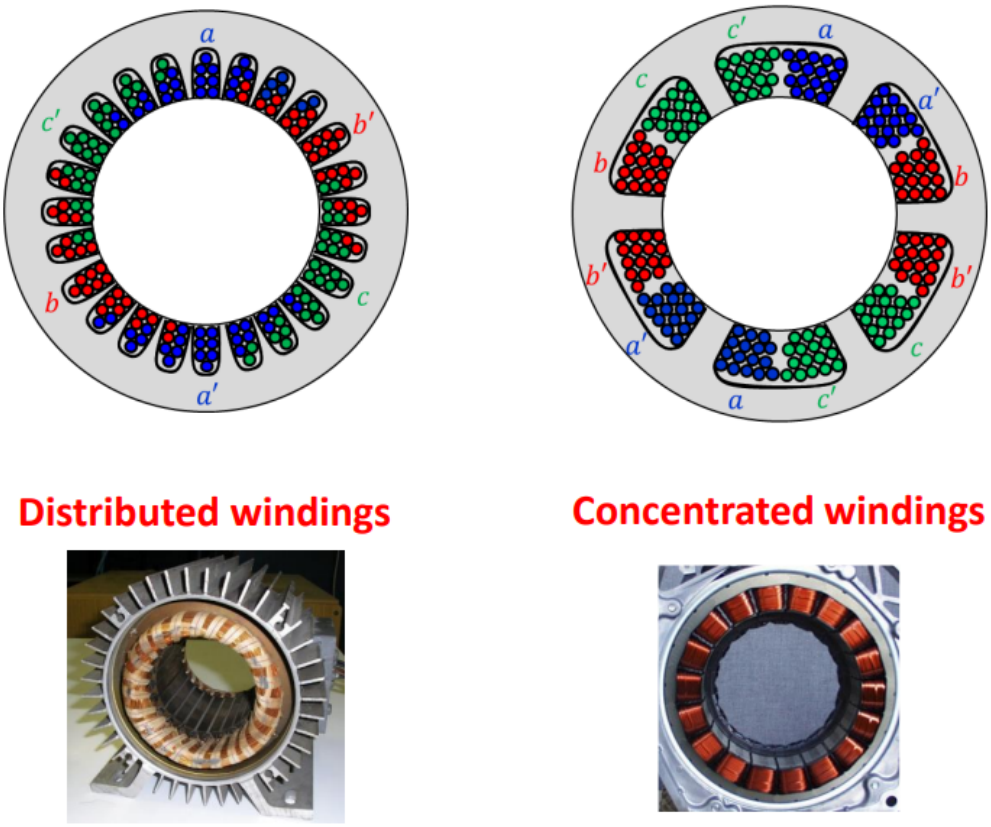

Figure 1.11: Distributed and Concentrated windings [5]

1.3.1 PMSM working principle

To summarize, the magnetic poles produce an excitation field that is rotating at the rotational speed of the rotor, the torque production requires the slot currents to be synchronized to the rotor field independently of the rotor speed. The rotor phase angle determines the phase of the back-emf sinusoids: a rotor positions transducer (i.e. encoder or resolver) is required to synchronize the stator currents to the rotor phase angle.
The working principle of PMSM is based on the interaction of sinusoidal back-emf waveforms and sinusoidal windings current waveforms, in particular it should balance the three-phase sinusoidal distribution of air gap flux and sinusoidal distribution of windings.

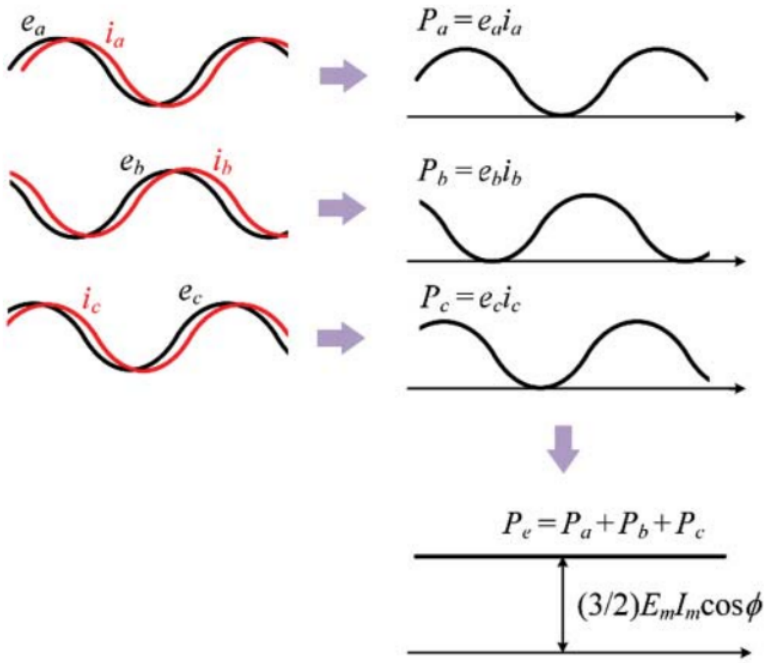

Figure 1.12: Power production of PMSM [6]

It is possible to express the three-phase induced back-emf waveforms as follows:

$$e_a = E_m sin(\omega t)$$

$$e_b = E_m sin(\omega t - 120°)$$

$$e_c = E_m sin(\omega t - 240°)$$

with E_m amplitude of back-emf and ω the angular frequency.
The three-phase sinusoidal currents can be expressed as:

$$i_a = I_m sin(\omega t - \Phi)$$

$$i_b = I_m sin(\omega t - 120° - \Phi)$$

$$i_c = I_m sin(\omega t - 240° - \Phi)$$

with I_m amplitude of current waveforms and Φ the phase difference with respect to the back-emf waveforms.
It is therefore possible to evaluate the converted electrical power as follows:

$$P_e = e_a i_a + e_b i_b + e_c i_c = \frac{3 E_m I_m}{2} cos\Phi$$

Finally, the produced torque (constant at given speed ω_r) will be:

$$T_e = \frac{P_e}{\omega_r} = \frac{3E_m I_m}{2\omega_r} cos\Phi$$

To obtain the maximum torque, it is necessary to set $\Phi = 0°$. In case of PMSM, it is convenient to refer to dq frame of reference. This is a frame which is rotating at speed $\omega_e = d\theta/dt$. The PM flux linkage is aligned with d, the stator axis is indicated as A and it is the direction of the maximum magnetomotive force, θ indicates the angle between q and the stator axis.

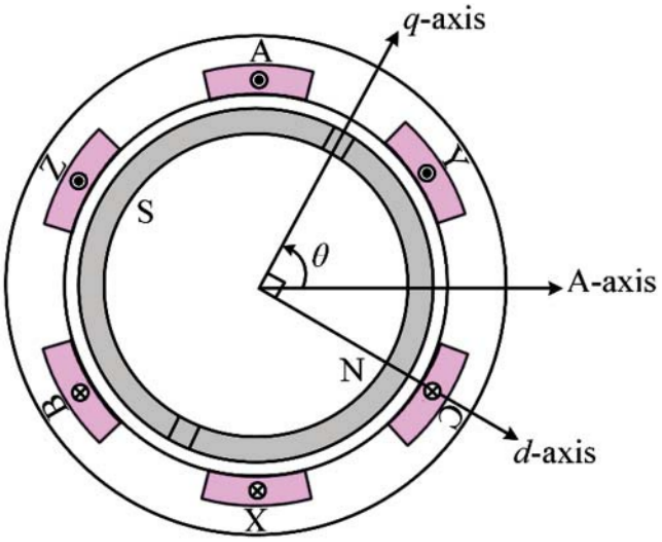

Figure 1.13: Scheme of PMSM in dq frame of reference [6]

Considering voltage, current, back-emf, magnetic saturation as sinusoidal, and neglecting hysteresis losses and eddy currents, the voltage equation of PMSM for the three phases can be written as:

$$\begin{bmatrix} v_a \\ v_b \\ v_c \end{bmatrix} = R_s \begin{bmatrix} i_a \\ i_b \\ i_c \end{bmatrix} + \frac{d}{dt} \begin{bmatrix} \lambda_a \\ \lambda_b \\ \lambda_c \end{bmatrix}$$

with v_i (with i=a,b,c) instantaneous three-phase stator voltages, i_i (with i=a,b,c) instantaneous three-phase stator currents, R_s armature resistance, λ_i (with i=a,b,c) instantaneous three-phase flux linkages:

$$\begin{cases} \lambda_a = L_{aa} i_a + L_{ab} i_b + L_{ac} i_c + \lambda_{ma} \\ \lambda_b = L_{ab} i_a + L_{bb} i_b + L_{bc} i_c + \lambda_{mb} \\ \lambda_c = L_{ac} i_a + L_{bc} i_b + L_{cc} i_c + \lambda_{mc} \end{cases}$$

with L_{ij} (with i=a,b,c, j=a,b,c) mutual inductances (symmetrical functions of angle θ), and λ_{mi} (with i=a,b,c) instantaneous three-phase PM flux linkages.
Please notice that, in the case of surface permanent magnets (SPM), the rotor is isotropic since the air gap is constant. Therefore, the phase inductance L is independent of the rotor position, hence the mutual terms simplify and it is possible to simply write $L_{ij} = L_s$ (with i=a,b,c, j=a,b,c). L_s is called synchronous inductance. Hence, if SPM it can be written:

$$\begin{bmatrix} \lambda_a \\ \lambda_b \\ \lambda_c \end{bmatrix} = L_s \begin{bmatrix} i_a \\ i_b \\ i_c \end{bmatrix} + \begin{bmatrix} \lambda_{ma} \\ \lambda_{mb} \\ \lambda_{mc} \end{bmatrix}$$

This simplification just performed is valid only in case of SPM. On the other hand, if internal permanent magnet (IPM), the rotor is anisotropic.

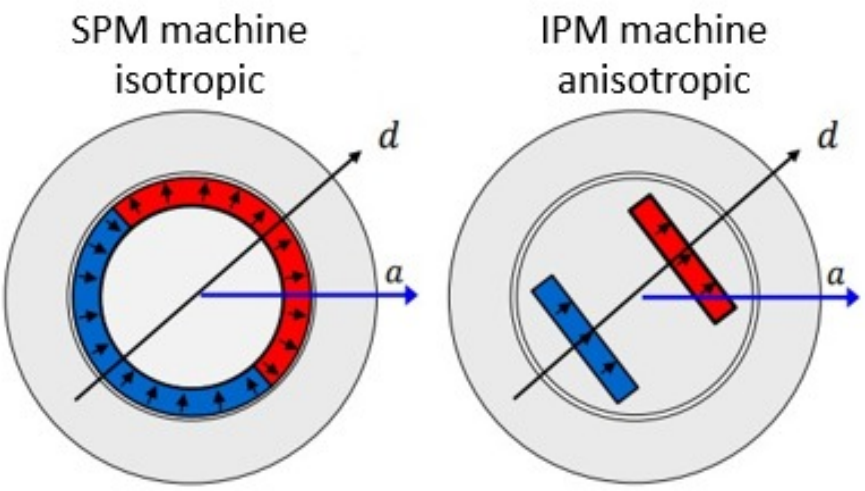

Figure 1.14: SPM: isotropic rotor; IPM: anisotropic rotor [5]

It is then possible to rewrite the d and q components of stator voltages as follows:

$$v_{dq} = R_s i_{dq} + \frac{d}{dt}\lambda_{dq} + j\omega\lambda_{dq}$$

with $R_s i_{dq}$ Joule losses, $\frac{d}{dt}\lambda_{dq}$ flux variation and $j\omega\lambda_{dq}$ motional term.
Separating the two components:

$$\begin{cases} v_d = R_s i_d + \frac{d\lambda_d}{dt} - \omega_e \lambda_q \\ v_q = R_s i_q + \frac{d\lambda_q}{dt} + \omega_e \lambda_d \end{cases}$$

with i_d and i_q the d and q components of stator current, respectively, and λ_d and λ_q the d and q components of flux linkages, expressed as:

$$\begin{cases} \lambda_d = L_d i_d + \lambda_m \\ \lambda_q = L_q i_q \end{cases}$$

with L_d and L_q d and q components of synchronous inductances, respectively, and λ_m the PM flux linkage. Note that, if SPM, then $L_s = L_d = L_q$.
Now, it is possible to evaluate input power of the machine:

$$P_s = v_a i_a + v_b i_b + v_c i_c = \frac{3}{2}(v_d i_d + v_q i_q)$$

Substituting the expressions of v_d and v_q inside the expression of the input power P_s, after some simple mathematical passages that are here omitted, it can be written:

$$P_s = \frac{3}{2} R_s \left(i_d^2 + i_q^2\right) + \frac{3}{2}\left(\frac{d\lambda_d}{dt} i_d + \frac{d\lambda_q}{dt} i_q\right) + \frac{3}{2}\omega_e \left(\lambda_d i_q - \lambda_q i_d\right)$$

The first term represents the Joule loss in R_s (P_{Cu} in Figure 1.15), the second term represents the magnetizing power, while the third term indicates the electromagnetic power P_e.
Finally, the electromagnetic torque T_e can be derived as follows:

$$P_e = \frac{3}{2}\omega_e \left(\lambda_d i_q - \lambda_q i_d\right) = T_e \omega_r$$

$$\omega_r = \omega_e / p$$

$$T_e = \frac{3}{2} p \left(\lambda_m i_q + \left(L_d - L_q\right) i_d i_q\right)$$

with p number of pole pairs. Remember that if SPM $L_d = L_q$.

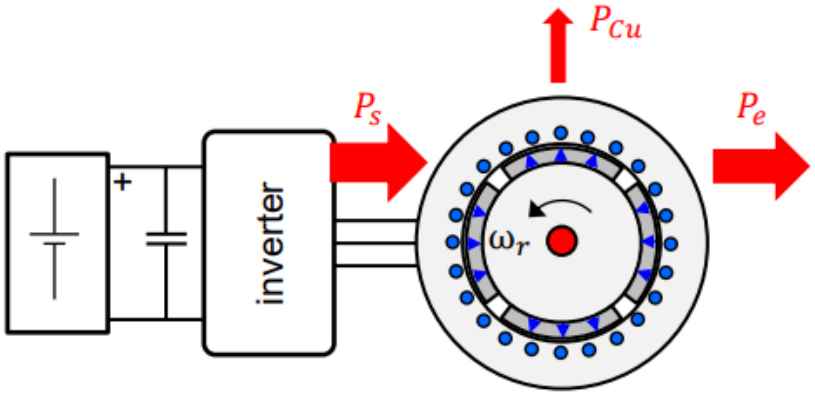

Figure 1.15: Power balance in PMSM [5]

The first component of T_e represents the PM torque, while the second one the reluctance torque (present only if IPM). The presence of the reluctance torque allows the motor to have flux weakening capability, for possible constant power speed range. Since at the base speed the terminal voltage reaches the rated voltage, and since the back-emf grows with speed, in order to increase the speed range the only possible choice is to perform flux weakening (i.e. reduction of air gap flux): the torque decreases while the speed increases, resulting into constant power.
In case of IPM, many geometries are allowed, reported in Figure 1.16. From left to right, since the anisotropy is increasing, then the reluctance torque is increasing, too.

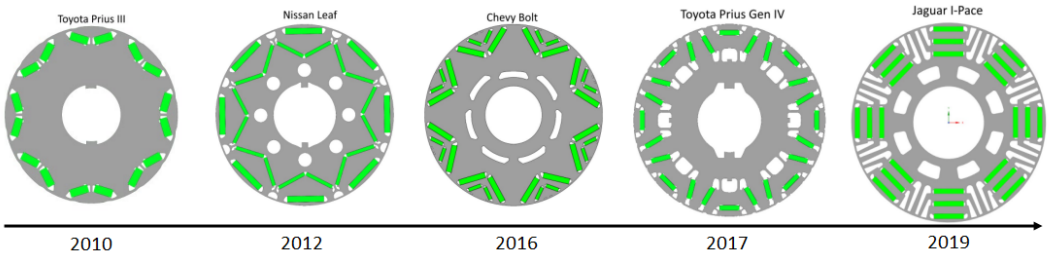

Figure 1.16: Different geometries of IPM [5]

1.3.2 Inverter

The PMSM is an example of brushless AC machine. Being an AC machine, it is crucial the presence of the power electronic converter (i.e. the inverter), that will convert the DC current, coming from battery, into AC one.
PMSM requires to be fed by sinusoidal current. To obtain this, it is possible to use a three-phase full-bridge inverter. The most used switching scheme is the pulse-width modulation (i.e. PWM), which allows to control electric motors at variable speeds. This switching scheme feeds the stator windings with quasi-sinusoidal current waveforms with variable frequency.

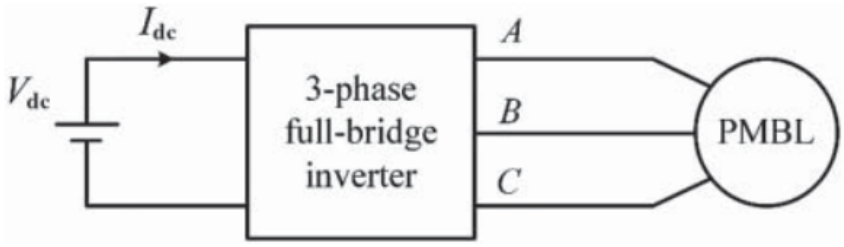

Figure 1.17: Scheme of PM brushless (PMBL) motor drive [6]

Electric vehicles require motors that allow four-quadrant characteristics: forward (FWD) motoring and regeneration, backward (BWD) motoring and regeneration. Referring to Figure 1.17, the input voltage is the one from the battery (i.e. V_{dc}), the input direct current I_{dc} is bidirectional, the motor speed depends on the stator frequency, and its polarity depends on the phase sequence.
If forward motoring, it is required that both the input and the output powers of the inverter should be positive, resulting in positive torque and speed. The battery voltage is positive, hence the average input I_{dc} should be positive. Being the motor speed positive, too, it means that the phase sequence of stator terminals should be positive, i.e. A-B-C. On the other hand, if forward regeneration, the speed is positive, but torque is negative, resulting in negative input and output powers of the inverter. Therefore I_{dc} will be negative, while, being the motor speed positive, then the phase sequence of stator terminals will remain positive. Similar reasoning are valid even as regard the backward motoring and regeneration. The only difference is that, being the motor speed negative, then the phase sequence of stator terminals will be negative, i.e. A-C-B.

	Quadrant	Torque	Speed	I_{dc}	AC sequence
FWD motoring	I	positive	positive	positive	positive
BWD regeneration	II	positive	negative	negative	negative
BWD motoring	III	negative	negative	positive	negative
FWD regeneration	IV	negative	positive	negative	positive

Different modulation techniques can be selected. A first distinction is between *on-line* techniques and *off-line* ones. The former indicates a modulation technique in which the switching angles are computed during the operation, whereas the latter indicates cases in which switching angles are computed off-line, as the name suggests.
Without going too in depth into the details, some common modulation techniques are space vector modulation (SVM), either optimized or randomized, or off-line optimized pulse patterns (OPPs).
As anticipated, the PWM creates additional currents harmonics in the windings, which lead to additional flux harmonics, resulting in additional force harmonics.
The aim of modulation techniques is to control the amplitude of the fundamental harmonic component and to reduce higher harmonics, too.

1.4 Sources of noise and vibration

In this section, the main sources of noise and vibration in a electric vehicle are analysed more in details.
As it was already anticipated before, any noise and vibration, in order to be felt by passengers, must pass through a certain transmission path.
Two different kinds of paths are possible:

- *Airborne noise path*, if the noise arrives to passengers through the air.

- *Structure-borne noise path*, if noise or vibration is transmitted to passengers through the structure of the vehicle.

Usually, it is possible to say that structure-borne noise is predominant below 400 Hz, whereas airborne one becomes more important above 400 Hz. The type of transmission path is very important, since it helps to understand which is the best way to follow in order to reduce the noises and vibrations.
Another important distinction that can be made considering the noise and vibrations that are felt by passengers concerns the source:

- *Powertrain noise*, which indicates any noise coming from the powertrain itself, and that is transmitted to passengers through some transmission paths.
  In case of electric vehicles, powertrain noise is constituted by two main sources: the transmission systems and the electric motor.

- *Rolling noise*, which indicates any noise coming from the interaction between the vehicle and the external environment. In particular it can be divided in road noise (i.e. coming from contact between tyre and road) and in aerodynamic noise (i.e. coming from the air flow to which the vehicle is subjected). Typically, the rolling noise is the most important contribution in case of high speeds.

In Figure 1.18, an overview of the main noise and vibration sources is showed. More details about each kind of source will be given in the following sections.

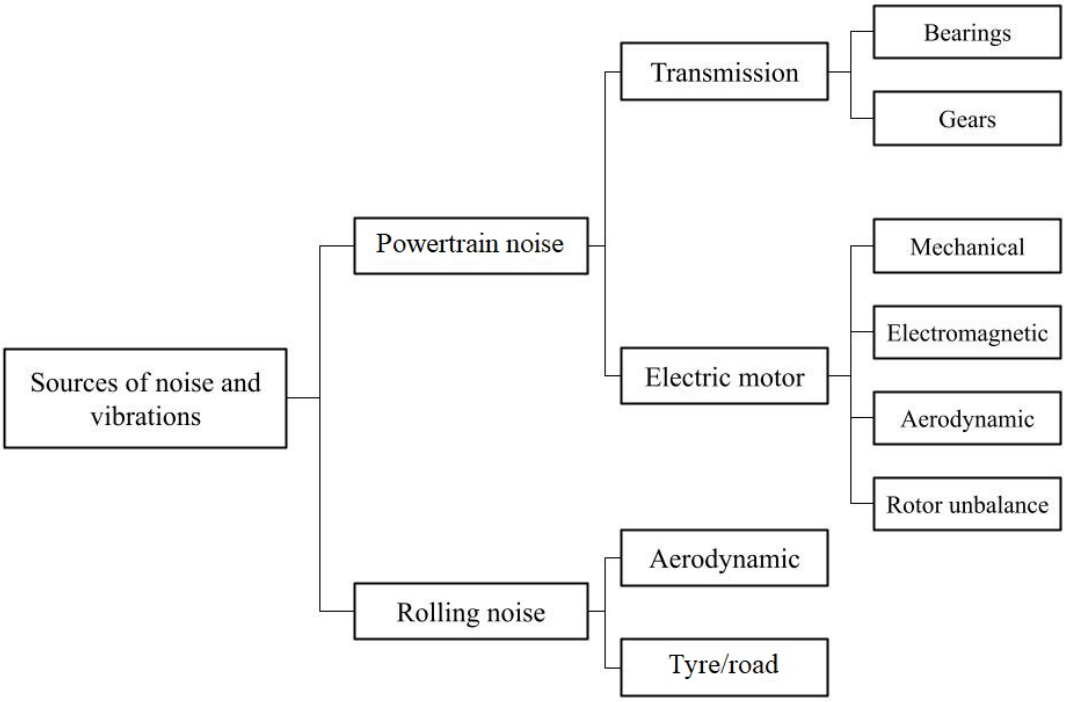

Figure 1.18: Overview of noise and vibration sources

1.4.1 Rolling noise

Road noise

Generally, some studies, such as [7], demonstrated that the road noise increase logarithmically with speed, in particular there is approximately an increase of 10 dB for each doubling of the vehicle speed.
Tyre/road noise is not so easy to be determined, since it depends on several factors. The type and quality of tyres have a strong influence, since it has been demonstrated that there is a range up to 10 dB between the best and the worst tyre.
Another important aspect to be considered concerns the influence of pavements. Some studies such as [7] demonstrated that a difference of about 10 dB can be noticed changing the type of road, from a *quiet* one to a *noisy* one.
Moreover, the weather conditions can also have a strong influence on this type of noise. In general, if the environment temperature increase, the noise decrease, in a range of about 4 dB. The noise level also changes depending on the fact if the road is either wet or dry.

There are several generation mechanisms of the tyre/road noise and vibrations. The main distinction is between structure borne and airborne ones:

- Structure borne:
  - Tread impact: impact of tyre tread on road surface
  - Texture impact: impact of road surface texture on the tyre tread
  - Running deflection: deflection of tyre tread at trailing and leading edges
  - Stick/slip: relative motion of tyre tread with respect to the road surface
- Airborne:
  - Air pumping: air displaced into/out of cavities between tyre tread and road surface
  - Air turbulence: turbulence around tyre due to tyre displacing air during rolling

Most of the times, the road noise is a structure-borne noise: the vibrations are transmitted from the road to the passenger through a certain path within the vehicle resulting in a low-frequency noise. The typical path of this vibrations is from the tyre to the spindle, then to the chassis through the suspensions and finally to the occupants of the cabin.
However, there is also a component of the road noise that transmits through airborne noise path. This happens if the noise generated at tyres propagates either under the vehicle and then it is transmitted through the floor panels, or if it propagates around the body of the vehicle and it is transmitted to passengers through body panels. This contribution is more significant in case of high frequency.
The tyre/road noise which is transmitted through airborne noise path is caused by movements of the air, mainly the pumping effect in the zone between the tyre tread and the road.
Moreover, some amplification effects can be present, too: the most important one is the so called *horn effect*. The horn is defined by the volume between the tyre leading and trailing edges and the road itself. The matching of the acoustic impedance in the horn and the ambient one results in a sound amplification.

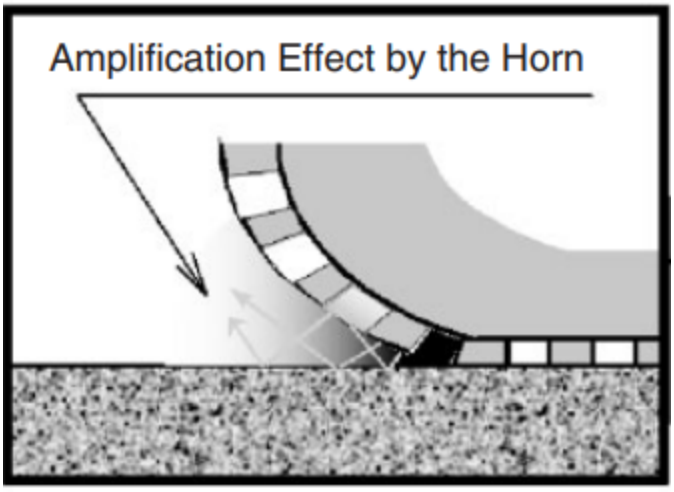

Figure 1.19: Horn effect [7]

Aerodynamic noise

The aerodynamic noise is generated by the interaction of the air flow around a vehicle with the vehicle body structure. The pressure fluctuations cause structural vibration that can be felt as noise inside the cabin. The design of the vehicle geometry is very important in order to try to reduce this produced noise: abrupt changes in the geometry, or appendages such as external rear-view mirror, increase the turbulent boundary layer, resulting in an increase of the noise.
Usually, if the vehicle speed exceeds 130 km/h, then the aerodynamic noise is more relevant than the road one, and it will increase with speed to the sixth power.
Typically, the aerodynamic noise is transmitted through air by airborne noise paths.

1.4.2 Electric motor noise

From now on, let's focus more in the powertrain noise, in particular the main interest is on the electric powertrain. Let's recall the definition of the powertrain, which is the combination of all the components that generate power that will be transmitted to tyres in order to move the vehicle, containing therefore the inverter, the electric motor and the transmission system.
Powertrain noise includes any sound from all sources associated with generating and supplying power to move the vehicle. Any component is source of noise or vibrations that can be transmitted either by a structure-borne path or by an airborne one.
Going more in the details, it is possible to say that the two most important sources of noise of an electric powertrain are related to either the electric motor or to the

transmission system.
The powertrain noise consists of a set of rotational speed proportional harmonics which are dominated by electric motor harmonics and transmission noise.
Let's firstly focus on the noise produced by the electric motor.
The sources of noise and vibrations of the electric motor can be distinguished in:

- Mechanical source: noise generated by mechanical components of motors, such as fasteners and bearings.
- Electromagnetic source: it refers to vibrations produced within the motor due to the electromagnetic forces. It is either caused by PWM harmonic of the power supply control-unit or by excessive electromagnetic harmonics coming from the motor.
- Aerodynamic source: generated by the fans, ventilation ducts, the rotating rotor, airflow effect.
- Unbalance of the rotor: it can causes relevant vibrations especially at high speeds.

The intensity of electromagnetic noise is mainly dependent on the load, while aerodynamic and mechanical ones depend more on the vehicle speed.
As already indicated in section 1.3, the following considerations are performed considering a permanent magnet synchronous motor.

Mechanical sources

It is usually characterized by low frequency, therefore it is less annoying for humans' ear.
Considering the noise produced by the bearings, it is strongly dependent on the manufacturing quality of these components.

Electromagnetic sources

Electromagnetic sources represent usually the most important contribution to the noise produced by an electric motor.
Electromagnetic noise can be either caused by the PWM harmonic of the power supply control-unit, or by excessive electromagnetic harmonics coming from the motor. Let's start by analysing the latter.
Electromagnetic forces are active in the air gap between stator and rotor, and they are characterized by rotating or pulsating power waves.

Several reasons that generate noise due to the variation of electromagnetic forces:

- Maxwell forces: forces acting on rotor and stator teeth. It is possible and convenient to decompose this kind of force in two components: the radial one and the tangential one. The former acts on the inner surface of the stator and its teeth. The latter produces electromagnetic torque, but it also causes vibration of rotor teeth and torque ripple (i.e the torque undulation caused by neglected non-fundamental effects).
- Laplace forces: forces that act on stator coils causing the vibration of the stator itself.
- Cogging torque: parasitic torque created by attraction forces generated by stator teeth and permanent magnets of rotor. Its periodicity per revolution depends on the number of magnetic poles and the number of teeth on the stator. It can be explained as the tendency of the rotor to align in a certain number of stable positions even if there is no current. Being a parasitic torque, it does not contribute to the net effective torque, but it can induce undesired vibrations. Cogging torque is affected by several parameters, such as the slot and pole number, the air-gap length, magnet thickness, disposition of the magnets, skewing of slots and magnets. Generally, some studies, such as [8], demonstrate that the larger is the smallest common multiple between the slot number and the poles number, and the smaller the number of slots or poles, then the smaller will be the resultant cogging torque.

Some studies in literature prove that, considering the electric motor, the main excitation source is represented by the Maxwell forces, therefore more details about those forces will be given in the following pages.
As anticipated, Maxwell forces can be distinguished in radial and tangential ones, and both components represent important sources of excitations and vibrations. Not only the global effect (i.e. torque ripple and also cogging torque according to [9]) is critical to be analysed, but local components (considering both radial and tangential) acting directly on teeth are responsible for vibrations, too.
To obtain the force harmonics of both radial and tangential forces based on periodicity of the magnetic field, as expressed by [10], [11] and [12], it can be useful to refer to Maxwell's stress method. It is assumed that the machine is working in steady-state and that the current is three-phase symmetrical but not necessarily sinusoidal. Maxwell's stress method allows to express the radial (σ) and tangential (τ) force density as follows:

$$\sigma = \frac{1}{2\mu_0}\left(B_r^2 - B_\theta^2\right)$$

$$\tau = \frac{1}{\mu_0} B_r B_\theta$$

Where μ_0 is the air permeability, while B_r and B_θ are respectively the radial and tangential component of the magnetic flux density in the air-gap. All these four quantities (force densities and magnetic flux densities) depend both on space and on time. These equations clearly show that the force density depends on flux density: therefore, if any periodicity is noted in the magnetic field, then even the force density will be periodic.
The magnetic field fluctuates periodically with the current and the rotor's rotation. Due to the periodicity of the current and due to the symmetry of the rotor, the temporal period of the magnetic field is equal to the electrical period. Considering that the current is antiperiodic, and that the magnetic polarities of the successive magnets are reversed, [9] states that the magnetic field respects the following condition:

$$B_{r,\theta}(t) = -B_{r,\theta}\left(t + \frac{T_t}{2}\right)$$

with t indicates the time, while, T_t indicates the electrical period.
Moreover, the magnetic field varies periodically not only with respect to the time, but also to the angular coordinate θ. The spatial period of the force density can be equal to the one of the magnetic field, or the half of that, depending on whether the magnetic field satisfies the following condition or not.

$$B_{r,\theta}(\theta) = -B_{r,\theta}\left(\theta + \frac{T_s}{2}\right)$$

with T_s indicates the spatial period of the electromagnetic field.
Magnetic field is composed by two main components: PM field and armature one, but more details will be given in the following pages.
The analysis performed by [9] states that the number of basic PM field units can be expressed by the greatest common divisor between the pole-pairs p and the number of slots N_s (i.e. $GCD(p, N_s)$). It can be demonstrated that:

$$GCD(p, N_s) = \begin{cases} p/d, & \text{if d is an odd number} \\ 2p/d, & \text{if d is an even number} \end{cases}$$

If d is an odd number, the first row is valid, and the condition concerning $B_{r,\theta}(\theta)$ is satisfied, on the other hand, if d is even, then that condition is not satisfied.
Armature field is generated by the windings, and it can be proven that the number of basic winding units can be denoted with $GCD(p, N_s)$, and again the condition concerning $B_{r,\theta}(\theta)$ is satisfied only if d is odd.
Hence, spatial periods of both radial and tangential force density are both $2\pi/(2p/d)$, independently from the load or no-load condition.
According to Fourier series, it is possible to rewrite the radial and tangential force density as:

$$\sigma(\theta, t) = \sum_u \sum_v H_{u,v} cos(u\omega_e t + v\theta + \phi_{u,v})$$

$$\tau(\theta, t) = \sum_u \sum_v H'_{u,v} cos(u\omega_e t + v\theta + \phi'_{u,v})$$

with u, v respectively temporal order and spatial order, $H_{u,v}$, $H'_{u,v}$ are amplitudes, $\phi_{u,v}$ and $\phi'_{u,v}$ phases. It has been proved that u is even and v is an integer multiple of $GCD(2p, N_s)$. Hence, spatial and temporal distribution of tangential and radial force harmonics have the same structure.
[11] states that the deformation amplitude, is inversely proportional to the fourth power of the mode number, therefore the low modes are the most critical in terms of amplitudes. This is a very important and strong statement, which is demonstrated by [13].
As anticipated, the spatial order is an integral multiple of $GCD(2p, N_s)$, hence the lowest spatial harmonic is exactly the $GCD(2p, N_s)$. For this reason, generally, motors with low values of $GCD(2p, N_s)$ lead to high vibration level.
Let's now focus more on the global component, too [9]. The torque of the motor can be obtained by integrating the tangential force density in the air-gap:

$$T_m = r^2 L_{ef} \int_0^{2\pi} \tau(\theta, t) d\theta =$$

$$= 2\pi r^2 L_{ef} \sum_u H'_{u,v}|_{v=0} cos(u\omega_e t + v\theta + \phi'_{u,v}|_{v=0})$$

with r is the radius of the integral path, and L_{ef} is the active length of the machine. From the last equation is evident how the local tangential force harmonic contribute to the torque just considering only with nil spatial harmonic (i.e. $v = 0$). On the other hand, considering temporal harmonics u, if $u = 0$ the local tangential force harmonic contribute to the constant torque, while if $u \neq 0$ the contribution regards the cogging torque or torque ripple.
Some studies in literature, for instance such as [12] and [14], state that the radial forces causes the majority of vibrations, therefore let's focus more on the radial force harmonic. If interested even in the contribution of the tangential components, many other studies are focused on it, for instance [12], considers both tangential and radial forces.
Considering just the radial forces, the tangential air-gap flux density is typically way smaller than the radial air-gap one, and therefore the tangential can be neglected. Going more into details, as already anticipated, the air-gap field is composed by two main components: PM field (i.e. B_{rm}) and armature reaction field (i.e. B_{ra}). Hence, being more exhaustive, the radial air-gap flux density can be expressed as:

$$B_r = (B_{rm} + B_{ra})\, \lambda_r$$

with λ_r representing the real part of the relative permeance.
The analytical expressions of each term are given by [14].

Let's start considering B_{rm}, which has a frequency equal to upf_1, with f_1 rotational mechanical frequency ($f_1 = \omega_r/2\pi$), ω_r rotational mechanical angle speed of the motor, p pole-pair number and $u = 2n + 1$ (with $n = 0,1,2,...$); whereas the mode number is demonstrated to be $-up \pm kN_s$, where $k = n$ (with $n = 0,1,2,...$) and N_s is the slot number.
Then, the radial force harmonics are proportional to the square of the radial air-gap flux density:

$$F_{rm} \propto (B_{rm})^2$$

Hence, the frequency of the radial force harmonics will be $2npf_1$, while the mode number will be $-2np \pm lN_s$, with $n, l = 0,1,2,....$
Now let's consider the armature reaction field (B_{ra}), which analytical expression is given by [14].
In this case, the frequency of air gap flux density harmonics on the armature-reaction field is pf_1, while the mode number is $-p \pm 3\xi GCD(p, N_s)l$, with $l = 0,1,2...$ and ξ that varies depending on the fact that phase-belts are equal or not. The phase-belt is defined by [15] as the group of adjacent coil-sides belonging to a phase. Using a totally analogous approach with respect to what was explained in the previous passages, the radial force is proportional to the square of the radial air-gap flux density, hence the frequency of radial force harmonics becomes $2pf_1$, while the mode number is $-2p \pm 3\xi GCD(p, N_s)l$.
Moreover, radial force harmonics can be generated by the combination of the no-load field and armature-reaction one, and they are proportional to the product of the two air-gap flux density harmonics:

$$F_{rma} \propto B_{rm}B_{ra}$$

with frequency $2npf_1$ and mode number $-2np \pm 3\xi GCD(p, N_s)l$. These two last expressions are valid for all radial force harmonics on either no-load or load condition of PMSM with symmetrical three-phase double-layer winding.
[14] proves that it is possible to define the slot number N_s and the pole-pairs number p as:

$$N_s = 3\xi C_1 GCD(p, N_s)$$

$$p = (3\xi C_2 \pm 1)GCD(p, N_s)$$

with C_1, C_2 integers.
Finally, [14] proves that the lowest mode number of radial force harmonics is equal to $GCD(2p, N_s)$. Moreover, it can be proven that the radial force harmonics with the lowest mode number cause large vibration at low frequency, therefore an effective way to reduce amplitudes of vibrations is to aim to the reduction of the lowest mode number radial force harmonic.
Let's see a brief example. Let's consider a 48/8 (48 slots, 8 poles) motor which

has symmetrical three-phase equal phase-belt winding. Recalling that frequency and mode number are expressed as $2npf_1$ and $-2np \pm 3\xi GCD(p, N_s)l$, respectively, having $\xi = 2$, $p = 4$, $GCD(p, N_s) = GCD(4,48) = 4$, it is possible to state that the frequency is $8nf_1$ and the mode number is $-8n \pm 24l$. Finally, the lowest mode number will be $GCD(2p, N_s) = GCD(8,48) = 8$.
As already stated, the magnetic flux density harmonics are strongly affected by the number of pole-pairs and number of slots. A non effective combination of these two numbers can lead to high vibrations and noises.
Some studies in literature, such as [10] and [16], prove that, considering p the number of pole-pairs, and N_s the number of slots, the combinations that provoke the lowest noises and vibrations are the ones that have $N_s = 6kp$, with $k \in \mathbb{N}^*$ (i.e. motors with distributed overlapping windings), and the main vibration mode will be $2p$.
Moreover, asymmetry of electromagnetic pressure cause strong vibrations, therefore, a motor with a number of slots that is a multiple of pole-pairs number ($N_s = (2k + 1)p$) will be less noisy than one with $N_s = 2p + 1$.
Considering electromagnetic force harmonic content, if a configuration with $N_s = 6kp$ is taken into account, the ranks of the excited harmonics in no-load condition are $2ip$, with i positive integer. Moreover, it can be proven that an increase of $GCD(N_s,2p)$ results in to an increase of harmonic ranks. This can lead to first non-zero harmonic excited at frequency above the upper audible frequency threshold, and therefore only rank 0 harmonics contribute to noise in these cases. Furthermore, [16] shows that for a fixed pole number, increasing the number of slots per pole and per phase leads to an increase of harmonic amplitudes.
[10] clearly shows the advantages in terms of vibrations produced of a symmetrical motor ($p = 4$, $N_s = 12$) with respect to an asymmetric one ($p = 4$, $N_s = 9$). In the case of asymmetric motor, with fractional number of slots per pole, also odd sub-harmonics are present due to the interaction between flux densities of the rotor and stator in the air-gap, in particular the 1^{st} harmonic component produces unbalance force leading to strong vibrations.
Moreover, [10] gives important relationships useful to understand the cogging torque, torque ripple and normal local forces frequencies (respectively f_{cog}, f_{rip}, f_{norm}) with respect to the motor frequency (f_e).

$$\begin{cases} f_{cog} = LCM(P, N_s)nf_e/p \\ f_{rip} = 6nf_e \\ f_{norm} = 2nf_e \end{cases}$$

with n = 1,2,3, ..., P number of poles ($P = 2p$), p number of pole-pairs, LCM stands for least common multiple.
As regards the electromagnetic vibrations, there is also another source, deeply

studied by [17], which is represented by a mainly radially uneven electromagnetic force, called *Unbalanced Magnetic Pull (UMP)*. It results from the asymmetry of the air gap magnetic flux density distribution, which is caused by several sources:

- Mechanical sources (unbalance mass, shaft bow, assembly error, bearing wear, stator & frame vibration, shape deviation, etc.)
- Electromagnetic sources (short circuit, open circuit, magnetization unevennes, winding topology asymmetry, etc.)

Many effects of the UMP are investigated by [17]. Generally, UMP leads to significant vibrations in the electric machine, and it can causes rotordynamic instability, too. Moreover, when the exciting force frequencies from UMP coincide with the modal frequencies of the stator, [17] reports that the motor can generate high noise and vibration peaks.
As anticipated before, the electromagnetic noise is strongly influenced by additional noise generated by current harmonics from inverter operation, usually indicated as switching noise. Since the inverter is a non-sinusoidal power supply, it injects harmonic currents into windings, that will affect the magnetic field within the air-gap. Each current harmonic produces a rotating magnetic field, which interacts with the rotating magnetic field of the rotor creating an electromagnetic force, leading to noise and vibrations, indeed. If harmonics frequencies are close to natural frequencies of the motor, then the noise will remarkably increase.
To achieve high efficiency, the inverter uses switching devices, energy storage elements and transformers, and it relies on proper modulation techniques of the switches.
Switching noise is not affected by the machine design parameters, such as combination of number of slots and pole-pairs, but on the contrary it is only influenced by the modulation technique. Moreover, it is possible to say that switching noise represents a major contribution especially at lower motor speeds, during starting phase.
The spectrum current coming from the inverter, as exposed by [18], can be written as:

$$i_s = \sum_{i=1}^{n} H_i sin(\omega_i t + \phi_i)$$

with n number of the considered harmonics, H_i, ω_i and ϕ_i represent the amplitude, the angular frequency and the phase displacement of the harmonic i, respectively. Each harmonic, with frequency f_i, interacts with rotating magnetic field of the rotor, which has a frequency f_1. Hence, the harmonic force component generated by this interaction will have a frequency equal to $f_i \pm f_1$. [18] claims that the harmonic frequency f_i strongly depends on the switching frequency (or carrier frequency) f_{sw}, as well as on f_1. For instance, in the case of an inverter with triangular PWM

signal, $f_i = n_1 f_1 \pm n_2 f_{sw}$, with n_1 and n_2 constants with opposite parity. Therefore, in the cases in which the harmonic frequency is close to the mechanical resonance frequency of the machine, very strong vibrations can be detected.
Considering PWM techniques, mentioned in section 1.3.2, with fixed switching frequency, the harmonic spectra of inverter's output waveforms contain narrowband harmonic clusters concentrated around the switching frequency of the inverter itself and its multiples. The issue is that the harmonic flux waves produced by these harmonics interact with fundamental flux wave resulting in vibrations. Moreover, the switching frequency and its harmonics could be within the audible range, hence disturbing narrowband noise can be emitted.
As already explained, the amplitude and frequency of these harmonics will depend on the modulation technique.
An example of the harmonic components of the output voltage for the SVM is shown in Figure 1.20. In the graph it is considered the modulation index: it indicates the relation of the fundamental harmonic of the output voltage to the voltage of the input voltage.

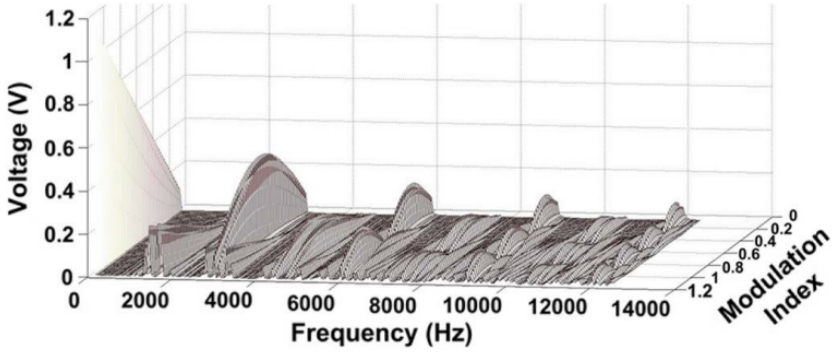

Figure 1.20: Output voltage with respect to modulation index [19]

Thanks to Figure 1.21, it is possible to observe a qualitative characteristic representation of the dominant current harmonic components with respect to modulation index. These characteristic patterns will be also observed in the motor's noise, as investigated by [19]. Note that f_{sw} indicates the switching frequency.

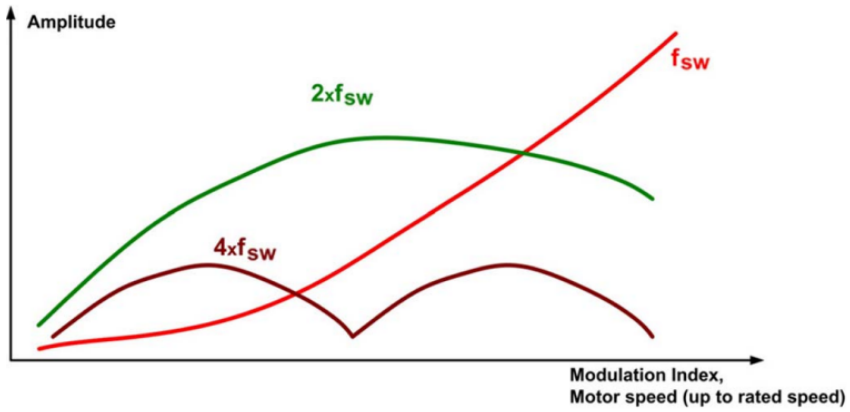

Figure 1.21: Characteristic patterns of dominant harmonic components [19]

Aerodynamic sources

Aerodynamic source is mainly constituted by cooling fans, ventilation ducts designed for dissipating heat. The noise generated by these sources depends mostly on the design features, geometric dimensions and operating speed. The noise typically increases by increasing the operating speed, therefore this source is more important at high speeds.
If the air gaps in the machine are not that regular, then a noise spectra with pure tones components can be obtained, resulting in more annoying effects.
However, nowadays most of EVs have motors which are liquid-cooled, therefore the aerodynamic noise of the motor is not so relevant.

Unbalance of the rotor

The unbalance of the rotor represents another noise and vibration source of the electric motor. In cases in which the center of mass (inertia axis) of the rotor is not exactly coincident with the center of rotation (geometric axis), then an unbalance is obtained. This will cause for sure some dynamic problems, in particular vibrations. Since the mass of the rotor is rotating, the force also rotates and tries to move the rotor along the line of action of the force itself. This will result in vibrations transmitted to bearings, decreasing their operation life and therefore the life of the whole system.
The unbalance can be either static unbalance or couple one. The former is characterized by the eccentricity, which indicates the distance between the center of mass and the center of rotation. On the other hand, the latter is characterized by the angle between the principal axis of inertia of the rotor and the rotation axis. In the cases in which both types of unbalances are combined together, it is hence

obtained the dynamic unbalance.
It is possible to reduce these negative effects by performing balancing of the rotor, obtaining then an improvement of the life of the system and its reliability.

1.4.3 Transmission system noise

Gears

One of the most important component of the transmission system are certainly the gears.
There are different types of gears, one of the main distinction is in two classes: gears with parallel axes (for instance spur or helical) or non parallel axes (such as straight bevel or spiral bevel). In their respective classes, the noisiest are usually the spur and the straight bevel gears, while helical and spiral bevel are quieter. This is due to the fact that the in case of helical and spiral bevel the load is transferred between gears in a more smooth way and more gradually. As the gear teeth mesh, a pulsating force is generated in tooth in contact, with a certain meshing frequency and its harmonics.
In general, the noise produced depends on the speed of rotation and on the load transmitted. If speed and load are low, then some studies, such as [7], demonstrated that the sound pressure level increase by about 3 dB doubling the speed or the load, while, if high speed and load, it can increase by 6 dB doubling the speed and the load.
In general terms, it is true that the manufacturing quality and the tolerances obtained play a dominant role in the noise and vibrations produced. If some errors are committed during the manufacturing process, for instance if the tooth profile is not precise, for sure the vibration will be more significant. But some kind of vibration and noise will be always present even if the manufacturing process is performed optimally and no remarkable errors are present.
The frequency of the noise and vibration will occur at gear meshing frequency f_m and its harmonics.

$$f_m = \frac{N_p n_p}{60} Hz$$

with N_p number of pinion teeth and n_p is the pinion speed in rpm.
Going more into details, speaking of gears, two kinds of noises are usually distinguished: *whine* and *rattle*. The latter is an impulsive sound that occurs in gears that are excited by an oscillating torque, but generally this is less important than the whine, therefore only the gear whine will be analysed more in depth. Gear whine is a periodic sound which has main components at f_m and its harmonics.
In the literature, as reported by [7], the main quantities that represent an excitation of gear whine noise are indicated:

- Transmission Error (TE): deviation from perfect motion transfer of gears. It can be caused by either profile deviation from perfect involutes or to gear deflections due to the load. It is possible to evaluate the angular transmission error as follows: $TE = \theta_p - m_g\theta_g$, with θ_p and θ_g are the angular rotation of the pinion and of the gear respectively and m_g is the transmission ratio.

- Mesh stiffness variation: stiffness of teeth can be modified when the lengths of lines of contact change as the number of tooth pairs in contact change.

- Axial shuttling force: force at bearings due to the barycenter of the mesh force axially translating along the tooth face width.

- Friction force: force that is originated by the relative sliding between teeth in contact.

- Lubricant and/or air entrapment: if high speed gear, air and lubricant can gives birth to pulsating fluid motion at high velocities.

From the scientific literature, it is usually considered that the leading source of mechanical excitation is given by the the transmission error of the gears. In order to properly take into account the amplitude of the mechanical excitation generated by the transmission error, it is required to consider the loaded tooth contact, the macro and micro geometry of the gear and the deflection of the system.
Moreover, gear meshing misalignment can increase transmission error and degrade gear contact patches, thus increasing the overall noise.
As already anticipated, the TE strongly depends on the stiffness of teeth in contact. If two tooth pairs are in contact, then the mesh stiffness is about twice the value that it would have been when just one pair of teeth is in contact. In Figure 1.22, the above mentioned effect is shown; moreover it indicates the relationship that links the stiffness change to the value of TE. In the top of the figure it is possible to identify the lengths of the contact path in which just one tooth pair is in contact and where two tooth pairs are in contact. A perfect gear is considered, with no defects. When the load is nil, also the TE is nil. As soon as the gears are loaded, the mesh deflection, which indicates TE, changes in a stepwise way as the number of tooth pairs in contact changes.

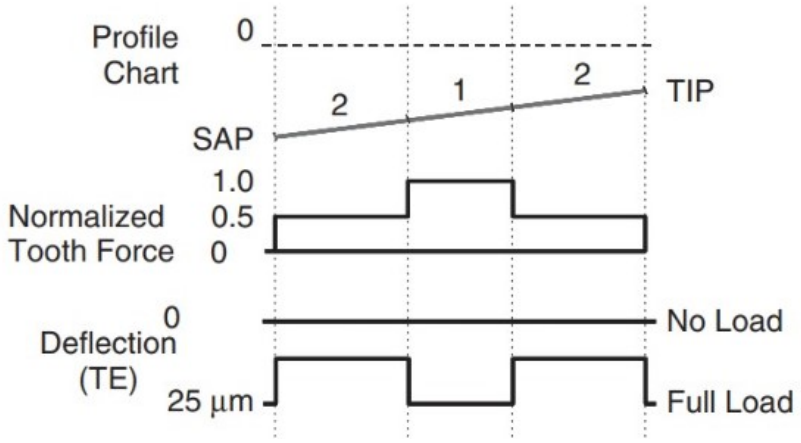

Figure 1.22: Example of transmission error [7]

In conclusion, gears are the main source of high-frequency vibration and noise.

Bearings

Other important components concerning the transmission system are the bearings. Bearings are key components whenever it is required to connect a rotating part to a fixed one. To correct predict the system life, to perform fatigue and contact analysis of bearings assume a crucial importance.
Usually, the noise caused by bearings in good condition is uniform and it does not create any remarkable issue. However, in some conditions, such as if there is the generation of a defect, if bearings are subjected to damage due to fatigue, if bearings are subjected to pitting and spalling, then the noise and vibration can become relevant. Usually, the presence of unpleasant noise or vibration is symptomatic of some kind of problem. Moreover, it is necessary to consider the connection of the bearings to the housing. To perform any NVH analyses, is mandatory to consider the housing, which does not have an infinite stiffness. Therefore, the outer race of bearings will have a non-zero displacement that must be taken into account.

1.5 How to reduce NVH issues

Generally speaking, two main techniques can be used in order to reduce noise and vibrations:

- Source control approaches: modifications directly of noise/vibration source, but sometimes it can be costly or even difficult to accomplish.

- Path control approaches: also called passive control approaches, they require to modify the path of the noise/vibration, and not the source itself. It can be accomplished by using vibrations insulators, noise barriers, damping materials. One typical example can be the housing of the powertrain, which has the aim of reduce the noise and vibration dissipation coming from the powertrain to the vehicle's cabin.

1.5.1 Rolling noise

As regard the tyre/road noise, the noise reduction techniques should be distinguished considering if the noise follows either a structure-borne path or an airborne one. To reduce the structure-borne noise, it is necessary to improve the design and the quality of the suspensions. Moreover, a reduction of noise and vibration can be obtained also by modifying the tyre itself, changing its quality and especially the pattern of the tread. As regard the airborne noise, a reduction of the noise can be obtained by improving the sealing of the doors, panels and the floor structure, too. To summarize, the main road noise reduction techniques are the following:

- Using insulators or structural design to minimize force transmission
- Damping materials to minimize panel vibration
- Sound insulation to block airborne noise path
- Tyre geometry and properties optimization to reduce source noise

To decrease the aerodynamic noise, the design of the vehicle plays a dominant role: abrupt changes in the geometry, or appendages such as external rear-view mirror, increase the turbulent boundary layer, resulting in an increase of the noise. Therefore, having a more smooth geometry and with fewer appendages certainly will help in the noise reduction. Moreover, the quality of door sealing system has a crucial relevance. At high speeds, doors tend to move outward due to the pressure difference between the aerodynamic pressure outside and the internal pressure of the cabin. Whenever the quality of the sealing is not good enough, air can travel from the outside to the inside of the cabin causing aspiration. Even the loss of seal material elasticity over time can cause aspiration, too. Since aspiration noise is broadband high-frequency noise, can be easily perceived by the passengers and it should be limited as much as possible. To try to avoid this issue, vehicles usually have more layers of seals.
Other strategies for noise reduction include the use of damping materials in doors and in doors panels. Even the damping of the glass can be increases moving from the regular glass to the laminated glass. The latter has high internal damping, resulting in radiating much less sound when it vibrates, as shown by Figure 1.23.

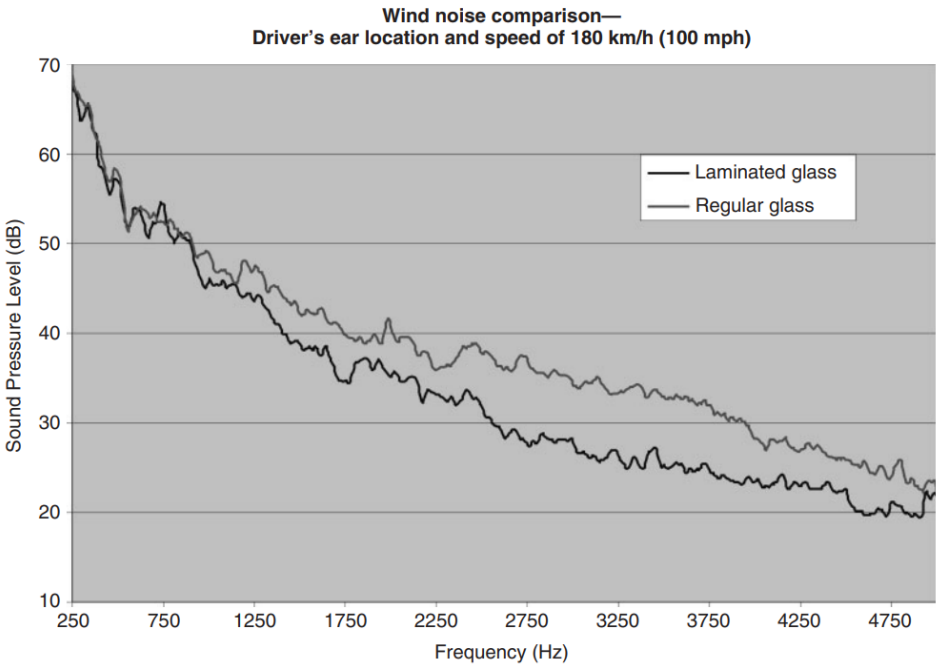

Figure 1.23: Wind noise comparison regular vs laminated glass [7]

1.5.2 Electric motor noise

It is possible to identify two different methods for noise and vibrations suppression of EVs powertrains: passive device and active control algorithm. The former has the aim of reducing the vibration transmitted from the powertrain to the vehicle cabin by directly modifying the dynamic properties of the components. For instance, by increasing the damping and reducing the stiffness of the transmission shaft it is possible to reduce the frequency and the amplitude of the vibrations. However, generally, a passive approach can strongly increase the manufacturing costs and affect the vehicle dynamics. Therefore, it is usually preferred to use advanced control algorithms, such as Proportional, Integral, Derivative (PID), Linear Parameter-Varying (LPV), Model Predictive Control (MPC) and fuzzy controls.
Generally, these controls are not difficult to be implemented and cost-effective, too. Using them it is possible to effectively suppress motor vibrations.
The above mentioned control methods can reduce the torque and current fluctuation of the PMSM, and the torque ripple can be decreased, too.
Another approach that can be followed is the structural motor parameter optimization, with the aim to avoid resonances by adjusting modal frequencies.
The motor optimization requires modifications of the design and the topology of

the motor itself. For instance, the poles can be designed specifically in order to reduce vibrations. One possible solution is to have skewed slots on stator: this method reduce the force harmonics, changing modal frequencies. Moreover, as explained in section 1.4.2, an appropriate selection of slot-pole combination can reduce the overall noise.
To summarize, the main techniques used to mitigate noise and vibrations are:

- Optimize the arrangement of permanent magnets to compensate for electromagnetic noise
- Optimize the shape of rotor and stator to reduce torque ripple
- Improve dynamic characteristics of drivetrain by dissipating the resonance frequency.
- Improve acoustic transfer function by adding sound-absorbing materials and dampers

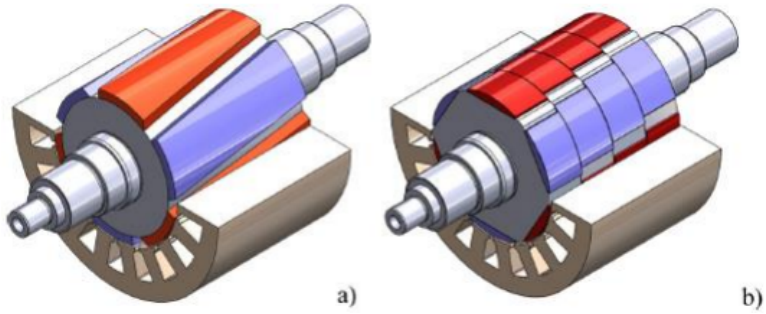

Figure 1.24: a: Rotor skewing; b: Step-skewing [5]

To reduce the cogging torque, two solutions are the most used: rotor skewing or step-skewing. The former requires the magnets to be divided into several parts: the second one offsets a certain angle with respect to the first one, then the third one with an offset with respect to the second one and so on. The effect is to change the phase of the PM field. Some studies from literature (for instance [20]) indicate how to evaluate the optimal offset angle. To obtain it, if a peak of noise/vibration occurs at a certain frequency, the force on the first part and on the second part (only two parts if the magnets is divided in just two parts, if more parts the reasoning is similar, considering all parts) should be opposite in phase in order to cancel their contribution to the vibration. If many peaks of the force should be reduced, then many optimum offset angles will be obtained. Hence, the offset angle will be a compromise. It is assumed by [20] that the sound pressure is proportional to the square of the force integral along the axial direction. Therefore, reducing the peaks

of the force leads to a reduction of noise.
Rotor skewing is another solution implemented in order to reduce cogging torque: selecting a proper skewing angle it is possible to reduce vibration and noise. The procedure to follow to obtain the skewing angle is similar to the step-skewing case, as explained more in details by [20].
Moreover, using concentrated windings rather than distributed ones can lead to a reduction of cogging torque, too.
Let's now focus on the reduction of the noise and vibrations caused by inverter: in the literature, many techniques have been proposed. The aim is to control the amplitude of the fundamental harmonic component and to reduce higher harmonics, too.
Some passive filtering techniques have been studied, but they leads to too remarkable increase of costs.
As already anticipated before in the discussion, one effective way is to act on the modulation technique of the inverter itself. Moreover, the switching frequency can be selected in order to reduce the amplitude of the harmonics and avoiding resonance phenomena.
Especially in case of hybrid electric vehicles, a technique that can be used in order to reduce the noise produced by inverters require to prevent the switching frequency to drop below the upper threshold of unmasked audible range. This can be achieved by a closed-loop control strategy, as demonstrated by [21], as reported in Figure 1.25.

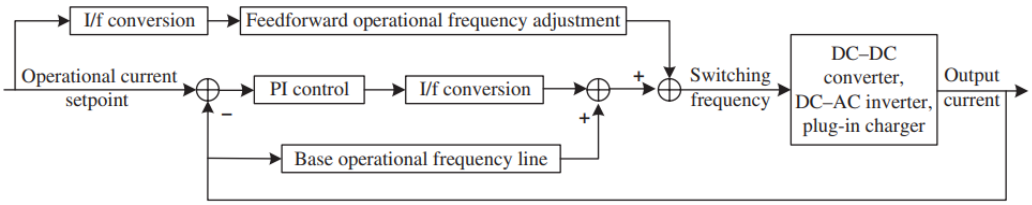

Figure 1.25: Example of closed-loop control strategy, studied by [21]

It is possible to maintain the switching frequency above the upper threshold of unmaksed audible noise by feeding back and forward the output current of the inverter.

1.5.3 Transmission system noise

Gears

As was already said, many ways can be followed in order to decrease the amount of transmission error (TE), such as modifying the micro and macro geometry of

tooth, or analysing the contact surface of tooth pair.
Since it has been demonstrated by literature that gear acoustic harmonic plays a dominant role in the sound quality of electric powertrains, and since the micro-geometry of tooth is determinant in the quality of the transmission system, it results that optimising micro-geometry is an effective way to improve the sound quality: micro-geometry optimisation leads to a minimization of contact and bending stress, and of TE, leading to noise and vibration reduction and improved gear durability.
Several types of micro-geometry modifications are possible:

- Involute or Profile modification: along profile direction, i.e. from root to tip of the gear
- Lead modification: across the face width of the gear, such as lead slope correction and lead crowning
- Bias: it refers to twist that can be induced in the manufacturing process

Let's analyse some modifications more in details.
To properly understand micro-geometry modifications, it is important to refer to a sign convention.
A *positive involute slope* indicates material removal at the lower region (i.e. Start of Active Profile, SAP), whilst the upper region (i.e. End of Active Profile, EAP) is not affected. The opposite is valid if *negative involute slope*.

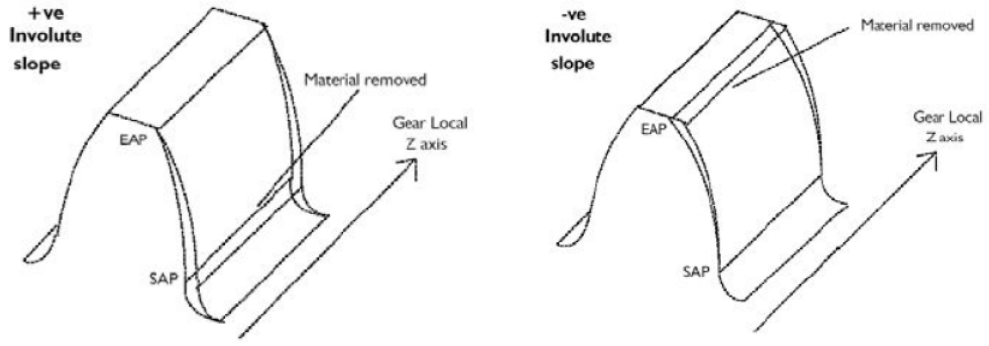

(a) *Positive involute slope* **(b)** *Negative involute slope*

Figure 1.26: Involute slope [22]

A *positive involute barreling* indicates modification just on the values of SAP and EAP, while the mid-point between them will be zero. The opposite is valid if *negative involute barreling*.

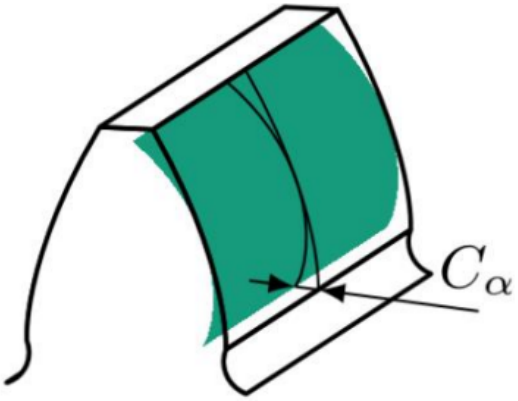

Figure 1.27: Positive involute barreling [23]

A *positive lead slope* leads to material removal at the bottom of the face width, whilst the top of face width is not affected. The opposite is valid in case of *negative lead slope*.

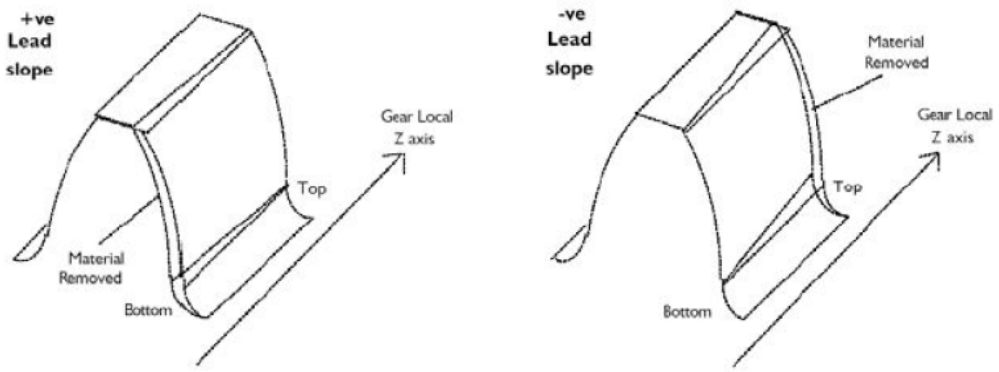

(a) *Positive lead slope* **(b)** *Negative lead slope*

Figure 1.28: Lead slope [22]

Tip relief is the amount of material removed, by the extent that it drops down the flank.

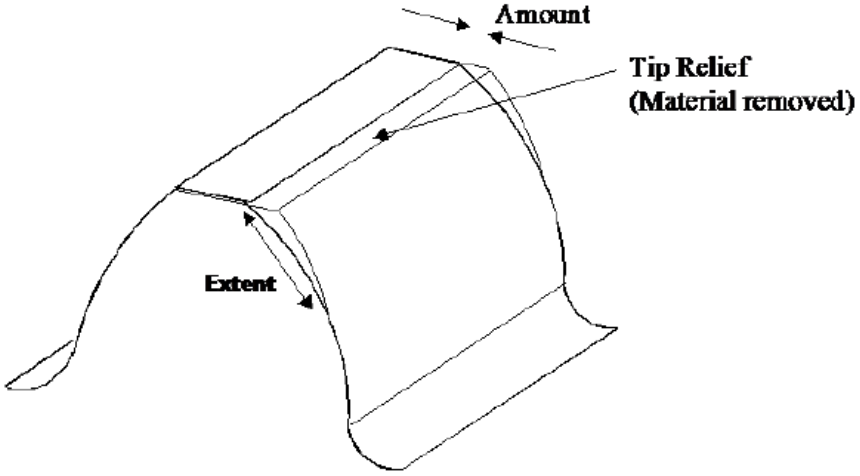

Figure 1.29: Tip relief [22]

The opposite of the tip relief is the *root relief*, in which the material is not removed by the tip, but from the root of the mating teeth. Doing so, the material removed compensates for the motion errors caused by the change in stiffness.
Lead crowning indicates the crowning along the face width of the tooth flanks. A positive lead crowning leads to material removal to both the bottom and the top lead evaluation limits, while the middle point will not be affected: the material removal is just at the two ends and not in the middle.

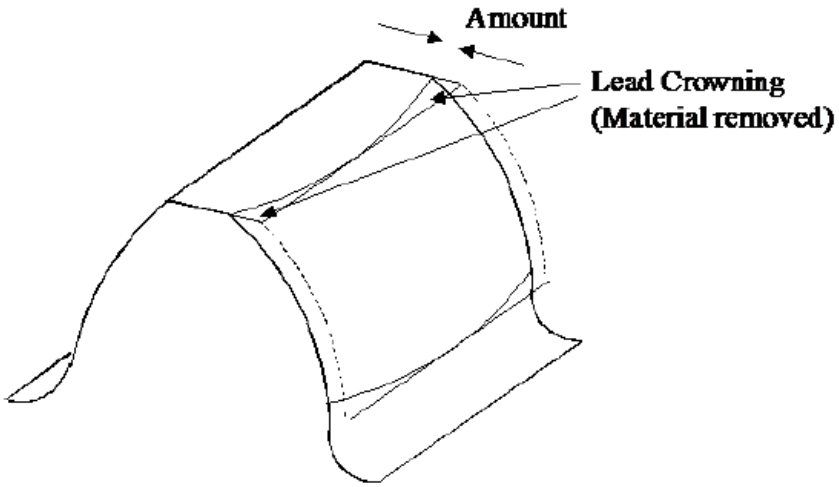

Figure 1.30: Lead crowning [22]

Another approach used to reduce TE is to increase the contact ratio of the gear pair, resulting in a decrease of the mesh stiffness variation. The most common ways to increase the contact ratio of the gear pair are:

- Increase tooth height.
- Increase helix angle, so to decrease the axial pitch.
- Increase face width.

Bearings

The unwanted noises and vibrations generated by bearings can be limited by optimizing the bearing quality, design parameter. If a bearing is manufactured to a higher grade of precision, then it will be quieter.
It is possible to optimize also the preload, and the clearance during installation into the housing.

Chapter 2

How to create the model of an electric powertrain in Romax

The aim of this thesis is to try to understand and explore possibilities and study opportunities that the software Romax, from Hexagon AB, offers, especially from the NVH point of view. This software represents a functional tool to perform effectively NVH analysis considering a very high level of details. Romax offers abounding quantity of supporting material [22], including several models ready to be analysed.

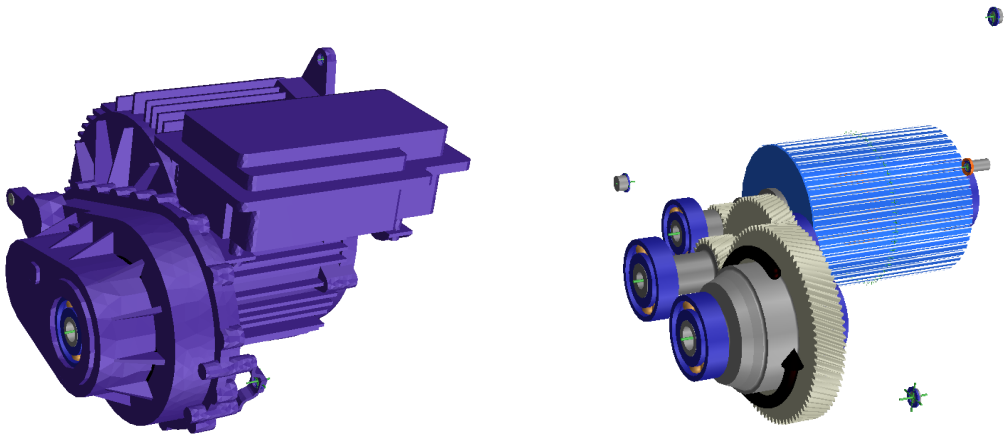

(a) *Gearbox with housing* **(b)** *Gearbox without housing*

Figure 2.1: Single speed electric powertrain gearbox

In particular, as previously stated, the main focus will be on a single speed electric powertrain model, which is represented in Figure 2.1.
Before starting with the main analyses, a more detailed overview of the software can be useful.
Romax is constituted by several modules, each of which allows to perform high detailed analysis focusing on a specific aspect.
The main packages that have been exploited during this thesis work are:

- Concept: it allows to effectively build a preliminary version of the model.
- Enduro: it allows to increase the detail level of the model, and to perform detailed static analysis.
- Spectrum: it allows to perform thorough NVH analysis.
- Energy: it allows to perform detailed efficiency analysis.

As already stated, the main core of this thesis will be the NVH analysis of an electric powertrain model directly given by Romax supporting materials [22].
In this thesis work, four different models will be analysed, from both a static and a dynamic point of view: the reference will always be the model given directly by Romax supporting material reported in Figure 2.1. The differences among the four models will concern some important characteristics and parameters of both gear sets.
The four models that will be analysed are the following:

- Model A: model in which in both gear sets the helix angle is 0. Moreover, no profile shifting will be considered.
- Model B: model in which in both gear sets the helix angle is 0. However, in contrast with model A, profile shifting will be considered.
- Model C: model in which in both gear sets a certain helix angle is considered, with profile shifting, too.
- Model D: model in which in both gear sets a certain helix angle is considered, as in model C, however in model D some microgeometry modifications are considered, too.

The list above just gives an overview about the different models, more details will be provided in the following sections.
More details about the process to be followed to obtain all these models will explained in the following pages. As anticipated before, the usual path followed in order to create the model is usually to start building a very preliminary version of the model in Romax Concept, then more details will be added only moving to Romax Enduro.

2.1 Romax Concept

This section is indeed dedicated in examining the role of Romax Concept: it provides a very straight-forward modelling approach in an efficient and effective way.
Two possibilities are available, either starting from a blank sheet or some basic starting templates are accessible to the user, too.
Starting from the blank sheet, the path to follow is pretty linear. A design step by step is followed, in each step an additional element or an additional detail is added, until a satisfactory model is obtained.
Therefore, the first step to do is to place the required shafts in the desired positions, with their proper geometries and dimensions. It is possible to accurately define the relative positions of the shafts, in all planes. Please remember that the goal is to show how to reach the final model depicted in Figure 2.1, therefore the dimensions and the geometries are selected according to it.
Hence, three shafts are added, as represented in Figures 2.2, 2.3, 2.4:

- Input Shaft

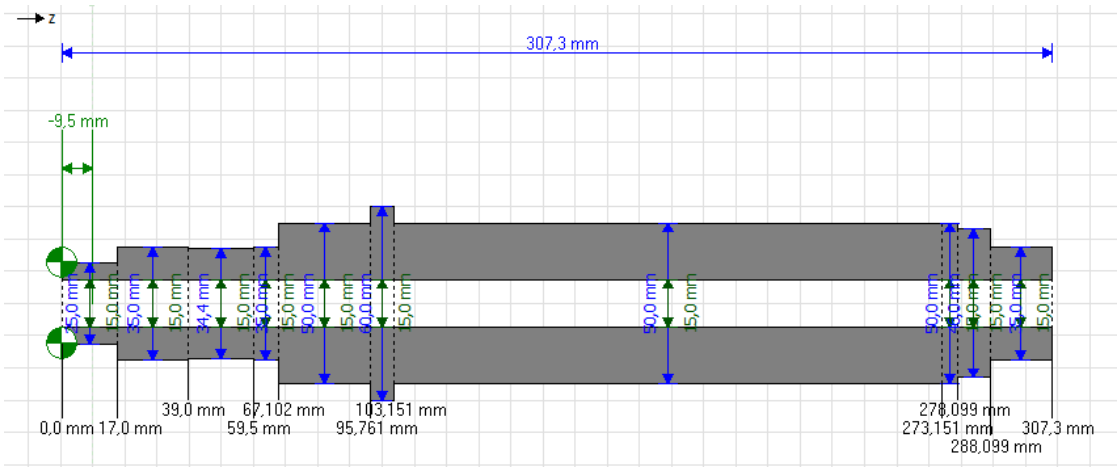

Figure 2.2: Input Shaft

- Intermediate Shaft

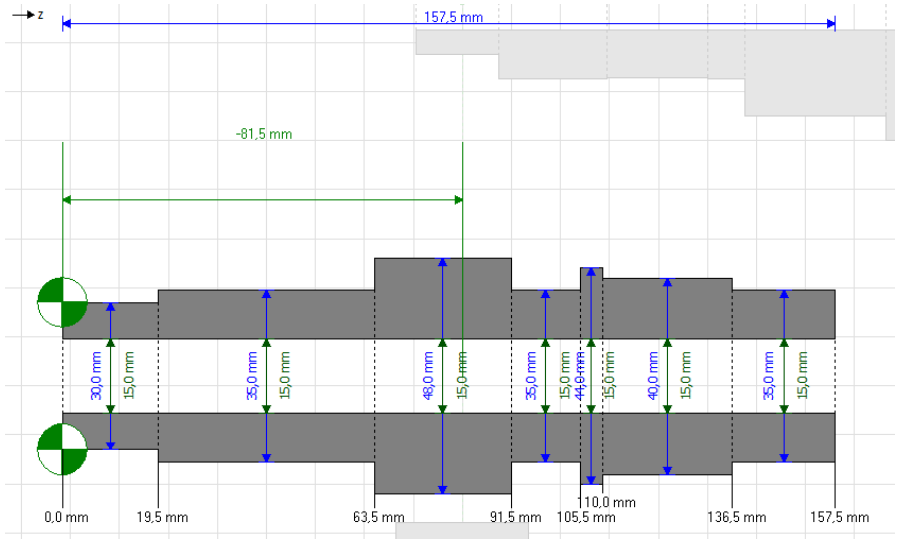

Figure 2.3: Intermediate Shaft

- Differential Shaft

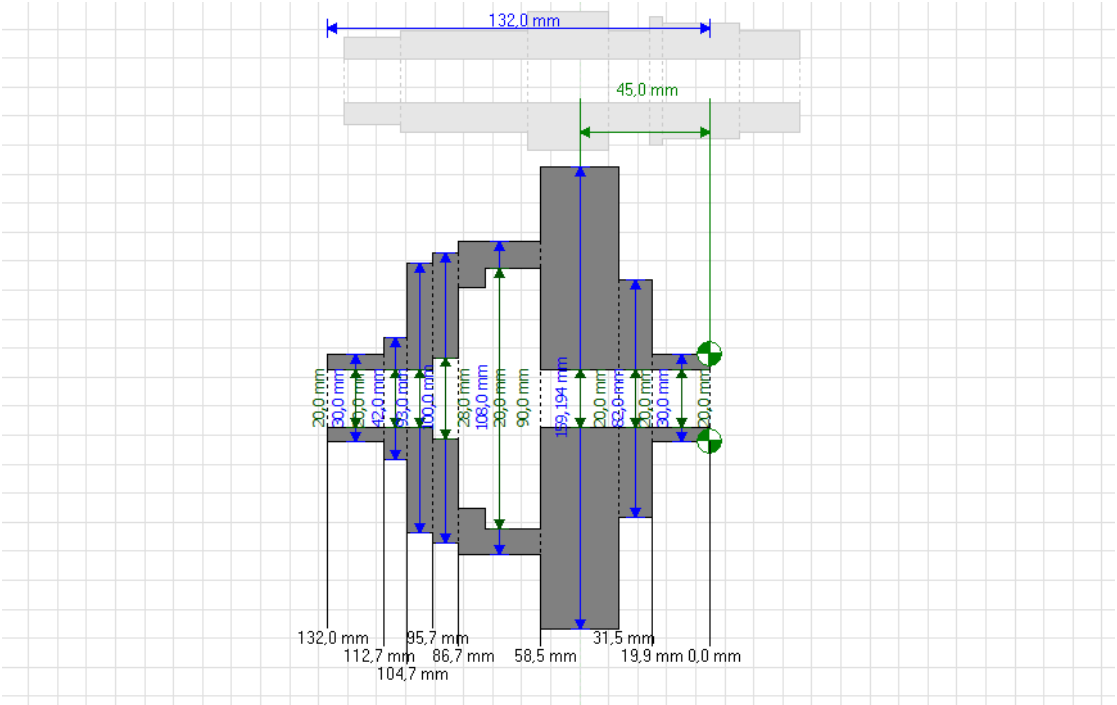

Figure 2.4: Differential Shaft

Moreover, Figure 2.5 represents the position of the shafts in the xy plane.

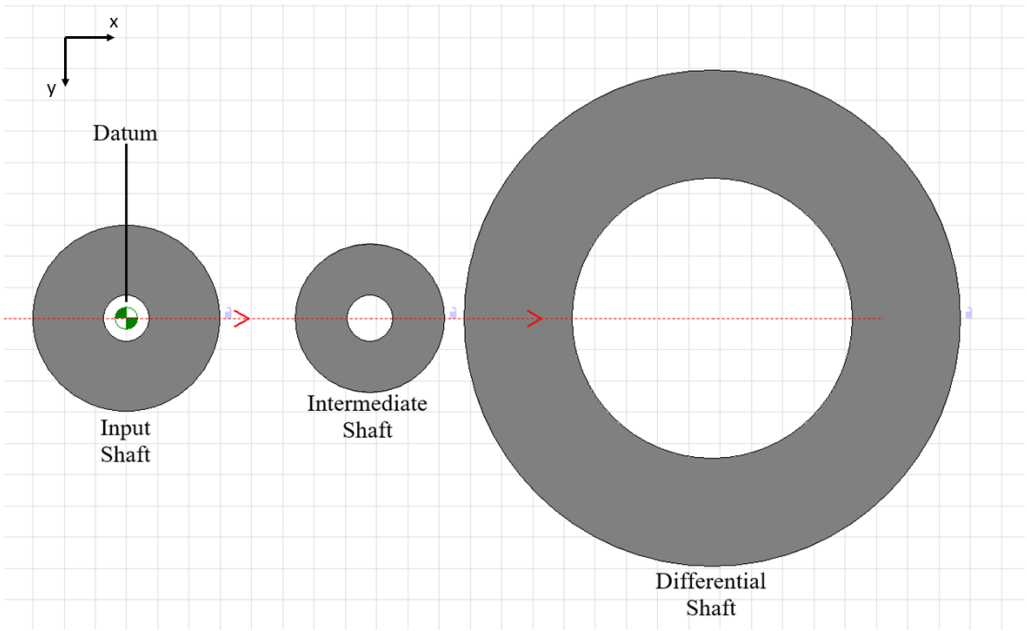

Figure 2.5: Shafts in the xy plane

The position of the shafts is defined with respect to the datum, which is indicated in the xy plane of Figure 2.5.
To clearly understand the positions of the shafts in the xz plane please refer to Figure 2.6.
The following step requires to add the gears that connect the shafts in the proper way. After adding them in proper position, it is certainly necessary to mesh them correctly. Two gear sets will be defined:

- Gear Set - Input:
  - Input pinion, positioned on Input shaft
  - Input wheel, positioned on Intermediate shaft
- Gear set - Output:
  - Output pinion, positioned on Intermediate shaft
  - Output wheel, positioned on Differential shaft

Finally, the last elements that are still missing are the constraints: the first type of constraint that is added in the proper position is the so called stiffness bearing. It is a conceptual component that represents bearing with constant axial, radial

and tilt stiffness. These kind of bearings have on/off point contacts with constant stiffness to represent rolling elements. In particular, each contact point has a contact stiffness equal to $1 \cdot 10^7$ N/m and a non-contact stiffness of 10 Nm.
Up to this point, all required elements constituting the system are disposed correctly, as shown in Figure 2.6.

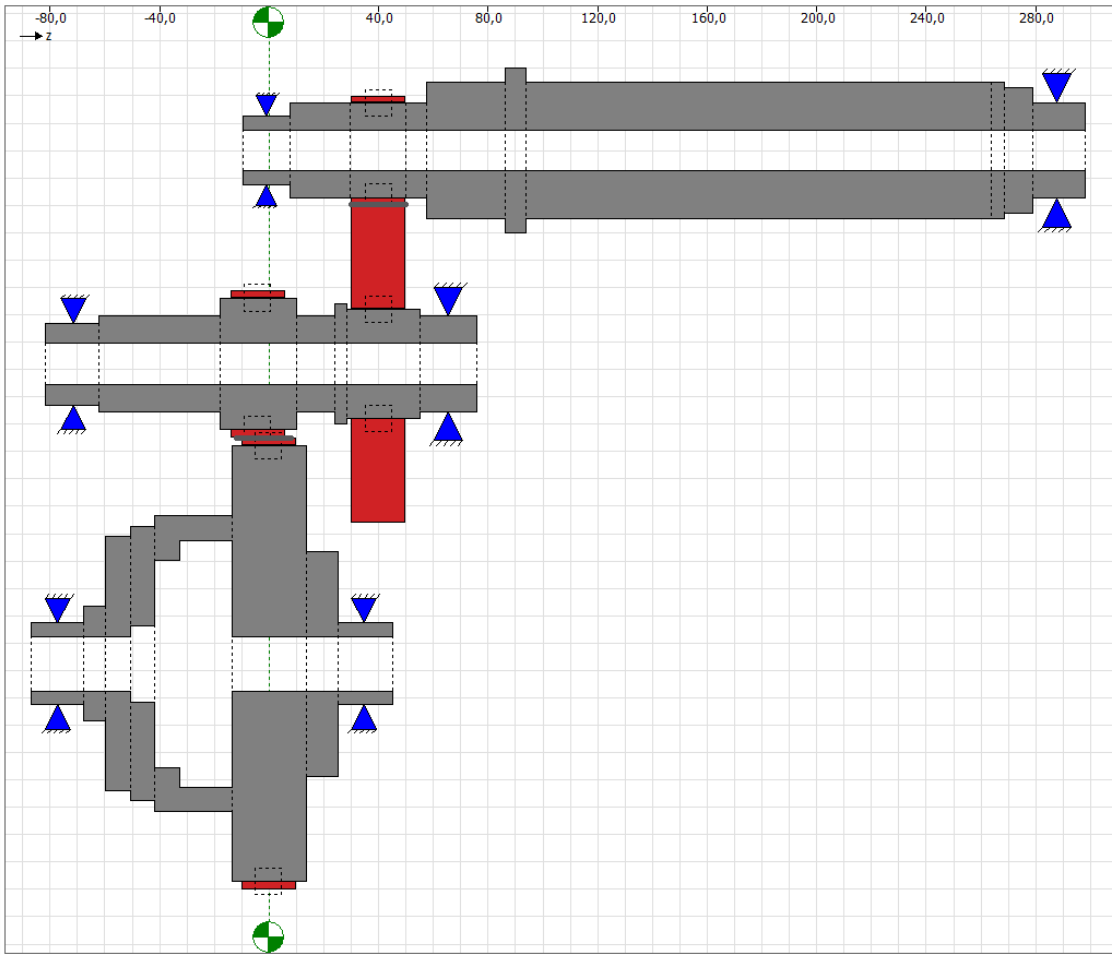

Figure 2.6: Preliminary gearbox

The positions of each element, with respect to the datum, are listed in the tables below:

Name	Position (x,y,z) (mm)	Shaft length [mm]
Input shaft	(0, 0, -9.5)	307.3
Intermediate shaft	(78, 0, -81.5)	157.5
Differential shaft	(187.5, 0, 45.0)	132.0

Table 2.1: Position of shafts

Name	Position (x,y,z) (mm)
Input pinion	(0, 0, 40.0)
Input wheel	(78, 0, 40.0)
Output pinion	(78.0, 0, -4.0)
Output wheel	(187.5, 0, 0)

Table 2.2: Position of gears

Name	Position (x,y,z) (mm)
Input Shaft LH	(0, 0, -1.0)
Input Shaft RH	(0, 0, 287.6)
Intermediate Shaft LH	(78.0, 0, -71.5)
Intermediate Shaft RH	(78.0, 0, 65.5)
Differential Shaft LH	(187.5, 0, -77.2)
Differential Shaft RH	(187.5, 0, 34.6)

Table 2.3: Position of bearings

Please notice that LH and RH indicate left and right bearing respectively. The terms *left* and *right* refer to the 2D view of Figure 2.6.
The following steps are devoted to increase the level of details of each element. For instance, regarding the shafts, the correct material is specified. Different materials are available in the software, and this is certainly an important aspect to consider, since the material selected will affect the performance, the durability and the

life of the system. For instance, concerning the static analysis, it is essential to consider the correct material. The selected material for each shaft of this gearbox is indicated as Steel (medium), which properties are reported in Table 2.4.

Property	Value
Yield strength (MPa)	380
Ultimate tensile strength (MPa)	660
Young modulus (MPa)	$2.07 \cdot 10^5$
Density (kg/m^3)	7800
Poisson's ratio	0.29
Material loss factor	$2 \cdot 10^{-3}$
Cost/unit mass ($1/kg$)	10

Table 2.4: Properties of shafts material

Please notice that the cost/unit mass is defined without specifying the currency, that should be known by the user. Another option is to directly input the cost of a component. However, the aspects related to the cost will not be investigated in the present thesis.
Moreover, considering the constraints of the shafts, even in Concept it is possible to move from just ideal stiffness bearing to real bearings. It is possible to select bearings from many catalogues directly implemented in the software.

Name	Type	Catalog	Designation
Input Shaft LH	Radial ball	Koyo	6305R
Input Shaft RH	Radial ball	SKF	6207
Intermediate Shaft LH	Radial ball	SKF	6306
Intermediate Shaft RH	Radial ball	FAG	6307E
Differential Shaft LH	Radial ball	SKF	6306
Differential Shaft RH	Radial ball	SKF	6306

Table 2.5: Bearings

Then, also some details about the mounting of each bearings on shafts can be highlighted, as reported by Table 2.6.

Bearing		Inner mounting	Outer mounting
Input LH	Axial	Constrained on right	Fixed
	Radial	Fixed	Fixed
Input RH	Axial	Constrained on left	Fixed
	Radial	Fixed	Fixed
Intermediate LH	Axial	Constrained on right	Fixed
	Radial	Fixed	Fixed
Intermediate RH	Axial	Constrained on left	Fixed
	Radial	Fixed	Fixed
Differential LH	Axial	Constrained on left	Fixed
	Radial	Fixed	Fixed
Differential RH	Axial	Constrained on right	Fixed
	Radial	Fixed	Fixed

Table 2.6: Bearing mounting details

Investigating more in depth the mounting conditions of the bearings, it can be noticed that, in all bearings, the outer mounting is always *fixed*, considering both the axial and the radial constraint. This means that all the outer rings of the bearings are fixed on the housing.
A simple scheme of the fixed condition is given by Figure 2.7.
On the other hand, considering the inner mounting, only the radial constraint is fixed for all bearings. As regards the axial constraints, they are either constrained on the left or on the right depending on the mounting condition. The inner rings of the bearings of input and intermediate shaft are constrained just on one side by the shoulder of the shaft. This configuration leads to the so called *X configuration*. This is typical in cases of longer shafts.
On the other hand, for which concerns the differential bearing, the mounting condition is different, leading to an *O configuration*. This is more typical of shorter shafts, as the differential one.
Simple schemes of the inner mounting constraints are reported in Figure 2.8.

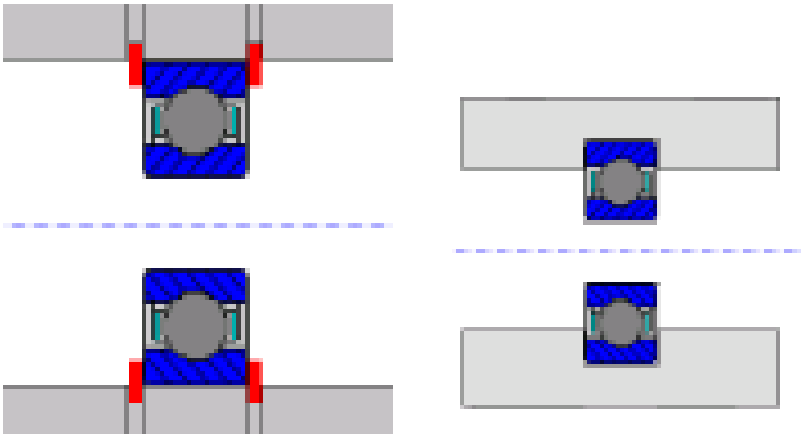

(a) *Axial: Fixed* **(b)** *Radial: Fixed*

Figure 2.7: Outer mountings bearings

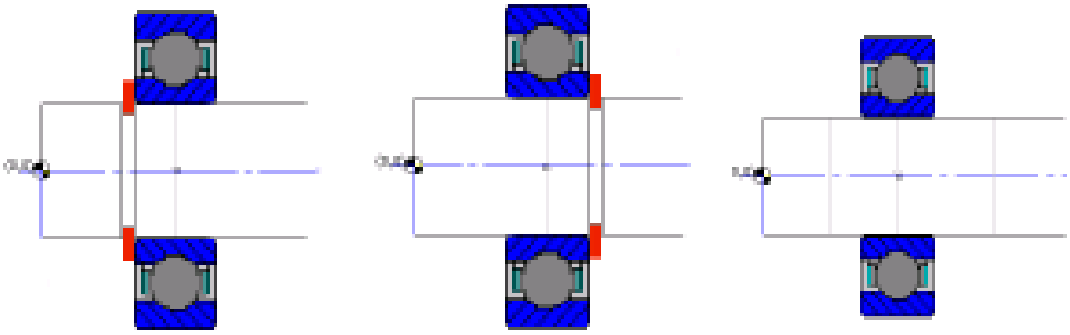

(a) *Axial: Constrained on the left* **(b)** *Axial: Constrained on the right* **(c)** *Radial: Fixed*

Figure 2.8: Inner mountings bearings

Finally, it is possible to add more details concerning the gears. To be compliant with the final model provided by Romax supporting material [22], the following values are defined:

	Gear Set - Input		Gear Set - Output	
	Pinion	Wheel	Pinion	Wheel
Number of teeth $z_{1,2}$	22	65	27	83
Hand	Right	Left	Left	Right
Face width $b_{1,2}$ (mm)	20.5	23.0	27.0	27.0
Normal pressure angle α_n (deg)	21.914		21.000	
Helix angle β (deg)	25.081		24.987	
Working center distance a_w (mm)	78.0		109.5	
Normal linear backlash j_{bn} (mm)	0.100		$9.921 \cdot 10^{-2}$	

Table 2.7: Properties of the gears, Romax Concept

The normal linear backlash is defined at finished thickness. It is defined by [24] as the minimum distance between each meshed tooth flank in a gear set.
Moreover, by defining the values of Table 2.7, the values of Table 2.8 are hence computed by the software itself. In particular, as regards the backlashes, always defined at finished thickness, the definitions are given by [24]. The circumferential backlash is the length of arc on the pitch circle representing the distance the gear is rotated until the meshed tooth flank is in contact while the other mating gear is held stationary; the radial one is the displacement in the stated center distance when the meshed tooth flanks of the paired gears get contact each other. To help in the understanding, please refer to Figure 2.9.

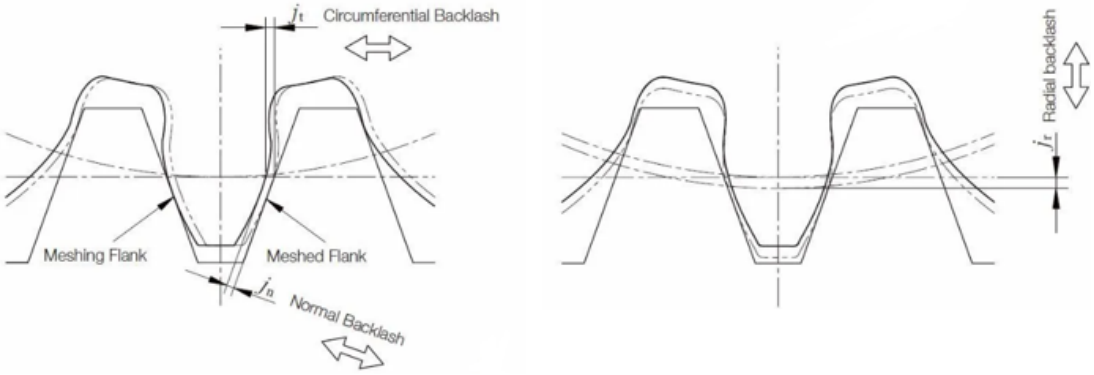

Figure 2.9: Backlash [24]

	Gear Set - Input		Gear Set - Output	
Mean pitch diameter $d_{1,2}$ (mm)	Pinion 39.593	Wheel 116.980	Pinion 53.723	Wheel 165.147
Mean normal module m_n (mm)	1.630		1.803	
Normal base pitch (mm)	4.751		5.290	
Ratio (wheel/pinion)	2.955		3.074	
Working trans. press. angle α_{wt}(deg)	23.471		23.033	
Working norm. press. angle α_w(deg)	21.481		21.073	
Trans. circumfer. backlash j_{wt} (mm)	0.119		0.117	
Radial backlash j_r (mm)	0.137		0.138	

Table 2.8: Properties of the gears, computed by Romax Concept

Please notice that all these values are referring to the model provided by the Romax supporting material [22]. Moreover, in order to be coherent with the model in Figure 2.1, the material of all gears has been selected as *Steel, case hardened, AGMA grade 2*, which properties are reported in Table 2.9.

Property	Value
Yield strength (MPa)	314
Ultimate tensile strength (MPa)	2300
Young modulus (MPa)	$2.07 \cdot 10^5$
Density (kg/m^3)	7800
Poisson's ratio	0.3
Material loss factor	$2 \cdot 10^{-3}$
Cost/unit mass ($1/kg$)	10

Table 2.9: Properties of material Steel, case hardened, AGMA grade 2

So far, it has been described the process related to Model C, however, apart for what concern the microgeometry, the models C and D of this thesis have the exact same macro dimensions and geometrical parameters of that model supplied by the supporting material, [22]. On the other hand, since models A and B have nil helix angle, the dimensions will be different. However, the reasoning behind this building process is exactly the same.
Up to this point, only one last, but fundamental, element is still missing: the electric machine. It is possible to define properly both the stator and the rotor of

the electric motor, and also a preliminary version of the housing. The complete version of the housing will be available later on as a finite element in the final version of the gearbox.
The most important parameters of the electric motor, derived from supporting material [22], are reported in Table 2.10.

Parameter	Value
Number of slots	48
Number of phases	3
Number of pole pairs	4
Rotor length (mm)	170
Rotor inner diameter (mm)	50
Rotor outer diameter (mm)	140
Stator length (mm)	170
Stator inner diameter (mm)	142
Stator outer diameter (mm)	216
Air gap (mm)	1
Rotor mass (kg)	16.26
Rotor polar inertia ($kgmm^2$)	$4.445 \cdot 10^4$
Rotor transverse inertia ($kgmm^2$)	0

Table 2.10: Properties of the electric motor

Remember that, to design this gearbox, nothing changes if one decides to either start from the blank sheet or to simply change some dimensions and parameters of the already available template: the final result is the same and it is depicted in Figure 2.10.

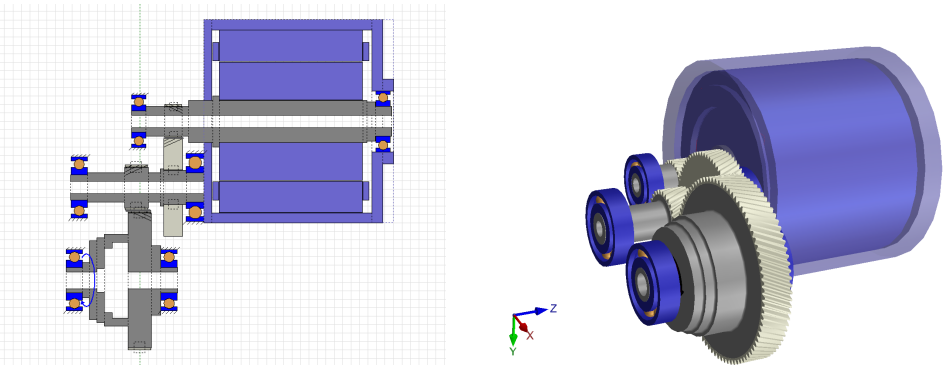

(a) *2D Gearbox* **(b)** *3D Gearbox*

Figure 2.10: Gearbox defined in Romax Concept

2.2 Romax Enduro

To increase the level of details, Romax Concept is not enough, it is indeed necessary to export the model just created to Romax Enduro. In fact, so far, only concept gears have been defined: in Enduro it is possible to convert concept gears to detailed ones. This represents a fundamental step in order to further obtain a more detailed analysis, in particular as regards the rating of the gears.
Defining a detailed gear set allows to impose many more parameters, whose values are set according to the Model supplied by [22]:

	Pinion	Wheel
Profile shift coeff.	-0.102	-7.161 $\cdot 10^{-2}$
Generating profile shift coeff.	-0.144	-0.113
Other diameter (mm)	39.593	116.980
Gear blank type	Solid (integral with shaft)	Symmetric carrier
Tip diameter (mm)	43.154	119.438
Tip alteration coeff.	0	0
Rack root fillet radius (mm)	0.3	0.3
Gear root diameter (mm)	34.295	111.782
Effective protuberance	2.0 $\cdot 10^{-2}$	2.0 $\cdot 10^{-2}$
Protuberance angle (deg)	14.958	14.958
Stock allowance / flank (mm)	0.1	0.1

Table 2.11: Properties of the detailed Input gear set, Romax Enduro

The first two defined parameters, i.e. *Profile shift coefficient* and *Generating profile shift coefficient*, are crucial to define the basic involute profile. The former defines the nominal tooth thickness, while the latter defines the actual tooth thickness, according to ISO 21771:2007 [25]. To better understand, please refer to Figure 2.11. The profile shift xm_n is defined by [25] as the displacement of the basic rack datum line from the reference cylinder. [25] states that the magnitude of the profile shift can be made non-dimensional by dividing by the normal module, and it is then expressed by the profile shift coefficient, x.
The parameter *Other diameter* is simply used to define the *Measurement diameter*, which is the diameter at which tooth thickness is evaluated.
Then, the following parameters are related to the pre-finish tool. *Tip diameter* and *Tip alteration coefficient* are useful to determine the *Rack addendum*. In particular, *Tip alteration coefficient* is defined by ISO 21771:2007 [25], and a nil value leads to a direct link between tip diameter and rack addendum.
Defining the *Rack root fillet radius*, then the *tool tip radius* will be defined as a consequence.
Then, defining the value of *Gear root diameter*, the *Rack dedendum* is directly computed by Romax.
Effective protuberance represents the residual protuberance of the finished gear, while *Protuberance angle* defines the angle between the rack protuberance profile and the rack transverse plane, as indicated by [22].
The protuberance is represented in Figure 2.12 by the parameter q_{Fs}, given by [25].

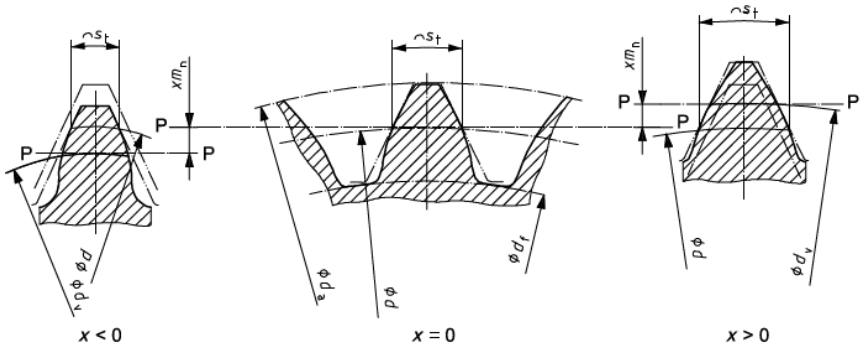

Figure 2.11: Profile shifting, [25]

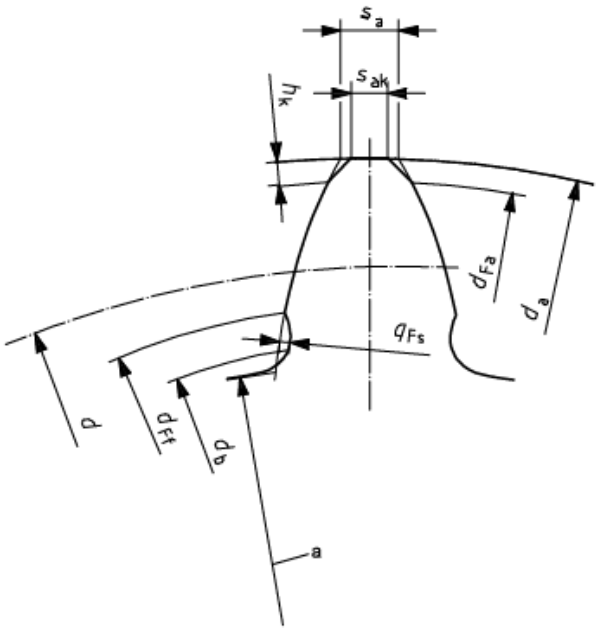

Figure 2.12: Protuberance, [25]

The definition of all above parameters allows Romax to compute by itself the following values:

	Pinion	Wheel
Rack addendum (mm)	1.236	0.867
Rack dedendum (mm)	1.481	1.481
Rack protuberance (mm)	$1.227 \cdot 10^{-2}$	$1.227 \cdot 10^{-2}$
Tool tip radius (mm)	0.489	0.489

Table 2.12: Properties of the detailed Input gear set, computed by Romax Enduro

Standard ISO 53:1998 [26] is useful to better understand the parameters of the rack just exposed, referring to Figure 2.13. Moreover, even the protuberance can be better understood looking at Figure 2.13. In that figure many parameters are highlighted, however the most relevant are: h_{aP} represents the addendum of the rack tooth, h_{fP} is the dedendum, α_{FP} is the protuberance angle while U_{FP} is the protuberance size.

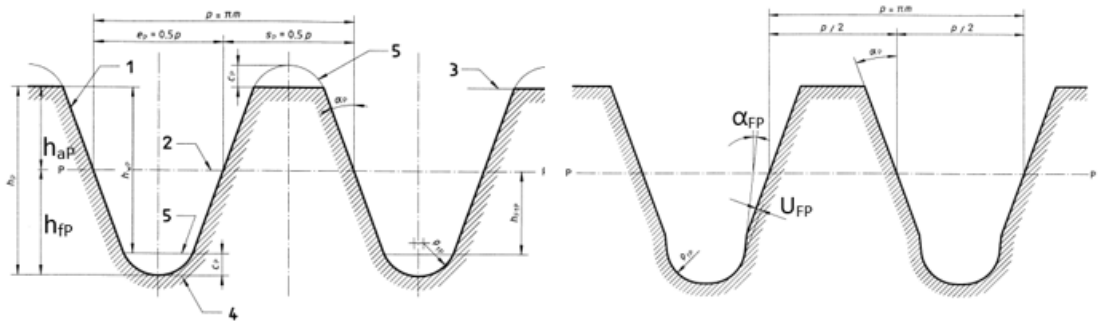

Figure 2.13: Rack profile, [26]

Similar reasoning is valid for Output gear set, too.

	Pinion	Wheel
Profile shift coeff.	0.109	-7.203 $\cdot 10^{-2}$
Generating profile shift coeff.	7.002 $\cdot 10^{-2}$	-0.111
Other diameter (mm)	53.723	165.147
Gear blank type	Solid (integ. w. shaft)	Solid (integ. w. shaft)
Tip diameter (mm)	58.906	168.555
Tip alteration coeff.	0	0
Rack root fillet radius (mm)	0.3	0.3
Gear root diameter (mm)	48.421	159.194
Effective protuberance	2.0 $\cdot 10^{-2}$	2.0 $\cdot 10^{-2}$
Protuberance angle (deg)	16.000	16.000
Stock allowance / flank (mm)	0.1	0.1

Table 2.13: Properties of the detailed Output gear set, Romax Enduro

	Pinion	Wheel
Rack addendum (mm)	1.367	1.055
Rack dedendum (mm)	1.540	1.540
Rack protuberance (mm)	1.109 $\cdot 10^{-2}$	1.109 $\cdot 10^{-2}$
Tool tip radius (mm)	0.541	0.541

Table 2.14: Properties of the detailed Output gear set, computed by Romax Enduro

Moreover, having defined the above parameters, Romax compute more detailed geometry dimensions, reported in Table 2.15.

	Gear Set - Input		Gear Set - Output	
	Pinion	Wheel	Pinion	Wheel
Root diameter (mm)	34.295	111.782	48.421	159.194
Form diameter (mm)	36.958	113.369	50.847	160.908
Tip diameter (mm)	43.154	119.438	58.906	168.555
Reference pitch circle diameter (mm)	39.593	116.980	53.723	165.147
Base diameter (mm)	36.185	106.909	49.469	152.072
Working pitch diameter (mm)	39.448	116.552	53.755	162.245
Addendum (mm)	1.781	1.229	2.592	1.704
Dedendum (mm)	2.649	2.599	2.651	2.977
Protuberance (mm)	0.12	0.12	0.12	0.12
Backlash angle θ_j (deg)	0.346	0.117	0.250	$8.135 \cdot 10^{-2}$

Table 2.15: Properties of the gears, Romax Enduro

The backlash angle is defined by [24] as the maximum angle that allows the gear to move when the other mating gear is held stationary. It can be computed once the circumferential backlash is known.
Moreover, Romax gives details about the contact geometry, too.

	Gear Set - Input		Gear Set - Output	
	Pinion	Wheel	Pinion	Wheel
Transverse contact ratio ϵ_α	1.416		1.650	
Axial contact ratio ϵ_β	1.697		1.864	
Total contact ratio ϵ_γ	3.113		3.514	
Contact length (mm)	7.319		9.496	
Length of line of action (mm)	31.066		42.843	
Transverse base pitch p_{bt} (mm)	5.167		5.756	

Table 2.16: Properties of the gears, contact geometry, Romax Enduro

The contact ratio is defined as the average number of couple of teeth in contact during the operation of the gears. It is crucial to have a contact ratio higher than 1 in order to have a continuous and regular contact between gears. Indeed, if the

contact ratio is higher than 1, it means that as soon as a couple of teeth is not anymore in contact, another couple of teeth is already in contact.
In case of spur gear, the contact ratio is simply computed as the ratio between the contact length and the normal base pitch.
On the other hand, in case of helical gears, the definition of contact ratio is more complex since it involves two components: transverse and axial. Then, the total contact ratio of helical gears is the sum of the transverse and axial components.
It is possible to obtain a plot which represents the profile of the tooth of each gear and all the important diameters, which are the following (definition from [27],[28]):

- Base Diameter: circle that is used as the basis for drawing the involute curve.
- Reference Pitch Diameter: imaginary circumference used to express the size of the gear teeth. It is the imaginary circle which passes through pitch point.
- Root Diameter: circle obtained connecting the roots of teeth.
- Tip Diameter: circle obtained connecting the tips of teeth.
- Form Diameter: diameter of a circle at which the root fillet curve intersects or joins the involute.

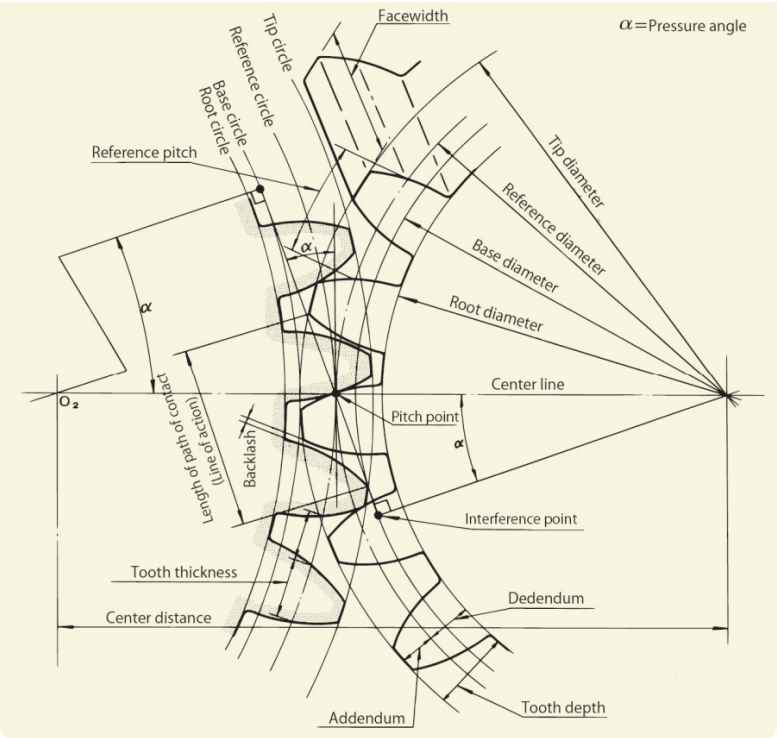

Figure 2.14: Definition of important diameters [29]

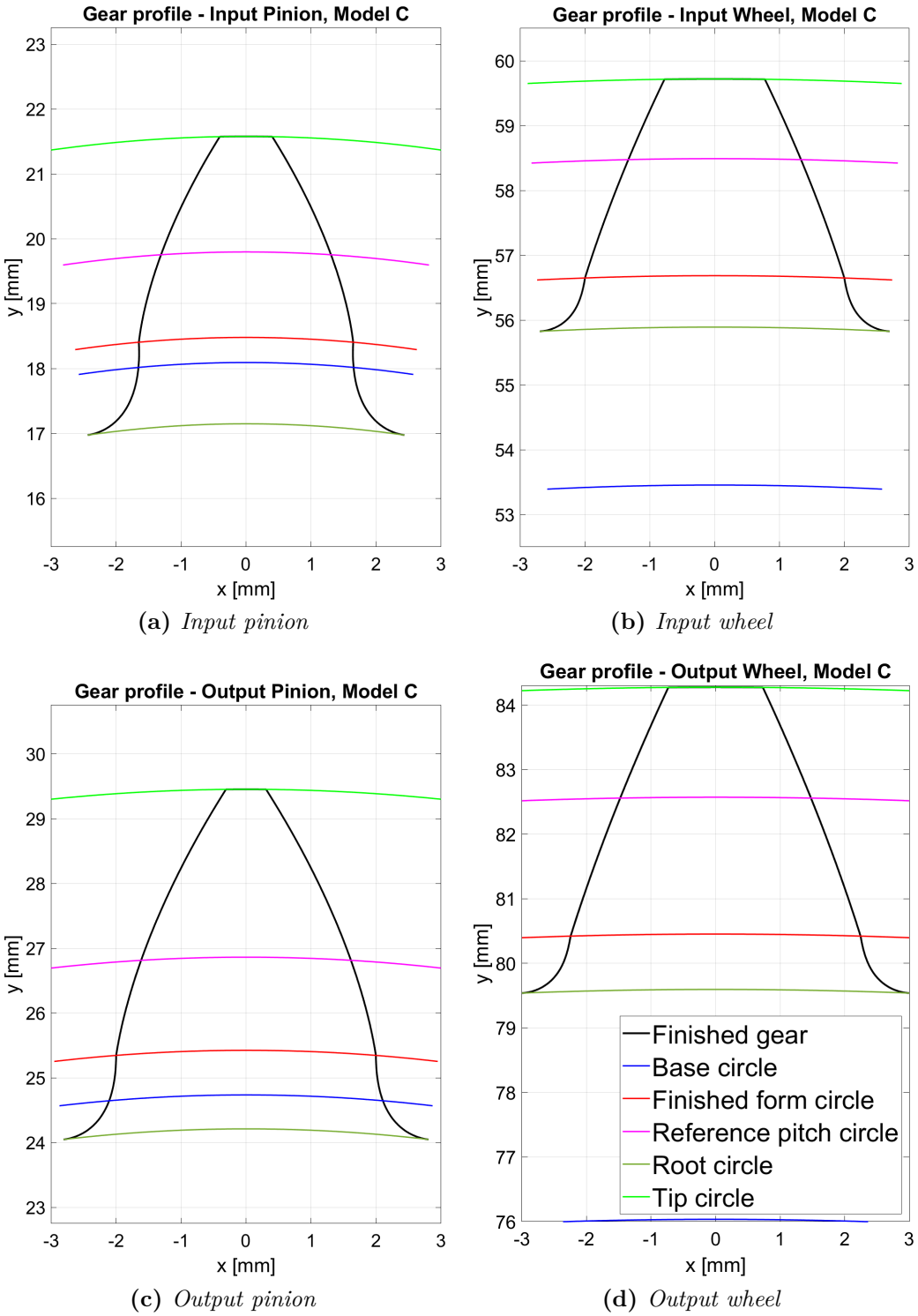

(a) *Input pinion* **(b)** *Input wheel*

(c) *Output pinion* **(d)** *Output wheel*

Figure 2.15: Tooth profile of each gear, Model C

Please be aware that all the above steps are all referring to the model C, which is the one with the helix angle given by Romax supporting material [22] and the profile shifting.
To build models A and B, both with nil helix angle, without and with profile shifting, respectively, the steps to follow are exactly the same. Hence, to avoid redundancy, the explanation of each passage is not repeated. However it is important to remind that all models are built trying to maintain constant the size and overall dimension of the gears.
However, gears are not the only modified components moving from Concept to Enduro, even details regarding the stator of the electric machine assembly are added. First of all, the stator material is defined: Steel (Mild), then, the slots are defined:

Parameter	Value
Slot height	14 mm
Slot width	3.5 mm

Table 2.17: Slots details

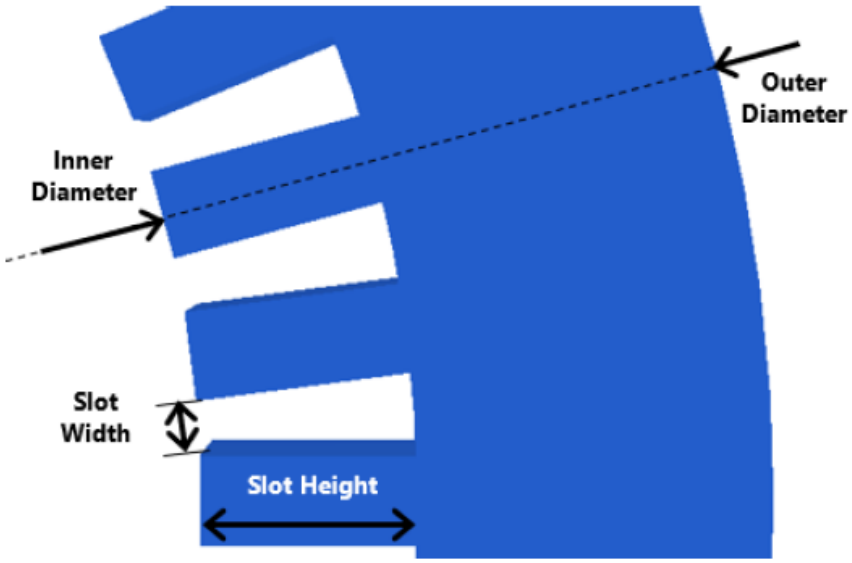

Figure 2.16: Slots characteristic dimensions [22]

In Figure 2.17 just a graphical representation of the stator of the motor is provided. To be more precise, moving then to Enduro, to perform the computations,

the stator is constituted by a FEM element, which is represented in Figure 2.18, where the nodes are highlighted.

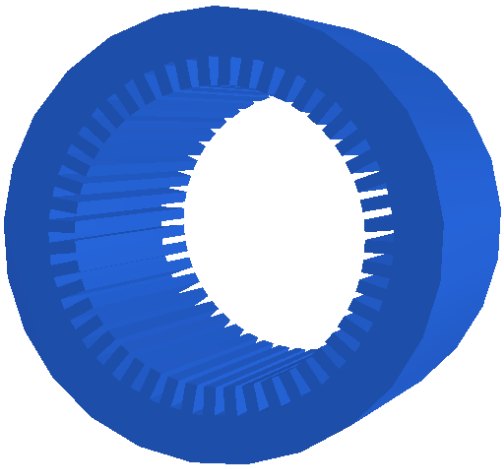

Figure 2.17: Stator graphical representation

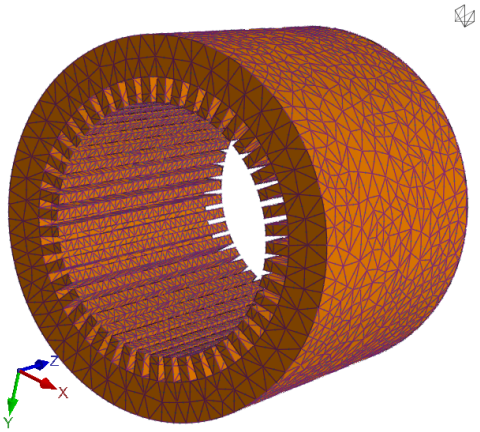

Figure 2.18: Stator nodes

2.3 Comparison among models A, B, C

As anticipated, the building steps will not be repeated for each model, but in this section just the differences among the first three models will be highlighted.
On the other hand, model D requires to add microgeometry modifications to the gears. This will be explained more in details in Section 2.4.

Hence, in this section the comparison among models A, B, and C will be investigated, the major differences are highlighted by Tables 2.18 and 2.19.

Model	Helix angle, Input Gear set	Helix angle, Output Gear set
Model A	0°	0°
Model B	0°	0°
Model C	25.081°	24.987°

Table 2.18: Comparison among models, helix angle

		Model A	Model B & C
Profile shift coefficient	In pinion	0	-0.102
	In wheel	0	$-7.161 \cdot 10^{-2}$
	Out pinion	0	0.109
	Out wheel	0	$-7.203 \cdot 10^{-2}$
Generating profile shift coeff.	In pinion	0	-0.144
	In wheel	0	-0.113
	Out pinion	0	$7.002 \cdot 10^{-2}$
	Out wheel	0	-0.111

Table 2.19: Comparison among models, profile shifting

The first distinction detectable among the models is whether or not profile shifting is used.
Profile shifting is a very effective way to modify gear macro geometry without a complete re-engineering of the gear itself. In particular, the main effects are related to change the shape of the tooth, and in particular to the thickness. To obtain profile shifting is necessary to change the relative distance of the cutting tool (i.e. rack) from the gear.
Moreover, another crucial difference is between spur gear and helical one.
In general, the contact between teeth in spur gears is distributed and applied along a line. On the other hand, in case of helical gears, the contact happens in a smaller area, and it is more regular, more smooth, gradually applied in time. These differences lead to have generally a less noisy contact in case of helical gears, as explained by [29]. Having a punctual contact, helical gears feature less noise and vibration generation, but the applied pressure will be higher than in case of

distributed contact.
It can be interesting to visualize, with the aid of the following plots, the differences of the tooth profiles among Models A, B, C.

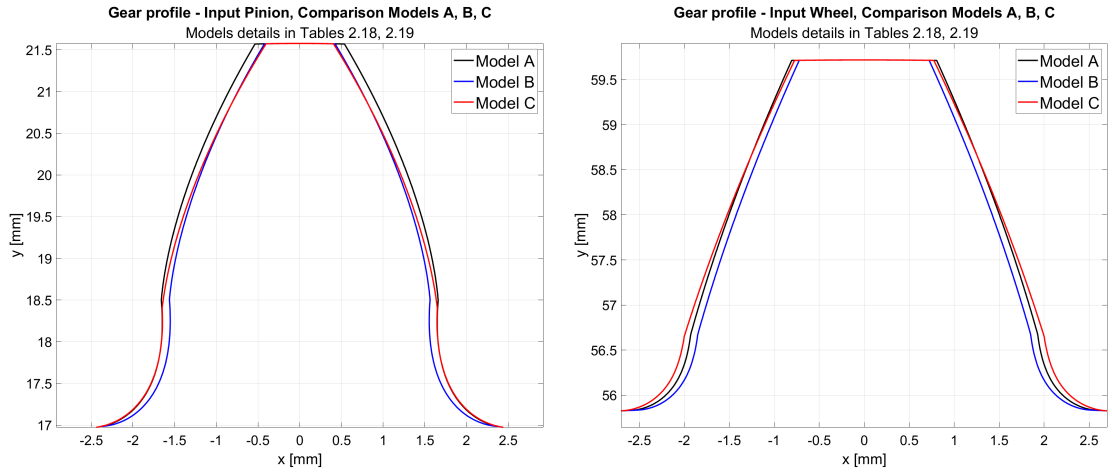

(a) *Input pinion*

(b) *Input wheel*

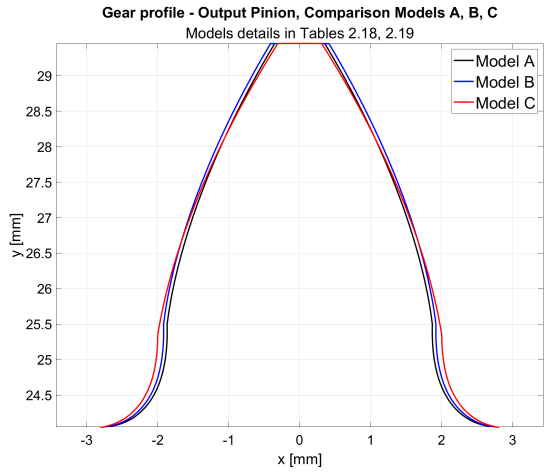

(c) *Output pinion*

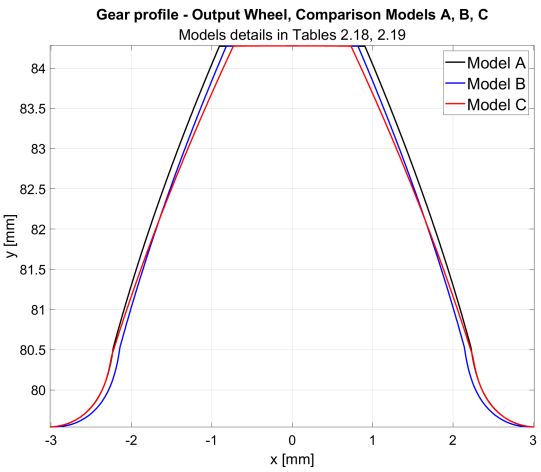

(d) *Output wheel*

Figure 2.19: Tooth profile of each gear, Comparison among models A, B, C

Moreover, it can be interesting to analyse the difference among the contact geometry among the three models:

	Model A	Model B	Model C
Transverse contact ratio	-	-	1.416
Axial contact ratio	-	-	1.697
Total contact ratio	1.471	1.471	3.113
Contact length (mm)	7.686	7.686	7.319
Length of line of action (mm)	29.111	29.111	31.066
Transverse base pitch p_{bt} (mm)	5.226	5.266	5.167

Table 2.20: Contact geometry, Gear Set - Input, Comparison among models A, B, C

	Model A	Model B	Model C
Transverse contact ratio	-	-	1.650
Axial contact ratio	-	-	1.864
Total contact ratio	1.736	1.736	3.514
Contact length (mm)	10.136	10.136	9.496
Length of line of action (mm)	39.241	39.241	42.843
Transverse base pitch p_{bt} (mm)	5.839	5.839	5.756

Table 2.21: Contact geometry, Gear Set - Output, Comparison among models A, B, C

First of all, it can be noted that the profile shifting is not affecting the values of contact geometry.
Moreover, a clear difference between spur gears (i.e. Models A and B) and helical gear (i.e. Model C) can be observed. Indeed, an higher contact ratio is obtained in case of helical gears. This should lead to a more smooth and quieter operation of the gear set, as it will be investigated in Chapter 6. In fact, the lower is the contact ratio, the higher is the deflection of the tooth and the vibration and noise produced by the gears.

2.4 Microgeometry optimization

To obtain the model D, the microgeometry modifications should be added. However, selecting properly the microgeometry parameters is not an easy task: it requires a lot of experience by the designer, and not always the modifications lead to the desired result. To overcome this issue, Romax makes available a very important and useful tool, the so called *microgeometry study tool*, which allows to choose among several optimization algorithms to perform parametric studies that help to select the proper parameters considering a certain target. Among all the available algorithms, it has been chosen to deepen the so called *Romax genetic algorithm*. This is the selected one since it is the only one that allows a proper optimization. This algorithm aims to find the optimum design, based on precise targets. In the first stage, a certain amount of random design candidates are composed, composing the 1^{st} generation. A score is assigned to each candidate, according to the optimization criteria, then the best candidates are selected and combined together to compose the 2^{nd} generation and so on, till the last iteration is reached. Some random effects are added in order to avoid premature convergence of the results. It is possible to either choose manually the number of iterations (i.e. the number of generations created) and the population size (i.e. number of candidates for each generation), or to leave the Romax default settings.
To go more in depth, the steps to follow are:

1. *Choose variable*: it allows to select which variables are to be varied, and how to vary them, during the iterations.

2. *Select constraints*: it lists the variables that are selected to be constrained by another variable in the *Choose variable* tab.

3. *Define actions*: it allows to define which actions have to be performed during the optimization process.

4. *Set targets*: it allows to define which are the targets of the optimization, which results should be obtained. A weight factor can be defined for each target.

5. *Run the optimization process.*

Finally, a score is assigned to each candidate. The score is generally defined as:

$$Score = weight \cdot (target\,variable - aim\,value)$$

Therefore, the best candidates are the ones with the lowest score.
Moreover, to really understand if a microgeometry optimization is satisfying or not, it is necessary to perform static and NVH analysis. Therefore, in this section only the process to follow in order to obtain the microgeometry modifications is described, but the real process of optimization will be performed in the following chapters.

Chapter 3

Electric vehicle performance

It can be interesting to correlate this kind of powertrain just exposed to a real application. To properly understand in which vehicle this powertrain can be used, it is fundamental to analyse the electric motor.
The main characteristic of this motor, coming from Romax supporting material, are reported in the following table:

Parameter	Value
Number of slots	48
Number of phases	3
Number of pole pairs	4
Absolute value of Max torque in drive conditions	160 Nm
Absolute value of Max speed in drive conditions	12000 rpm
Input power	$\approx$ 63 kW

Table 3.1: Properties of the electric motor for vehicle performance

Looking at the values of the table 3.1, especially considering the value of the power and of the maximum torque, it can be assumed that this motor can properly work in case of a city car. For instance, some electric vehicles, such as Smart EQ forfour, Smart EQ fortwo or Dacia spring have motors with very similar characteristics to the ones described in the table 3.1 (data of real vehicles obtained by consulting [30], [31]).
Moreover, it is interesting to analyse the graph representing the relationship between the torque and the speed of the electric motor and, in the same graph, between the power and the speed of the electric motor, Figure 3.1.
Remember the relationship that defines the power: $P = T \cdot \omega$. In the left part of

the plot, where the speed is below the nominal value, there is a section in which the motor torque is constant at its maximum value, whereas the power is increasing in a linear way, according to $P = T_{max} \cdot \omega$. In this initial phase, the supply voltage to the motor is increasing, while the flux is maintained constant.
Beyond the value of the nominal speed, the power reaches its maximum constant value, while the torque starts decreasing according to $T = P_{max}/\omega$.
The nominal speed is reached when the motor voltage equals the source voltage: beyond that point the flux decreases and the maximum constant power is maintained.
From Figure 3.1, the base speed of the motor is $\approx 3760\ rpm$.
These behaviours represented in the graph are typical of an electric motor, which has the important characteristic of allowing high values of torque starting from zero speed.

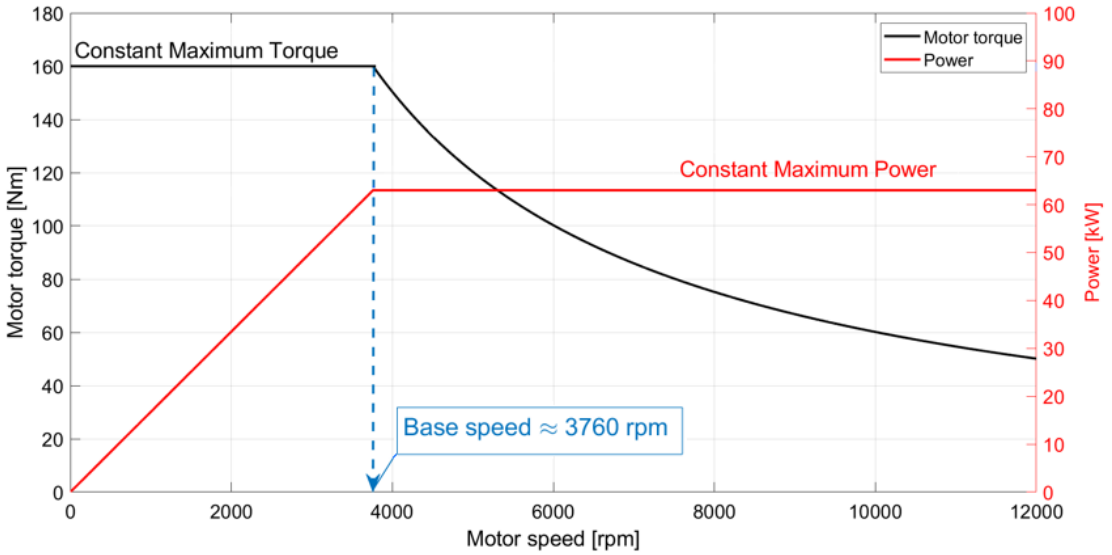

Figure 3.1: Torque vs Motor Speed and Power vs Motor Speed

Once assumed city car as kind of vehicle, it is possible to evaluate the performances of the vehicle itself: the maximum speed, the maximum acceleration and the maximum slope.
To do so, the first necessary step is to compute the resistive forces of the vehicle, which of course are opposed to the motion of the vehicle.
It is possible to distinguish resistive forces in three contributions:

- Rolling resistance force: it represents the resistance to motion of rotating parts. It is mainly caused by the the hysteretic behaviour of the tyre material.
- Gravitational force: it is caused by the slope of the road in which the vehicle

is moving. Surely, the gravitational force will have opposite sign considering either uphill or downhill motion of the vehicle.

- Aerodynamic force: since the vehicle moves through the air, the forces exerted by the air to the vehicle will affect the motion.

Now let's focus more on each contribution, starting from the rolling resistance. Several parameters can affect the rolling resistance, the most relevant ones are: tyre construction, tyre operating conditions and road surface. Generally, the rolling resistance depends on the vehicle speed, and some studies state that the general trend is an increase of the rolling resistance coefficient with speed. But many references, such as [32], agree on neglecting the dependency of rolling resistance on speed: only a constant term remains, which depends on the type of the vehicle and on the road surface. Considering a city car, with for instance tyres of dimensions *165/65 R15*, a tyre of class *C1* of fuel efficiency class *B* can be selected, leading to, according to [33], a rolling resistance coefficient equal to $f_0 = 0.007$.
The rolling resistance force shows a linear relationship between the rolling resistance coefficient and the wheel load (indicated as W), and it can be defined as:

$$F_{RR} = W f_0$$

where the wheel load is $W = Mg$, with M mass of the vehicle, g the gravitational acceleration.
Hence:

$$F_{RR} = Mgf_0$$

Moreover, if a certain slope α of the road is considered, the rolling resistance force becomes:

$$F_{RR} = Mgf_0 cos\alpha$$

Then, let's shift the focus on the gravitational forces. As already state, the sign of this contribution is opposite considering either uphill or downhill motion of the vehicle. Considering an angle α describing the slope, with respect to the horizontal, then the gravitational force will be:

$$F_G = \pm W sin\alpha = \pm Mgsin\alpha$$

The last important contribution concerning the resistive force is the aerodynamic resistance. This kind of resistance is generated by the fact that the vehicle is moving through the air, and the air itself will exert a certain force on the vehicle that will influence the motion.

Three main effects contribute to the aerodynamic resistance:

- Form resistance: caused by the difference in pressure between the front and the rear of the vehicle due to the airflow. The pressure in the front part of the vehicle will be higher than the one on the rear, hence a net force will be applied on the vehicle. Concerning this kind of contribution, the cross-sectional area of the vehicle plays a dominant role.
- Skin friction: frictional forces opposite to the direction of motion will be exerted by the air in contact with a relative speed with the vehicle body.
- Internal flow: resistive force caused by the air entering within the vehicle.

The form resistance is the one that plays the dominant role among the three.
The aerodynamic force is considered exerted on a specific point of the vehicle, called *centre of aerodynamic force*, C_p. Generally, aerodynamic forces are described by three-dimensional force system, but focusing on the longitudinal motion of the vehicle, only one component, called *drag force*, is relevant, which is opposed to the motion.
From a mathematical point of view, the aerodynamic force can be expressed as:

$$F_A = qC_sA_F$$

where C_s is the aerodynamic force coefficient (in this case, i.e. longitudinal motion, drag coefficient), A_F is the frontal area of the vehicle and q is the dynamic pressure, $q = \frac{1}{2}\rho_a v^2$, with ρ_a air density. The term v represents the air speed relative to the vehicle, but, assuming no wind conditions, the relative air speed coincides with the vehicle speed.
Therefore, the aerodynamic force is:

$$F_A = \frac{1}{2}\rho_a C_s A_F v^2$$

Finally, the total resistive force will be:

$$F_R = F_{RR} + F_G + F_A$$

$$F_R = Mgf_0cos\alpha + Mgsin\alpha + \frac{1}{2}\rho_a C_s A_F v^2 =$$

$$= \underbrace{Mg\left(f_0cos\alpha + sin\alpha\right)}_{A} + \underbrace{\frac{1}{2}\rho_a C_s A_F}_{B} v^2$$

$$F_R = A + Bv^2$$

Please be aware that just the longitudinal resistance (drag effect) is considered, while any lift or downforce effect is neglected.

Considering as kind of vehicle a FWD (front-wheel drive) city car, in normal conditions, the following parameters are selected:

Parameter	Symbol	Value	Unit of measure
Mass of the vehicle	M	1200	kg
Acceleration of gravity	g	9.81	m/s^2
Slope	α	variable	deg
Air density	ρ_a	1.225	kg/m^3
Frontal area	A_F	2	m^2
Aerodynamic force coefficient	C_s	0.35	-
Input transmission ratio	τ_{in}	2.955	-
Output transmission ratio	τ_{out}	3.074	-
Overall transmission ratio	τ	9.084	-
Transmission system efficiency	η_T	0.95	-

Table 3.2: Considered parameters to define vehicle performance

In Table 3.2 also some important parameters concerning the gears are reported, since they will be crucial in the following analyses.
Moreover, for the sake of clarity, in Table 3.3 a summary of the most important parameters of the selected tyres, according to [33], are reported.

Parameter	Value
Marking	165/65 R15
Class	C1
Fuel efficiency class	B
Rolling resistance coefficient f_0	0.007

Table 3.3: Tyre parameters

Having defined the total resistive force, it is then possible to evaluate the performance of the vehicle: the main characteristics to be obtained are:

- Maximum vehicle speed
- Maximum slope of the road (i.e. the max angle α)
- Maximum acceleration of the vehicle

3.1 Maximum speed

To obtain the maximum speed, it is possible to follow two different paths.
The first one is exploiting the relationship between the power needed by the vehicle and the vehicle speed.
The power needed by the vehicle can be expressed as:

$$P_n = F_R v = (A + Bv^2)v$$

Therefore, entering in the plot with the maximum power that can be delivered by the motor, multiplied by a certain efficiency of the transmission system, assumed $\eta_T = 0.95$ (reasonable value also according to [34], [35], [36]), it is possible to obtain by the graph the maximum vehicle speed.
Hence, considering as input in the graph the power $P_{IN} = P_{max} \cdot \eta_T = 63 \cdot 0.95 = 59.85\ kW$, the maximum speed of the vehicle is $v_{max} \approx 182\ km/h$.

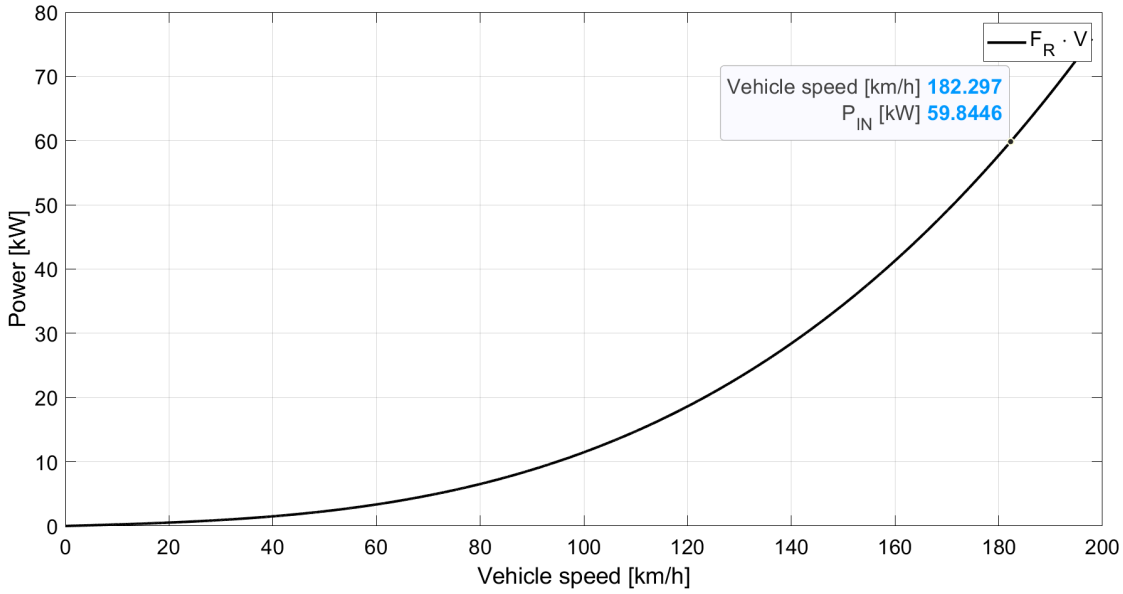

Figure 3.2: Power vs Vehicle Speed

The second possible path involves another graph that represents the relationship between the tractive force F_T (expressed in terms of force on tyres F_{tyres}), the resistive force F_R and the vehicle speed, Figure 3.3.
The tyres force can be expressed as:

$$F_{tyres} = T_m \tau \eta_T / R$$

where T_m is the motor torque, τ is the overall transmission ratio, η_T is the efficiency of the transmission system, R is the wheel radius.

The overall transmission ratio τ is equal to the product of the two ratios of the two gear sets, i.e. $\tau = 2.955 \cdot 3.074 = 9.084$. Considering, as already said, a city car, an example of tyre can be *165/65 R15*, which leads to a wheel radius equal to $R \approx 0.3\ m$.
Knowing the maximum torque produced by the motor, i.e. 160 Nm, it is possible to compute the maximum force on the tyres. Notice that the value of the force on tyres does not refer to a single tyre, but, considering a front-wheel drive vehicle (FWD), on the two front wheels.
Hence, the maximum force on tyres is equal to:

$$F_{tyres,max} = 160 \cdot 9.084 \cdot 0.95/0.3 = 4602.4N$$

This value of force will be the upper horizontal threshold of the graph of Figure 3.3: it sets an upper limit to the tractive force F_T.
As already stated, the graph in Figure 3.3 represents the values of tractive and the resistive forces depending on the vehicle speed v. The resistive force F_R is already debated in the previous lines, while the tractive force can be defined as:

$$F_T = \frac{P}{v}$$

where P is the power delivered to the wheels, i.e. $P_n \cdot \eta_T$.

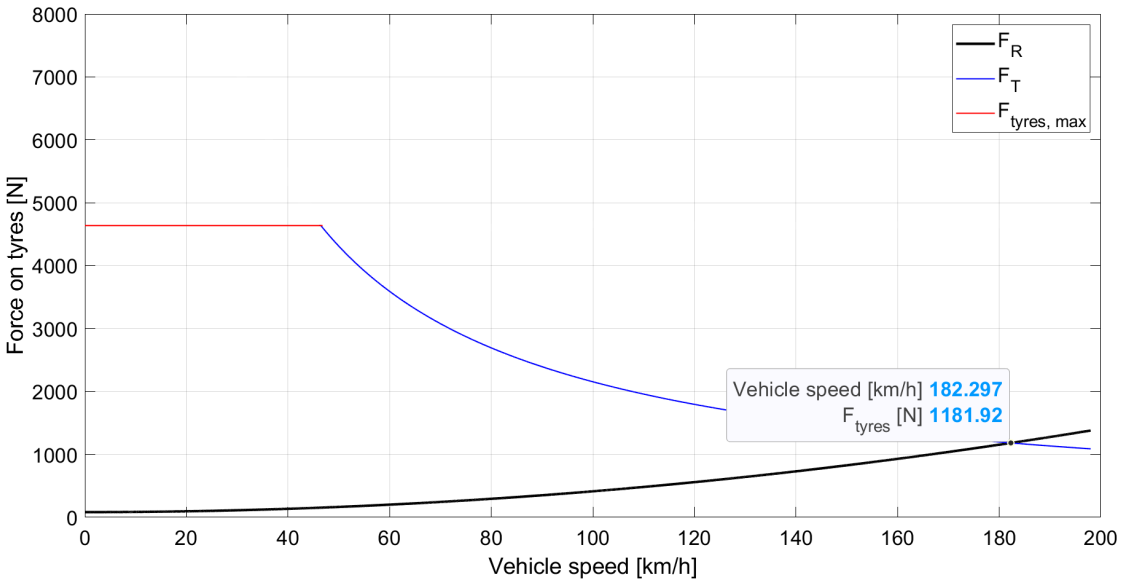

Figure 3.3: Tractive and Resistive Force vs Vehicle Speed

When the tractive force balances the resistive one, i.e. the intersection between the two lines in the graph, the maximum speed is obtained. Hence, looking at

Figure 3.3, the maximum speed of the vehicle should be equal to $v_{max} \approx 182\ km/h$. Notice that both graphs, Figure 3.2 and 3.3, lead to the same result.
However, this value of vehicle speed can not be reached in reality, due to the maximum speed of rotation of the electric motor (i.e. 12000 rpm).
It is possible to compute the maximum vehicle speed ($v_{max,vehicle}$) knowing the maximum speed of the electric motor ($n_{max,motor} = 12000\ rpm$) as follows:

$$v_{max,vehicle} = n_{max,motor} \frac{2\pi}{60} \frac{R}{\tau} \cdot 3.6 = 148.287 km/h$$

Hence, considering the electric motor speed limit, the two graphs modify as follows:

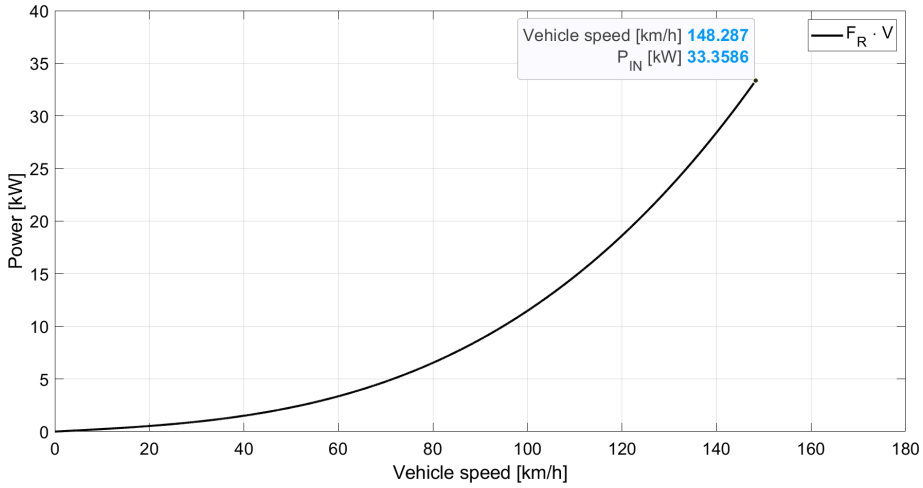

Figure 3.4: Power vs Vehicle Speed, considering motor speed limit

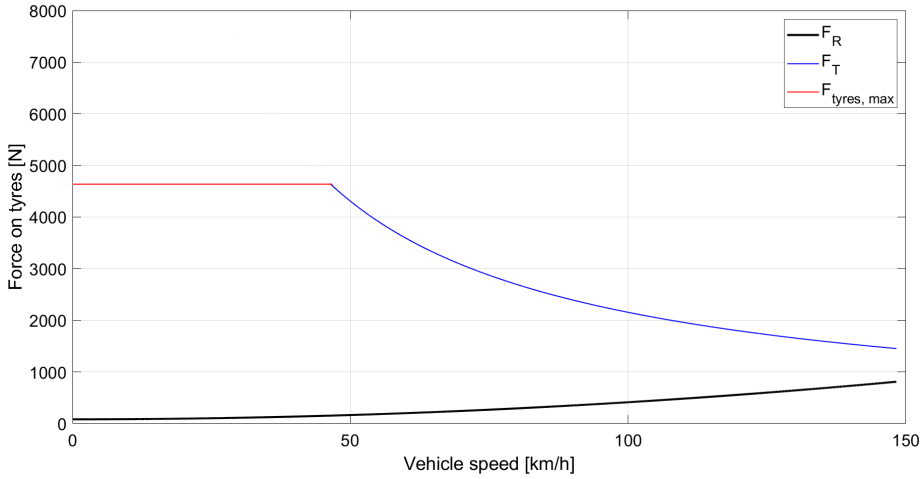

Figure 3.5: Tractive and Resistive Force vs Vehicle Speed, considering motor speed limit

3.2 Maximum slope

Defining the maximum slope is another critical step in order to properly evaluate the performance of the vehicle.
Changing the slope, the resistive force will be modified: in particular the rolling resistance and the gravitational force will be significantly changed.
It is possible to obtain the maximum slope graphically from the graph of Figure 3.5. As just stated, changing the slope α, the resistive force F_R will change and therefore the graph will show a different plot. An example of how the plot, and in particular the resistive force, changes modifying the value of the slope is reported in Figure 3.6.
Notice that the road slope is usually indicated in percentage. To obtain the slope value in percentage by knowing the angle α, it is required to compute the tangent of the angle and then multiplying it by 100.

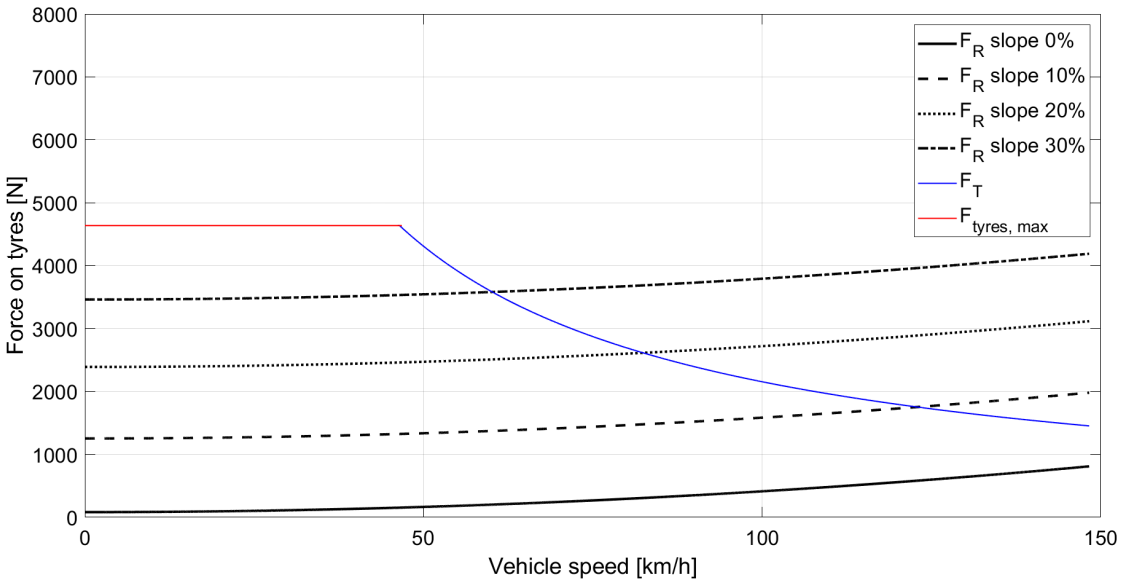

Figure 3.6: Different slopes

To find the value of the maximum slope, it is possible to follow an iterative procedure, modifying the angle α till a maximum velocity of $\approx 10\ km/h$ is obtained: the iterative procedure requires to change the angle α till the intersection between the resistive force F_R and the tractive force F_T is at $\approx 10\ km/h$.
The speed of $\approx 10\ km/h$ has been selected as reasonable value of minimum required speed by the vehicle to overcome a certain slope.
Following this iterative procedure, according to Figure 3.7, the maximum slope that allows to have a vehicle speed $\approx 10\ km/h$ is $\alpha = 22.78°$. Computing the tangent

of the angle and multiplying by 100 is then possible to obtain the slope in %.

$$\alpha_{max} = 22.78° \rightarrow tan(\alpha_{max}) \cdot 100 = 42.00\%$$

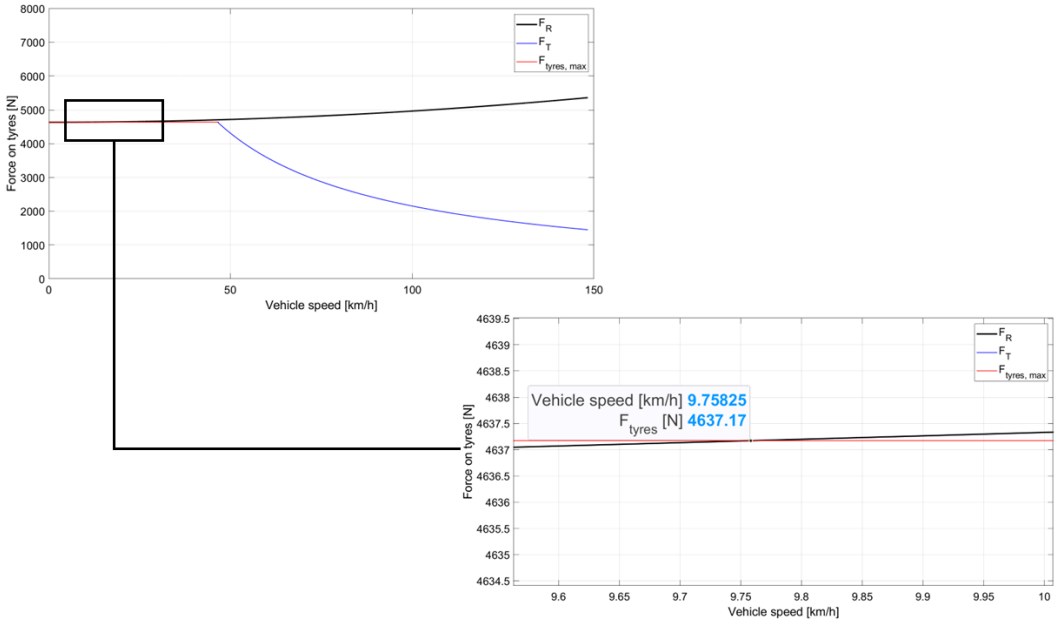

Figure 3.7: Maximum slope

However, there is also another effective way to determine the maximum slope of a FWD vehicle, performing some dynamic considerations, that will be now exposed. Let's consider the dynamic equilibrium of a vehicle proceeding along an inclined road with a certain slope α. Without going too much into details, as demonstrated by [37], the expression of normal forces at the road surface acting on the front (F_{z1}) and rear (F_{z2}) are the following:

$$\begin{cases} F_{z1} = Mg\left(\frac{b}{L}cos\alpha - \frac{h_G}{L}sin\alpha - \frac{\rho_a C_s A_F v^2}{2Mg}\frac{h_a}{L} - \frac{h_G}{L}\frac{\ddot{x}}{g}\right) \\ F_{z2} = Mg\left(\frac{a}{L}cos\alpha + \frac{h_G}{L}sin\alpha + \frac{\rho_a C_s A_F v^2}{2Mg}\frac{h_a}{L} + \frac{h_G}{L}\frac{\ddot{x}}{g}\right) \end{cases}$$

The equations above help in understanding the weight distribution between the front and rear axle due to the slope of the vehicle, or, being more precise:

- the first two terms of the second member represent the static weight distribution due to the slope.
- the third term represents the load distribution due to aerodynamic effects.
- the fourth term represents load distribution due to longitudinal acceleration.

L is the wheel base of the vehicle, a and b are the distance between the centre of gravity of the vehicle and the front and rear wheels, respectively, h_G is the distance between the ground and the centre of gravity of the vehicle (i.e. the height from the road plane), while h_a is the distance between the ground and the point of application of the aerodynamic forces. It is not granted that $h_G = h_a$, but in this case it is assumed so.
Moreover, notice that in these equations the effect of the rolling resistance on the ground distribution of the vertical load is neglected, since the longitudinal distances of the centre of gravity of the vehicle from the rear and front axles are always way higher than the rolling friction parameters.
To compute the maximum slope, let's consider to have very low speed and zero acceleration, therefore the third and fourth addends can be neglected. In this specific case, the maximum power transmissible to the ground is:

$$P_{max,2WD,front} = \mu v F_{zF}$$

Imposing the equality between transmissible and required power:

$$\mu F_{zF} = Mgsin\alpha$$

In this case, a FWD vehicle is considered, hence $F_{zF} = F_{z1}$, and neglecting the terms related to aerodynamic and acceleration effects, it is possible to simply rewrite:

$$\mu Mg \left(\frac{b}{L} cos\alpha - \frac{h_G}{L} sin\alpha \right) = Mgsin\alpha$$

Computing some simple passages it is possible to end up writing:

$$tan\alpha = \frac{b\mu}{L + \mu h_G}$$

Where μ is the friction, or adhesion, coefficient.
To compute the maximum slope, the following parameters are assumed, according to this kind of vehicle (i.e. electric FWD city car):

Parameter	Value
L	$2.490\ m$
a	$0.4 \cdot L$
b	$0.6 \cdot L$
h_G	$0.5\ m$

Table 3.4: Assumed dimensions of the vehicle

Moreover, considering dry asphalt, a friction coefficient equal to $\mu = 0.9$ is assumed.
Finally, it is possible to compute the maximum slope:

$$tan\alpha = \frac{a\mu}{L - \mu h_G} \rightarrow \alpha_{max} = atan\left(\frac{a\mu}{L - \mu h_G}\right) = 24.58° = 45.74\%$$

Therefore, it has been proved that the maximum slope obtained thanks to the graph in Figure 3.7, considering these parameters, is allowed.
Please, be aware that this value of maximum slope has been obtained by considering an high value of friction (i.e. $\mu = 0.9$). On the other hand, when the adhesion coefficient decreases, the maximum slope will decrease as well.

3.3 Maximum acceleration

To compute the maximum acceleration a level road is considered (i.e. $\alpha = 0°$).
In order to compute the maximum acceleration of the vehicle, it is necessary to start reasoning about the equation of longitudinal dynamic equilibrium:

$$F_{x1} - F_R - Mgsin(\alpha) = M\ddot{x}$$

- F_{x1} represents the total available force delivered by the powertrain to the front axle.
- F_R is the resistive force, considering both rolling and aerodynamic resistance.
- $Mgsin(\alpha) = 0$ since $\alpha = 0$.

Since it is required to obtain maximum acceleration, it is necessary to impose the drive axle (i.e. the front one) is in saturation condition, which coincides with the maximum allowable tractive force, i.e. $F_{tyres,max}$, as explained in section 3.1.
Therefore:

$$F_{x1} = F_{tyres,max}$$

Hence, it is possible to rewrite:

$$F_{tyres,max} - F_R = M\ddot{x}$$

Hence, the relationship between the acceleration and the vehicle speed will be given by the following equation (please keep in mind that the resistive force F_R depends on velocity):

$$\ddot{x} = \frac{F_{tyres,max} - F_R}{M}$$

Since the term representing the resistive force, which depends on the speed, is subtracted, it means that the maximum acceleration will be obtained at zero speed:

$$a_{max} = 3.8 \quad m/s^2$$

To obtain the plot representing the values of the acceleration over the whole vehicle speed range (Figure 3.8), it is necessary to do not consider anymore the saturation condition of the drive axle. Therefore, the front axle force is now given by $F_{x1} = F_T$, with F_T defined by section 3.1. Hence the relationship between vehicle acceleration and vehicle speed becomes:

$$\ddot{x} = \frac{F_T - F_R}{M}$$

Of course, as expected, the graph of Figure 3.8 confirms that the value of the acceleration at zero speed coincides with the maximum one. Furthermore, since F_T decreases with vehicle speed, while F_R increases with speed, as depicted by several plots in previous sections, it is expected that the higher is the vehicle speed, the lower is the acceleration of the vehicle.

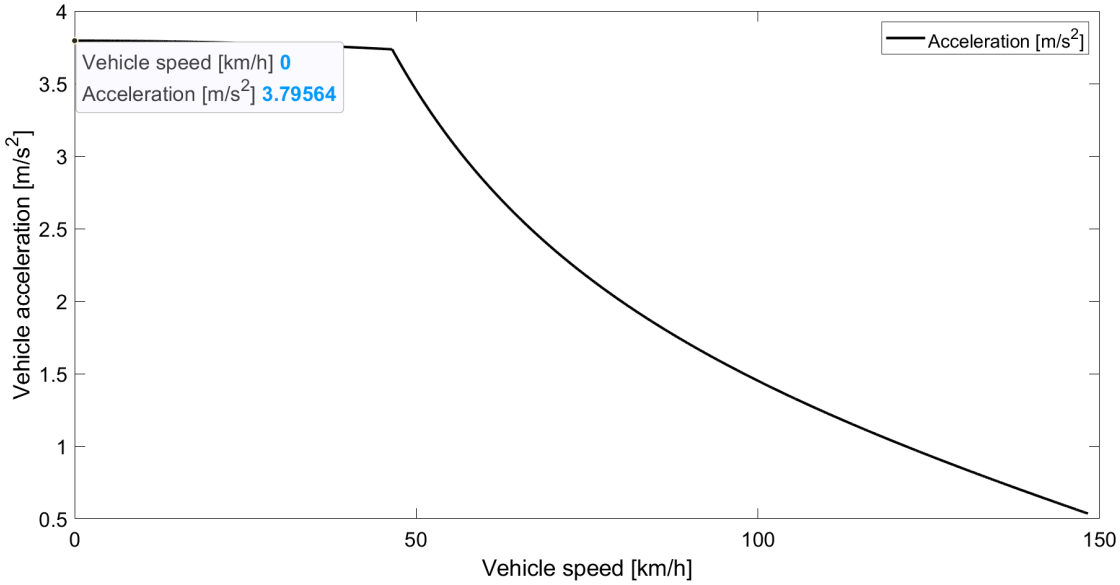

Figure 3.8: Acceleration vs Vehicle Speed

An interesting observation is that it should be expected to reach nil acceleration at the maximum speed of the motor, however in Figure 3.8 a certain value of acceleration is detectable even at the maximum speed. This is due to the fact that this motor does not exploit fully its power, on the contrary the speed of the vehicle is limited by the maximum speed of the electric motor, as explained in section 3.1.

Chapter 4

Static analyses

Once that the models are available, before performing any NVH analyses, it is required to carry out static analyses. This goal can be reached using both Romax Concept and Enduro. Surely the level of details of the achievable results in Concept is lower with respect to Enduro.

4.1 Analyses in Concept

In this section, a brief overview of the static analyses results achievable using Romax Concept is offered. Only the Model C, i.e. the one with helix angles different from zero, is investigated. More detailed analyses, considering all models are provided in Section 4.2.
In order to analyse a powertrain, it is necessary to define a certain duty cycle, which contains some load cases. In particular, the input values of each load case are reported in Table 4.1. All these input values come from supporting material from [22]. These are values representing the most important load cases, i.e. the maximum speed and torque conditions, considering both drive and coast condition. Coast is a condition in which the speed and the torque have opposite sign, in particular the speed has the same sign of the driving mode. In coast condition, the tyres drive the motor, rather than the motor drives the tyres. Notice that in this specific case, due to the way in which the model was defined, considering the sign convention used, the driving condition is defined by a negative speed and negative torque, while the coast mode has negative speed and positive torque.
Moreover, an additional load case, called *NVH*, is reported, since it represents interesting values of speed and torque to be analysed later on the NVH analyses. More details will be given in Section 6.1.
Hence, the duty cycle of Table 4.1 is considered as reference for static analysis.

		Input Rotor		
Load case	Duration (h)	Speed (rpm)	Torque (Nm)	Power (kW)
Max Speed (coast)	10	-12000	50	-62.83
Max Speed (drive)	10	-12000	-50	62.83
Max Torque (coast)	10	-7600	80	-63.67
Max Torque (drive)	10	-3800	-160	63.67
NVH	10	-5000	-25	13.09

Table 4.1: Duty cycle, input rotor

As a consequence of these input parameters, the output values are reported in Table 4.2. Remember the total transmission ratio:

$$\tau = \tau_{IN} \cdot \tau_{OUT} = 2.955 \cdot 3.074 = 9.068$$

The output speed is given by dividing the input speed by the total transmission ratio, while the output torque is given by multiplying the input torque by the total transmission ratio.

		Power output		
Load case	Duration (h)	Speed (rpm)	Torque (Nm)	Power (kW)
Max Speed (coast)	10	1321	454.12	62.83
Max Speed (drive)	10	1321	-454.12	-62.83
Max Torque (coast)	10	837	726.60	63.67
Max Torque (drive)	10	418	-1453.20	-63.67
NVH	10	551	-227.06	-13.09

Table 4.2: Duty cycle, power output

This duty cycle is interesting to be considered since it is representative of an accelerated endurance test of the vehicle. Indeed, the duration of each load case is not very high, but the torque and speed condition are pretty extreme, since the maximum speed and maximum torque are taken into account. This is a pretty common procedure, called *Palmgren-Miner model* (explained in [38]): a more extreme duty cycle (*extreme* from the speed and torque viewpoint) is used in order to have an accelerated test. The accelerated duty cycle will cause the same damage of an equivalent load case that will cover a realistic distance for the endurance

validation of the vehicle. The values of the accelerated duty cycle (Table 4.1), cause an equivalent damage, that to be obtained with the more realistic equivalent load case would require an incredible amount of hours. The aim of this duty cycle is to obtain a proper endurance test spending way less hours.
In this case, the load case taken as reference is the *NVH*, hence with, in absolute values, a rotational speed of $5000\,rpm$ and a torque of $25\,Nm$.
Hence, the goal is to correlate the load cases of the accelerated duty cycle (Table 4.1) to an equivalent duration in terms of covered distance in km which cause the same damage.
First of all, it is necessary to compute the damage number of the i-th load case d_i, as follows:

$$d_i = rev_i T_i^k$$

with rev_i total number of revolution of the load case, evaluated as:
$rev_i = speed_i(rpm) \cdot 60 \cdot D_i$, with D_i duration (in h); T_i is the torque of the i-th load case, k is the torque exponent.
The torque exponent varies depending on which component is the most critical, $k = 3.0 - 3.3$ if the bearings are considered as the most critical, $k = 7.0 - 9.0$ if the gears are more critical. In this case it has been selected a value equal to $k = 3$, since the bearings are considered more critical.
To better understand, look at Figure 4.1. The figure shows the values of torque against the time. Two curves are available, one related to the bearings and one to the gears. For a certain duration T_{test}, two different torques are obtained, depending on the fact if either bearings or gears are considered. In particular, the torque required by bearings is higher with respect to the one of gears. If, as it has been chosen in this case, the bearings are considered more critical, it is found, as highlighted by [38], that the duration that should be had to have the same damage on gears is less than T_{test}, meaning that the gears are over stressed.

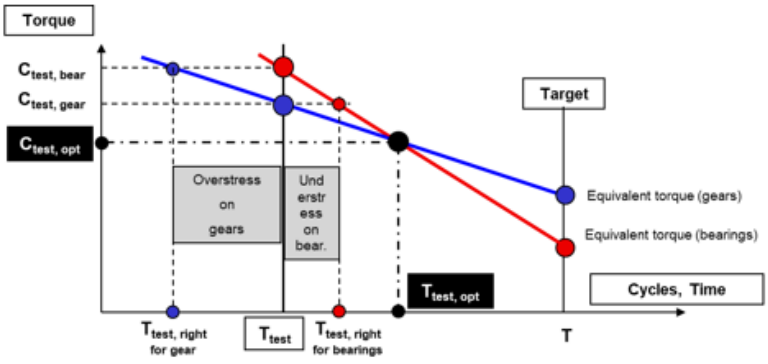

Figure 4.1: Time diagram for accelerated test [38]

Then, as already anticipated, the load case of the accelerated duty cycle causes the same damage of a longer load case with a torque of $25\,Nm$ and a speed of $5000\,Nm$, which is called *equivalent load case*. The damage of the equivalent load case will be:

$$d_{eq,i} = n_{eq,i} T_{eq,i}^{k} = 5000 \cdot 60 \cdot D_{eq,i} \cdot 25$$

By imposing $d_i = d_{eq,i}$, it is possible to obtain the duration of the equivalent load case, $D_{eq,i}$, in h.
Then, it is necessary to obtain the vehicle speed at the equivalent load case, in order to correlate the duration in hours in a covered distance in km. Knowing the speed of the *equivalent load case*, and the transmission ratio τ and the tyre radius R, it is possible to obtain the vehicle speed in km/h:

$$vehicle\,speed = n \cdot \frac{2\pi}{60} \cdot R \cdot 3.6 = 62.36\,km/h$$

Where $\tau = 9.068$ and $R = 0.3\,m$. In the following tables, the values of torque and speed are reported in absolute terms, since the computation does not depend on the sign convention.

Load case	Speed (rpm)	Torque (Nm)	D_i (h)	k	d_i
Max speed (Drive and Coast)	12000	50	20	3	$1.80 \cdot 10^{12}$
Max torque (Drive)	3800	160	10	3	$9.34 \cdot 10^{12}$
Max torque (Coast)	7600	80	10	3	$2.33 \cdot 10^{12}$

Table 4.3: Accelerated test

Therefore, imposing the same value of damage, as already explained is possible to obtain the duration of the *equivalent load case*, which cause the same damage, simply applying the inverse formula:

$$D_{eq,i} = \frac{d_{eq,i}}{speed_{eq,i} \cdot 60 \cdot T_{eq,i}^{k}}$$

Remember that $d_i = d_{eq,i}$, $speed_{eq,i} = 5000\,rpm$, $T_{eq,i} = 25\,Nm$, $k = 3$. Hence, the duration of each equivalent load case $D_{eq,i}$ is highlighted in Table 4.4.

Load case	$d_{eq,i}$	$duration\,(h)$	$D_{eq,i}\,(h)$	$distance_{eq,i}\,(km)$
Max speed (Drive and Coast)	$1.80 \cdot 10^{12}$	20	384	23946.24
Max torque (Drive)	$9.34 \cdot 10^{12}$	10	1992.53	124254.38
Max torque (Coast)	$2.33 \cdot 10^{12}$	10	497.07	30997.08

Table 4.4: Equivalent test

By summing the equivalent distance covered by each equivalent load case, considering also the load case *NVH*, that has not being accelerated (which has a duration of $10\,h$, leading to $623.6\,km$), it is possible to obtain the equivalent total duration in h (i.e. $D_{eq,tot}$) and the equivalent total distance covered in km (i.e. $distance_{eq,tot}$):

$$D_{eq,tot} = 2883.60\,h$$

$$distance_{eq,tot} = 179\,821.30\,km$$

Therefore, it has been proven that the duty cycle in Table 4.1 is equivalent to a covered distance of $179\,821.30\,km$ considering the equivalent load case *NVH*.
After having proven that the considered duty cycle is representative of an accelerated test, the static and fatigue analysis can be performed.

Thanks to Romax Concept it is possible to perform some preliminary static analysis that are synthesized in reports. The main available results are:

- Excitation order report: This report shows both the tooth passing frequencies and harmonics of all gears as well as the harmonics related to all the considered electric machine excitations. This report is useful in order to understand which harmonics will be the most interesting to analyse during the NVH analyses. Here below only the results concerning the NVH load case are reported, but a report is available for each load case.

Excitation Source	Harmonic	Excitation order
Electric Machine	Radial force harmonic 1	8
	Radial force harmonic 2	16
	Radial force harmonic 3	24
	Torque ripple harmonic 1	24
	Radial force harmonic 4	32
	Radial force harmonic 5	40
	Radial force harmonic 6	48
	Torque ripple harmonic 2	48
	Torque ripple harmonic 3	72
Input gear set	Harmonic 1	22
	Harmonic 2	44
	Harmonic 3	66
Input gear set	Harmonic 1	9.138
	Harmonic 2	18.28
	Harmonic 3	27.42

Table 4.5: Excitation orders

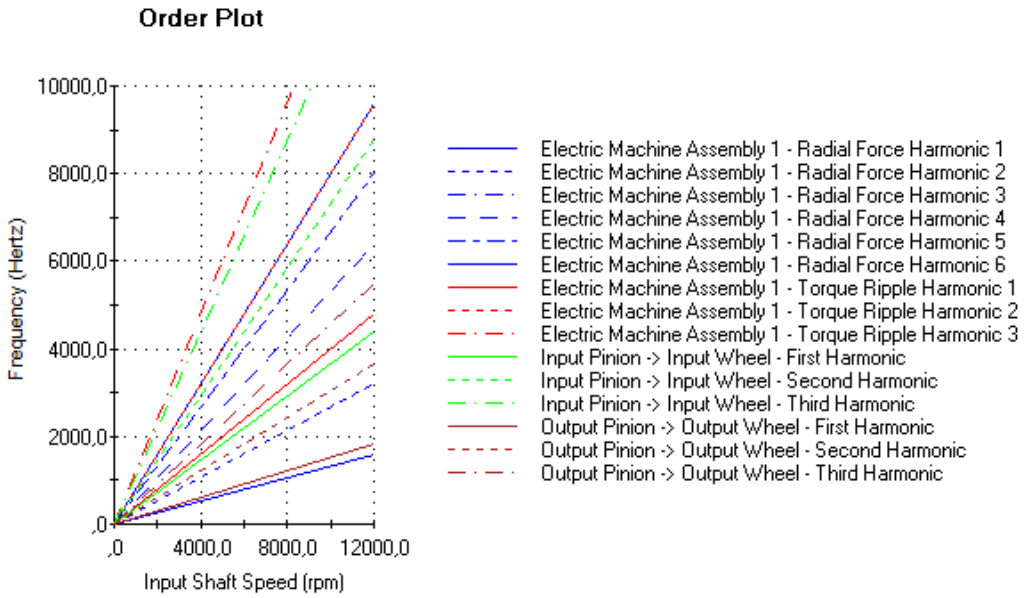

Figure 4.2: Excitation order NVH load case plot

The input gear set has the first harmonic of order 22, since it is the number of teeth of input pinion.
Considering the output gear set, the first harmonic reported has order 9.138. This is given by the following formula, given by [39]:

$$z_{output,pinion}/\tau_{IN} = 27/2.955 = 9.138$$

As regards the electric machine, knowing the characteristic of the motor (e.g. number of poles and slots) it is possible to obtain the harmonic orders. The motor of this model has 48 slots and 8 poles, therefore the noise orders are multiples of the number of motor poles, i.e. 8, as explained in Chapter 1. More details will be given in Chapter 6.

- Gear rating summary: This report lists the damage and safety factors for the contact and bending of each gear mesh for each load case according to ISO 6336. It is possible to obtain the safety factors considering the whole duty cycle; moreover it is possible to investigate more into details each load case specifically, too, if required. In the tables below the results for the entire duty cycle are reported. Remember that the damage is referred to the duty cycle of Table 4.1, which has a total duration of 50h.

Gear	Contact damage (%)		Bending damage (%)	
	Left flank	Right flank	Left flank	Right flank
Input pinion	2.10	0.00	0.00	0.00
Input wheel	0.71	0.00	0.00	0.00
Output pinion	5.40	$2.79 \cdot 10^{-3}$	2.40	0.00
Output wheel	1.80	$9.06 \cdot 10^{-4}$	0.72	0.00

Table 4.6: Gear rating of the whole duty cycle, Damage

Gear	Safety factor contact		Safety factor bending	
	Left flank	Right flank	Left flank	Right flank
Input pinion	1.32	1.65	1.56	2.62
Input wheel	1.45	1.80	2.11	3.37
Output pinion	1.28	1.63	1.22	2.08
Output wheel	1.41	1.79	1.47	2.46

Table 4.7: Gear rating of the whole duty cycle, Safety Factors

- Bearing life ratings: it shows the life of the bearings subjected to the whole duty cycle according to ISO 281. Moreover, it is also possible to investigate more in depth a certain bearing if the life is the particularly low or the damage is high. Considering this duty cycle, the reports is the following.

Bearing	Mod. life(h) L_{10mh}	Damage to mod. life(%)	ISO76 SF
Input shaft LH	310.89	16.1	1.69
Input shaft RH	$7.65 \cdot 10^{4}$	$6.53 \cdot 10^{-2}$	15.61
Different. shaft LH	1322.08	3.80	2.76
Different. shaft RH	101.28	49.4	0.89
Intermed. shaft LH	188.55	26.50	1.22
Intermed. shaft RH	401.66	12.4	1.48

Table 4.8: Bearing life rating considering whole duty cycle

From the report it is noticeable that a bearing of the differential shaft, in particular the Differential Shaft RH, is critical, since it has a worst ISO 76

safety factor lower than 1. Romax gives the possibility to investigate more in details each bearing, in order to better understand why a failure can be obtained.
In particular, it can be noted that the issue is that the dynamic capacity of Differential Shaft RH is not high enough.
Hence, a possible solution is to change the bearing from the catalogue, as investigate in the following sections.

- Torque and tangential force: it gives the torque, tangential and separating forces applied to the shafts and the gear sets. This report can be obtained for each load case, but now only the results concerning the load case *Max Torque (Drive)* are reported, since it is the most critical one. The values of torque are obtained simply taking into account the transmission ratios of the gears (the intermediate shaft torque is equal to the input shaft one multiplied by the input gear set transmission ratio, while the differential shaft one is the intermediate one multiplied by the output gear set transmission ratio).

Shaft	Load case: Max Torque (Drive)
Input Shaft	160.00 Nm
Intermediate Shaft	472.73 Nm
Differential Shaft	1453.20 Nm

Table 4.9: Total applied torque

Gear set	Gear	Load case: Max Torque (Drive)
Input	Input Pinion	-160.00 Nm
	Input Wheel	-472.73 Nm
Output	Output Pinion	472.73 Nm
	Output Wheel	1453.20 Nm

Table 4.10: Total torque

Gear set	Load case: Max Torque (Drive)
Input	8111.90 N
Output	$1.76 \cdot 10^4$ N

Table 4.11: Tangential force

Gear set	Load case: Max Torque (Drive)
Input	3522.20 N
Output	7477.70 N

Table 4.12: Separating force

The separating, or radial, forces are obtained by multiplying the tangential forces by the tangent of the working pressure angle.
The tangential force are computed dividing the torque by the gear pitch radius.

- Axial force report: it gives the axial forces generated by the helical gears

Shaft	Gear	Helix angle (deg)	Hand	Max Torque (Drive)
Input Shaft	Input Pinion	25.081	right	-3782.60 N
	Total			-3782.60 N
Interm. Shaft	Output Pinion	24.987	left	-8201.50 N
	Input Wheel	25.081	left	3782.60 N
	Total			-4418.90 N
Diff. Shaft	Output Wheel	24.987	right	-8201.50 N
	Total			-8201.50 N

Table 4.13: Axial force

- System loads report: it gives for each load case the forces and the moments applied to the inner raceway of each bearing by the shaft. As before, the focus is just on the most critical load case, i.e. *Max Torque (Drive)*.

	Force (N)				Moment (Nm)	
Bearing	X	Y	Radial	Z (Axial)	X	Y
Input Shaft LH	-3362.20	7155.80	7906.30	-2984.40	-50.09	-22.79
Input Shaft RH	-159.80	955.80	969.00	-797.50	-6.57	-0.91
Interm. Shaft LH	-6609.90	$-1.14 \cdot 10^4$	$1.31 \cdot 10^4$	-3118.80	64.60	-33.09
Interm. Shaft RH	2654.50	$-1.43 \cdot 10^4$	$1.46 \cdot 10^4$	-1300.00	28.24	13.21
Diff. Shaft LH	-4177.20	4021.60	5798.50	2637.30	31.66	40.27
Diff. Shaft RH	$1.16 \cdot 10^4$	$1.36 \cdot 10^4$	$1.79 \cdot 10^4$	5564.20	92.10	40.27

Table 4.14: System loads report

4.2 Analyses in Enduro

Using Romax Enduro is possible to obtain many more details concerning the static and fatigue analysis.
It is possible to investigate the three models with the three different level of details of gears, defined in Chapter 2, in order to inspect the main differences.
In the following sections, more details will be given, and the main results for each model with its own level of detail will be provided. The analyses will focus mainly on three critical components: shafts, bearings and gears.
Let's start investigating the first three models, while Model D (i.e. the one with microgeometry modifications) will be analysed in details in a dedicated chapter.

4.2.1 Shafts

To obtain the shaft static results, each shaft is divided into nodes, which are created at shaft steps, evenly along constant diameter sections and at any connection point. Graphs representing forces, moments, displacements and stresses of each node and for each load case of the whole duty cycle can be obtained.
Moreover, Romax gives the possibility to consider the standard DIN743, which enables to obtain fatigue and deformation safety factors for each node of any shaft in each load case. The standard sets the minimum value of fatigue safety factor equal to 1.2 in order to avoid failures related to fatigue issues, while the minimum value of deformation safety factor in order to avoid plastic deformation, incipient crack and force rupture is set to be 1.2, too.
In the next figures, the fatigue and deformation safety factors are highlighted by vertical lines in each node. The vertical lines are not just qualitative, but also quantitative: indeed, the longest the line the higher is the safety factor.

As anticipated, the density of the nodes depend on the presence of external elements. Indeed, the nodes are created at each shaft steps, and evenly along constant diameter sections. Moreover, if some element such as bearing or gear are present, more nodes are created to better describe the system behaviour. For instance, looking at the input shaft, many nodes are present at both ends of the shaft, due to the presence of two bearings and the gear. In the intermediate shaft the nodes are created by the presence of two bearings and two gears, while in the differential shaft two bearings and just one gear are present. For each shaft, other than the safety factors, stresses and displacement plots, also the representations of the shafts themselves are reported, in order to highlight the position of bearings and gears, to make more clear the creation of nodes.
To be concise, in the tables only the worst safety factor of each shaft, considering the most critical load case in term of torque (i.e. *Max torque (drive)*), are reported below, in order to identify the most critical points that might be further analysed, if required.

Model A, Model B, spur gears

Models A and B are reported together since they differ only due to some modification on the gear sets. In particular, profile shifting is considered in case of Model B. Therefore, the shaft static results are the same in both the models.

- Input Shaft:
  First of all, the stresses (tension, torsion and bending) and the maximum radial displacement plots are reported in Figure 4.3.

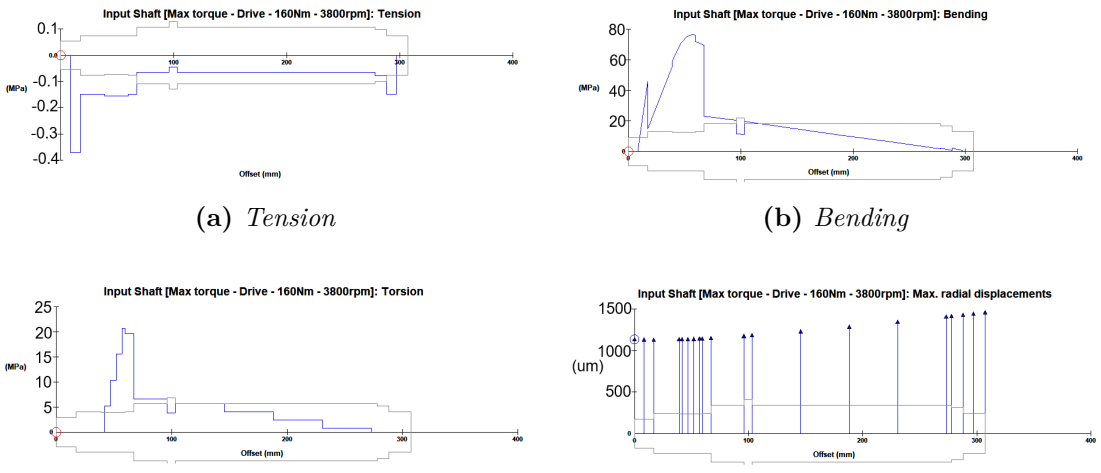

(a) *Tension* **(b)** *Bending*

(c) *Torsion* **(d)** *Maximum Radial Displacement*

Figure 4.3: Stresses and displacements, Input shaft

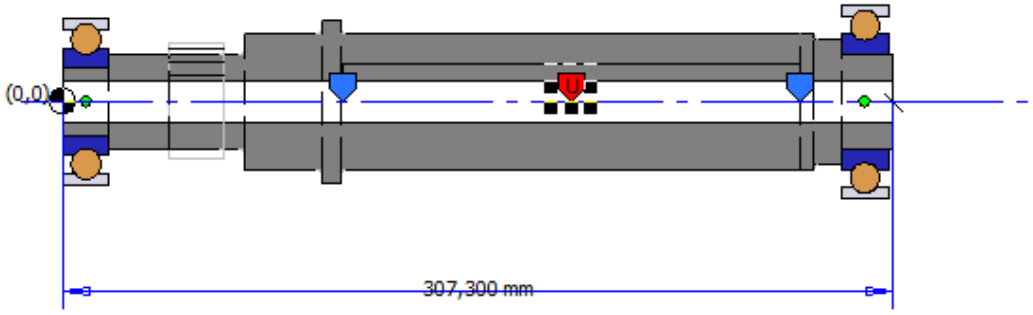

Figure 4.4: Input shaft

From the plots below (Figure 4.5, 4.6), it clearly appears that the input shaft is widely verified in each node. The most critical nodes, i.e. the ones with the lowest value of safety factor, for either fatigue or deformation are reported in Table 4.15.
With the help of Figure 4.4 it is possible to understand that the lowest safety factor are in correspondence of the gear, where also the stresses are generally the highest computed, as highlighted by Figure 4.3.

Load case	Node Offset (mm)	Fatigue SF	Deformation SF
Max Torque (Drive)	57.188	4.26	4.49
	67.102	2.88	5.30

Table 4.15: Fatigue and deformation safety factors of the most critical nodes, input shaft, Model A and B

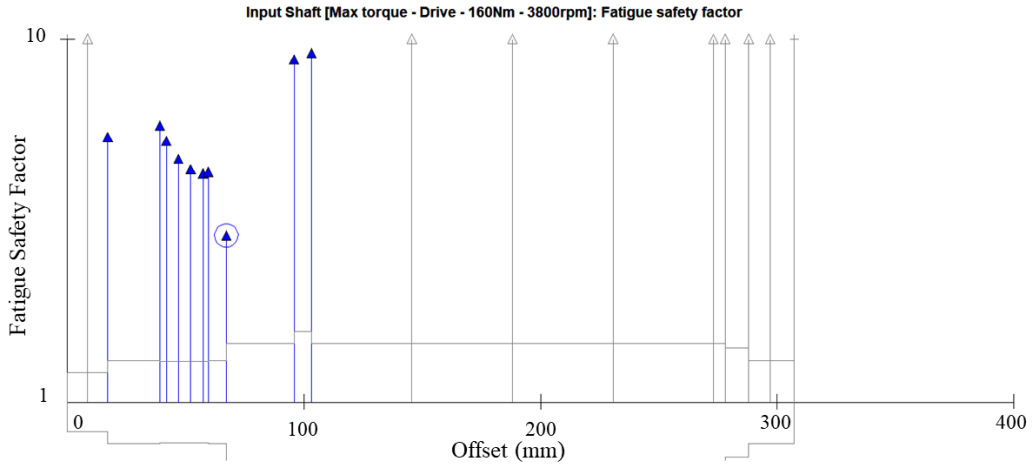

Figure 4.5: Fatigue safety factor, Input shaft

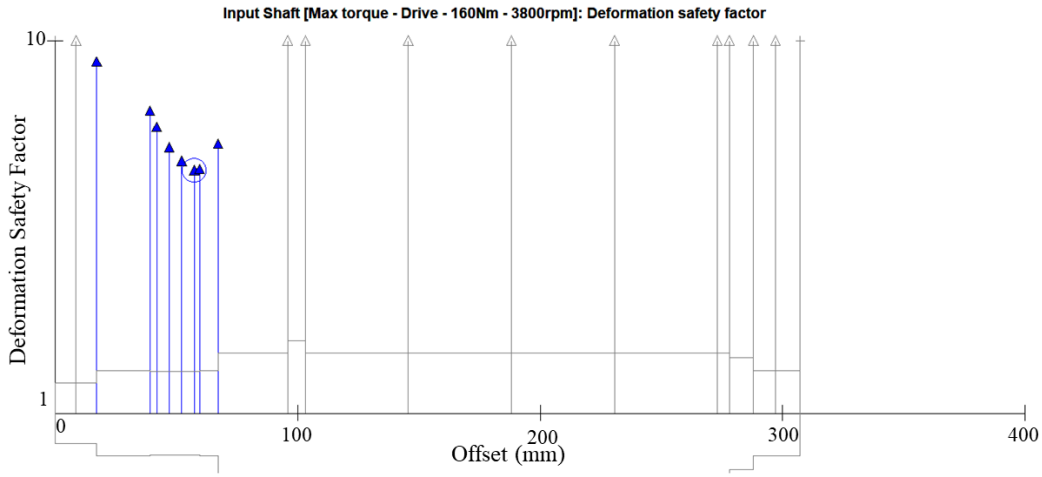

Figure 4.6: Deformation safety factor, Input shaft

- Intermediate Shaft:

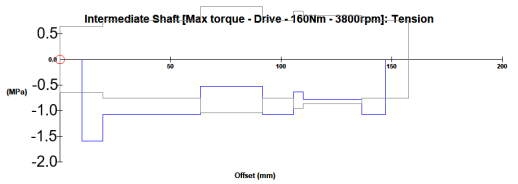

(a) *Tension*

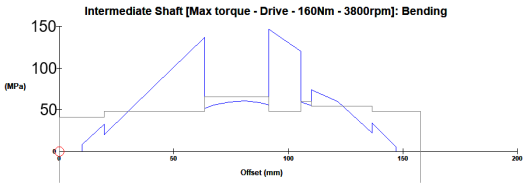

(b) *Bending*

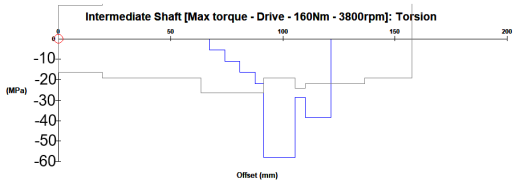

(c) *Torsion*

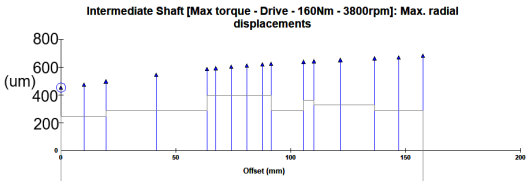

(d) *Maximum Radial Displacement*

Figure 4.7: Stresses and displacements, Intermediate shaft

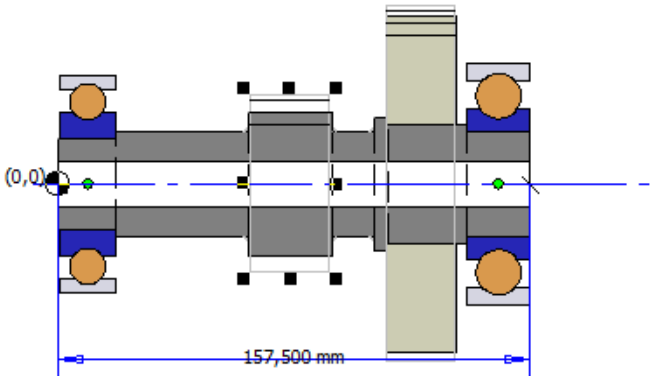

Figure 4.8: Intermediate shaft

Notice that the lowest safety factor is found where there is an important reduction of the cross section. There is a fillet radius of 2 mm in each change of cross section. In order to increase the safety factor, a possible path to follow in the design stage is to reduce the stress concentration factor. This aim can be achieved by increasing the fillet radius at the change of cross section.

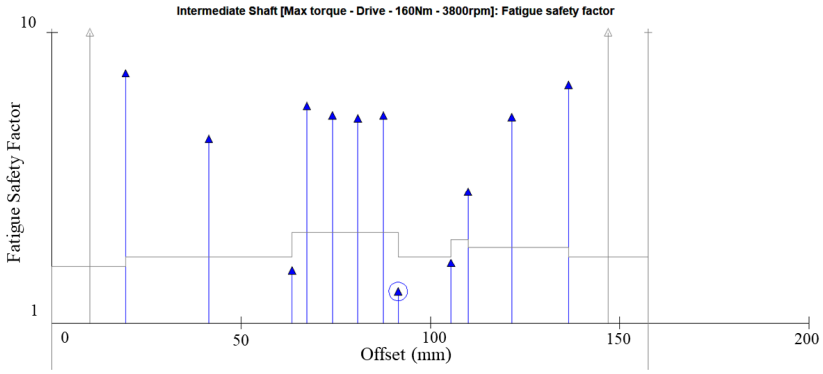

Figure 4.9: Fatigue safety factor, Intermediate shaft

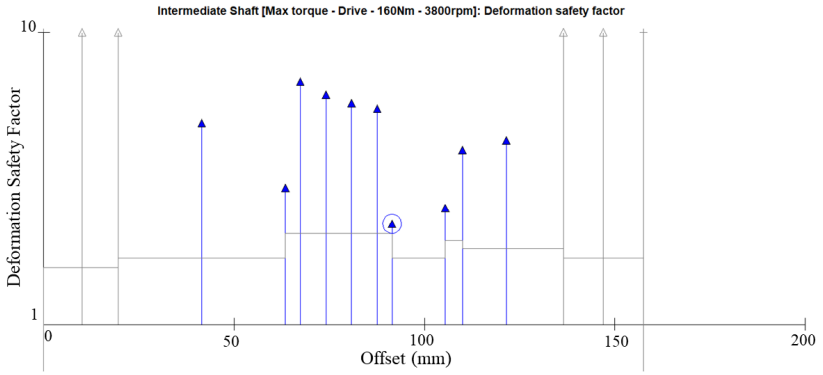

Figure 4.10: Deformation safety factor, Intermediate shaft

Load case	Node Offset (mm)	Fatigue SF	Deformation SF
Max Torque (Drive)	91.500	1.29	2.21

Table 4.16: Fatigue and deformation safety factors of most critical nodes, intermediate shaft

- Differential Shaft:

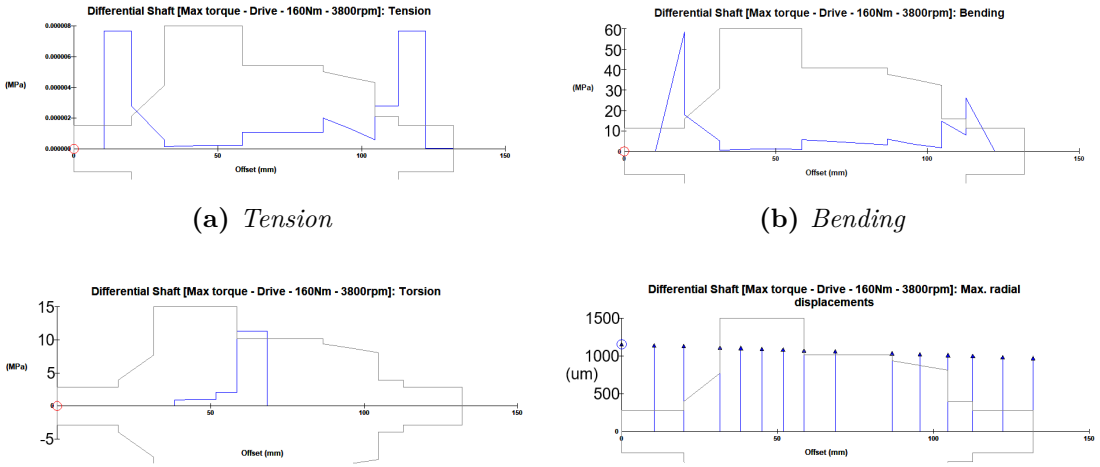

(a) *Tension* **(b)** *Bending*

(c) *Torsion* **(d)** *Maximum Radial Displacement*

Figure 4.11: Stresses and displacements, Differential shaft

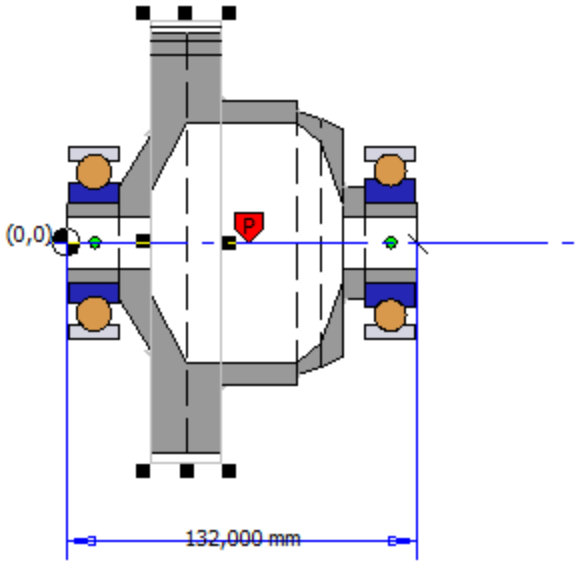

Figure 4.12: Differential shaft

Looking at Figure 4.12, it is noticeable that the lowest safety factors are close to the bearing *differential shaft LH*.

Load case	Node Offset (mm)	Fatigue SF	Deformation SF
Max Torque (Drive)	19.900	3.85	6.84

Table 4.17: Fatigue and deformation safety factors of the most critical nodes, differential shaft

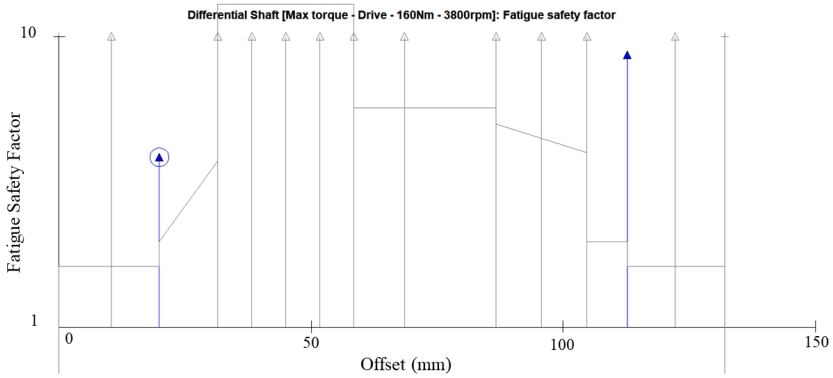

Figure 4.13: Fatigue safety factor, Differential shaft

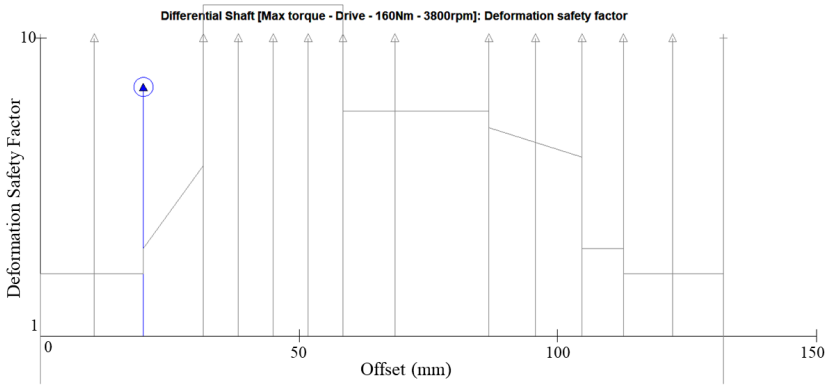

Figure 4.14: Deformation safety factor, Differential shaft

All the shafts are verified statically, however the one with the lowest value, especially considering fatigue, is the intermediate shaft.

Model C, helical gears

- Input Shaft:

Load case	Node Offset (mm)	Fatigue SF	Deformation SF
Max Torque (Drive)	59.750	4.23	5.82
	67.102	3.43	6.36

Table 4.18: Fatigue and deformation safety factors of the most critical nodes in all load cases, input shaft

- Intermediate Shaft

Load case	Node Offset (mm)	Fatigue SF	Deformation SF
Max Torque (Drive)	91.500	1.28	2.19

Table 4.19: Fatigue and deformation safety factors of the most critical nodes in all load cases, intermediate shaft

- Differential Shaft

Load case	Node Offset (mm)	Fatigue SF	Deformation SF
Max Torque (Drive)	10.400	6.32	10.65
	19.900	8.29	52.16

Table 4.20: Fatigue and deformation safety factors of the most critical nodes in all load cases, differential shaft

Notice that in Table 4.20, even the safety factors at the node with offset 19.900 mm are reported, even if this is not the most critical node. This has been done in order to make a more effective comparison with Models A and B.

It can be noted that, moving from Models A and B to Model C, the safety factors are almost the same in case of Intermediate shaft, while, considering Input shaft, a slight increase is present. Moreover, considering Differential shaft, the most critical node is not the same comparing Models A, B and C, and the value of safety factor is way higher in case of Model C, considering both fatigue and deformation.

4.2.2 Bearings

Since in section 4.1 it has been demonstrated that the right bearing of the differential shaft (i.e. Differential Shaft RH) is not able to pass the static analyses, a modification of that bearing has been performed. In particular, the radial ball bearing 6306, from SKF catalogue, has been substituted with a radial ball bearing from Koyo 2015 catalogue, with designation 6306R.
The dimensions of the two bearing are the same, however they have different load rating, as highlighted by Table 4.21.

Catalogue	SKF	Koyo 2015
Designation	6306	6306R
ISO 281 dynamic load rating (C)	28100 N	41700 N
Static load rating	16000 N	17700 N

Table 4.21: Comparison between bearing 6306 and 6306R

Using Romax Enduro, it is possible to estimate the life of the bearings considering the entire duty cycle. In particular, the software allows to use several standards, however, it has been chosen to use the standard ISO/TS 16281, since it consider more influence factors with respect to other standards (e.g. ISO 281), and therefore it should be more accurate. This standard ([40]) permits to compute the modified life and the damage to modified life of each bearing. The damage is computed as the ratio of duty cycle duration (50h in this example) to bearing life.
If wanted, it is possible to analyse more in depth each bearing considering individually each load case, in order to investigate the most critical bearings (i.e. the ones with the shortest life).
Moreover, if wanted, more details about the data used by standard ISO/TS 16281 can be obtained by reports directly available in Romax.
Finally, exploiting the formula provided by in standard ISO 76 ([41]), the worst static safety factor for each bearing can be evaluated.

Model A, Model B, spur gears

The results of the whole duty cycle are reported in Table 4.22.
The results concerning Model B are not reported to avoid redundancy: indeed they are almost equal to Model A, since only small modifications of gears are applied.

Bearing	Modified life (h) L_{10mrh}	Damage to mod. life (%)
Input shaft LH	385.69	13.0
Input shaft RH	$6.26 \cdot 10^{5}$	$7.99 \cdot 10^{-3}$
Differential shaft LH	3139.80	1.6
Differential shaft RH	922.64	5.4
Intermediate shaft LH	329.81	15.2
Intermediate shaft RH	349.35	14.3

Table 4.22: Bearing duty cycle summary, Model A, considering ISO/TS 16281

Bearing	Worst ISO 76 Static Safety Factor
Input shaft LH	1.79
Input shaft RH	12.31
Differential shaft LH	2.74
Differential shaft RH	1.36
Intermediate shaft LH	1.48
Intermediate shaft RH	1.41

Table 4.23: Worst ISO 76 Static Safety Factor, Model A

Model C, helical gears

Bearing	Modified life (h) L_{10mrh}	Damage to mod. life (%)
Input shaft LH	317.10	15.8
Input shaft RH	3988.60	0.13
Differential shaft LH	1289.19	3.9
Differential shaft RH	346.43	14.4
Intermediate shaft LH	193.82	27.5
Intermediate shaft RH	381.42	13.1

Table 4.24: Bearing duty cycle summary, Model C, considering ISO/TS 16281

Bearing	Worst ISO 76 Static Safety Factor
Input shaft LH	1.69
Input shaft RH	11.10
Differential shaft LH	2.62
Differential shaft RH	1.00
Intermediate shaft LH	1.23
Intermediate shaft RH	1.46

Table 4.25: Worst ISO 76 Static Safety Factor, Model C

Changing the bearing Differential shaft RH allows to achieve the desired results: in fact, all bearings pass the static analyses: all safety factors are ≥ 1. This means that all bearings survive for the required amount of hours of the duty cycle.
Moreover, it can be noted that no major improvements are obtained changing the helix angle, from 0° (i.e. Models A, B) to $\approx 25°$ (Model C). As it will be investigated more in depth in the following pages, the greatest improvement is concerning the gears.

4.2.3 Gears

Considering the gears, many results can be obtained thanks to Romax Enduro. First of all, it is fundamental to analyse the duty cycle results.
Please be aware that, to properly perform the gears duty cycle analyses, it is mandatory to consider the effect of the mesh misalignment. Gear mesh misalignment

is the total displacement of the gear axes due to shaft, bearing and housing deflections, and it is defined by ISO 6336 as $F_{\beta X}$. It represents the largest gap between two points on the face width of the gears, once the two gears have been brought into contact. $F_{\beta X}$ has a sign, defined by convention as positive if the gap between the gear teeth increases moving along the Z axis in positive direction along the pinion. On the other hand, if the gap is decreasing, the sign will be negative.

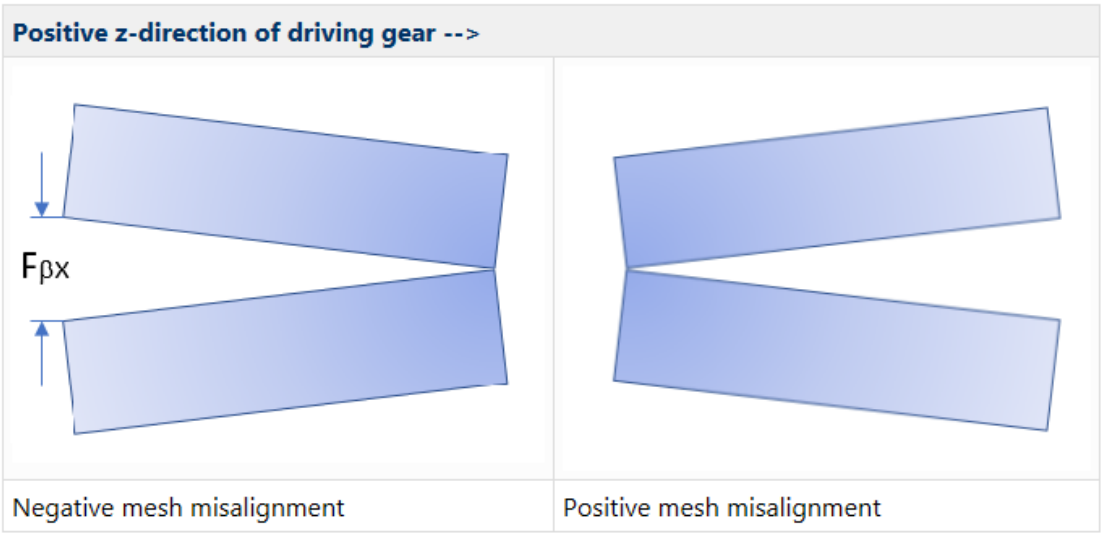

Figure 4.15: $F_{\beta X}$

It is important to start defining the gear mesh misalignment since it will affect the gear rating. In fact, considering zero misalignment is equivalent to consider that the gears are working in a perfect and ideal environment. However, in reality it is impossible to avoid having some system deflection, therefore a reduction of the safety factor is obtained considering real conditions.

Model A, spur gears

As anticipated, the first analysed result is the mesh misalignment, which is reported for each load case in Table 4.26.

Gear set	Load case	Misalignment (μm)
Input	Max Speed Coast	-1.87
Output	Max Speed Coast	-5.58
Input	Max Speed Drive	-1.86
Output	Max Speed Drive	5.86
Input	Max Torque Coast	-3.00
Output	Max Torque Coast	-7.89
Input	Max Torque Drive	-5.86
Output	Max Torque Drive	14.20
Input	NVH	-0.90
Output	NVH	3.51

Table 4.26: Misalignment values over the duty cycle, Model A

After having defined the mesh misalignment, the duty cycle analysis can continue. To consider the damage of the gears, the contact and bending damages of each flank of each gear will be analysed in details.
To perform the rating of the gears the standard ISO6336:2019 has been exploited. In Table 4.27, the life summary of each gear is reported. Moreover, it is possible to obtain also the results in terms of damage (Figure 4.16) and in terms of safety factors (Figure 4.17). The damage of the whole duty cycle is a cumulative damage of each load case evaluated using Miner's rule.
Furthermore, if required, more detailed results concerning individually each gear and each load case are available in reports, too.
Please, keep in mind that the required duty cycle lasts 50 h, therefore any value of combined life below 50 h leads to a failure of the static analysis.
Since the gear can be subjected to damage due to both contact (pitting) and bending, the resulting combined life of the gear will be the lowest value between the contact life and the bending one. Moreover, it is possible to obtain not only the life of the gears, but also the value of the safety factor and damage suffered by each flank of each gear, as reported by the following figures and tables. To obtain the values of the safety factors, Romax computes the permissible stress and the actual stress with formula given by standard ISO 6336:2019 ([42]), then the safety factors are simply evaluated as the ratio of permissible stress over the stress. This procedure just described is valid for both contact and bending.
The Figures 4.16, 4.17 report the damage and the safety factors of the worst flank of each gear of both gear sets.

Gear	Contact life (h)		Bending life (h)		Comb. life (h)	Pass/Fail?
	Left	Right	Left	Right		
In pinion	23.40	164.75	14561.90	+Inf	23.40	Fail
In wheel	117.54	897.58	+Inf	+Inf	117.54	Pass
Out pinion	534.32	63.56	+Inf	39.77	39.77	Fail
Out wheel	198.32	1670.41	7925.63	+Inf	198.32	Pass

Table 4.27: Gears life summary, Model A

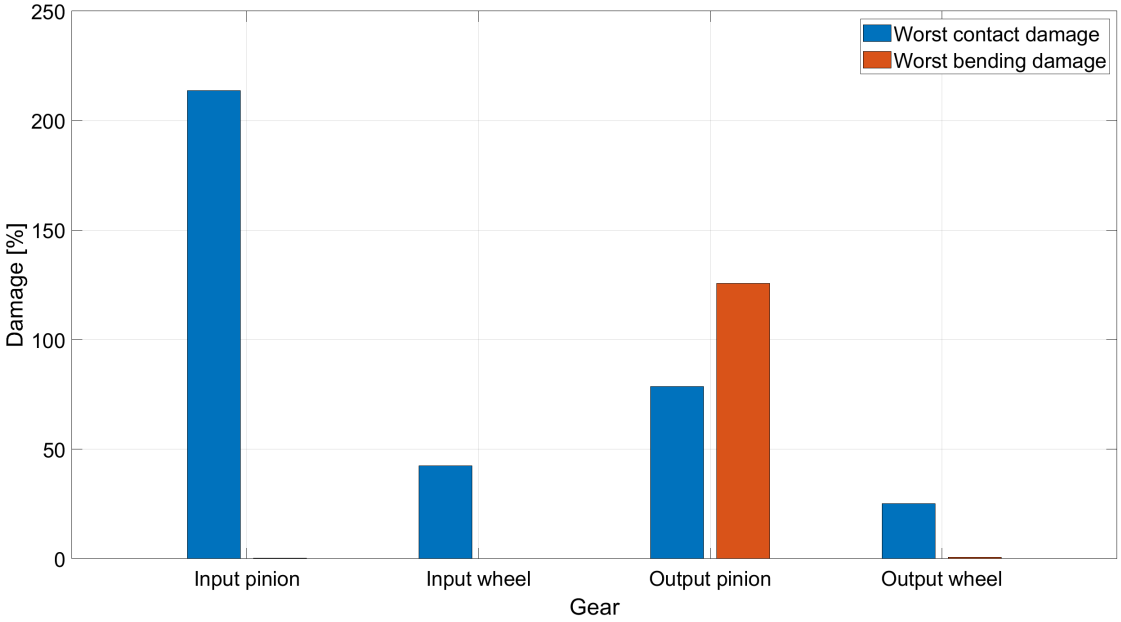

Figure 4.16: Damage of gears summary, Model A

Gear	Contact damage (%)		Bending damage (%)	
	Left flank	Right flank	Left flank	Right flank
Input pinion	213.66	30.35	0.34	0.0
Input wheel	42.54	5.57	0.0	0.0
Output pinion	9.36	78.66	0.0	125.71
Output wheel	25.21	2.99	0.63	0.0

Table 4.28: Damage of gears, Model A

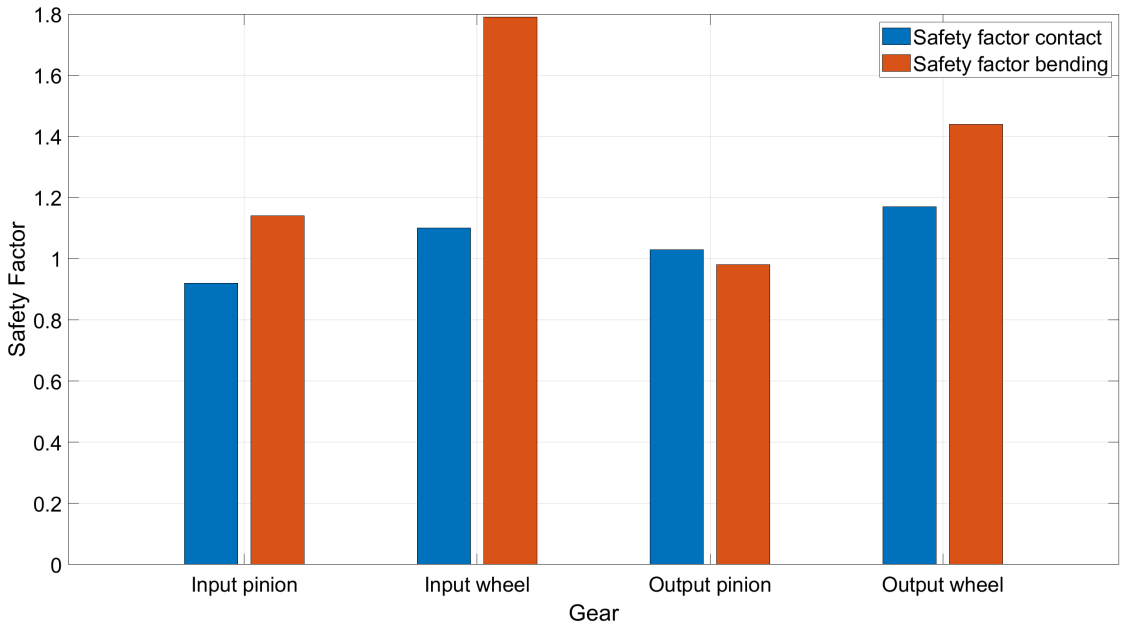

Figure 4.17: Gears safety factor summary, Model A

Gear	Safety factor contact		Safety factor bending	
	Left flank	Right flank	Left flank	Right flank
Input pinion	0.92	1.12	1.14	2.00
Input wheel	1.10	1.34	1.79	2.97
Output pinion	1.28	1.03	1.72	0.98
Output wheel	1.17	1.45	1.44	2.51

Table 4.29: Gears safety factors, Model A

It can be noted that failure of the gear is obtained, in particular the most critical flanks are the left flank of the input pinion due to the contact and the right flank of the output pinion due to the bending.
There are several reasons that cause this failure: first of all, the not optimal contact that mating teeth have in case of spur gears. In fact, helical gears offer a more smooth contact, and generally a greater teeth load carrying capacity. Moreover, also the surface roughness can be improved in order to enhance the life of the gears. Another reason of the failure can be the gears material.
Romax allows to investigate the details about the gear rating results coming from the ISO6336:2019 rating standard, in order to better understand the cause of the failure.
The safety factor of a gear, considering either contact or bending, is defined by the ratio between the permissible stress and the actual one. The permissible stress is affected by several parameter, such as the material (which defines the σ_{lim}) and the surface roughness.
So, as anticipated, the failure happens due to contact on the left flank of the input pinion and due to bending on the right flank of the output pinion. In the following tables, the values σ_{Hlim} and σ_{Flim} are defined by the material itself, while σ_{HP} and σ_{FP} are defined by ISO6336:2019 standard.

Property	Value
Allowable contact stress σ_{Hlim}	1500.00 MPa
Permissible contact stress σ_{HP}	1678.86 MPa
Actual contact stress σ_H	1828.12 MPa
Contact safety Factor	0.92

Table 4.30: ISO6336:2019 rating results, Input pinion, Contact stress

Property	Value
Allowable bending stress σ_{Flim}	500.00 MPa
Permissible bending stress σ_{FP}	1150.18 MPa
Actual bending stress σ_F	1178.42 MPa
Bending safety Factor	0.98

Table 4.31: ISO6336:2019 rating results, Output pinion, Bending stress

Maintaining the same geometry and design of the gears, a possible choice to

enhance the gears life, reducing the damage and increasing the safety factors, is to modify the material of the gears.
For both gear sets (i.e. input and output) Steel, case hardened, AGMA grade 3 is chosen.

Property	Value
Yield strength (MPa)	314
Ultimate tensile strength (MPa)	2300
Young modulus (MPa)	$2.07 \cdot 10^5$
Density (kg/m^3)	7800
Poisson's ratio	0.3
Material loss factor	$2 \cdot 10^{-3}$
Cost/unit mass ($1/kg$)	10

Table 4.32: Properties of material Steel, case hardened, AGMA grade 3

The main differences between the two materials, i.e. Steel, case hardened, AGMA grade 2 and Steel, case hardened, AGMA grade 3 are reported in the following table:

	AGMA grade 2	AGMA grade 3
Allow contact stress σ_{Hlim} (MPa)	1500	1650
Allow bending stress σ_{Flim} (MPa)	500	525

Table 4.33: Comparison Steel, case hardened, AGMA grade 2 and Steel, case hardened, AGMA grade 3

Modifying the material, and therefore the values of allowable contact and bending stress, is enough to obtain the success of the static analysis of all gears, as shown by Table 4.34.

Gear	Contact life (h)		Bending life (h)		Comb. life (h)	Pass/Fail?
	Left	Right	Left	Right		
In pinion	54.56	425.92	$1.66 \cdot 10^5$	+Inf	54.56	Pass
In wheel	271.44	4667.28	+Inf	+Inf	271.44	Pass
Out pinion	1292.29	145.27	+Inf	63.03	63.03	Pass
Out wheel	453.17	4033.28	90499.24	+Inf	453.17	Pass

Table 4.34: Gears life summary, Model A, Material AGMA grade 3

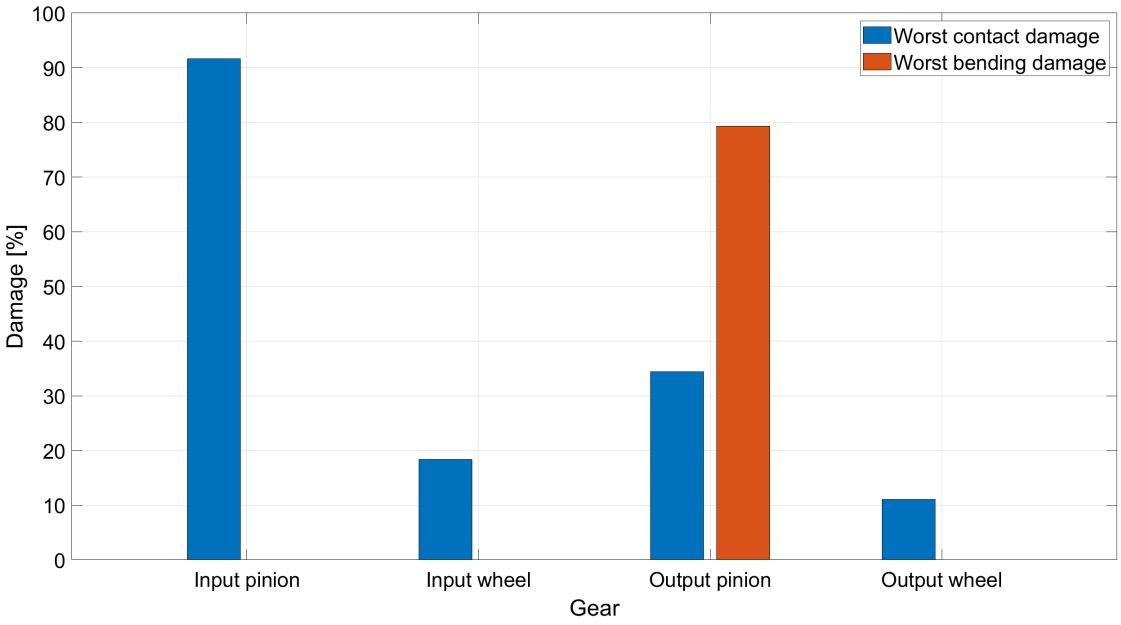

Figure 4.18: Damage of gears summary, Model A, Material AGMA grade 3

Gear	Contact damage (%)		Bending damage (%)	
	Left flank	Right flank	Left flank	Right flank
Input pinion	91.64	11.74	$3.01 \cdot 10^{-2}$	0.0
Input wheel	18.42	1.07	0.0	0.0
Output pinion	3.87	34.42	0.0	79.33
Output wheel	11.03	1.24	$5.52 \cdot 10^{-2}$	0.0

Table 4.35: Damage of gears, Model A, Material AGMA grade 3

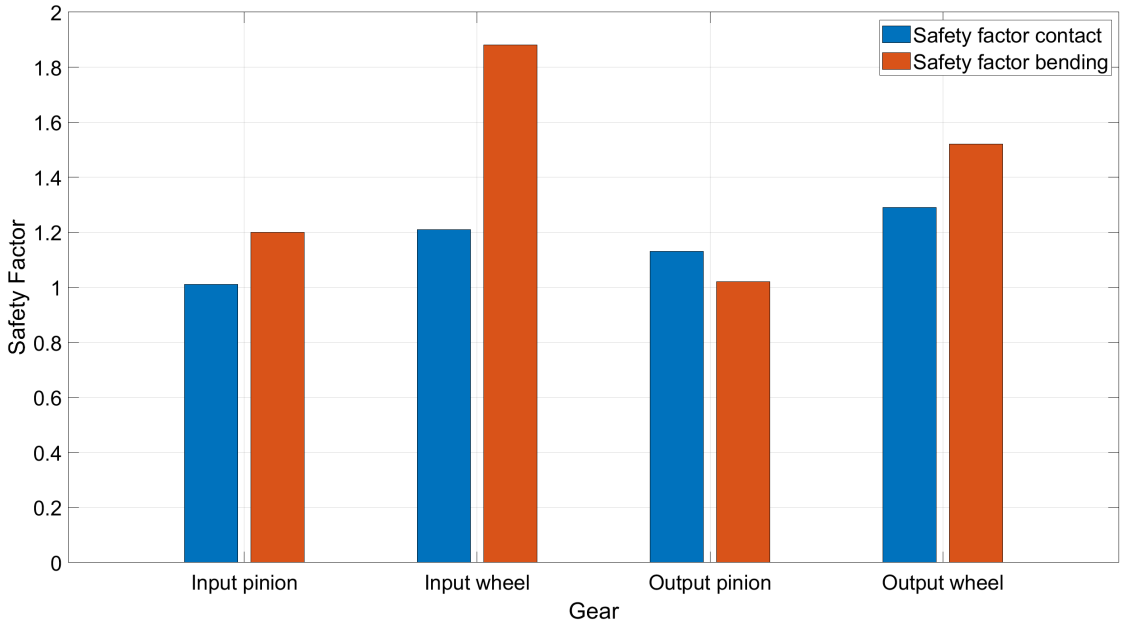

Figure 4.19: Gears safety factor summary, Model A, Material AGMA grade 3

Gear	Safety factor contact		Safety factor bending	
	Left flank	Right flank	Left flank	Right flank
Input pinion	1.01	1.23	1.20	2.10
Input wheel	1.21	1.47	1.88	3.12
Output pinion	1.40	1.13	1.80	1.02
Output wheel	1.29	1.60	1.52	2.63

Table 4.36: Gears safety factors, Model A, Material AGMA grade 3

With this updated material, all safety factors are above 1 and the required life is obtained. However, although larger than 1, the safety factors are not so high, especially in cases of pinions considering contact. This can be explained by several reasons, for instance the contact path is not ideal (as will be investigated later on, helical gears lead to better results), and also the surface roughness is still not optimal.
Of course, changing the material of the gear sets, no major changes in the safety factor concerning the shafts are reported, as expected.
Moreover, gear mesh misalignment is not affected by the change of material.
From now on, to perform a more effective comparison among the models, the considered material for all gears will be Steel, case hardened, AGMA grade 3, in

all the following models.
Another important result concerning the gear rating is the load distribution factor, $K_{H\beta}$, defined by the ISO standard as the ratio of the maximum load per unit length, over the average load per unit length, along the midpoint of the tooth face. It can be calculated automatically by Romax considering the defined microgeometry. Romax offers the possibility to calculate the $K_{H\beta}$ factor considering both the value of $F_{\beta X}$ (which is evaluated from the static analyses), using standard ISO 6336, and the microgeometry analysis. Hence, it is possible to consider together shaft deflections and any possible microgeometry modification.

Load case	Gear set	$K_{H\beta}$
Max Speed (Coast)	Input	1.18
	Output	1.19
Max Speed (Drive)	Input	1.17
	Output	1.20
Max Torque (Coast)	Input	1.18
	Output	1.17
Max Torque (Drive)	Input	1.18
	Output	1.16
NVH	Input	1.16
	Output	1.24

Table 4.37: Values of $K_{H\beta}$ over the whole duty cycle, Model A

Moreover, if wanted, even other results can be obtained by the software, including face and transverse load factor for bending stress, and transverse load factor for contact stress.
Finally, to proceed in the gears analysis, it is required to run the microgeometry analysis for each load case, in order to obtain several results that will be useful for the NVH analyses, too.
It is indeed possible to get many graphs concerning different achievable results specifically for each tooth flank, of both gears for any load case. One of the most important graph that can be analysed is the plot showing the maximum contact stress over the flank, which is fundamental in order to perform the gear contact analysis. In the following graphs, the maximum contact stress plots will be displayed considering just the loaded flank.
Moreover, another fundamental result achievable by the microgeometry analysis concerns the transmission error of gears.

Since these results are crucial for the NVH analysis, they are investigated in details in dedicated sections, 4.2.4 and 4.2.5, respectively.

Model B, spur gears

Please remember that, from now on, the considered material for both gear sets will be Steel, case hardened, AGMA grade 3, in all the following models. The first result to analyse is the gear mesh misalignment, which is reported in Table 4.38.

Gear set	Load case	Misalignment (μm)
Input	Max Speed Coast	-1.87
Output	Max Speed Coast	-5.58
Input	Max Speed Drive	-1.86
Output	Max Speed Drive	5.85
Input	Max Torque Coast	-3.00
Output	Max Torque Coast	-7.89
Input	Max Torque Drive	-5.86
Output	Max Torque Drive	14.20
Input	NVH	-0.91
Output	NVH	3.52

Table 4.38: Misalignment values over the duty cycle, Model B

With respect to 4.26, no major distinctions can be noted.
Then, the gear duty cycle analysis can be performed.

Gear	Contact life (h)		Bending life (h)		Comb. life (h)	Pass/Fail?
	Left	Right	Left	Right		
In pinion	55.60	432.90	3662.04	+Inf	55.60	Pass
In wheel	276.63	4945.53	+Inf	+Inf	276.63	Pass
Out pinion	1291.69	145.29	+Inf	88.49	88.49	Pass
Out wheel	453.23	4031.45	7965.62	+Inf	453.23	Pass

Table 4.39: Gears life summary, in Enduro, Model B

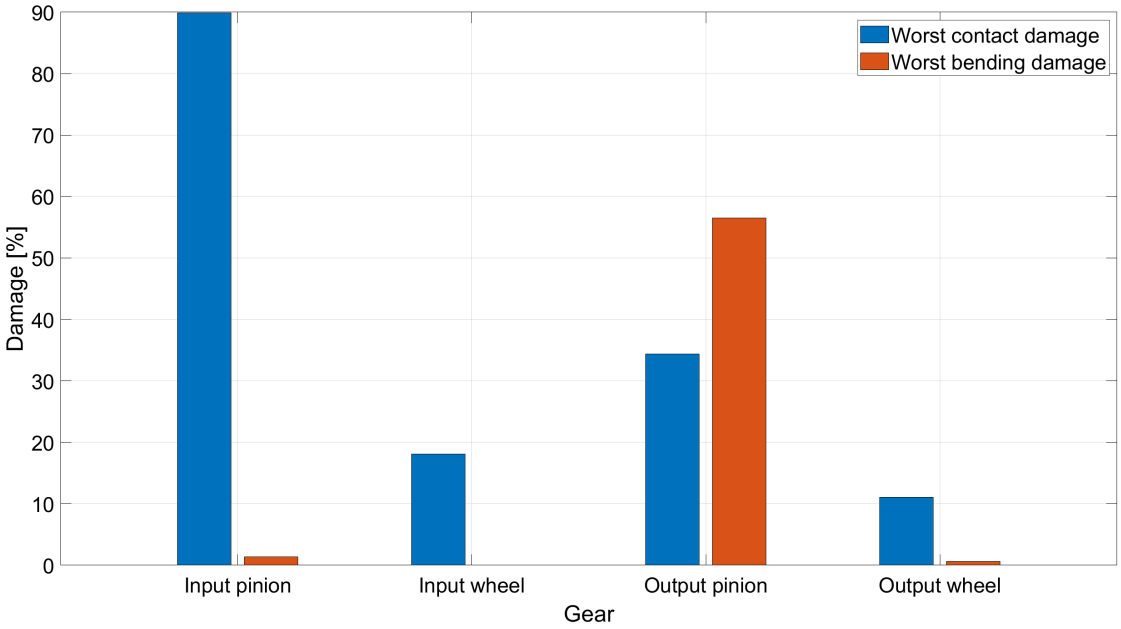

Figure 4.20: Damage of gears summary, in Enduro, Model B

Gear	Contact damage (%)		Bending damage (%)	
	Left flank	Right flank	Left flank	Right flank
Input pinion	89.92	11.55	1.37	0.0
Input wheel	18.07	1.01	0.0	0.0
Output pinion	3.87	34.41	0.0	56.50
Output wheel	11.03	1.24	0.63	0.0

Table 4.40: Damage of gears, Model B

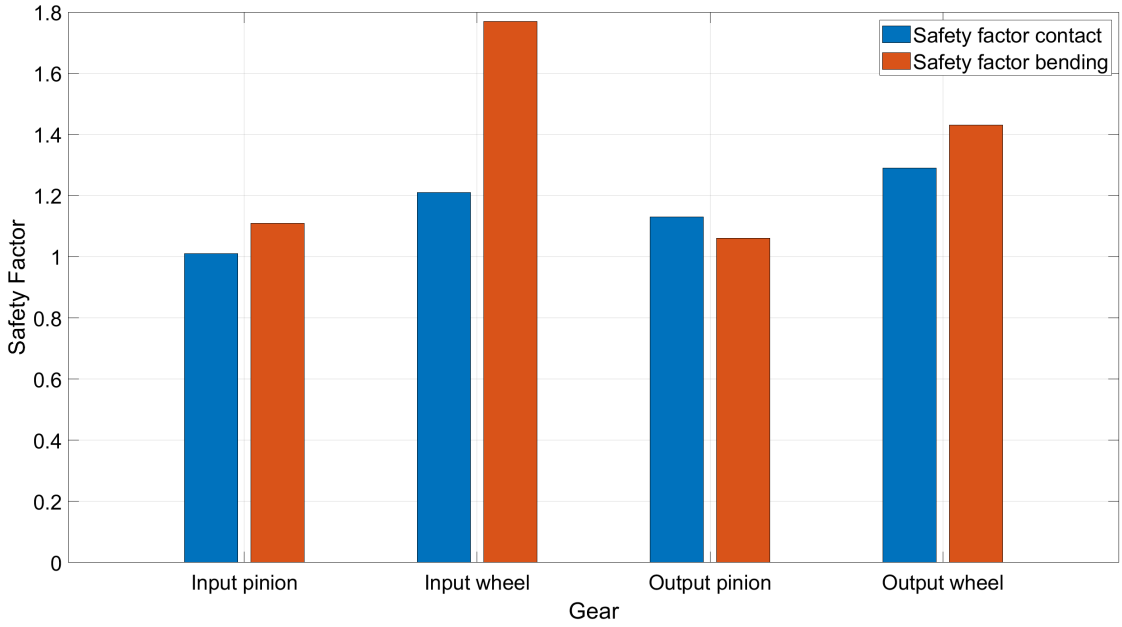

Figure 4.21: Gears safety factor summary, in Enduro, Model B

Gear	Safety factor contact		Safety factor bending	
	Left flank	Right flank	Left flank	Right flank
Input pinion	1.01	1.23	1.11	1.94
Input wheel	1.21	1.47	1.77	2.95
Output pinion	1.40	1.13	1.87	1.06
Output wheel	1.29	1.60	1.43	2.49

Table 4.41: Gears safety factors, Model B

Comparing the duty cycle results between model A and B, it can be noted a slight improvement of the combined life of all gears in case of Model B. However, the improvement is very modest, almost negligible.
The significant enhancement, as will be investigated later, will be moving to helical gears.
Finally, the load distribution factor $K_{H\beta}$ is computed.
With respect to Table 4.37, which refers to Model A, no major differences concerning values of $K_{H\beta}$ can be detected.

Load case	Gear set	$K_{H\beta}$
Max Speed (Coast)	Input	1.17
	Output	1.19
Max Speed (Drive)	Input	1.17
	Output	1.20
Max Torque (Coast)	Input	1.18
	Output	1.17
Max Torque (Drive)	Input	1.18
	Output	1.16
NVH	Input	1.16
	Output	1.24

Table 4.42: Values of $K_{H\beta}$ over the whole duty cycle, Model B

Model C, helical gears

As in the previous cases, the first step of the static analysis requires to analyse the gear misalignment.

Gear set	Load case	Misalignment (μm)
Input	Max Speed Coast	-4.92
Output	Max Speed Coast	-6.15
Input	Max Speed Drive	2.39
Output	Max Speed Drive	9.61
Input	Max Torque Coast	-6.28
Output	Max Torque Coast	-8.32
Input	Max Torque Drive	-0.04
Output	Max Torque Drive	25.03
Input	NVH	2.61
Output	NVH	5.55

Table 4.43: Misalignment values over the duty cycle

Doing a comparison with the values of gear misalignment of Models A and B,

an increase of the absolute values in case of Model C can be noted in almost all load cases. This means that, in overall, an higher deflection of shafts and bearing has been noted in Model C. Let's now proceed with the gear duty cycle analysis.

Gear	Contact life (h)		Bending life (h)		Comb.life(h)	Pass/Fail
	Left	Right	Left	Right		
In pinion	309.31	2255.25	+Inf	+Inf	309.31	Pass
In wheel	913.86	6663.24	+Inf	+Inf	913.86	Pass
Out pinion	$1.57 \cdot 10^4$	229.05	+Inf	330.94	330.94	Pass
Out wheel	704.11	$4.81 \cdot 10^4$	$4.65 \cdot 10^5$	+Inf	704.11	Pass

Table 4.44: Gears life summary, in Enduro, Model C

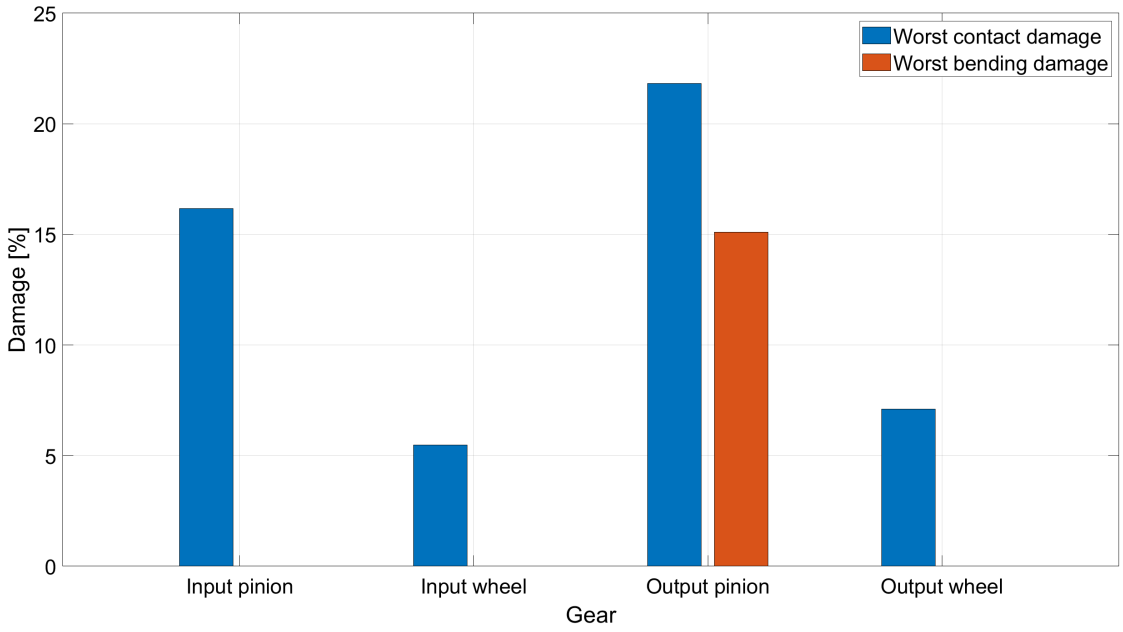

Figure 4.22: Damage of gears summary, in Enduro, Model C

Gear	Contact damage (%)		Bending damage (%)	
	Left flank	Right flank	Left flank	Right flank
Input pinion	16.16	2.22	0.0	0.0
Input wheel	5.47	0.75	0.0	0.0
Output pinion	0.32	21.83	0.0	15.11
Output wheel	7.10	0.10	$1.08 \cdot 10^{-2}$	0.0

Table 4.45: Damage of gears, Model C

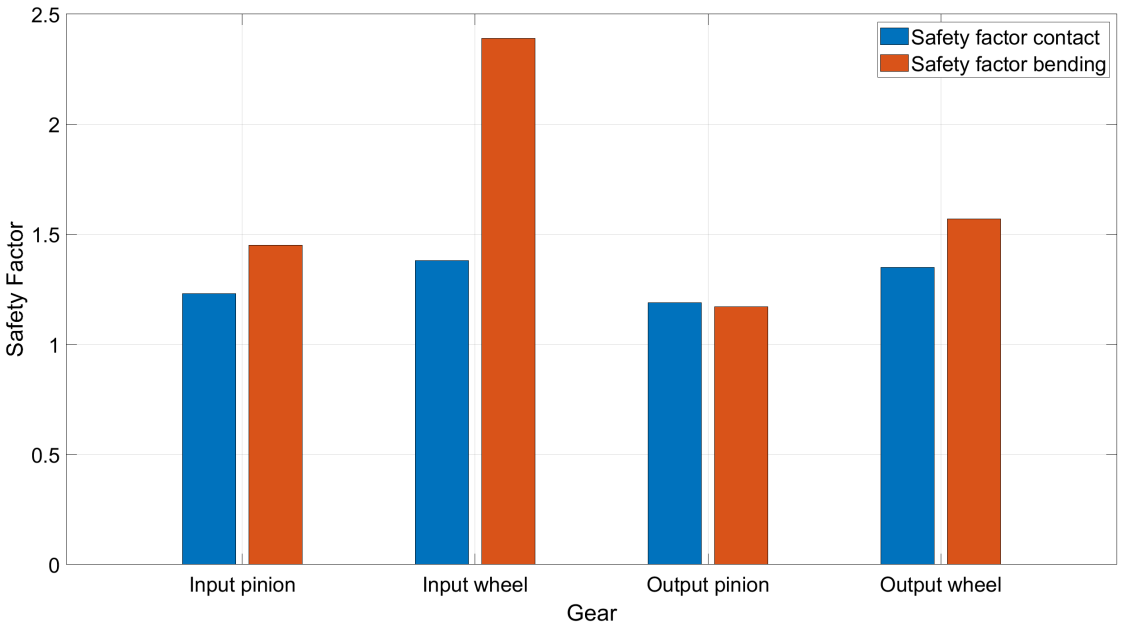

Figure 4.23: Gears safety factor summary, in Enduro, Model C

Gear	Safety factor contact		Safety factor bending	
	Left flank	Right flank	Left flank	Right flank
Input pinion	1.23	1.30	1.45	2.05
Input wheel	1.38	1.47	2.39	3.21
Output pinion	1.53	1.19	2.18	1.17
Output wheel	1.35	1.74	1.57	2.88

Table 4.46: Gears safety factors, Model C

It is interesting to compare the results considering either spur or helical gears. Since Model B is an evolution of Model A, with better static performance, the comparison is performed considering only Models B and C.
An overall improvement of the life of the gears is noted moving from Model B to Model C.
In particular, the combined life clearly is enhanced:

Gear	Combined life Model B (h)	Combined life Model C (h)
In pinion	55.60	309.31
In wheel	276.63	913.86
Out pinion	88.49	330.94
Out wheel	453.23	704.11

Table 4.47: Gears life summary, comparison Model B vs Model C

Then, in the following table it is reported the comparison among worst safety factors of each gear (i.e. the lowest value between left and right flank), considering both contact and bending. It can be denoted a clearly improvement in terms of safety factors moving from Model B to C.

Gear	Safety factor contact		Safety factor bending	
	Model B	Model C	Model B	Model C
Input pinion	1.01	1.23	1.11	1.45
Input wheel	1.21	1.38	1.77	2.39
Output pinion	1.13	1.19	1.06	1.17
Output wheel	1.29	1.35	1.43	1.57

Table 4.48: Gears worst safety factors, comparison Model B vs Model C

Looking at values of $K_{H\beta}$, Table 4.49, an increase of the values with respect to the cases of spur gears can be denoted. This is not surprising, since an increase of values of gear mesh misalignment was noticed moving from spur gears to helical gears. Please keep in mind that $K_{H\beta}$ depends on gear mesh misalignment: the greater is the gear mesh misalignment, the greater is $K_{H\beta}$.

Load case	Gear set	$K_{H\beta}$
Max Speed (Coast)	Input	1.46
	Output	1.29
Max Speed (Drive)	Input	1.15
	Output	1.49
Max Torque (Coast)	Input	1.38
	Output	1.23
Max Torque (Drive)	Input	1.10
	Output	1.41
NVH	Input	1.34
	Output	1.56

Table 4.49: Values of $K_{H\beta}$ over the whole duty cycle, Model C

4.2.4 Gear contact patch

Romax gives the possibility to investigate the gear contact patch, which is very useful to understand the quality of gear design. It is possible to obtain the contact pattern on each flank of each tooth of any gear. In particular, what is shown by Romax is the overall contact to which a flank is subjected to during an whole rotation of the gear. Many plots can be displayed: by experience the most important is the *Maximum contact stress*.
Looking at the graphs it is possible to understand the load distribution along the face of the tooth. Generally, it is desired to shift the contact patch towards the center of the tooth face, in order to reduce edge loading. Spreading the load widely on a larger area can be useful to reduce the peak load, however the most important objective is to move the contact are as much as possible towards the centre of the tooth face, in order to increase gear life.
It has been chosen to report only the contact patches related to the load case *Max torque drive*: it represents the load case with the highest value of torque, i.e. the most critical, hence it can be useful to better understand the maximum value of contact stress. However, even the other load cases shows similar plots. Moreover, the results of Model A and B are not divided in two different sections since the plots shows exactly the same behaviour, both in terms of contact patch and of values of contact stress.
Obviously, the maximum value of contact stress is reached considering the load case Max torque drive.

Model A, B, spur gears

Looking at contact patches of Models A and B, it can be noted that the contact is very poorly distributed along tooth face. It is clearly visible a division in bands of the contact, and the maximum contact is reached in the central band with respect to the roll diameter. Moreover, another issue is represented by the concentration of the stress on one of the two edges, with respect to the face distance. Remember that a good contact patch is constituted by an evenly distributed load, as much as possible on the center of tooth face.

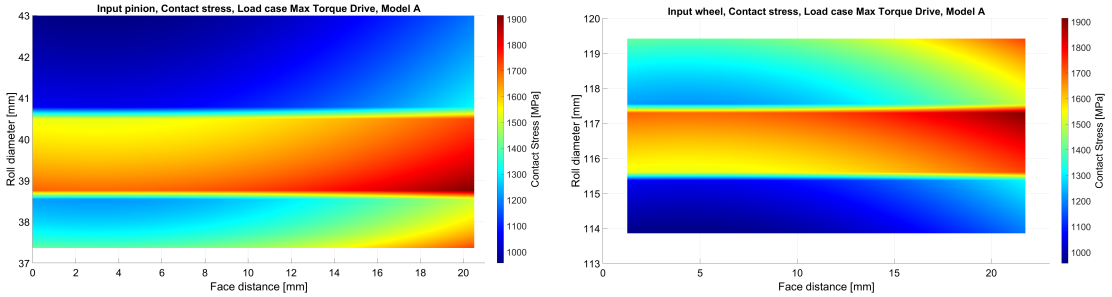

(a) *Input pinion, Max Torque Drive*

(b) *Input wheel, Max Torque Drive*

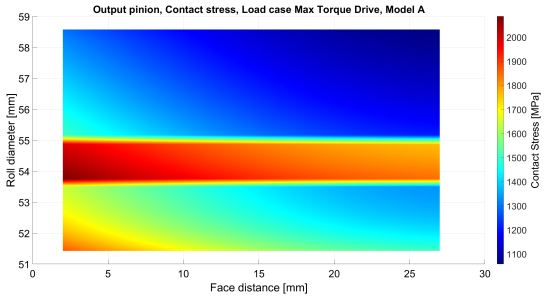

(c) *Output pinion, Max Torque Drive*

(d) *Output wheel, Max Torque Drive*

Figure 4.24: Contact stress, Load case Max Torque Drive, Model A

Model C, helical gears

Adding an helix angle clearly leads to some advantages. Indeed, the bands, visible in Models A and B, disappear and a more smoothly distributed stress is noticeable. Moreover, a slight reduction of the values of the stress is visible in Model C. However, since edge loading is present, the geometry of the gears can still be optimized in order to reach a better contact patch. This is exactly the aim of Model D, which will be explained in details in the following pages. A stress distribution more centered with respect to the tooth face can be reached, indeed, by adding some microgeometry modifications.

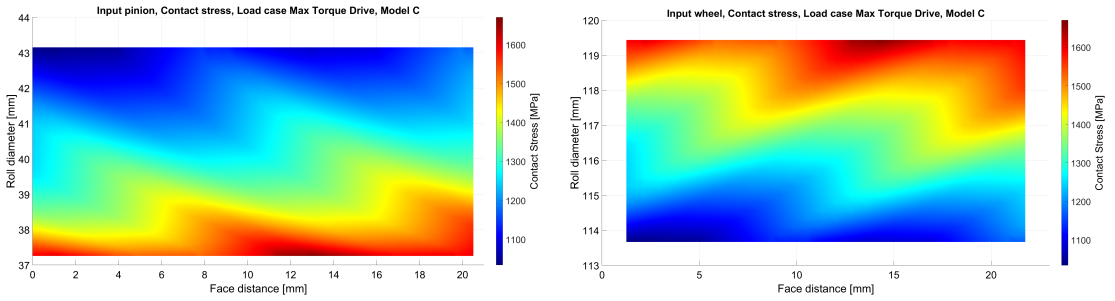

(a) *Input pinion, Max Torque Drive*

(b) *Input wheel, Max Torque Drive*

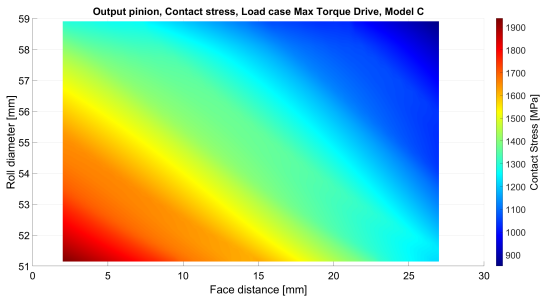

(c) *Output pinion, Max Torque Drive*

(d) *Output wheel, Max Torque Drive*

Figure 4.25: Contact stress, Load case Max Torque Drive, Model C

Looking at the above figures (4.24 and 4.25), comparing the peak values reached in the different models, it is clear the reduction of the maximum value of the contact stress moving from Models A and B to Model C. Obviously, this reduction leads to an enhancement of the contact safety factors in Model C, as showed by Table 4.48.

4.2.5 Transmission error

A very relevant result, especially for the NVH analyses that will be carried out later on this thesis, is the transmission error. In particular, it is possible to obtain both the peak to peak value (which indicates exactly the value of the transverse transmission error) and the values of the harmonics, for each load case.
The transmission error is one of the main source of noises and vibrations in a powertrain, therefore to evaluate its amplitude and its harmonic contribution is fundamental.
The harmonic contributions will be analysed more in details in Chapter 6.
However, in this section it can be interesting to analyse and compare the peak to peak values of the TE along the whole range of torque of the motor (i.e. -160 Nm ÷ 80 Nm). In all the graphs which compare the peak to peak values of the TE over the whole torque range (Figures 4.26, 4.27, 4.31, 4.34, 4.39, 4.44, 4.48), a vertical line is represented, too. The aim of the vertical line is to highlight the torque value

of the load case *NVH*, which is particularly important for the following analyses. First of all it can be interesting to compare the Model A with Model B.

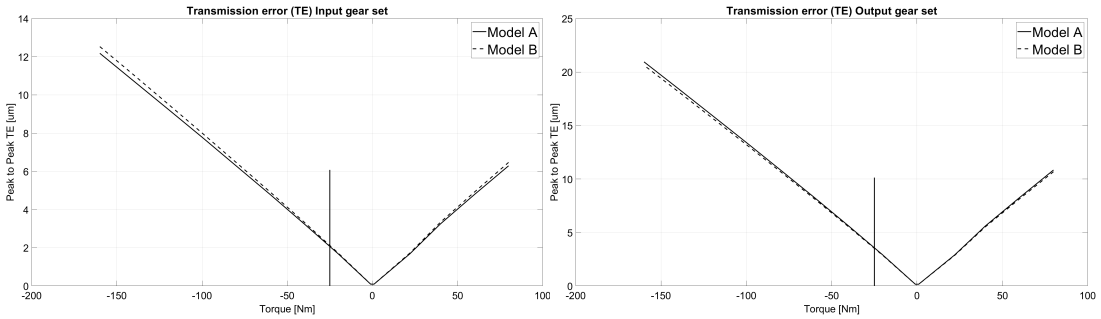

(a) *Input gear set, TE peak to peak* **(b)** *Output gear set, TE peak to peak*

Figure 4.26: Comparison TE peak to peak, Model A vs Model B

It can be noted that the two graphs are almost overlapping. Hence, the profile shifting performed helps in slightly increase the life of the gears but it does not give an important contribution on the reduction of the TE.
On the other hand, as clearly visible by Figure 4.27, moving to helical gear really leads to a strong reduction of the peak to peak value of the TE.

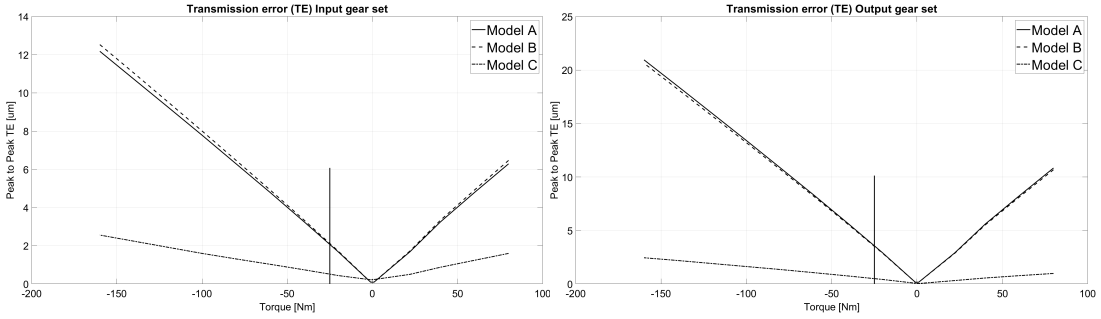

(a) *Input gear set, TE peak to peak* **(b)** *Output gear set, TE peak to peak*

Figure 4.27: Comparison TE peak to peak, Model A vs Model B vs Model C

Another interesting result is the plot showing the behaviour of the transverse transmission error over the roll angle. The roll angle is defined by [22] as the angle whose arc on the base circle of radius unity equals the tangent of the pressure angle at a selected point on the involute.

Model A, spur gears

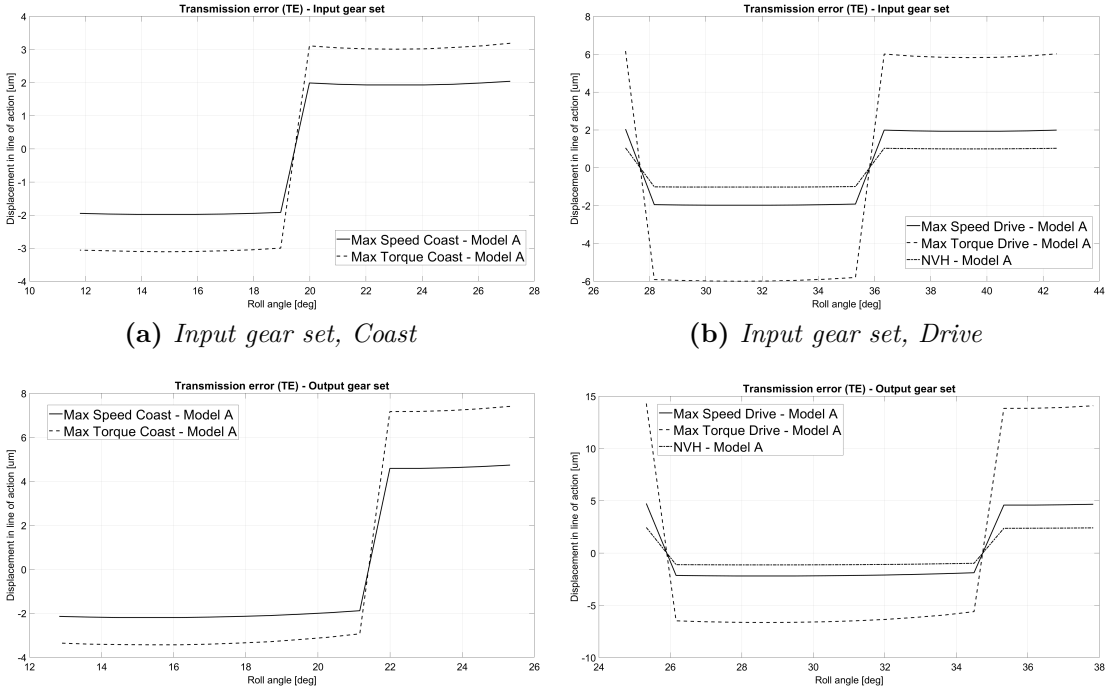

(a) *Input gear set, Coast*

(b) *Input gear set, Drive*

(c) *Output gear set, Coast*

(d) *Output gear set, Drive*

Figure 4.28: TE vs Roll angle, Model A

Model B, spur gears

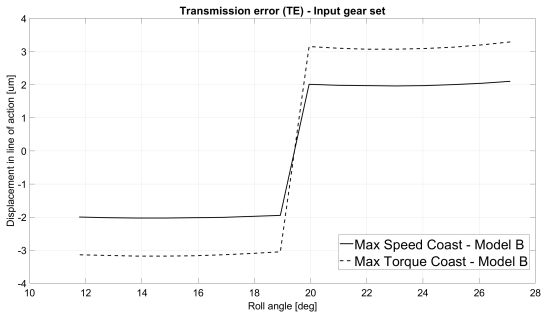

(a) *Input gear set, Coast*

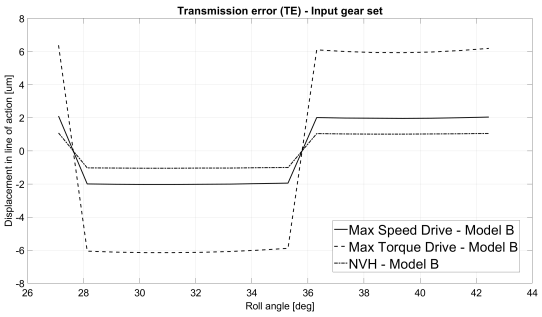

(b) *Input gear set, Drive*

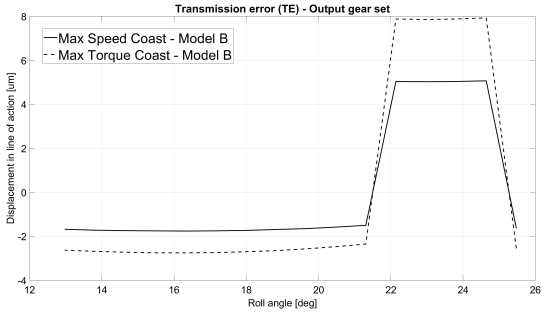

(c) *Output gear set, Coast*

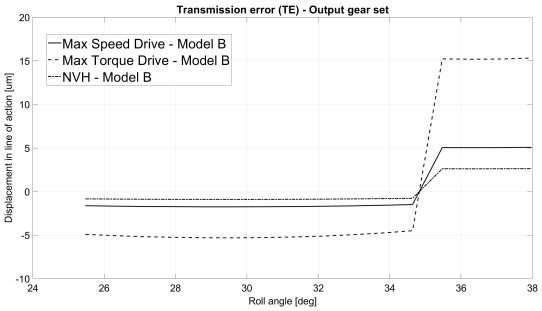

(d) *Output gear set, Drive*

Figure 4.29: TE vs Roll angle, Model B

Model C, helical gears

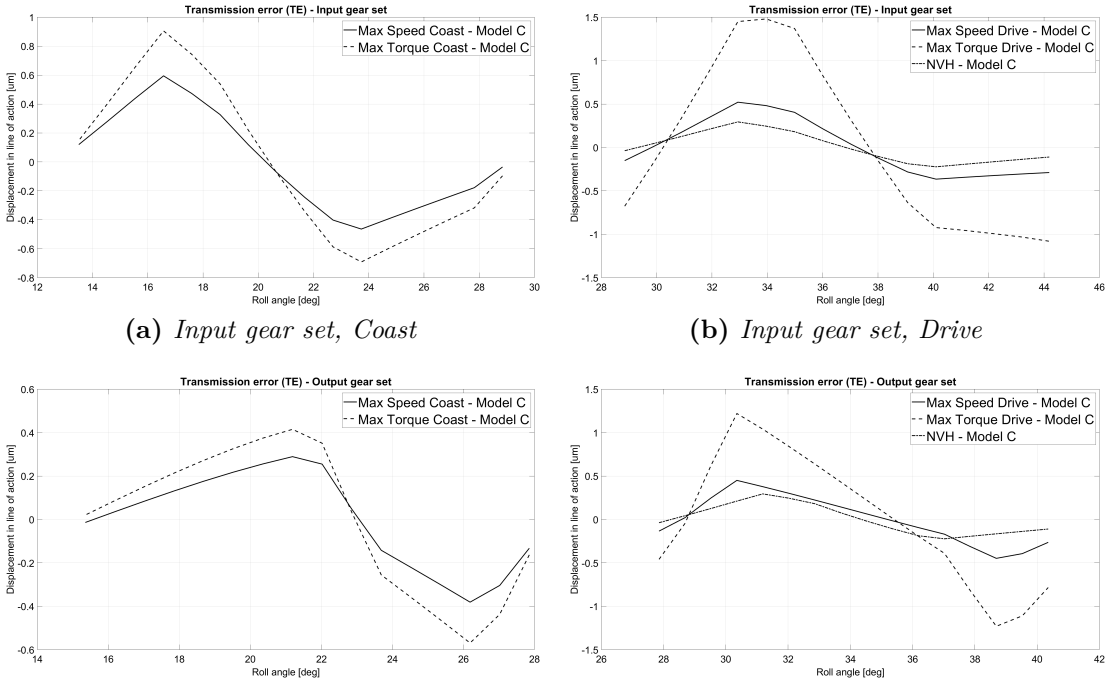

(a) *Input gear set, Coast* **(b)** *Input gear set, Drive*

(c) *Output gear set, Coast* **(d)** *Output gear set, Drive*

Figure 4.30: TE vs Roll angle, Model C

First of all, it is possible to notice that the plots produced by Models A and B are almost overlapping along the whole roll angle range. On the other hand, as expected, Model C produces way lower values of TE.
Moreover, the higher is the torque of the considered load case, the higher are the values of TE. Indeed, the load case with the highest torque, i.e. *Max Torque*, both in drive and in coast conditions, lead to the highest values of TE. The load case NVH has the lower values of torque, therefore the resulting values of TE are low. As anticipated, the TE values are very important for the NVH analysis that will be investigated in Chapter 6: in fact, TE is one of the most important excitation source. Therefore, the reduction of the TE values moving from spur gears to helical gears will be really helpful in NVH analysis, causing lower values of noise and vibrations produced. To be more precise, it will be necessary to analyse the harmonic contribution of the TE, however, just seeing this strong reduction of peak to peak TE values, moving from spur to helical gears, it is reasonable to predict a significant enhancement of NVH performance moving to helical gears.

4.2.6 Selection of the helix angle

So far, considering the Model C, the value of the helix angles were given by the supporting material provided by [22]. Recalling the values of helix angles of the Model C, reported in Table 2.7, it is interesting to compare them with two cases: the former with smaller helix angle, the latter with higher values of helix angles.

	Gear Set - Input	Gear Set - Output
Helix angle Model C (deg)	25.081	24.987
Helix angle Model C_{20} (deg)	20	20
Helix angle Model C_{35} (deg)	35	35

Table 4.50: Compared helix angles

First of all, a comparison of the TE values over the torque range is undoubtedly relevant.

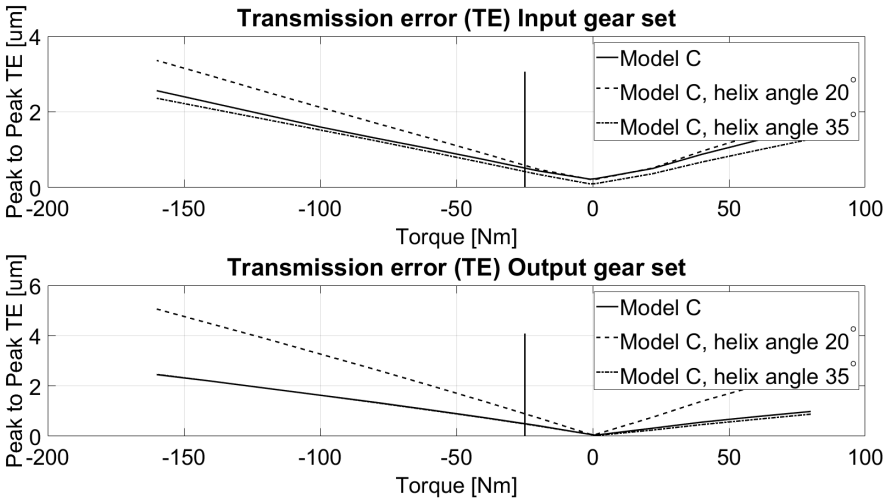

Figure 4.31: Comparison of TE values modifying helix angles

Figure 4.31 clearly highlights how the TE decreases as the helix angle increases. Therefore, selecting an helix angle of 20° is not a wise choice. It actually seems that the best choice is the highest possible helix angle, just by looking at TE values. But this analysis is not enough. Indeed, furthering the analysis, it is noticeable an increase of the generated forces in case of higher helix angles. This will lead to a reduction especially of output pinion life, as highlighted by Table 4.51.

Gear	Combined life Model C (h)	Combined life Model C_{35} (h)
In pinion	309.31	2720.36
In wheel	913.86	8037.5
Out pinion	330.94	38.175
Out wheel	704.11	1599.31

Table 4.51: Gears life comparison

Due to the above results, it has been selected to proceed with the values of helix angles provided by [22].

4.2.7 Models with optimized microgeometry

As anticipated, in order to optimize the contact patch on the tooth flank, it is possible to add microgeometry optimizations. However, the aim of microgeometry modification is dual, not only to optimize the contact patch, but also to reduce as much as possible the transmission error, in order to enhance the NVH performance of the powertrain, by reducing noise and vibrations generated by the transmission system. To properly set the microgeometry modifications, is useful to exploit the optimization tool available in Romax, *microgeometry study tool*, as explained in Section 2.4. Following the explained path, the first steps require to choose properly variables and constraints. Many parameters can be set as either variables or constraints, however, to have symmetric flanks, for manufacturing reasons, the selected ones are:

Variable	Constraint	Factor
LF Lead Crown	RF Lead Crown	1
LF Lead Slope	RF Lead Slope	-1
LF Involute Barreling	RF Involute Barreling	1
LF Involute Slope	RF Involute Slope	1

Table 4.52: Variables and constraints

The parameters on the left flank (LF) are set as variables, while the ones on the right flank (RF) are constrained with respect to the left flank, with factor 1, while considering lead slope the factor is -1, due to manufacturing reasons, as explained by [22].

Model D1: microgeometry optimization, first attempt

Many targets can be specified, but from experience, the first attempt can be done considering as target to minimize the average of the peak to peak value of the TE over the whole torque range of the motor. The selected variables are in Table 4.53.

Variable	Range
LF Lead Crown	$0 \div 10\ um$
LF Lead Slope	$-10 \div 10\ um$
LF Involute Barreling	$0 \div 10\ um$
LF Involute Slope	$-10 \div 0\ um$

Table 4.53: Variables, first attempt

As anticipated, the right flank parameters are constrained as indicated by Table 4.52, while the target is to minimize the average of the peak to peak value of the TE over the whole torque range of the motor. Obviously, this optimization process should be repeated for both gear sets. Doing the optimization, the parameters that lead to the best result are the following:

	Microgeometry modifications (um)			
Parameter	Input pinion	Input wheel	Output pinion	Output wheel
LF Lead Crown	1	0	3	0
LF Lead Slope	2	0	-5	-4
LF Involute Barreling	5	5	5	5
LF Involute Slope	0	0	0	0
RF Lead Crown	1	0	3	0
RF Lead Slope	-2	0	5	4
RF Involute Barreling	5	5	5	5
RF Involute Slope	0	0	0	0

Table 4.54: Optimization results, first attempt

Romax, [22], ensures that the microgeometry analysis is based on conjugate topology of mating gears. This means that the modifications can be indifferently applied to either just the pinion or to the wheel. But, due to the manufacturing processes to be performed to obtain these modifications, if the modification is

quite large (let's say higher than about 5 um) it usually preferred to then split the modifications between the two gears. Adopting these modifications, the flanks of each tooth modify as indicated by Figures 4.32 and 4.33.

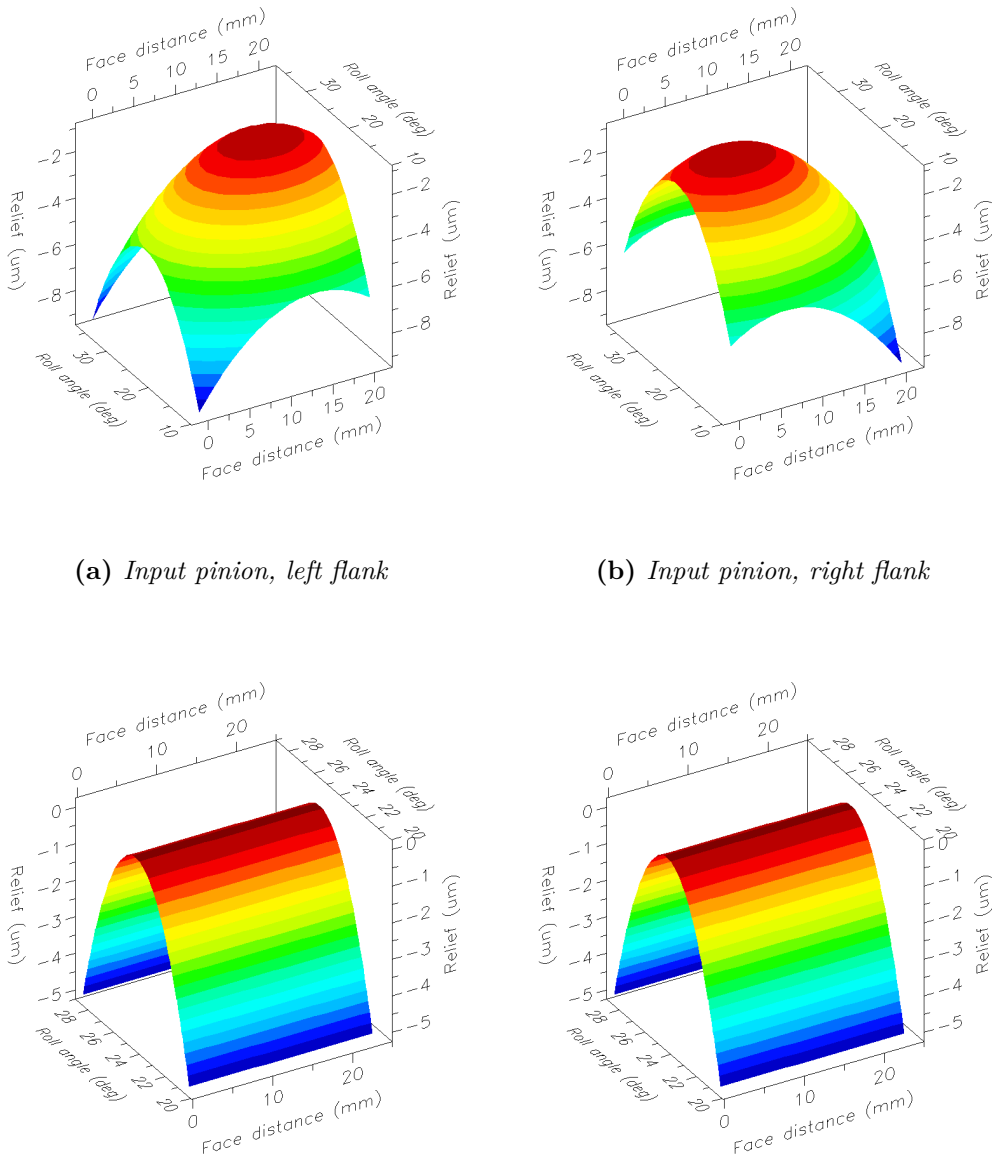

(a) *Input pinion, left flank*

(b) *Input pinion, right flank*

(c) *Input wheel, left flank*

(d) *Input wheel, right flank*

Figure 4.32: Input gear set, modified flanks, Model D1

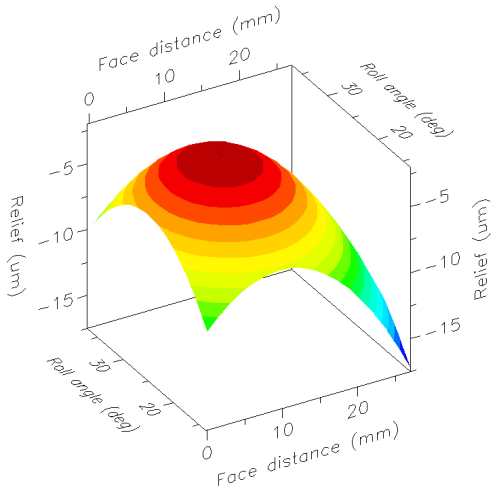

(a) *Output pinion, left flank*

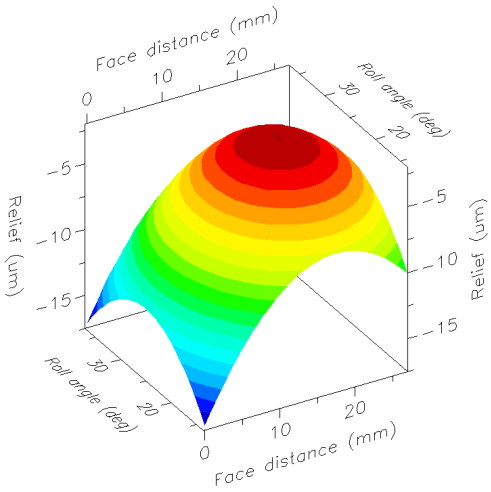

(b) *Output pinion, right flank*

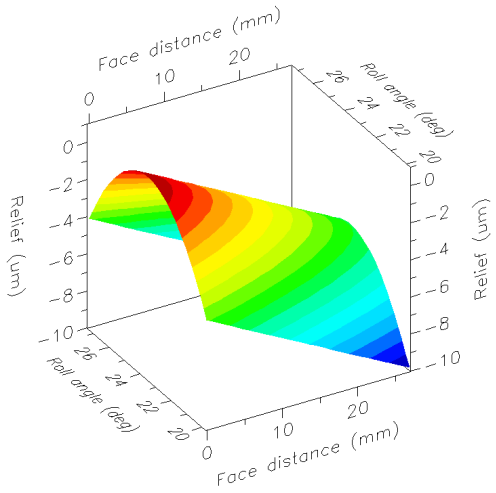

(c) *Output wheel, left flank*

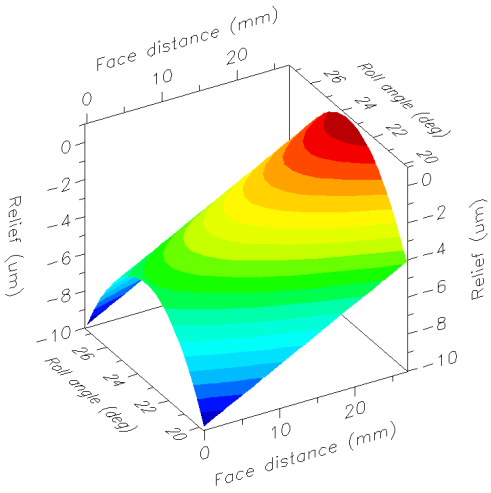

(d) *Output wheel, right flank*

Figure 4.33: Output gear set, modified flanks, Model D1

Considering these modifications, as can be seen from Figure 4.34, the average value of transmission error is decreasing both in input and output gear sets. However, considering certain torque values (around zero torque, from -25 Nm to +25 Nm), the value is not decreasing, on the contrary the TE is actually increasing. This will represent a problem in the following NVH analysis, as will be explained in Section 6.1. To be more precise, the NVH response depends on the amplitude of the harmonics of the TE, as better investigated in Section 6.2. However, just looking at Figure 4.34, it is reasonable to think that the NVH response of Model D1 will not improve with respect to Model C, considering low values of torque. Please remind that the vertical line in Figure 4.34 highlights the torque value of the load case *NVH* (i.e. -25 Nm).

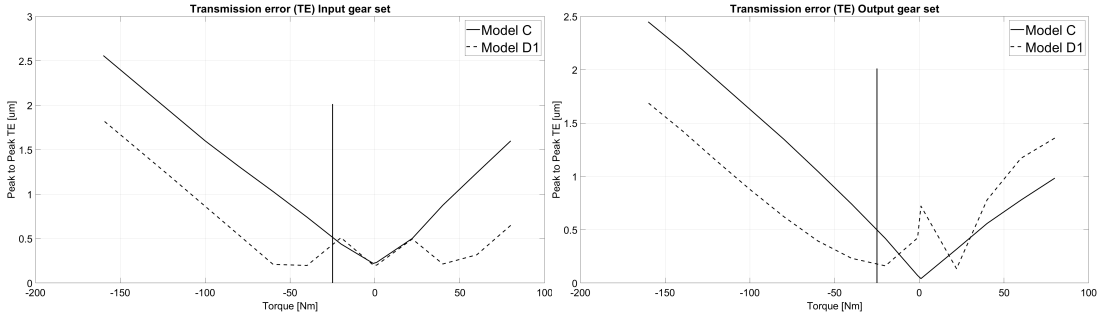

(a) *Input gear set* **(b)** *Output gear set*

Figure 4.34: Comparison TE, Model C vs D1

Moreover, even the contact patch is important to be analysed.
Comparing Figure 4.25, concerning Model C, and Figure 4.35, which refers to Model D1, it can be noted a slight improvement of the contact patch: the contact stress, indeed, the stress is more distributed along the tooth flank. However, the distribution is not optimal yet. This means that further optimization should be performed.
To further optimize the microgeometry it is possible to enlarge the ranges of variables, without modifying the targets. However, only slight improvements can be obtained, since since due to manufacturing, in reality, it is difficult to have modifications of values higher than $\approx 15\ um$. However, another attempt is performed.

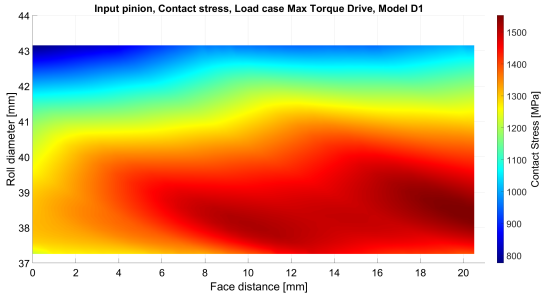

(a) *Input pinion, Max Torque Drive*

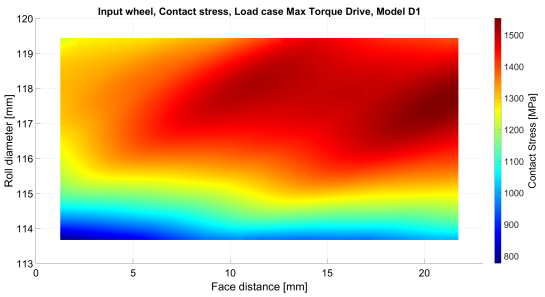

(b) *Input wheel, Max Torque Drive*

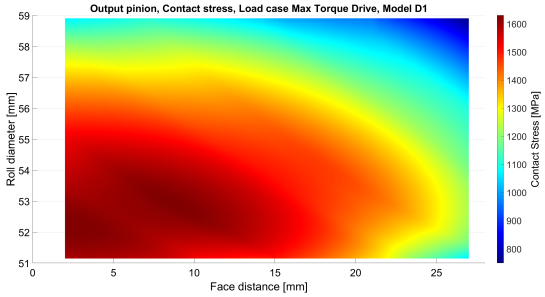

(c) *Output pinion, Max Torque Drive*

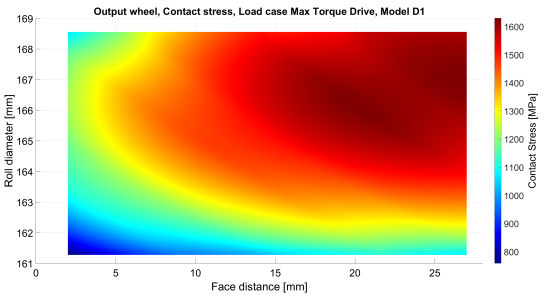

(d) *Output wheel, Max Torque Drive*

Figure 4.35: Contact stress, Load case Max Torque Drive, Model D1

Model D2: microgeometry optimization, second attempt

In this optimization, the target is exactly the same of Model D1: minimize the average value of the TE along the whole torque range of the motor. What changes is just the range of variability of the variables:

Variable	Range
LF Lead Crown	$0 \div 15\ um$
LF Lead Slope	$-15 \div 15\ um$
LF Involute Barreling	$0 \div 15\ um$
LF Involute Slope	$-15 \div 0\ um$

Table 4.55: Variables, second attempt

Running the optimization procedure, the obtained parameters are:

	Microgeometry modifications (um)			
Parameter	Input pinion	Input wheel	Output pinion	Output wheel
LF Lead Crown	1	0	2	0
LF Lead Slope	1	0	-4	-3
LF Involute Barreling	7	7	8	7
LF Involute Slope	0	0	0	0
RF Lead Crown	1	0	2	0
RF Lead Slope	-1	0	4	3
RF Involute Barreling	7	7	8	7
RF Involute Slope	0	0	0	0

Table 4.56: Optimization results, second attempt

Applying these modifications, the flanks become the following:

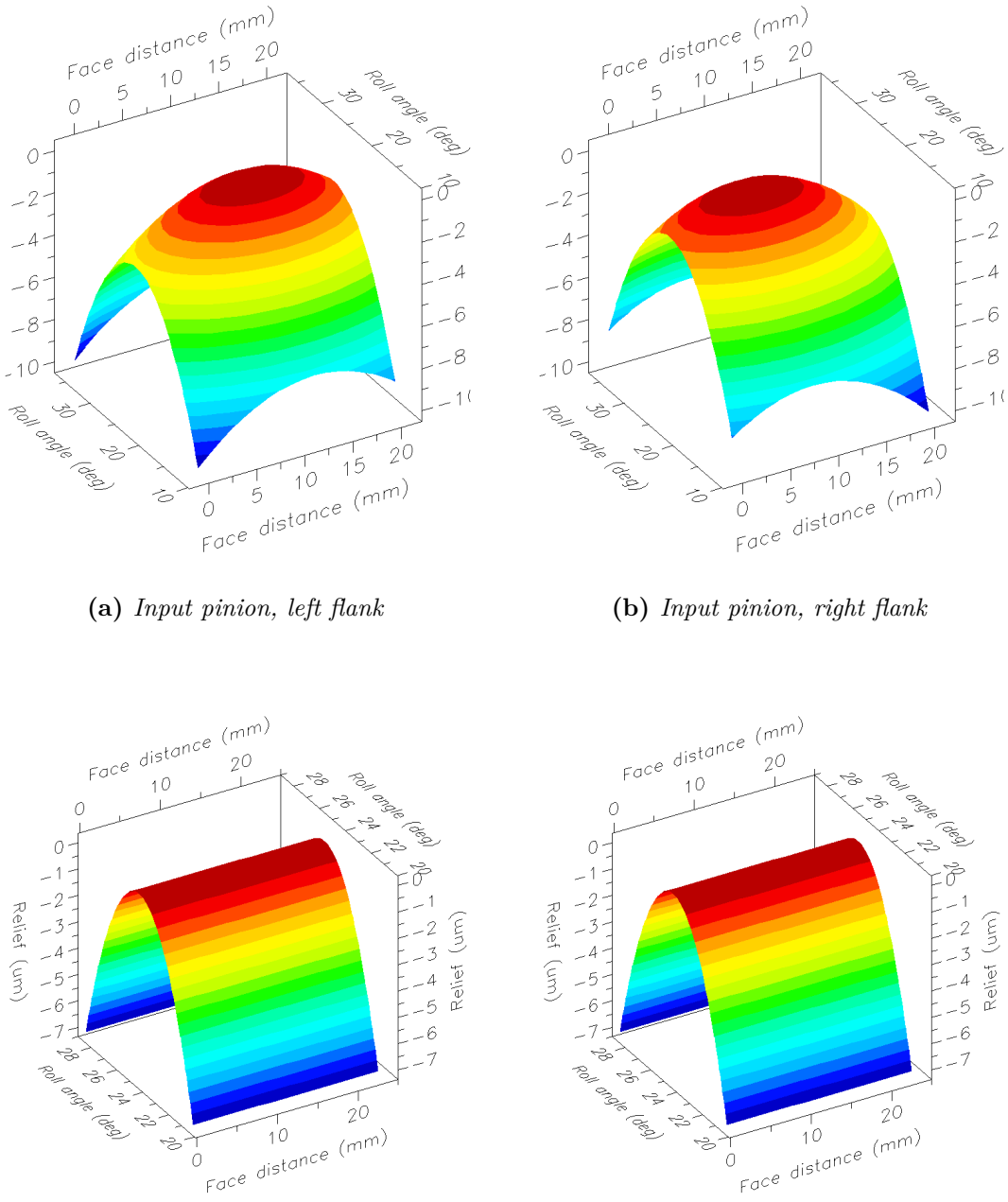

(a) *Input pinion, left flank*

(b) *Input pinion, right flank*

(c) *Input wheel, left flank*

(d) *Input wheel, right flank*

Figure 4.36: Input gear set, modified flanks, Model D2

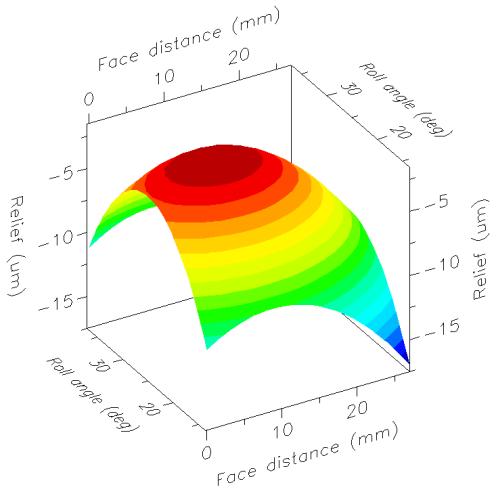

(a) *Output pinion, left flank*

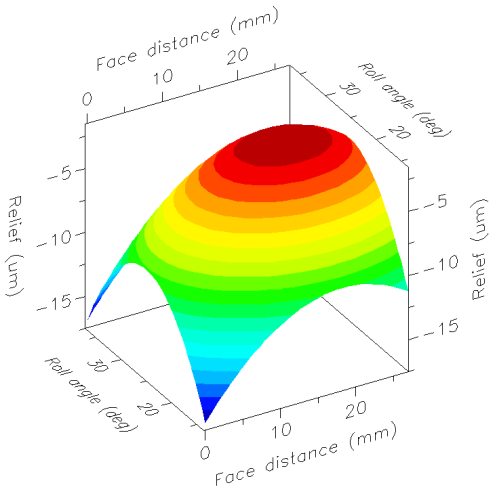

(b) *Output pinion, right flank*

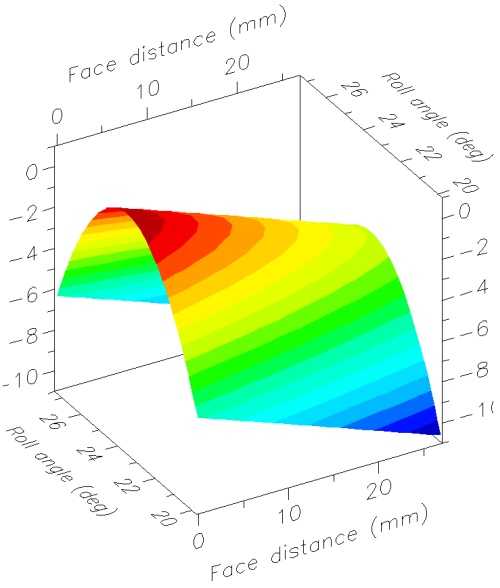

(c) *Output wheel, left flank*

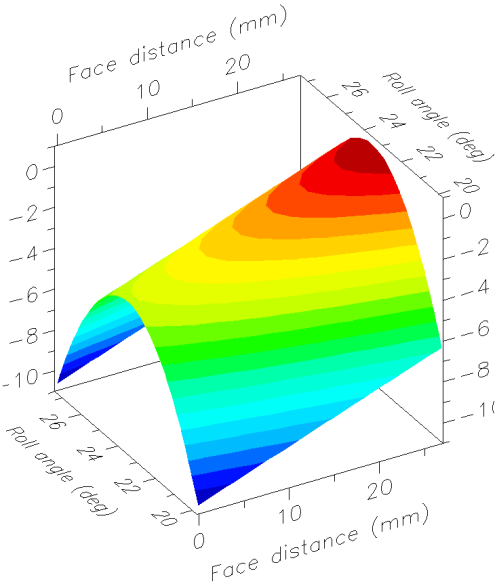

(d) *Output wheel, right flank*

Figure 4.37: Output gear set, modified flanks, Model D2

The contact patches become:

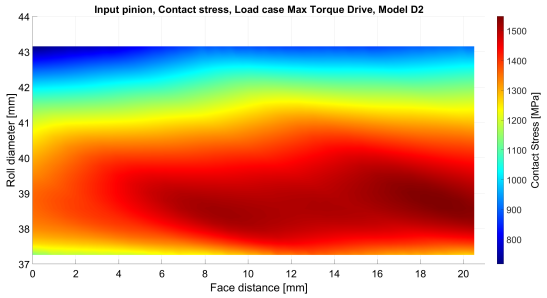

(a) *Input pinion, Max Torque Drive*

(b) *Input wheel, Max Torque Drive*

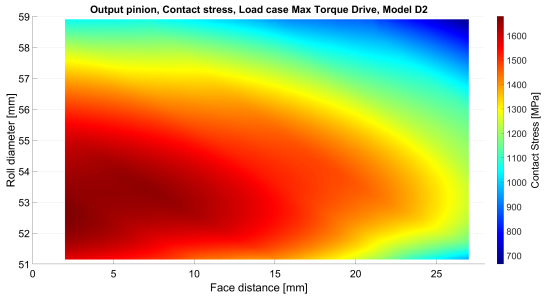

(c) *Output pinion, Max Torque Drive*

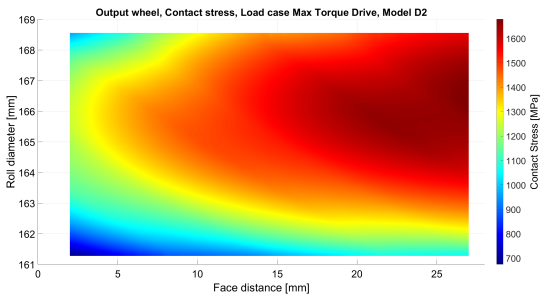

(d) *Output wheel, Max Torque Drive*

Figure 4.38: Contact stress, Load case Max Torque Drive, Model D2

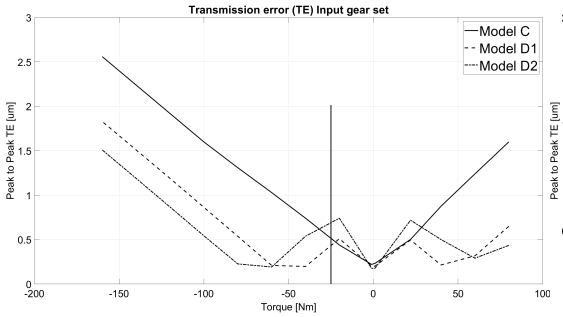

(a) *Input gear set*

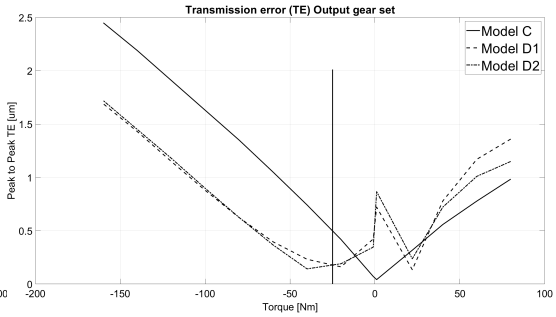

(b) *Output gear set*

Figure 4.39: Comparison TE, Model C vs D1 vs D2

Moving from Model D1 to D2, looking at Figure 4.39, it is possible an overall reduction of the peak to peak value of the TE. This is particularly evident for high values of torque, in both input and output gear set. Unfortunately, considering the value with low torque, the TE is actually increasing. This will represent a major

issue when the NVH analyses will be performed in Chapter 6.
Furthermore, comparing Figures 4.35 and 4.38, the contact patches are pretty similar, no major distinctions can be noted.
To try to enhance the stress distribution over the tooth flank is possible to select other targets during the optimization process.

Model D3: microgeometry optimization, third attempt

In the Model D3, different targets are selected with respect to the previous models, while the variables are exactly the same of Model D1 (Table 4.53).
In this case the targets are more specific to optimize the contact patch: they aim to obtain a more centered stress distribution.

Target	Aim	Weight
Peak contact stress roll distance position pinion	Target 8 mm	1
Peak contact stress roll distance position wheel	Target 23 mm	1
Right edge load ratio	Minimize	1
Left edge load ratio	Minimize	1

Table 4.57: Target Input Gear Set, Third attempt

Target	Aim	Weight
Peak contact stress roll distance position pinion	Target 11 mm	1
Peak contact stress roll distance position wheel	Target 32 mm	1
Right edge load ratio	Minimize	1
Left edge load ratio	Minimize	1

Table 4.58: Target Output Gear Set, Third attempt

These targets have been selected with the precise aim of better distribute the contact stress over the tooth flank, trying to center it as much as possible. In particular, the vertical axis on the contact patch plot (i.e. *roll axis*), can also be displayed as roll distance. Therefore, the selected targets aim to position the peak contact stress at half of the overall roll distance of the tooth flank. Furthermore, the right and left edge load ratio should be minimized in order to center the contact. The edge load ratio is defined by [22] as the highest load over the 10 % of the tooth, divided by the peak load over the full tooth.

The obtained values are then:

	Microgeometry modifications (um)			
Parameter	Input pinion	Input wheel	Output pinion	Output wheel
LF Lead Crown	4	3	5	5
LF Lead Slope	-3	-3	-4	0
LF Involute Barreling	5	4	5	5
LF Involute Slope	-1	0	-2	0
RF Lead Crown	4	3	5	5
RF Lead Slope	3	3	4	0
RF Involute Barreling	5	4	5	5
RF Involute Slope	-1	0	-2	0

Table 4.59: Optimization results, Third attempt

In this case, the flanks are:

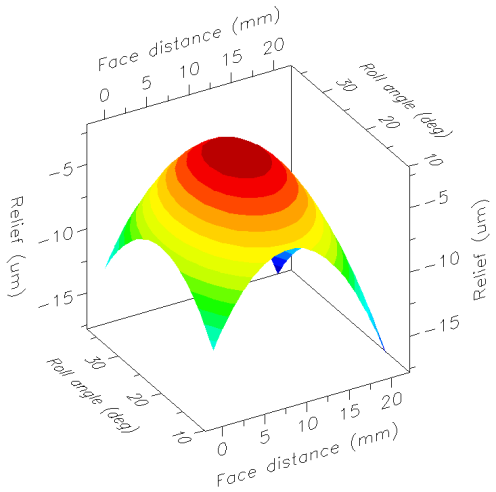

(a) *Input pinion, left flank*

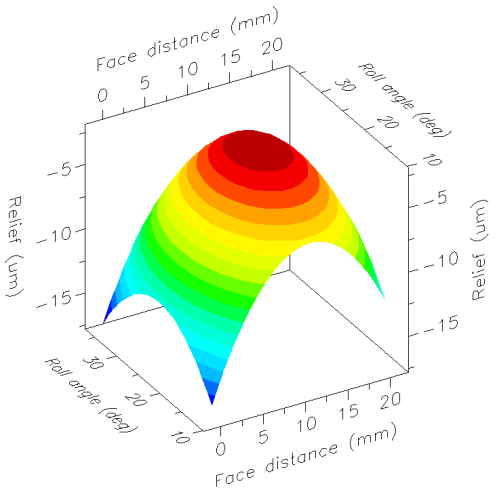

(b) *Input pinion, right flank*

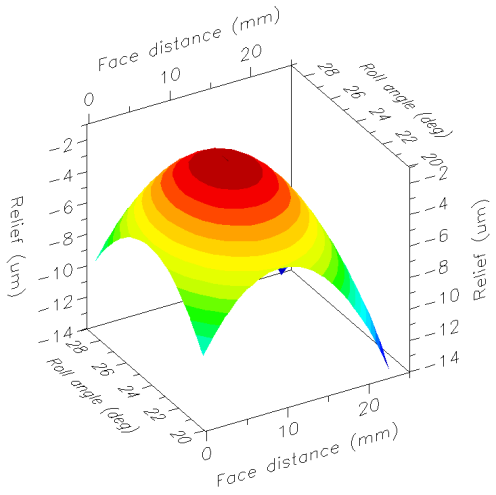

(c) *Input wheel, left flank*

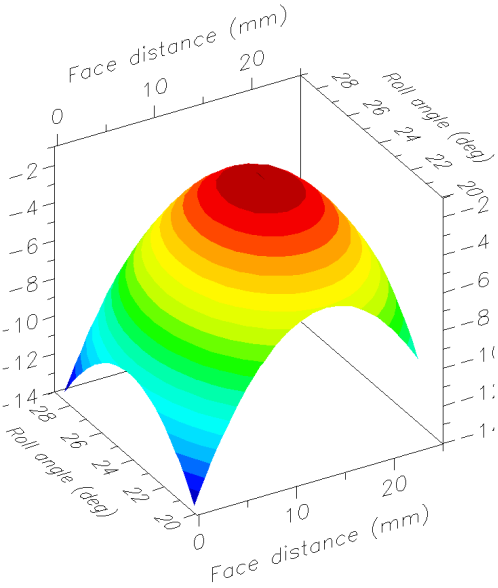

(d) *Input wheel, right flank*

Figure 4.40: Input gear set, modified flanks, Model D3

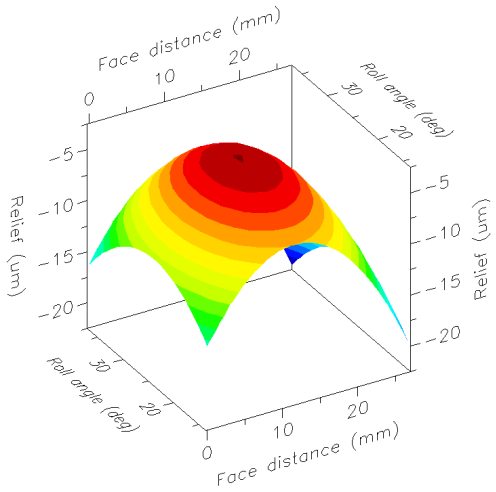

(a) *Output pinion, left flank*

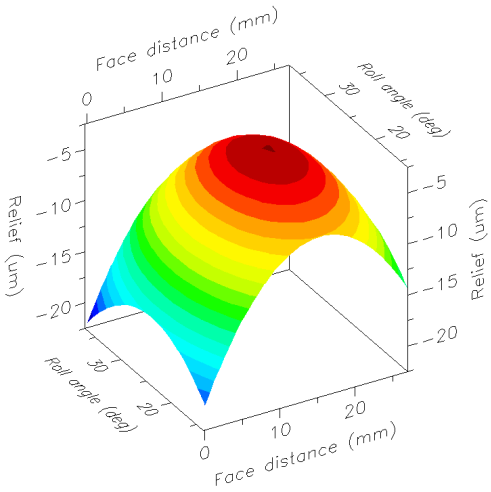

(b) *Output pinion, right flank*

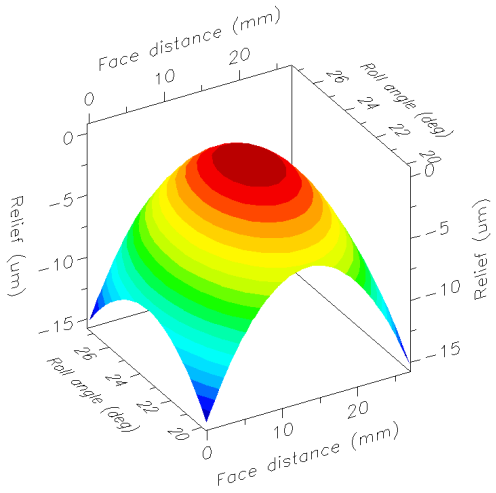

(c) *Output wheel, left flank*

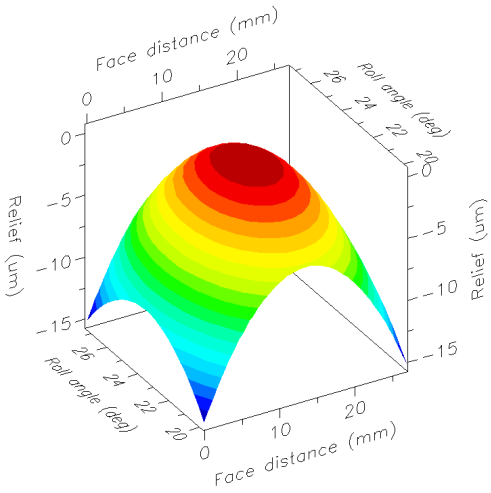

(d) *Output wheel, right flank*

Figure 4.41: Output gear set, modified flanks, Model D3

The contact patches become:

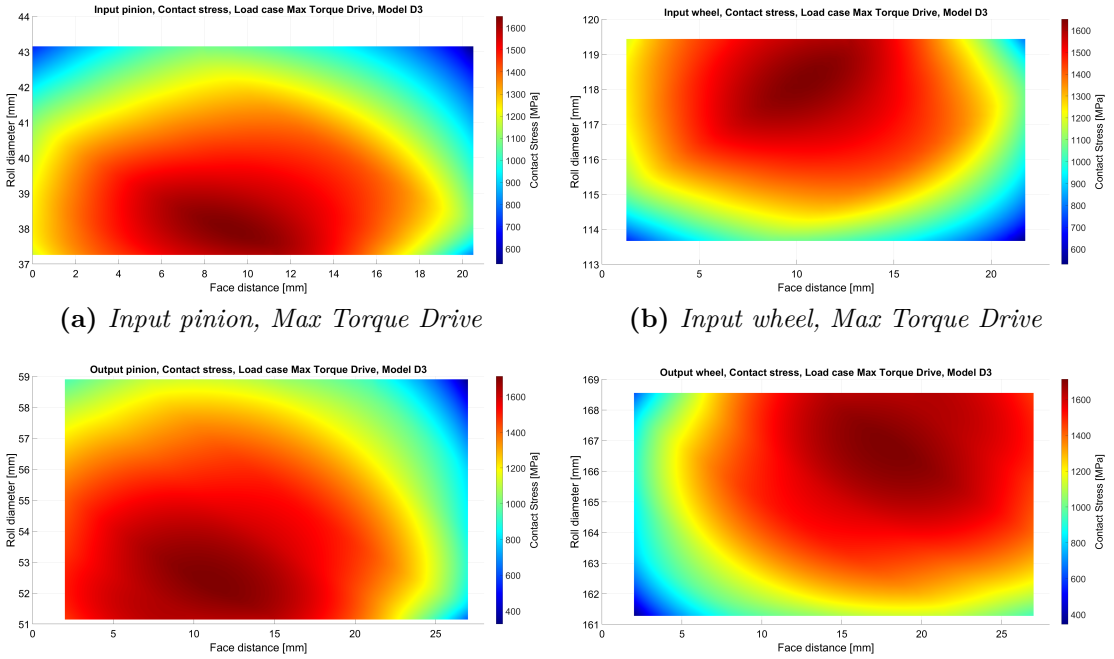

(a) *Input pinion, Max Torque Drive* **(b)** *Input wheel, Max Torque Drive*

(c) *Output pinion, Max Torque Drive* **(d)** *Output wheel, Max Torque Drive*

Figure 4.42: Contact stress, Load case Max Torque Drive, Model D3

Comparing Figures 4.38 and 4.42, a remarkable improvement is noted in Model 3. However, the *Max torque drive* load case is a pretty extreme condition, with very high values of torque and it is not that easy to optimize the contact stress in this load case.
However, the goodness of Model D3 is evident looking at the contact patch of the load case *NVH*, Figure 4.43. In Figure 4.43 the roll axis is shown in terms of roll distance, in order to make more clear the targets of this optimization.

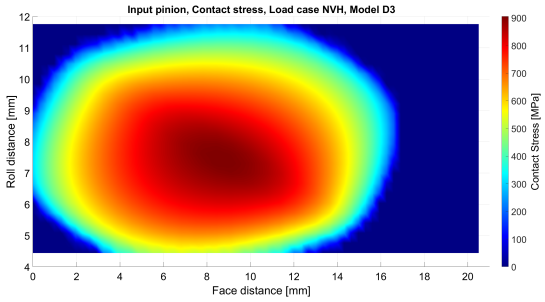

(a) *Input pinion, NVH*

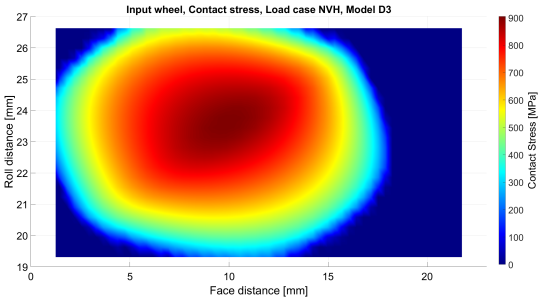

(b) *Input wheel, NVH*

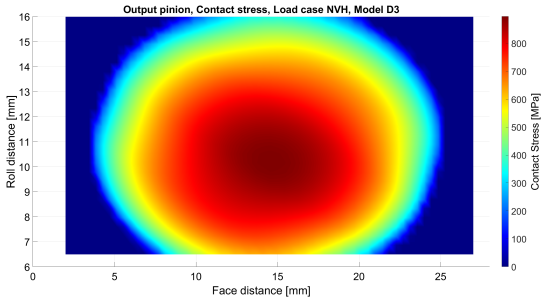

(c) *Output pinion, NVH*

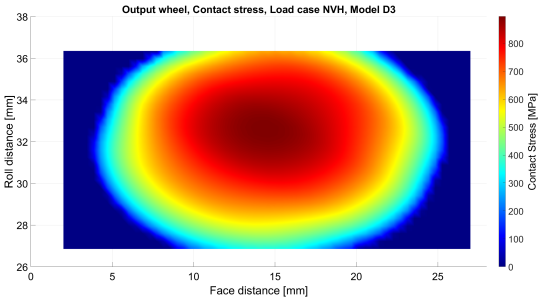

(d) *Output wheel, NVH*

Figure 4.43: Contact stress, Load case NVH, Model D3

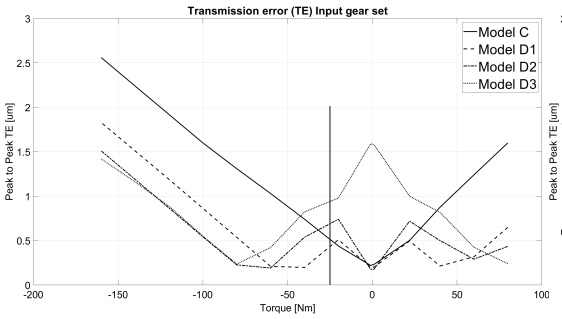

(a) *Input gear set*

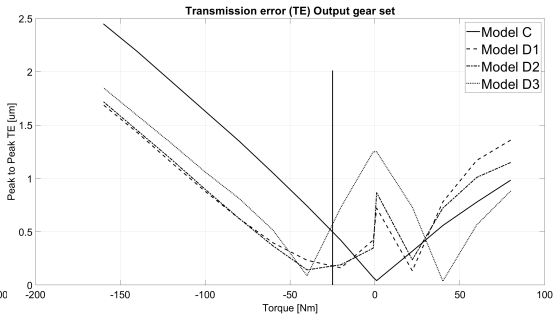

(b) *Output gear set*

Figure 4.44: Comparison TE, Model C vs D1 vs D2 vs D3

Looking at Figure 4.44, it appears evident the worsening of the peak to peak value of the TE moving to Model D3, especially at the torque value of the load case *NVH*, highlighted by the vertical line. This can be accepted only in the case in which the contact patch is way more relevant that the NVH performance.

Model D4: microgeometry optimization, fourth attempt

As already said, two main goals can be achieved through microgeoemetry modifications: optimization of contact patch or of NVH performance. Actually it is very tough to obtain an optimization that leads to a remarkable improvement of both targets, it would require a lot of experience. Moreover, it usually requires to accept a certain compromise, without really optimising either goal.
Therefore, since in this case the static analysis does not constitute a major concern, more interest will be dedicated on the enhancement of NVH performance.
In order to accomplish this goal, i.e. to improve the NVH performance of the electric powertrain, it is hence possible to try to optimize microgeometry with the aim of reducing the amplitudes of the harmonics in the specific load cases of interest. As will be explained better in Section 6.2, the crucial load cases for the NVH analysis will be the ones corresponding to low values of torque. Moreover, it will be seen that the first harmonic is the one with the greatest amplitude. Hence to minimize the 1^{st} harmonic of the TE of both input and output gear set, and also the peak to peak values, at specific load cases with low value of torque can be a reasonable choice to enhance NVH performance of the studied powertrain.
Hence, the variables are highlighted in Table 4.60.

Variable	Range
LF Lead Crown	$0 \div 15\ um$
LF Lead Slope	$-10 \div 10\ um$
LF Involute Barreling	$0 \div 15\ um$
LF Involute Slope	$-15 \div 0\ um$

Table 4.60: Variables, fourth attempt

As regards the targets, the aim was to reduce both the peak to peak value and the amplitude of the first harmonic of both input and output gear sets considering small values of torque. In particular, the optimized values of torque are (-40, -20, -1, 1 , 20, 40) Nm. This choice will be justified by Section 6.1.

Running the optimization process, the recommended values are:

	Microgeometry modifications (um)			
Parameter	Input pinion	Input wheel	Output pinion	Output wheel
LF Lead Crown	3	0	4	3
LF Lead Slope	5	0	-2	0
LF Involute Barreling	1	0	2	0
LF Involute Slope	0	0	0	0
RF Lead Crown	3	0	4	3
RF Lead Slope	-5	0	2	0
RF Involute Barreling	1	0	2	0
RF Involute Slope	0	0	0	0

Table 4.61: Optimization results, Fourth attempt

Please keep in mind that the modifications can be indifferently applied to either just the pinion or to the wheel: they are split to both pinion and wheel only if the values are too high, therefore in this case no modifications are applied to input wheel.

The flanks are the following:

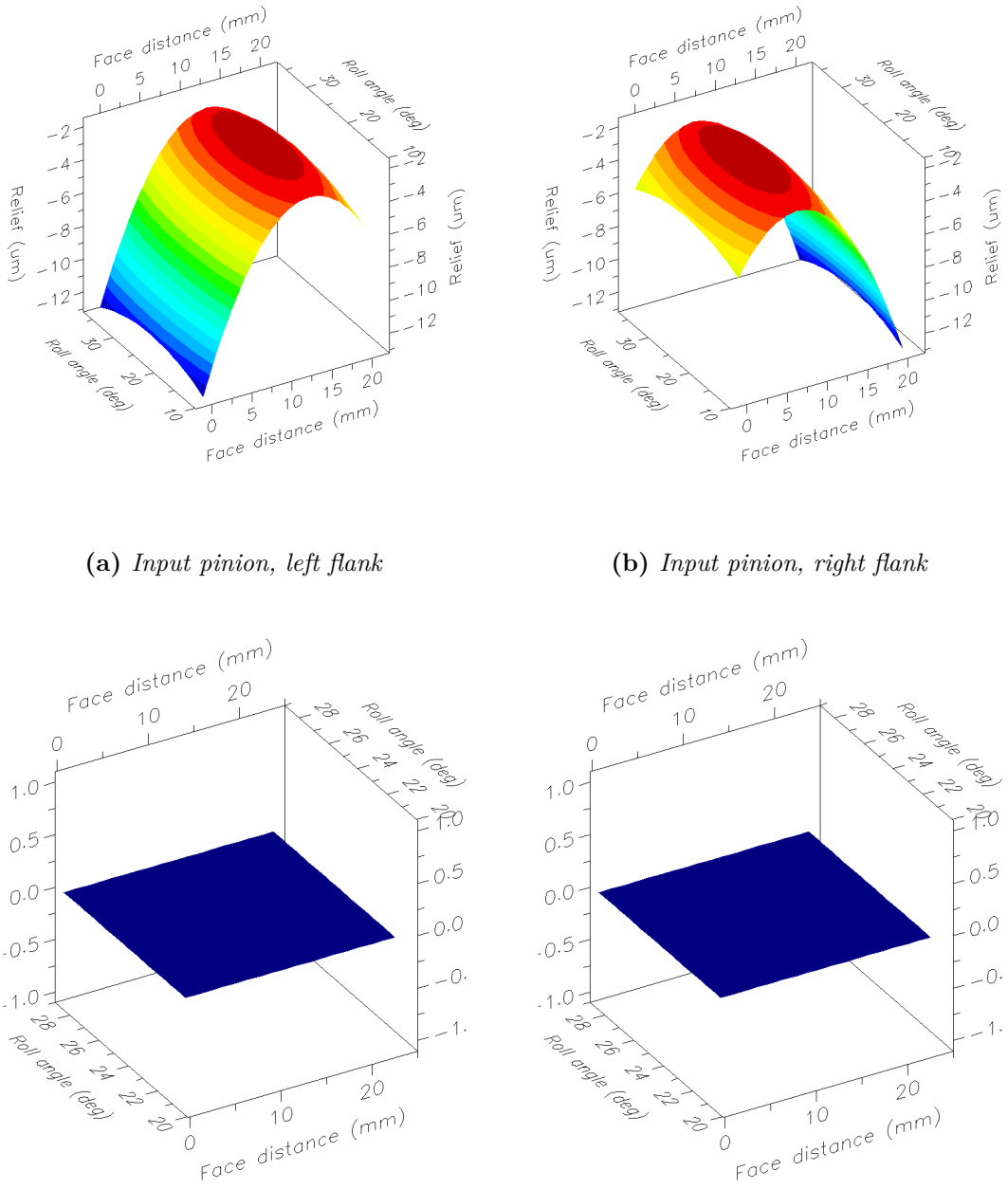

(a) *Input pinion, left flank*

(b) *Input pinion, right flank*

(c) *Input wheel, left flank*

(d) *Input wheel, right flank*

Figure 4.45: Input gear set, modified flanks, Model D4

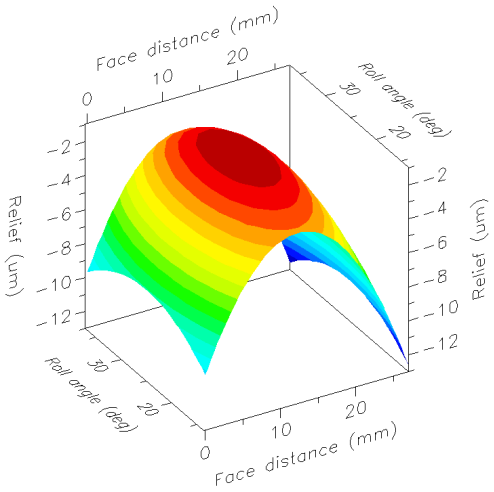

(a) *Output pinion, left flank*

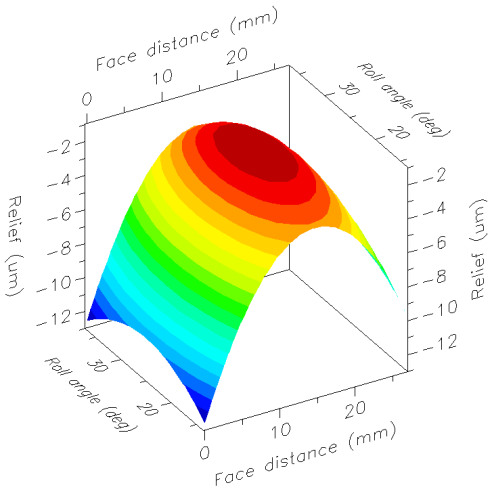

(b) *Output pinion, right flank*

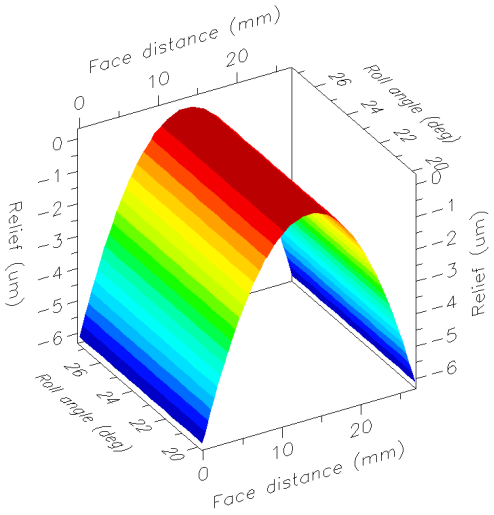

(c) *Output wheel, left flank*

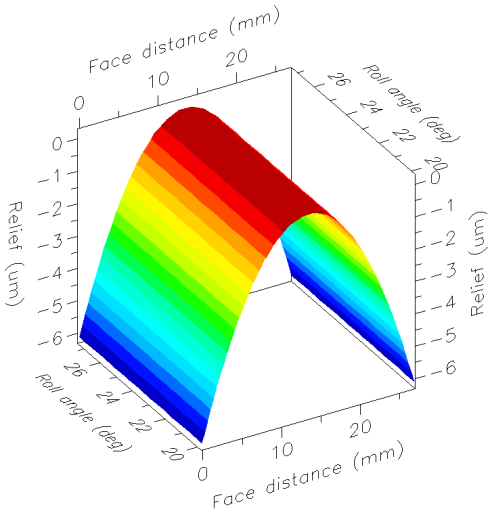

(d) *Output wheel, right flank*

Figure 4.46: Output gear set, modified flanks, Model D4

The contact patches become:

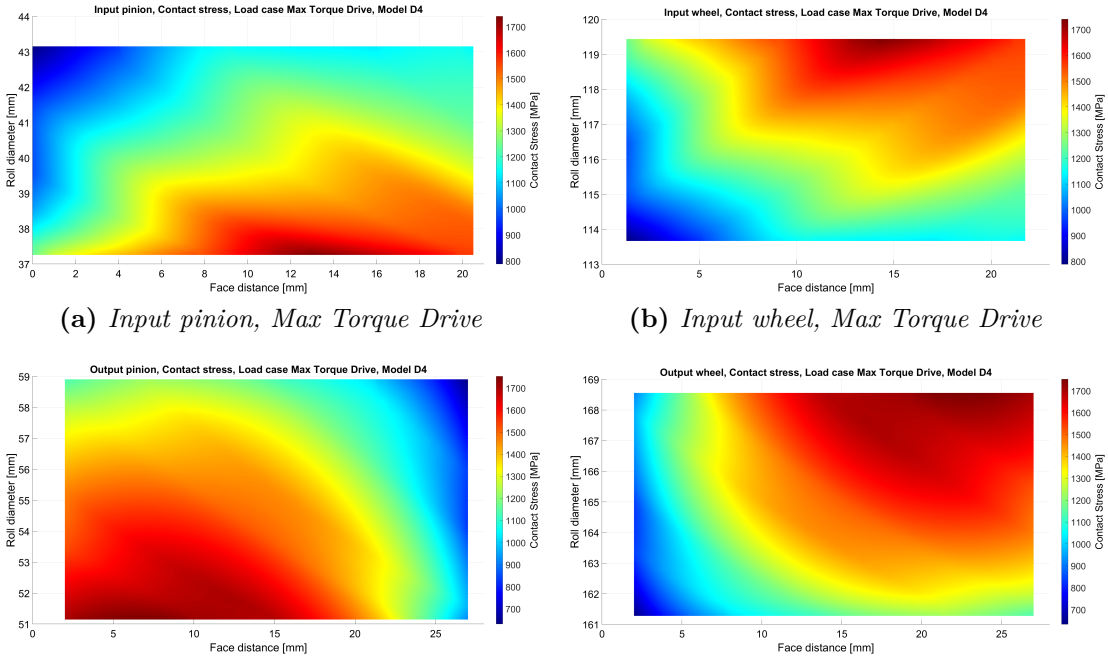

(a) *Input pinion, Max Torque Drive* **(b)** *Input wheel, Max Torque Drive*

(c) *Output pinion, Max Torque Drive* **(d)** *Output wheel, Max Torque Drive*

Figure 4.47: Contact stress, Load case Max Torque Drive, Model D4

The distribution of the contact stress is significantly worse than that of Model D3, but, as already said, in Model D4 the goal was different: it is accepted to have worse contact in order to heavily improve NVH characteristics.

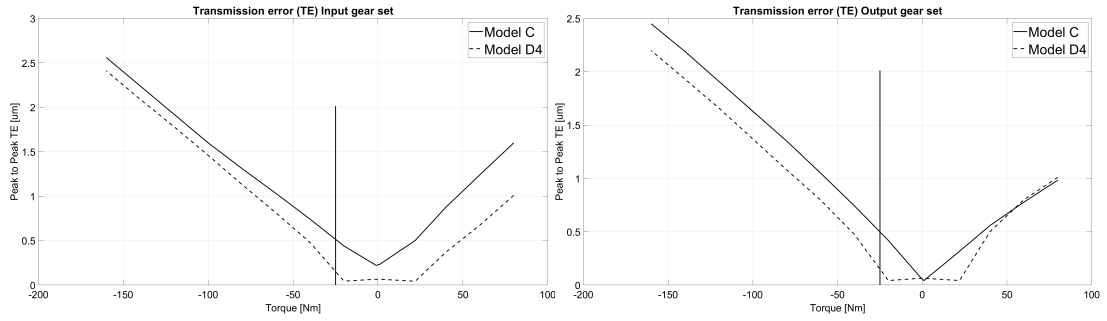

(a) *Input gear set* **(b)** *Output gear set*

Figure 4.48: Comparison TE, Model C vs D4

As it is possible to notice from Figure 4.48, the peak to peak value of the TE is way lower in the case of Model D4, especially at low values of torque. This result is exactly what was wanted, since it can be reasonable to think that it will follow a reduction also of the amplitude of the harmonic of the TE, as confirmed by Section 6.6.
Finally, a comparison among the safety factors of the different models is provided. The values are actually not increasing adding these microgeometry modifications. However, this does not represent a major problem, since the aim was more on the NVH or on centering the contact along the flank. The important aspect is that in all models the safety factors are always higher than 1.
Centering the contact can eventually lead to an increase of the peak value of the stress: the safety factor could decrease. But the fundamental aspect is that, centering the contact, the stress is not anymore concentrated on the flank edges, which are more critical.

Gear	Safety factor contact				
	Model C	Model D1	Model D2	Model D3	Model D4
Input pinion	1.23	1.23	1.24	1.18	1.19
Input wheel	1.38	1.38	1.39	1.33	1.33
Output pinion	1.19	1.31	1.29	1.27	1.26
Output wheel	1.35	1.49	1.47	1.45	1.44

Table 4.62: Gears worst contact safety factors, comparison Model C vs Models D

Gear	Safety factor bending				
	Model C	Model D1	Model D2	Model D3	Model D4
Input pinion	1.45	1.44	1.47	1.40	1.38
Input wheel	2.39	2.38	2.42	2.30	2.27
Output pinion	1.17	1.37	1.34	1.32	1.30
Output wheel	1.57	1.83	1.79	1.77	1.74

Table 4.63: Gears worst bending safety factors, comparison Model C vs Models D

Gear	Combined Life (h)				
	Model C	Model D1	Model D2	Model D3	Model D4
Input pinion	309.31	302.82	334.03	249.64	233.53
Input wheel	913.86	894.69	986.91	737.56	689.98
Output pinion	229.05	521.81	460.81	433.71	400.03
Output wheel	704.11	1604.08	1416.55	1333.27	1229.72

Table 4.64: Gears combined life, comparison Model C vs Models D

Chapter 5

Case studies

In this brief chapter, for the sake of clarity, a summary of all the case studies investigated during this thesis work is report, in order to highlight all the important models and configurations.
First of all, several models, considering differences just on the gear sets, are studied, increasing step by step the level of detail:

- Model A: spur gears, without profile shift, without microgeometry modifications
- Model B: spur gears, with profile shift, without microgeometry modifications
- Model C: helical gears, with profile shift, without microgeometry modifications
- Models D (D1-D4): helical gears, with profile shift, with different attempts of microgeometry modifications

In the following tables (5.1 and 5.2), a recap of the helix angles and of the profile shift coefficients are reported:

Model	Helix angle, Input Gear set	Helix angle, Output Gear set
A	0°	0°
B	0°	0°
C, D1, D2, D3, D4	25.081°	24.987°

Table 5.1: Comparison among models, helix angle

		Model A	Models B, C, D1, D2, D3, D4
Profile shift coefficient	In pinion	0	-0.102
	In wheel	0	$-7.161 \cdot 10^{-2}$
	Out pinion	0	0.109
	Out wheel	0	$-7.203 \cdot 10^{-2}$
Generat. profile shift coeff.	In pinion	0	-0.144
	In wheel	0	-0.113
	Out pinion	0	$7.002 \cdot 10^{-2}$
	Out wheel	0	-0.111

Table 5.2: Comparison among models, profile shifting

Let's now give more details about the Models D, which are the only ones in which microgeometry modifications are taken into account. Many attempts have been studied in order to find the best possible optimization. More details are given in Section 4.2.7.

- Model D1: the aim of the optimization is to minimize the average of the peak to peak value of the TE over the whole torque range of the motor. The final values obtained by this optimization are the following:

	Microgeometry modifications (um)			
Parameter	Input pinion	Input wheel	Output pinion	Output wheel
LF Lead Crown	1	0	3	0
LF Lead Slope	2	0	-5	-4
LF Involute Barreling	5	5	5	5
LF Involute Slope	0	0	0	0
RF Lead Crown	1	0	3	0
RF Lead Slope	-2	0	5	4
RF Involute Barreling	5	5	5	5
RF Involute Slope	0	0	0	0

Table 5.3: Optimization results, Model D1

- Model D2: the aim of the optimization is to minimize the average of the peak to peak value of the TE over the whole torque range of the motor. This is the same target of Model D1, but in Model D2 a wider range of values of the variables is considered. The final values obtained by this optimization are the following:

	Microgeometry modifications (um)			
Parameter	Input pinion	Input wheel	Output pinion	Output wheel
LF Lead Crown	1	0	2	0
LF Lead Slope	1	0	-4	-3
LF Involute Barreling	7	7	8	7
LF Involute Slope	0	0	0	0
RF Lead Crown	1	0	2	0
RF Lead Slope	-1	0	4	3
RF Involute Barreling	7	7	8	7
RF Involute Slope	0	0	0	0

Table 5.4: Optimization results, Model D2

- Model D3: the targets of this optimization are more specific to optimize the contact patch: they aim to better distribute the contact stress over the tooth flank, trying to center it as much as possible. The final values obtained by this optimization are the following:

	Microgeometry modifications (um)			
Parameter	Input pinion	Input wheel	Output pinion	Output wheel
LF Lead Crown	4	3	5	5
LF Lead Slope	-3	-3	-4	0
LF Involute Barreling	5	4	5	5
LF Involute Slope	-1	0	-2	0
RF Lead Crown	4	3	5	5
RF Lead Slope	3	3	4	0
RF Involute Barreling	5	4	5	5
RF Involute Slope	-1	0	-2	0

Table 5.5: Optimization results, Model D3

- Model D4: the aim of this optimization of this attempt is mainly related to the NVH performance of the electric powertrain. Hence the target is to minimize the 1^{st} harmonic of the TE of both input and output gear set, and also the peak to peak values, at specific load cases with low value of torque, since, as will be explained better in Section 6.2, the crucial load cases for the NVH analysis will be the ones corresponding to low values of torque. The final values obtained by this optimization are the following:

	Microgeometry modifications (um)			
Parameter	Input pinion	Input wheel	Output pinion	Output wheel
LF Lead Crown	3	0	4	3
LF Lead Slope	5	0	-2	0
LF Involute Barreling	1	0	2	0
LF Involute Slope	0	0	0	0
RF Lead Crown	3	0	4	3
RF Lead Slope	-5	0	2	0
RF Involute Barreling	1	0	2	0
RF Involute Slope	0	0	0	0

Table 5.6: Optimization results, Model D4

Then, a sensitivity analysis is carried out even considering different electric motors and hence different electromagnetic excitations.
Two different cases are studied. The former relies on the motor, and hence on the electromagnetic excitation, directly provided by Romax supporting material [22], while the latter consider a comparison between two different electric motors studied in details in SyR-e [43].
The electric motor provided by Romax [22], is based on a paper ([44]), even if some modifications are done by Romax itself (such as the number of poles), and the reliability of the electromagnetic excitations provided by Romax [22] has not been verified during this thesis work.
On the other hand, the two motors studied in SyR-e [43] are more trustworthy, from both excitations and efficiency viewpoint. The two motors are deeply studied by [45] and [44].
The NVH analyses performed on the electric motor coming from Romax supporting material [22] is given in Chapter 6, while the NVH analyses on the electric motors studied in SyR-e [43] are provided in Chapter 7.
For the sake of clarity, the main data of the motors are reported in the following table.

Parameter	Romax 48-8	IPM 48-4	SPM 6-4
Source	Romax [22]	SyR-e [43]	SyR-e [43]
Number of slots	48	48	6
Number of poles	8	4	4
Rotor outer diameter (mm)	140.00	140.20	103.00
Stator outer diameter (mm)	216.00	216.00	216.00
Stator inner diameter (mm)	142.00	141.80	105.00
Active length (mm)	170.00	170.00	170.00
Slot height (mm)	14.00	14.24	42.26
Slot width (at air gap) (mm)	3.5	4.91	37.43

Table 5.7: Parameters of the electric motors studied

The load cases of interest for the NVH analyses are highlighted in Section 6.1.

Chapter 6

NVH analyses, electric motor from Romax supporting material

To correctly perform an NVH analysis it is necessary to exploit Romax Spectrum, that allows the user to obtain very important results from vibration analyses. Several excitation forces can be considered, and different results and graphs can be analyzed. Moreover, not only results in terms of acceleration can be obtained, but they can also be translated in terms of power and noise, as will be more investigated in Chapter 6.7.
In Chapter 1 the main sources of noise and vibrations in an electric power train were investigated in details. Thanks to Romax Spectrum it is possible to take into account many of them, the main excitation forces considered by the software are the following:

- Electric motor noise:
  - Torque ripple: torque fluctuations in time caused by the rotation of the rotor past each of the stator teeth. This results in vibrations of the power train and of the housing, leading to radiated noise from the surface of the housing to the vehicle through the housing mounts and connections with the vehicle.
  - Rotating radial forces: forces acting between the rotor and the stator. These forces can be assumed negligible from the rotor point of view, however, as regards the stator, they act on the tips of on the stator teeth causing vibrations of the housing.
  - Tangential forces.

  - Rotor unbalance: it causes rotating radial forces on the shaft proportional to the square of the rotational speed.

- Transmission noise:

  - Transmission error of gears.

Several results can be obtained performing a vibration analysis using Romax Spectrum:

- Modal flexibility: it shows how easily modes can be excited by the transmission error.

- 2D responses at any system nodes, in terms of displacement, velocity, or acceleration. It is possible to distinguish the components on X, Y or Z axis, or if preferred the vector magnitude can be shown. The results can be obtained in the shaft speed range (rpm) or in the frequency range (Hz).

- Waterfall plots: vibration levels can be plotted as a function of frequency against rotation speed (rpm) of the gearbox. The harmonic components appear on radial lines through the point (0 Hz, 0 rpm), while structural resonances appear on horizontal straight lines (constant frequency). It can be used to check for a coincidence of vibration sources with natural resonances.

- Mode shapes: characteristic deflection shapes at the undamped natural frequencies of a particular excitation frequency on the structure.

- Operating Deflection Shapes (ODS): it shows the vibration response of the whole model at a single frequency to any kind of excitation of interest among the available ones.

- Equivalent Radiated Power (ERP): it gives an estimation of the noise radiated by the vibrating housing surface. It represents a fast way to investigate radiated airborne noise, even if ERP does not give information about the directivity of the noise.

- Mean Square Velocity (MSV): good initial indicator of expected NVH performance, since radiated airborne noise is proportional to MSV. The acoustic analyses performed in Chapter 6.7, will be based on MSV.

In the following sections, as regards the 2D responses, the main focus will be on the acceleration response of some particular nodes, where some virtual triaxial accelerometers are placed. The first choice is to consider some accelerometeres placed on the housing, as reported in Figure 6.1, while another choice is to consider

the system mounts, in order to consider the vibrations generated in the mounts of the system to the vehicle, as indicated in Figure 6.2.

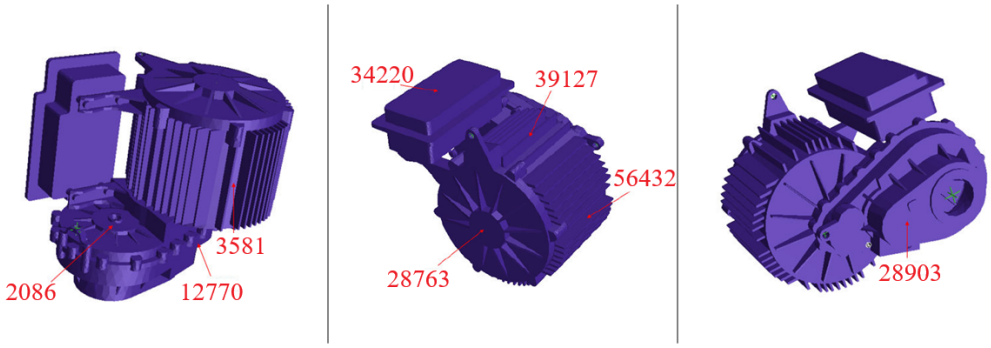

Figure 6.1: Virtual accelerometers positions

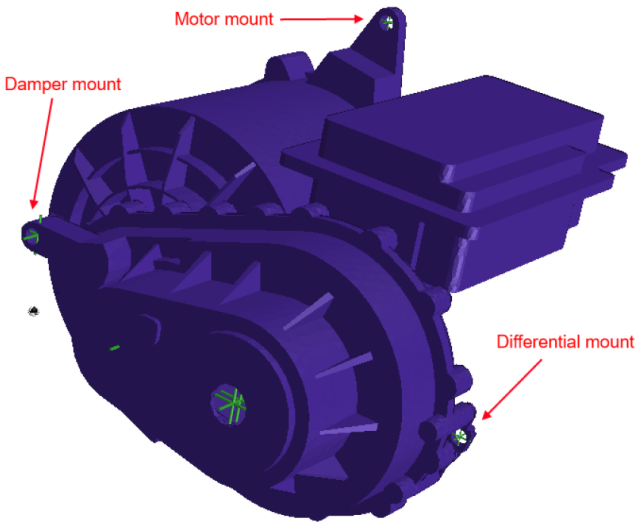

Figure 6.2: Housing mounts

In the following pages, the differential mount will be indicated as 8, the damper

mount as node 9, and the motor mount as node 10. It is possible to obtain all the graphs both on frequency range (Hz) and on the shaft rotational speed (rpm). Certainly, the two plots give exactly the same results, but in order to link the two plots, an effective conversion of the values from one plot to the other one. In particular, the conversion is the following:
frequency [Hz] = (shaft speed [rpm] · order of harmonic)/60.

6.1 Analyzed load cases

In order to perform the NVH analyses on the most important load conditions, different load cases will be considered.
First of all, the supporting materials provided by Romax [22] suggest to analyse the so called *NVH* load case, which foresees, according to Table 4.1, a rotational speed of the motor of $-5000\ rpm$, a torque of $-25\ Nm$, leading to an input power of $13.09\ kW$. Please mind the sign convention of this model, which includes negative sign for both the speed and the torque of the motor in case of drive condition.
It can be interesting to correlate this load case to a real driving condition of the vehicle, trying to investigate why this specific load case is of interest. To do so, knowing the rotational speed of the motor, it is possible to obtain the vehicle speed by exploiting the following reasoning, already explained in Chapter 4. First of all, knowing the overall transmission ratio, the speed of the wheel is obtained:

$$n_{wheel} = n_{motor}/\tau = 5000/9.084 = 550.42\,rpm$$

Then, knowing the wheel radius, see Table 6.1, the vehicle speed can be computed as:

$$v_{vehicle} = \omega_{wheel} R = 550.42 \cdot \frac{2\pi}{60} \cdot 0.3 = 17.29\,m/s = 62.25\,km/h$$

But the load case *NVH* has a torque of 25 Nm (in absolute terms), leading, as already said, to an input power of $13.09\ kW$. Hence, looking at Figure 6.4, which report the power vs vehicle speed plot with nil slope, it appears evident that to reach $62.25\,km/h$ with nil slope is necessary a power lower than $13.09\ kW$. This means that the excess of power is provided to overcome a certain slope (or alternatively to accelerate the vehicle). Through an iterative procedure, it has been proven by Figure 6.3 that, with a vehicle speed of $62.25\,km/h$, and a power $P_{IN} = 13.09 \cdot \eta_t = 12.43\,kW$, a constant slope of 2.45° is overcome. The angle in degree can be converted in a slope in percentage as follows:

$$\alpha = 2.45^\circ \rightarrow tan(\alpha) \cdot 100 = 4.28\%$$

Indeed, Figure 6.3 shows the plot power vs vehicle speed considering a slope of 4.28%.

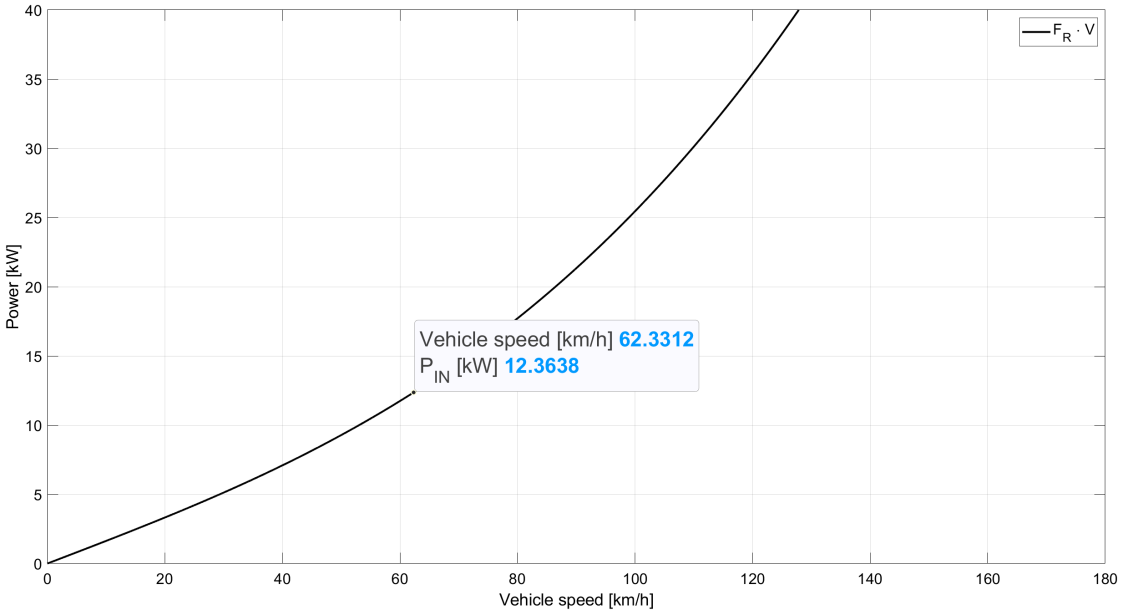

Figure 6.3: Power vs Vehicle speed, load case *NVH*, slope 4.28 %

Hence, the load case *NVH* is important to investigate an example of cruising speed of a city car in an extra urban road with a slope of 4.28%.
This load case is important but it is not the only one, other velocities to be investigated are 50 km/h (i.e. cruising speed within towns), 90 km/h (i.e. maximum speed in extra urban roads) and 130 km/h (i.e. maximum speed in motorways). They represents pretty common conditions at constant speed, in which NVH is particularly important. Indeed, NVH becomes even more relevant in situations in which a constant speed is kept for long time, hence the comfort turn into a crucial aspect. In other cases, for instance to overcome a steep slope, or to overtake another vehicle, NVH is less relevant, the priorities are others.
To obtain the load case knowing the vehicle speed is necessary to exploit both the plot representing power vs vehicle speed, and the one representing the tractive and resistive force vs vehicle speed. From the former, entering with the desired vehicle speed, the power can be derived; from the latter, entering with the desired vehicle speed, the force on the tyres can be derived. Then, knowing the force on the tyres the torque can be obtained. Hence, having defined the motor speed, the torque and the power, the load case is correctly defined.
Let's see in details one case, for instance the one related to a vehicle speed of 50 km/h.

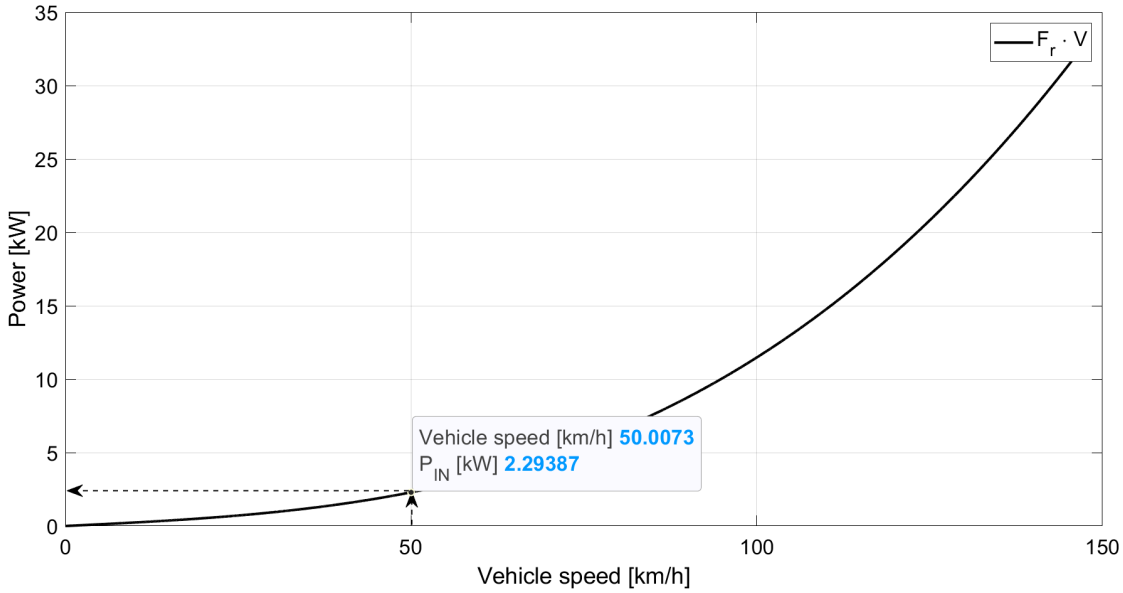

Figure 6.4: Power vs Vehicle speed, load case *NVH-50*

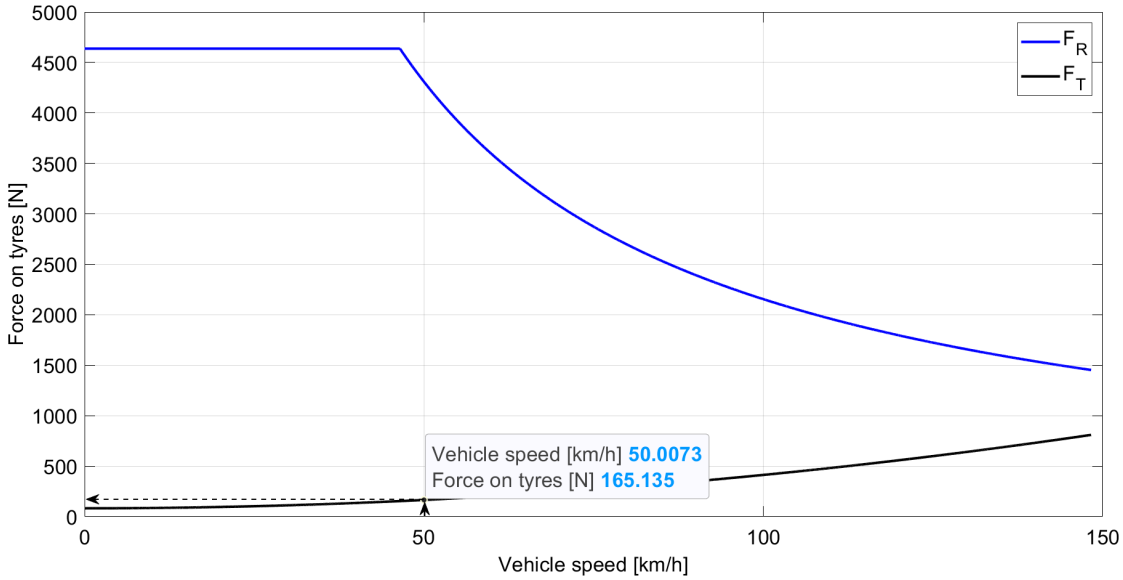

Figure 6.5: Tractive and Resistive Force vs Vehicle Speed, load case *NVH-50*

From the plot in Figure 6.4, the input power is $P_{IN} = 2.29\ kW$. Hence, the power given by the motor is $P = P_{IN}/\eta_t = 2.41\ kW$.
From Figure 6.5, once obtained the force on the tyres entering in the graph with the vehicle speed, i.e. $F_{tyres} = 165.14\ N$, the motor torque can be obtained as

follows:

$$T_m = \frac{F_{tyres} \cdot R}{\tau \cdot \eta_T} = 5.70Nm$$

Where T_m is the motor torque, τ is the overall transmission ratio (i.e. $\tau = \tau_{in} \cdot \tau_{out}$), η_T is the efficiency of the transmission system, R is the wheel radius.

Parameter	Symbol	Value	Unit of measure
Input transmission ratio	τ_{in}	2.955	-
Output transmission ratio	τ_{out}	3.074	-
Overall transmission ratio	τ	9.084	-
Transmission system efficiency	η_T	0.95	-
Wheel radius	R	≈ 0.3	m

Table 6.1: Considered parameters to define motor torque

Finally, knowing both the power and the torque, since $P = T_m \cdot \omega$, the rotational speed of the rotor can be obtained.

$$\omega = \frac{P}{T} = 423.78rad/s \rightarrow n = 4046.79rpm$$

The same procedure can be repeated for each speed of interest. The results are shown in Table 6.2. In the table the values are reported in absolute values (remind that if driving conditions, in this model both the torque and the motor speed should be negative).

Load case name	Vehicle speed [km/h]	P [kW]	T [Nm]	n [rpm]
NVH-50	50	2.41	5.70	4046.79
NVH	62	13.09	25	5000
NVH-90	90	9.22	12.09	7283.54
NVH-130	130	24.3	22.13	10520.27

Table 6.2: Analyzed load cases

Please, be aware that a level road (i.e. nil slope) is considered for all cases, with the exception of *NVH*.

6.2 Considered source of excitations

6.2.1 Rotor Unbalance

The first considered source of excitation is the dynamic unbalance of the rotor. The dynamic unbalance is defined according to ISO 1940-1:2003(E) ([46]). The data are the following, according from supporting material coming from [22]:

- Angle of unbalance: 0 deg
- Balance quality grade: G 6.3
- Unbalance mass: 16.26 kg
- Maximum service speed: 12000 rpm

The angle of unbalance is defined by [46] as the polar angle at which the unbalance mass is located with reference to the given rotating coordinate system, fixed in a plane perpendicular to the shaft axis and rotating with the rotor.
The balance quality grade G is defined by [2] as the maximum allowable peripheral velocity of the center of mass, expressed in mm/s. $G = \epsilon_{max} \cdot \Omega_{max}$, with ϵ eccentricity, in mm, and $Omega$ rotational speed, in rad/s. In this case $G = 6.3$ means maximum allowable peripheral velocity of the center of mass equal to $6.3\,mm/s$.
Even if the software call it *dynamic unbalance*, it is more correct to refer at it as *static unbalance*. Indeed, only a certain eccentricity is defined, thanks to [46]: knowing the balance grade and the maximum service speed is enough to obtain the maximum allowable eccentricity, which can be evaluated through some tables defined by that standard. On the other hand, the dynamic unbalance is present whenever, beyond the eccentricity, there is also an angle between the principal axis of inertia of the rotor and the rotation axis.
In this thesis work, the unbalance of the rotor is the only unbalance that will be taken into accout.

6.2.2 Electromagnetic Forces

As stated before, a very important source of excitations are the forces related to the electric machine assembly. There are two different ways to consider the electromagnetic force: it is possible to either import the values from some data tables, or to compute the excitations analytically directly in Romax, by using some simplified formulas. Only the former method is considered in this thesis, no analytical excitations will be considered.
It is necessary to define the electromagnetic excitations for each load case of interest.

Imported excitations

It is possible to import data importing them directly by Romax supporting material [22]. The imported excitations are related to the electric motor described in the previous chapters, in particular by Table 2.10, which has 48 slots, 8 poles and 3 phases. In the pre-processor section it is possible to import from external tables the values of torque ripple, radial and tangential forces for four operational speed, which are 1000, 5000, 8000 and 12000 rpm. It is possible to select how many harmonics should be extracted. Usually, the extracted harmonics are the ones with the highest amplitudes. For this reason, it has been chosen to extract the first 3 harmonics of the torque ripple, the first 6 of the radial forces (it is chosen to extract 6 harmonics, even if the sixth, i.e. order 48, has low amplitude, but it selected to consider the torque breathing effect of the stator), the first 5 of the tangential harmonics. To include the breathing mode is crucial, since it has been demonstrated by several papers, such as [47], that it usually constitutes the main acoustic issue.
The breathing mode of the stator is represented in Figure 6.6, indicating the tooth signals for the 48^{th} harmonic for all stator tooth nodes.

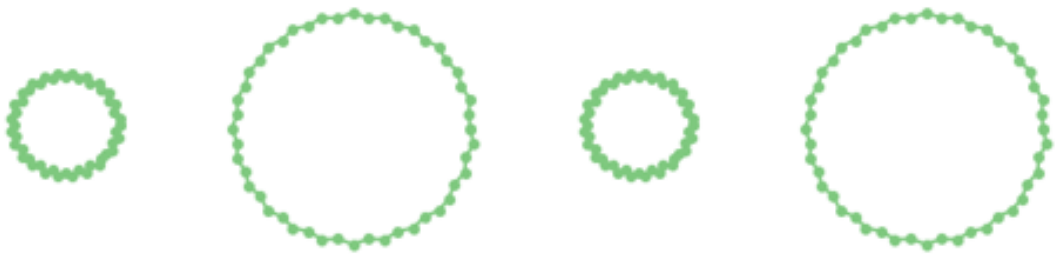

Figure 6.6: Tooth signal animation 48^{th} harmonic, breathing mode

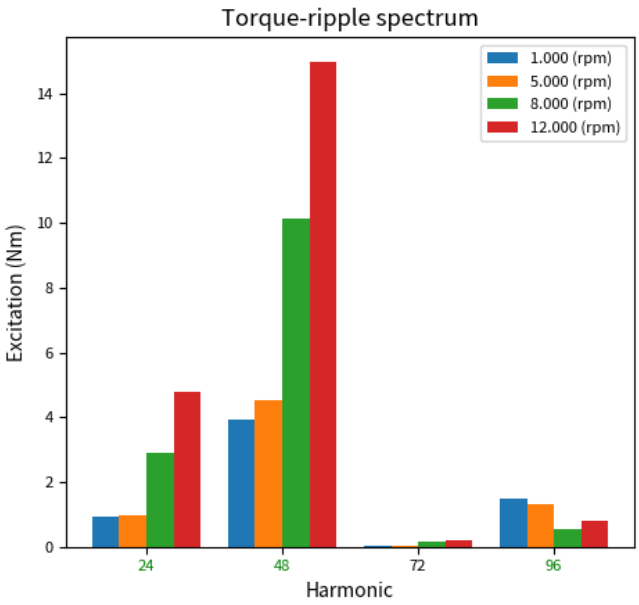

Figure 6.7: Torque ripple spectrum

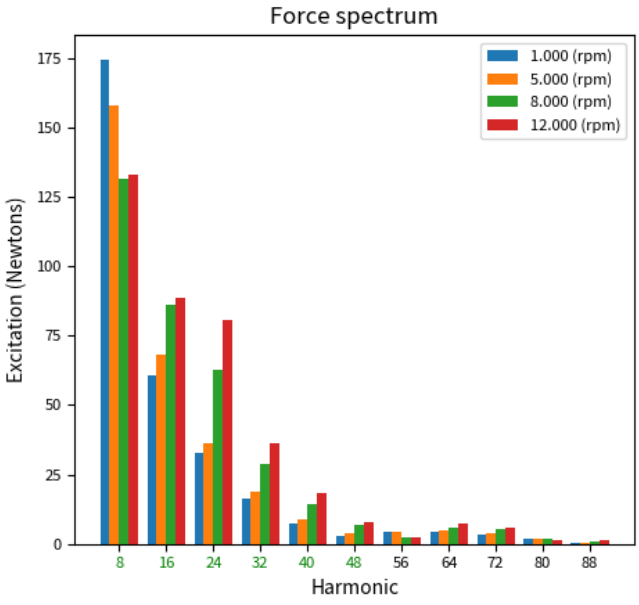

Figure 6.8: Radial forces spectrum

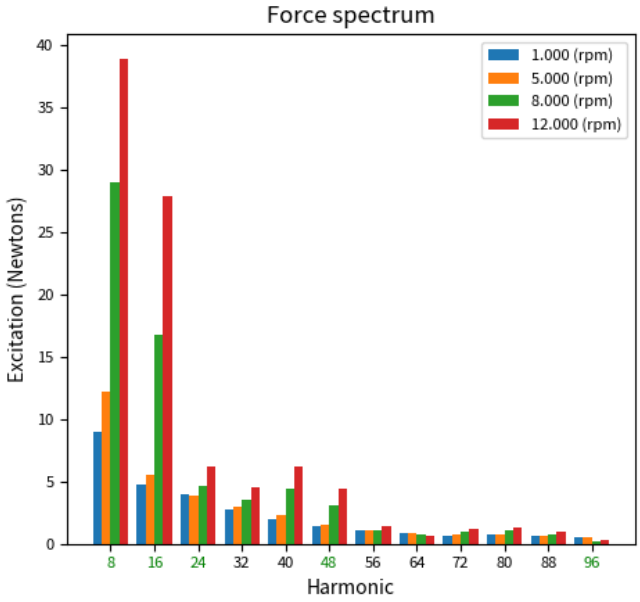

Figure 6.9: Tangential forces spectrum

It is possible to notice that the harmonic orders of the radial force and of the torque ripple are coherent with respect to the ones indicated by the analysis in Romax Concept, Section 4.1.
Therefore, in the following NVH analyses, the 48^{th} harmonic of all electromagnetic excitations (i.e. radial and tangential forces and torque ripple) will be taken into account. It is expected that the 48^{th} harmonic is particularly critical since a motor with an integer value of q (number of slots per pole per phase, better explained in Section 7) usually has as critical harmonic the one corresponding to the number of slots, i.e. 48.
However, it has been noticed that these imported electromagnetic excitation provided by Romax supporting materials [22] are not that reliable. In particular, exploiting a software (SyR-e [43], explained later in Section 7) lower values of the torque ripple are expected.

6.2.3 Transmission error

As anticipated in the previous chapters, the transmission error represents the main source of noise considering the transmission systems. In particular, it is crucial to analyse the harmonic contributions. The results of the first 8 harmonics have been extrapolated.
The transmission error strongly depends on the torque of the considered load case, hence it is necessary to calculate it for each load case of interest, Figure 6.2. Surely,

the macro and microgeometry of the gears will influence the transmission error, too.
Therefore, in the following Figures (6.12 - 6.17) are reported the amplitudes of the first 8 harmonics of both input and output gear set, considering each load case of interest, and considering Models A (spur gears), B (spur gears with profile shift), C (helical gears with profile shift). To better understand the amplitude of the harmonics, it can be useful to report even here the plot of the TE over the roll angle. In particular, just the plots related to the load case *NVH* are reported here below. Considering Models A and B, it is clear looking at plots 6.10 and 6.11 that they are square waves. In particular, considering input gear set, a whole period is represented along the contact, therefore only odd harmonics are present (Figures 6.12, 6.14), which is typical of square waves, indeed. On the other hand, considering output gear set, along the contact not the whole period is covered, hence it is not surprising to have also some even harmonics considering Models A and B (figures 6.13, 6.15). Considering instead Model C, the plot of the TE over the roll angle shows an almost perfect sinusoidal behaviour, leading to a remarkable amplitude of only the first harmonic (Figures 6.16, 6.17).

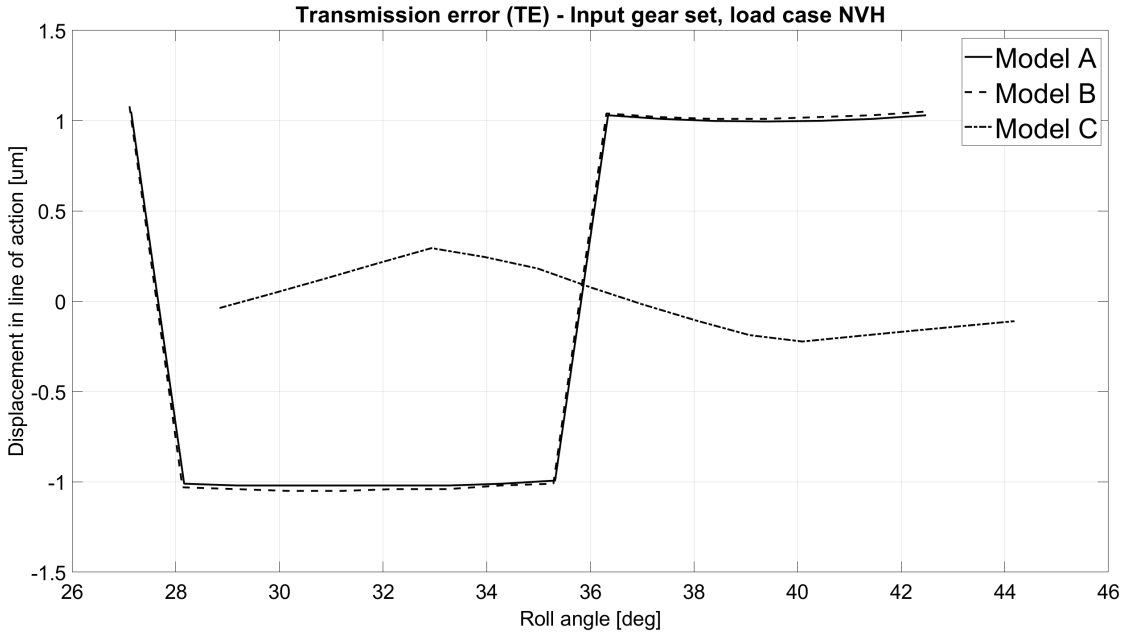

Figure 6.10: TE vs Roll angle, Input gear set, load case NVH

Figure 6.11: TE vs Roll angle, Output gear set, load case NVH

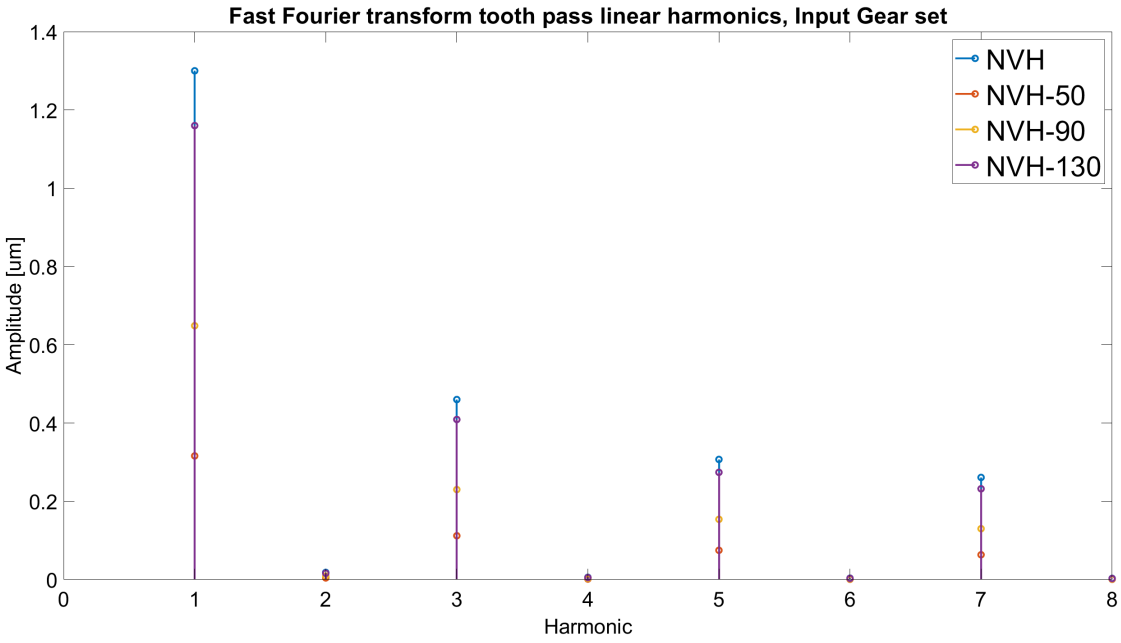

Figure 6.12: Amplitudes of TE harmonics, Input gear set, Model A

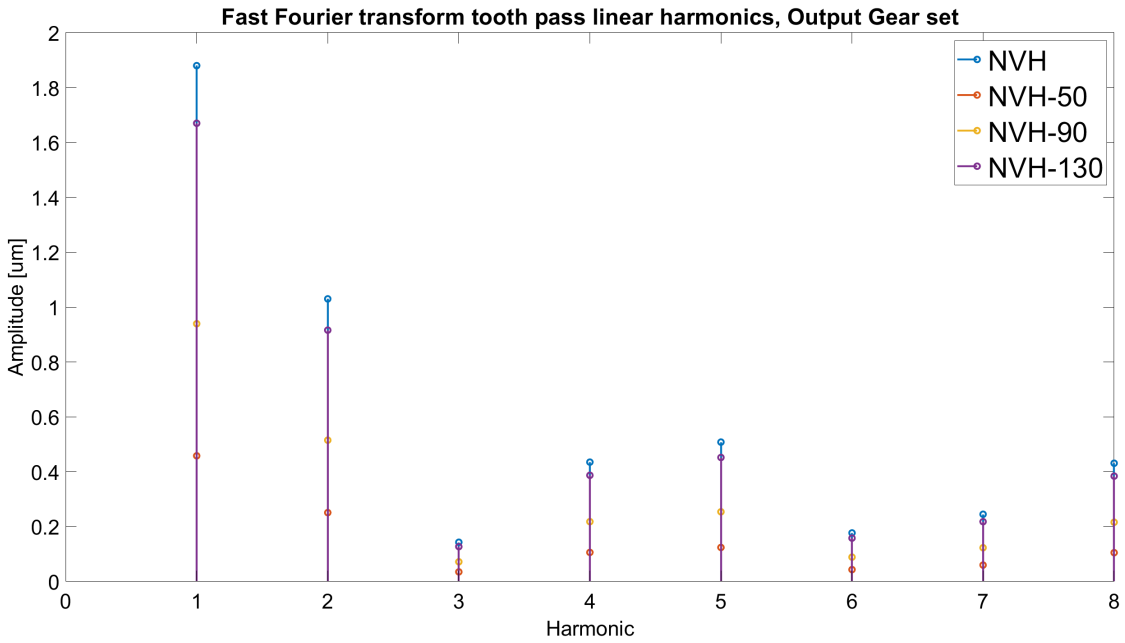

Figure 6.13: Amplitudes of TE harmonics, Output gear set, Model A

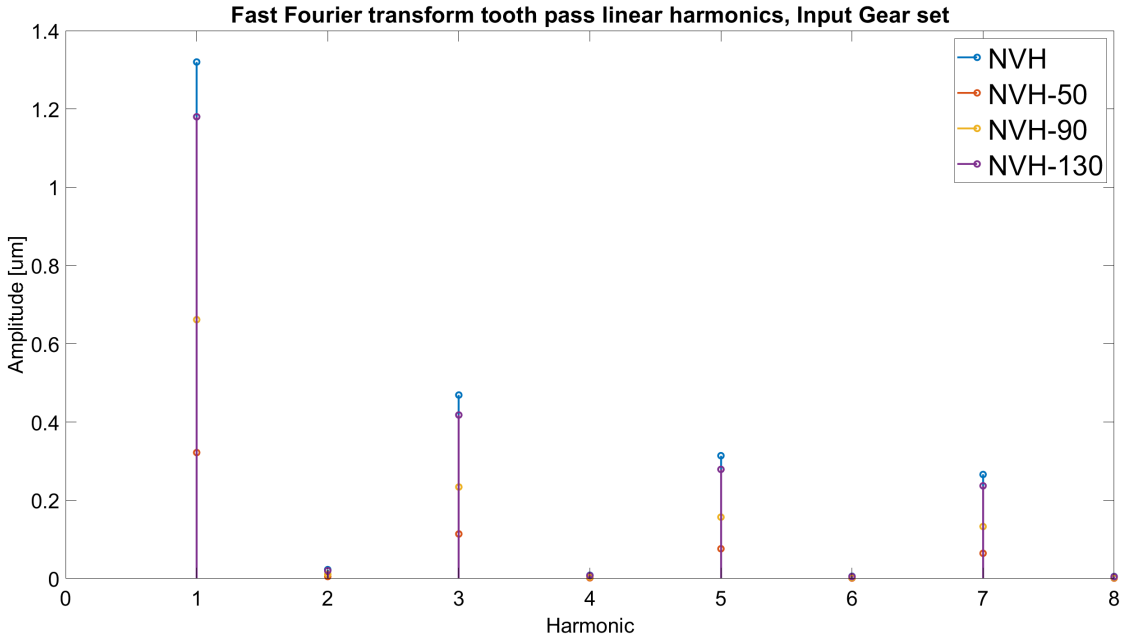

Figure 6.14: Amplitudes of TE harmonics, Input gear set, Model B

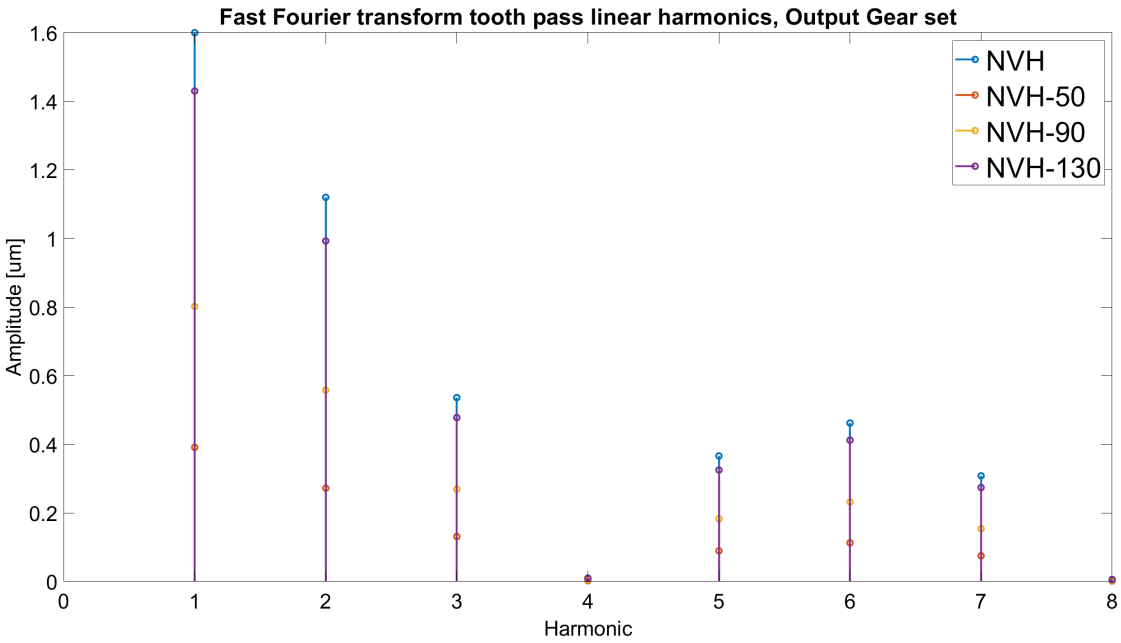

Figure 6.15: Amplitudes of TE harmonics, Output gear set, Model B

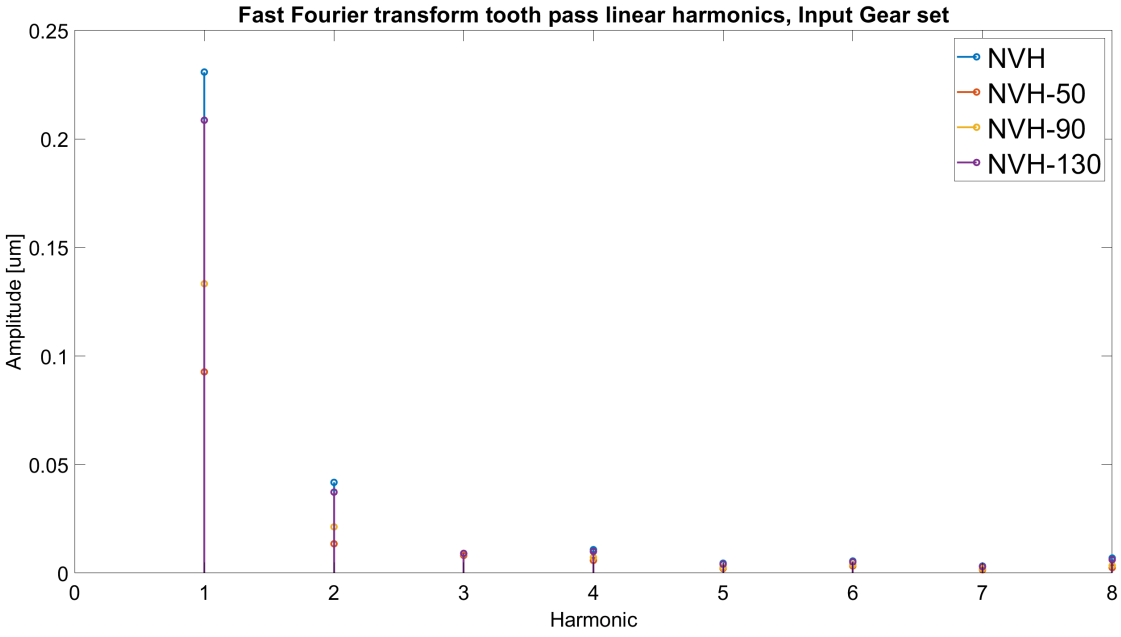

Figure 6.16: Amplitudes of TE harmonics, Input gear set, Model C

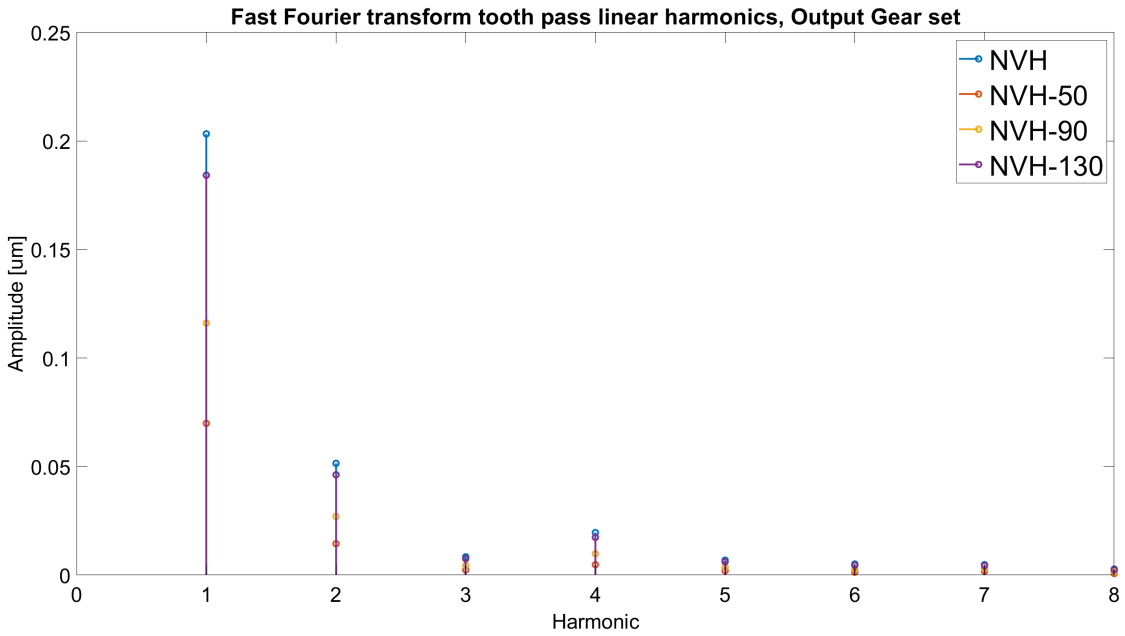

Figure 6.17: Amplitudes of TE harmonics, Output gear set, Model C

The first possible consideration is that the first order harmonic is the one with the largest amplitude, in all load cases and in all models. Therefore, when performing the NVH analysis it can be enough, as a starting point, to consider, as excitation, just the first order harmonic, and in this thesis work only the first order harmonic will be investigated. However, to be more precise, and to deepen the analyses, even the highest order harmonics should be considered. For instance, if with an higher order harmonic a low damped resonance frequency is excited, a remarkable response could be appreciated even if the input amplitude is limited.
Moreover, the load case *NVH* is the one which has the largest amplitudes in all models. This is not that surprising, being the load case *NVH* the one with the highest torque among the analysed ones. Indeed, the amplitude of the harmonics is proportional to the torque.
Moreover, of course, are confirmed the orders of the harmonic, already explained in Section 4.1. Indeed, considering the Input gear set, the first harmonic has order 22, the second 44, the third 66 and so on. As regards the Output gear set, the first harmonic has order 9.138, the second 18.28, the third 27.42 and so on. The abscissa indicates the meshing frequency harmonics.
Performing a comparison among the three models, it appears evident the remarkable improvement (i.e. reduction of amplitudes of TE harmonics) moving from spur gears (Models A and B) to helical gears (Model C).

6.3 Model A, spur gears

First of all, it can be interesting to perform the NVH analysis considering the Model A (i.e. spur gears).
The first analysis is performed taking into account the load case called *NVH*. All the sources of excitation will be considered during the analysis. In particular, as concern the electromagnetic forces, the imported data from Romax supporting material [22] will be taken into account.
To consider each excitation source is crucial in order to really understand which are the most critical excitation sources to be optimized.
As already stated, many results can be investigated in a NVH analysis. To give a complete overview of the performance, the following results are studied:

- Equivalent radiated power (ERP)
- Mean Square Velocity (MSV)
- Acceleration response at virtual accelerometers position
- Acceleration response at housing mounts

Please keep in mind that the first three results are indicators of the airborne noise. However, while the first two do not provide indications about the directivity of the propagated sound, the acceleration response, once the accelerometers are properly positioned, can give a clue about the directivity, too.
On the other hand, the acceleration response at housing mounts represents the structure borne noise. Indeed, the housing mounts represent the connection of the gearbox to the rest of the vehicle: hence, any kind of vibration felt by the mounts, will be transferred to the rest of the vehicle through a certain transmissibility function. However, if preferred, it is also possible to get the housing mounts response in terms of force, so to know the overall forces transmitted to the vehicle. To be more precise, it is possible to obtain the results, indifferently in terms of force or in terms of acceleration just on the housing mounts. But to really know the force or displacement transmitted to the rest of the vehicle, the transmissibility should be known: indeed, only through the transmissibility it is possible to get what is really transmitted to the vehicle.
The housing mounts are represented in the model with both axial and radial constraints fixed.

6.3.1 Excitation: 1^{st} Harmonic transmission error input gear set, Order 22

Remember that the amplitude of the harmonic of the TE strongly depends on the considered load case, i.e. in this case *NVH*. First of all, the linear dynamic

transmission error can be studied, in the whole range of velocity of the input shaft ($0 \div 12000$ rpm). The definition of the dynamic transmission error is given by [22]: it is a frequency dependent value which represents the actual displacement between two gear pair mesh nodes. It is the sum of the dynamic response of the gear mesh and the static transmission error.
The peaks of the linear dynamic transmission error are close to resonances involving the gear mesh.
Hence, at 0 rpm, the value of the dynamic TE corresponds to the static value of the amplitude of the harmonic of the proper gear set, as can be seen comparing the value at 0 rpm from Figure 6.18 and the amplitude of the first harmonic of the load case NVH, from Figure 6.12. Moreover, a resonance can be noted at about $8500\,rpm$. Being this resonance that evident, it should be performed an optimization with the aim of moving the resonance outside the working range of the transmission.

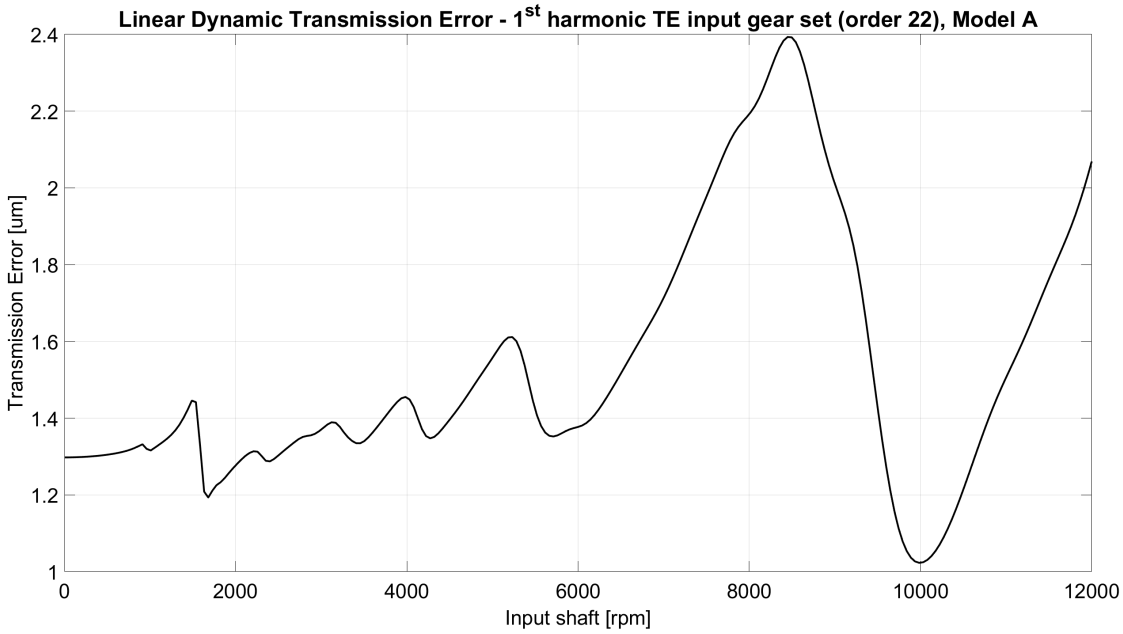

Figure 6.18: Linear dynamic transmission error - Input gear set, Model A

Moreover, to have a preliminary idea of the airborne noise radiated from the gearbox, it is important to analyse the ERP and MSV. These two results are strongly connected one to each other, therefore they are usually plotted together. To compute the ERP, the software gives the possibility to enable the A-weighting option, thanks to which the frequency results are filtered based on the sensitivity of the human ear as defined in the International standard IEC 61672:2003. Moreover, it is possible to set two properties of the acoustic medium: density and the speed

of sound. In this case, considering air, referring to 20 °C, the values are 1.2 kg/m^3 as regards the density, and 343.21 m/s as regards the speed of sound.
From Figure 6.19, it can be noted as general trend an increase of the ERP and MSV values as the input shaft speed increase.

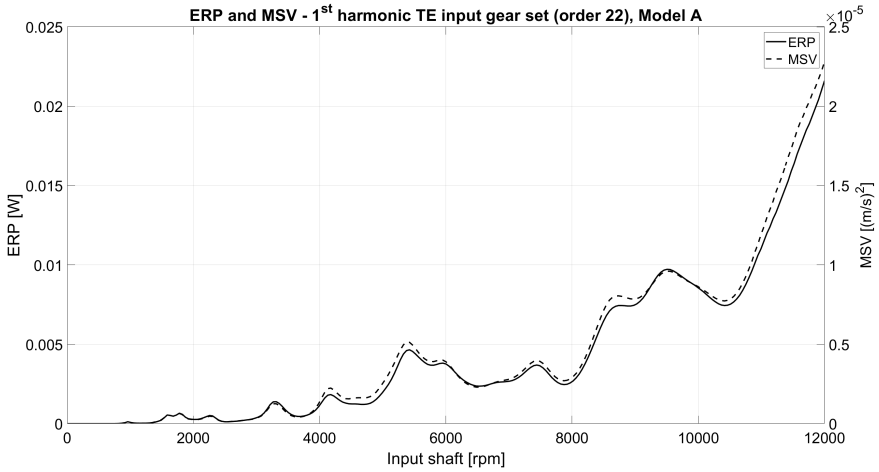

Figure 6.19: ERP and MSV, 1^{st} Harmonic TE, input gear set, Model A

Another important available response is in terms of acceleration recorded by virtual accelerometers on the housing of the gearbox, positioned as indicated by Figure 6.1. This result is significant because the vibration of the housing will lead to a certain amount of noise and vibration that propagate through an airborne path. Moreover, effectively positioning the accelerometers all around the housing can really help in the understanding of the directivity of the propagated sound.

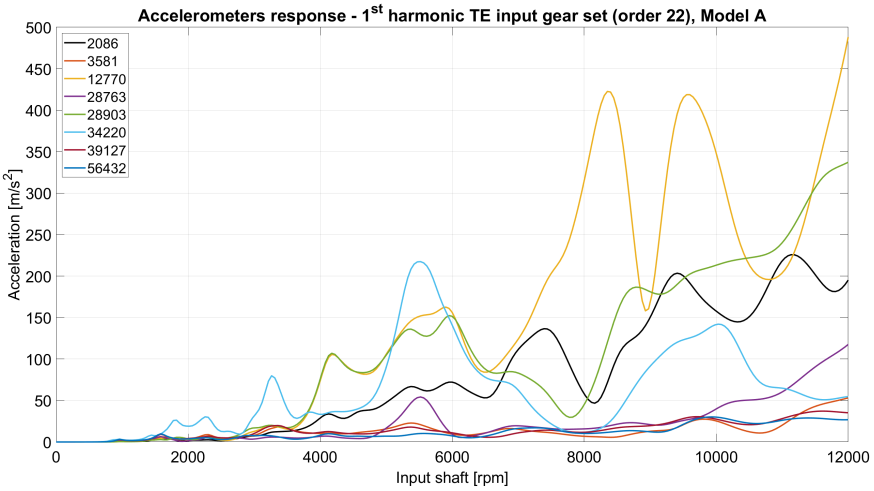

Figure 6.20: Accelerometers response, 1^{st} Harmonic TE, input gear set, Model A

Looking at Figure 6.20, there are few nodes that record pretty high values of acceleration, such as 12770, 28903, 2086: these are the nodes closest to the input gear set. Moreover, three main peaks can be detected, at about 5500 rpm, 8400 rpm and 9500 rpm. In particular, at $\approx$ 5500 rpm the highest peak is at node 34220. The highest peaks reach more than 400 m/s^2, which is a quite considerable value. Then, the accelerometers at nodes 3581, 56432, 28763, 39127 record a pretty flat response.
Focusing more on the structure borne noise, the acceleration response at housing mounts is crucial to be investigated.

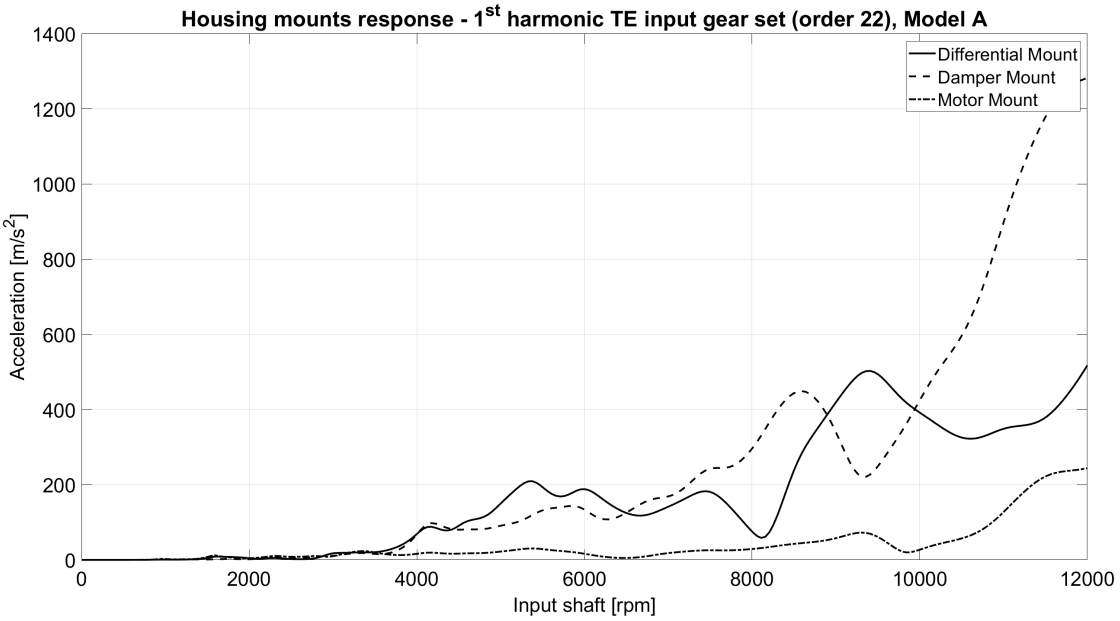

Figure 6.21: Acceleration response at housing mounts, 1^{st} Harmonic TE, input gear set, Model A

Investigating Figure 6.21, it results that all housing mounts shows a response, in terms of acceleration, with a general increasing trend with the rotational speed of the input shaft. Moreover, at the motor mount response the lowest values are recorded, whilst at the damper mount the highest. This outcome is not surprising, since the damper mount is the closest one to the input gear set, i.e. the considered excitation source. Please remind the housing mounts position, indicated in Figure 6.2.

6.3.2 Excitation: 1^{st} Harmonic transmission error output gear set, Order 9.138

Now let's consider another excitation source: the first harmonic of the TE of the output gear set. In this case, the plot of the linear dynamic TE along the input shaft speed range becomes the following (Figure 6.22), while the ERP and MSV plot is represented in Figure 6.23.

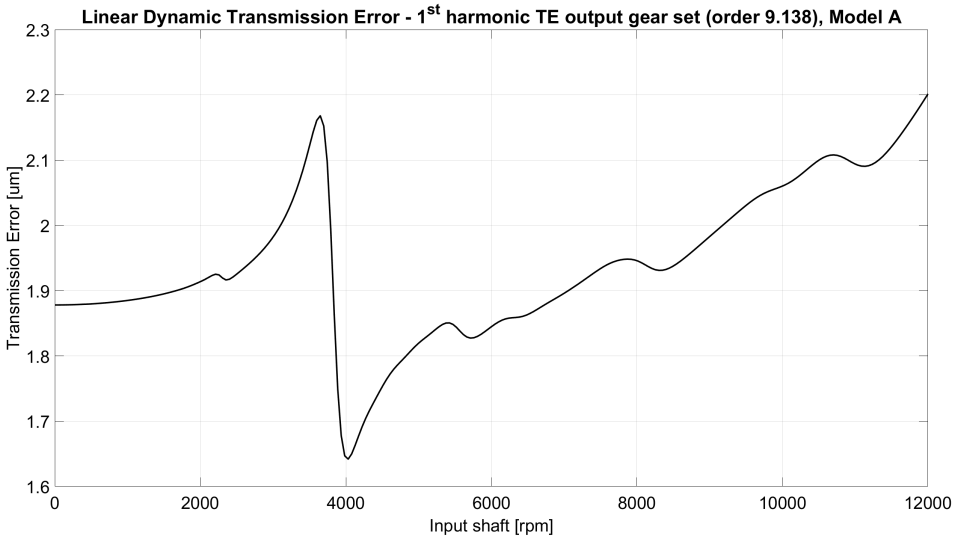

Figure 6.22: Linear dynamic transmission error - Output gear set, Model A

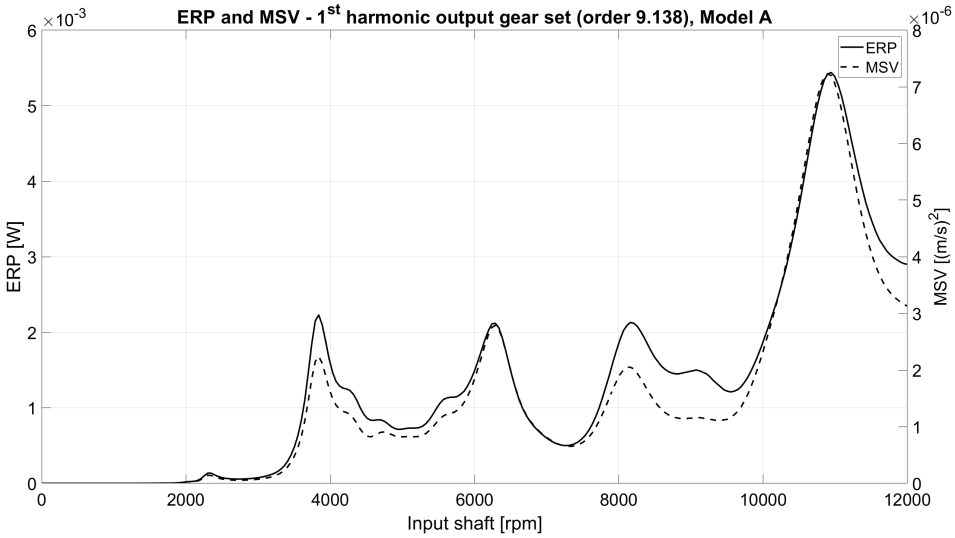

Figure 6.23: ERP and MSV, 1^{st} Harmonic TE, output gear set, Model A

Comparing Figure 6.19 and 6.23, it is clear that the input gear set leads to a remarkably higher response than the output one, this is somehow expected since the amplitude of the first order harmonic of the input gear set is higher than the one of the output gear set.

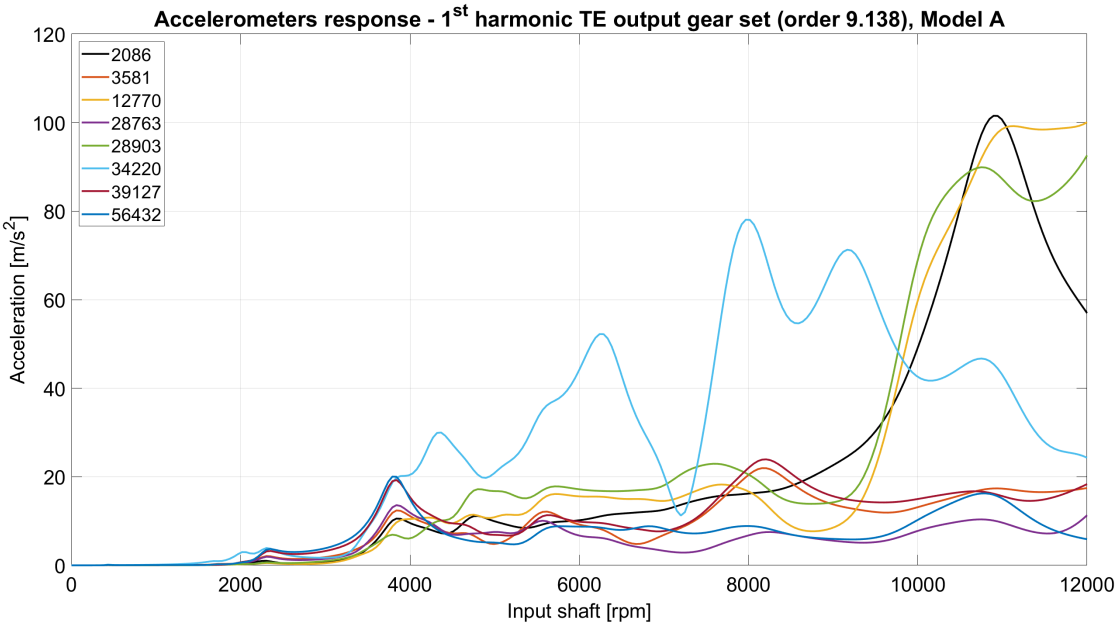

Figure 6.24: Accelerometers response, 1^{st} Harmonic TE, output gear set, Model A

Considering this excitation, the highest acceleration response is at nodes 2086, 28903, 12770, which show a relevant peak at about 1100 rpm. These are exactly the same nodes in which the highest acceleration were recorded even considering the input gear set.
Moreover, also the node 34220 has a remarkable response, even at lower shaft speeds, especially in the range $8000 \div 9000\ rpm$.
Considering the TE of output gear set (Figure 6.25), the response at housing mounts is significantly lower with respect to the input gear set. Furthermore, the housing mount which records the highest value of acceleration is the differential one in this case. Even in this case, i.e. output gear set, the motor mount shows a significantly lower response along the whole range.

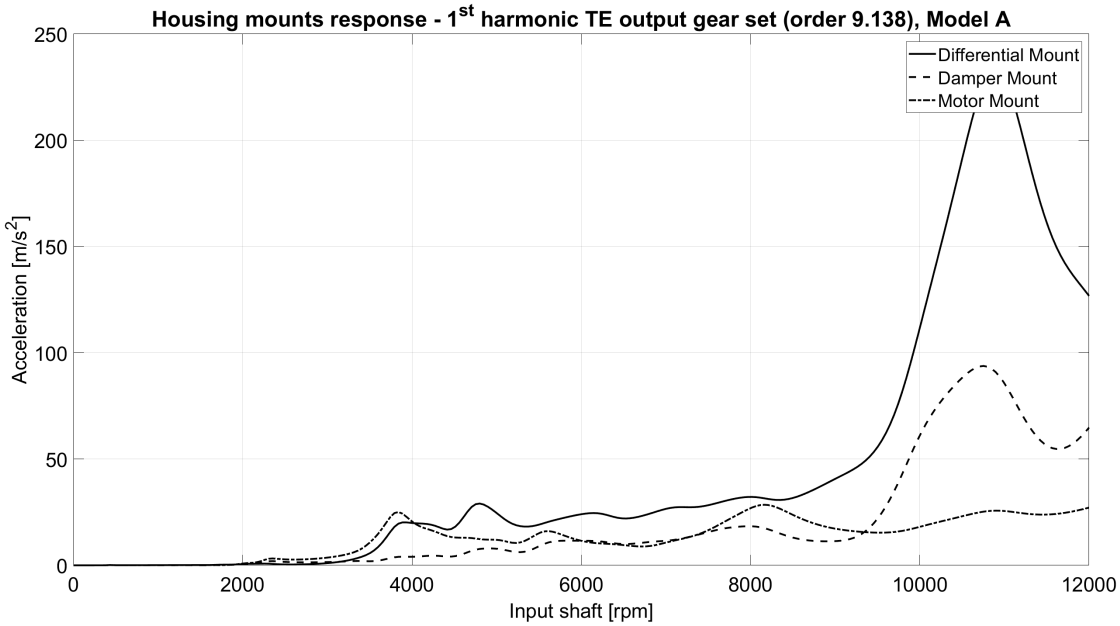

Figure 6.25: Acceleration response at housing mounts, 1^{st} Harmonic TE, output gear set, Model A

6.3.3 Excitation: 1^{st} Harmonic Unbalance, Order 1

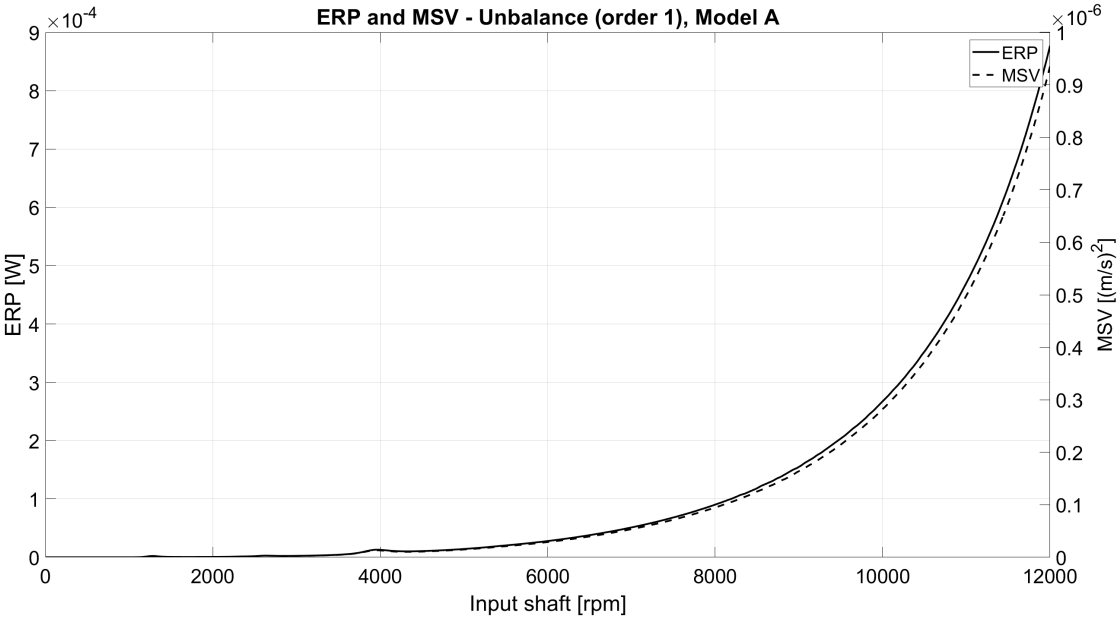

Figure 6.26: ERP and MSV, 1^{st} Harmonic Unbalance, Model A

Investigating the ERP and MSV plots, Figure 6.26, a growing behaviour as the shaft speed increases can be noted.

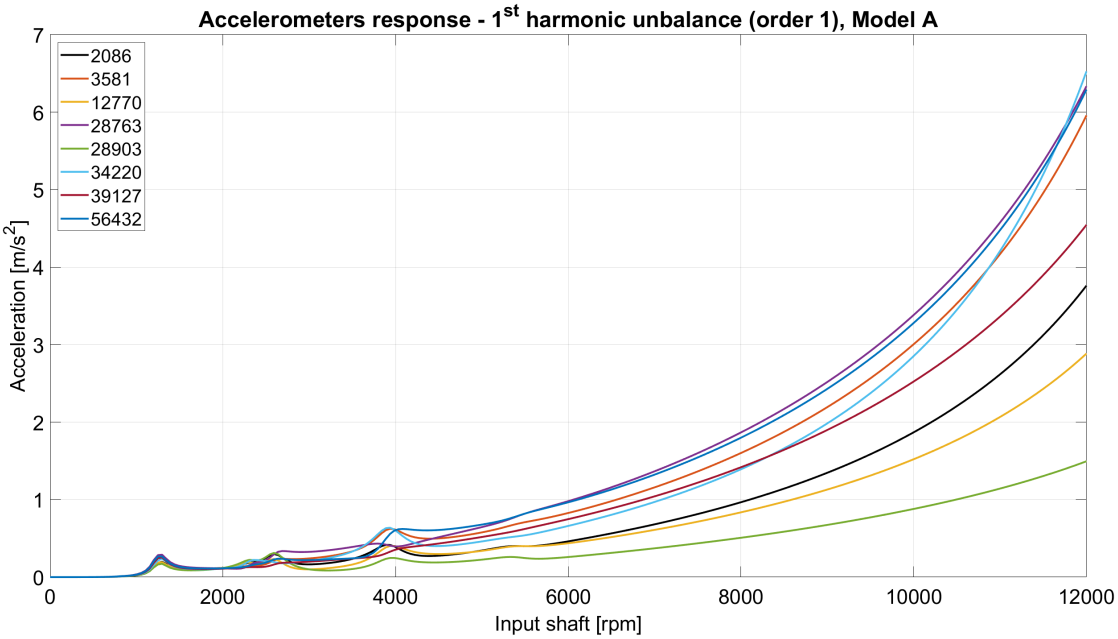

Figure 6.27: Accelerometers response, 1^{st} Harmonic Unbalance, Model A

All the accelerometers shows a similar behaviour (Figure 6.27), with the measured acceleration that increases as the shaft speed increases. The response values are all pretty low, especially considering nodes 28903 and 12770.
Moreover, looking at housing mount response (Figure 6.28), it is observable that the motor mount is the position in which the response is the highest. This is not surprising since it is the closest mount to the input shaft, i.e. the source of excitation.

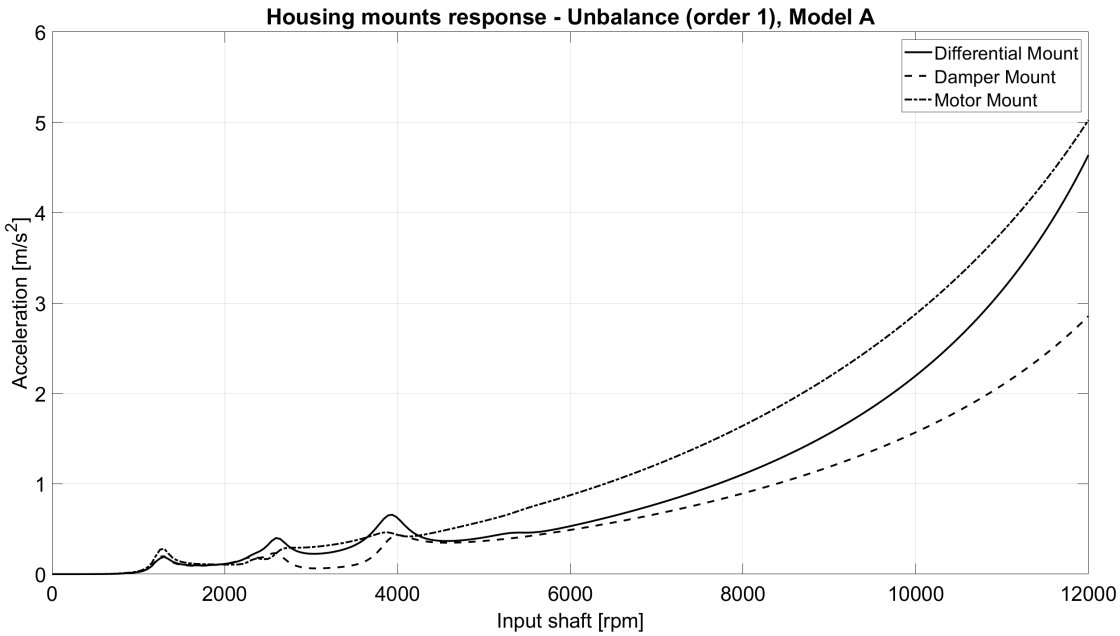

Figure 6.28: Acceleration response at housing mounts, 1^{st} Harmonic Unbalance, Model A

The response to the unbalance excitation shows a general growing behaviour as the input shaft velocity increase. This is not surprising, since the unbalance excitation is proportional to the square of the rotational speed ω, i.e. $m\epsilon\omega^2$, with m unbalance mass, ϵ eccentricity.

6.3.4 Excitation: N_{slots} Harmonic Electromagnetic Excitations, Order 48

Let's analyse the 48^{th} harmonic of the electromagnetic excitations (which in this case is the one corresponding to the number of slots of the motor, i.e. N_{slots}), even if, looking at the spectra reported in Figures 6.7-6.9, is not the order with the highest amplitude. Nevertheless, it has been selected to investigate the 48^{th} since it is representative of a very relevant vibration mode, the so called *breathing mode* of the stator-housing assembly.
Of course it is possible also to analyse even other order of harmonics, which have a higher amplitude in the spectrum. However, although the graphs are not reported below, it has been proved that the other orders lead to smaller response. Hence, the choice to report the analyses just concerning the 48^{th} harmonic is appropriate.

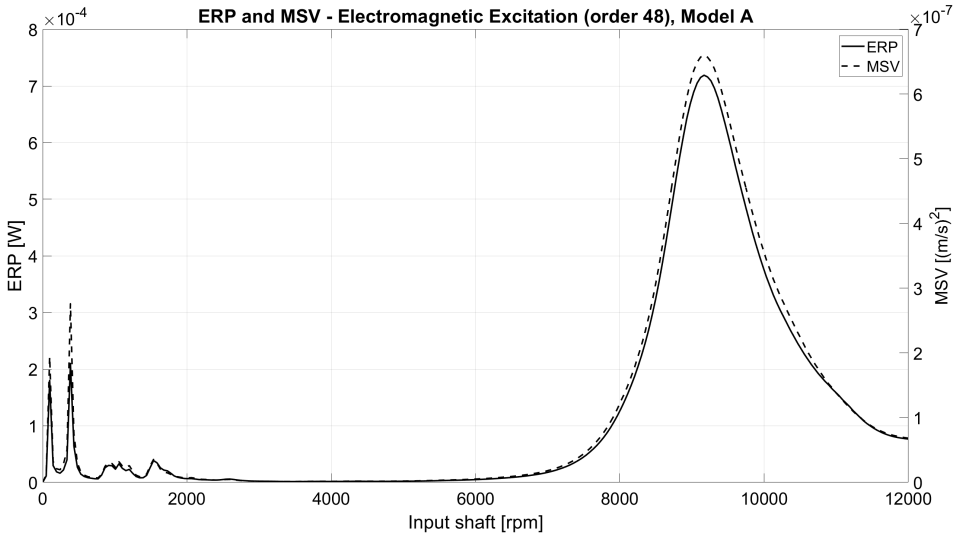

Figure 6.29: ERP and MSV, 1^{st} Harmonic 48^{th} Harmonic Electromagnetic Excitation, Model A

Examining Figure 6.29, two small peaks are evident at very low shaft speed, while the most relevant peak is slightly beyond 9000 *rpm*.
To further investigate the airborne noise, the accelerometers are considered.

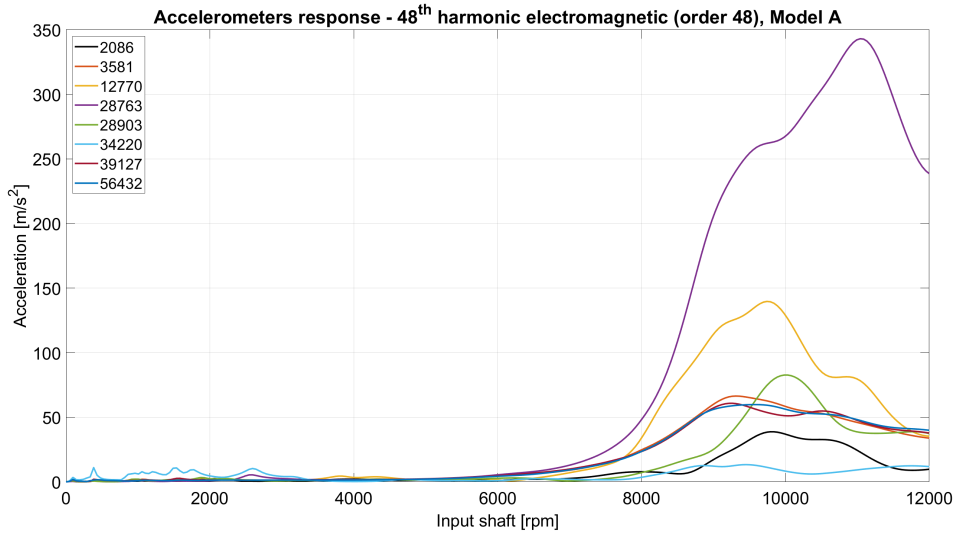

Figure 6.30: Accelerometers response, 48^{th} Harmonic Electromagnetic Excitation, Model A

The accelerometer 28763, which is the closest to the electric motor, displays a remarkably greater response with respect to other positions, reaching a peak value

of almost 350 m/s^2. Moreover, remembering the position of node 28763 in the housing, Figure 6.1, it is possible to have an initial clue about the directivity of the sound caused by the 48^{th} harmonic of the electromagnetic excitation.

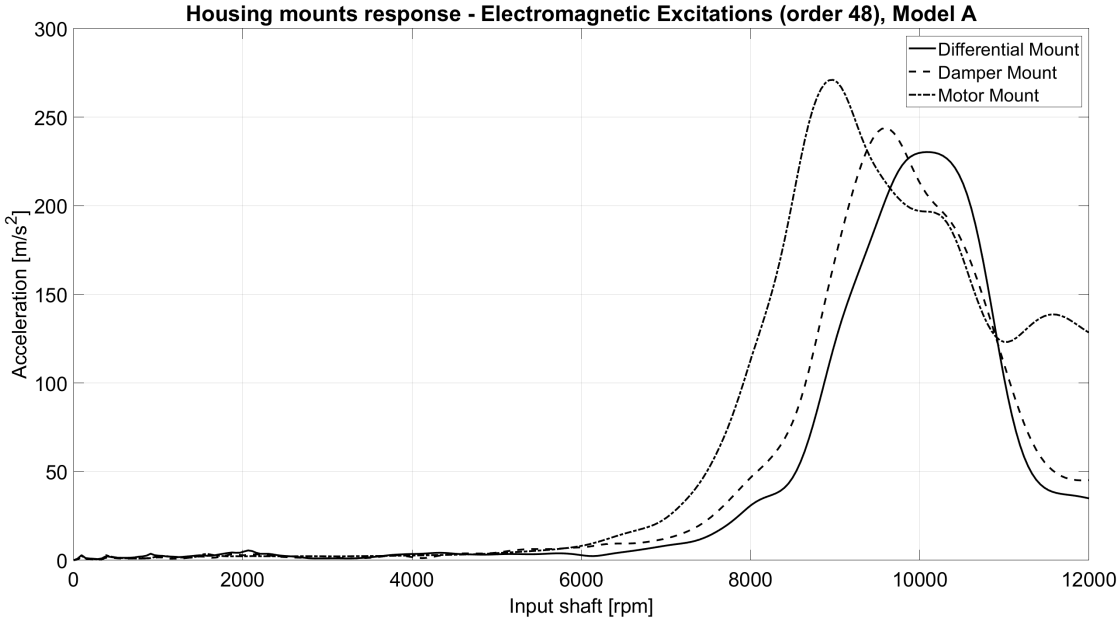

Figure 6.31: Acceleration response at housing mounts, 48^{th} Harmonic Electromagnetic Excitation, Model A

Considering the acceleration response at housing mounts, three peaks can be easily detected:

Response	Peak Value (m/s^2)	Speed (rpm)	Frequency (Hz)
Motor Mount	271.0	8976	7180.8
Damper Mount	243.9	9600	7680
Differential Mount	230.3	10080	8064

Table 6.3: Peak values, Housing mounts response to 48^{th} harmonic electromagnetic excitation, Model A

The peaks are hence characterize by quite high values of frequency. Moreover, as expected, the highest response is obtained in correspondance of motor mount, since it is the closest to the electric motor, i.e. the considered source.

6.3.5 Comparison among excitations

To compare the effects of the different excitations has a crucial importance. Indeed, knowing which excitation is the most critical, then the proper optimization can be performed.
First of all, to compare the airborne noise, it is possible to compare the values of ERP and MSV, as shown in Figure 6.32.

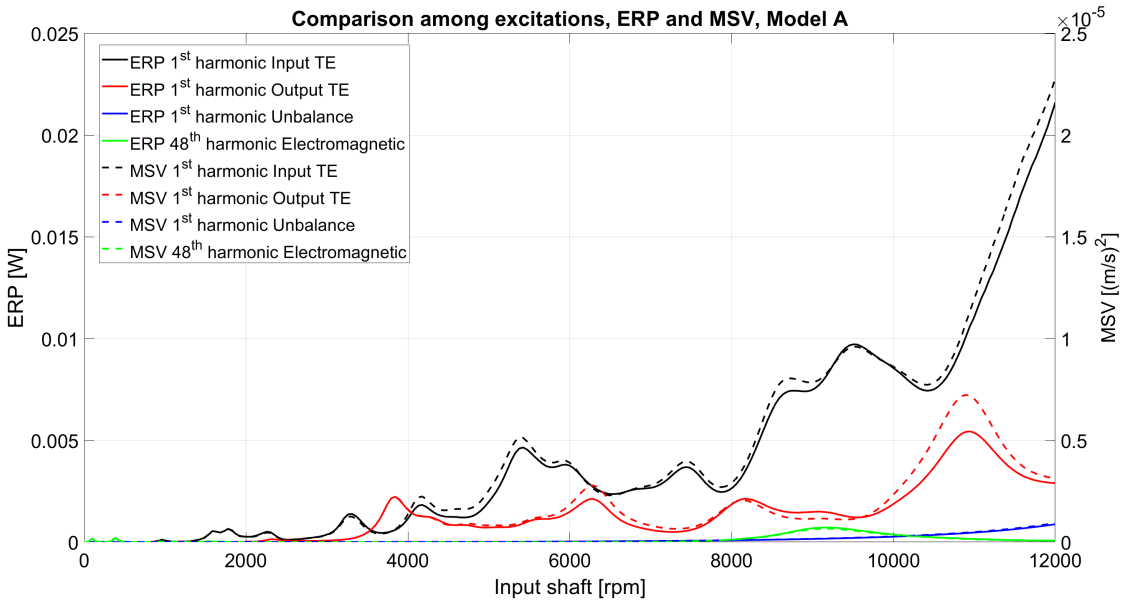

Figure 6.32: Comparison among excitations, ERP and MSV, Model A

A more detailed comparison of the actual ERP values is provided by Table 6.4. In particular, four different peaks have been investigated:

- Peak at 9504 rpm: speed of the most relevant peak considering 1^{st} harmonic input TE.
- Peak at 10944 rpm: speed of the most relevant peak considering 1^{st} harmonic output TE.
- Peak at 9168 rpm: speed of the most relevant peak considering 48^{th} harmonic electromagnetic.
- Peak at 12000 rpm: speed of the most relevant peak considering 1^{st} harmonic unbalance.

Furthermore, for each peak, also the values due to the other excitations are reported in order to make a more effective comparison.

Notice that, concerning the ERP caused by 1^{st} harmonic input TE, as peak has not been chosen the actual highest value at 12000 rpm, since it is a very extreme working condition, on the contrary the peak at 9504 rpm is more realistic to happen and can be more annoying.
Even the value in frequency is provided, recalling that to move from rpm to Hz is necessary to compute: frequency [Hz] = (shaft speed [rpm] · order of harmonic)/60. Table 6.4 confirms that the unbalance and the electromagnetic excitations cause very low response, at least one order of magnitude smaller with respect to the transmission error.

Excitation	Speed (rpm)	Frequency (Hz)	Value (W)
1^{st} harmonic input TE	9504	3484.8	$9.7 \cdot 10^{-3}$
	10944	4012.8	$1.1 \cdot 10^{-2}$
	9168	3361.6	$8.1 \cdot 10^{-3}$
	12000	4400	$2.2 \cdot 10^{-2}$
1^{st} harmonic output TE	9504	1447.5	$1.2 \cdot 10^{-3}$
	10944	1666.8	$5.4 \cdot 10^{-3}$
	9168	1396.3	$1.5 \cdot 10^{-3}$
	12000	1827.7	$2.9 \cdot 10^{-3}$
N_{slots} harmonic electromagnetic	9504	7603.2	$6.1 \cdot 10^{-4}$
	10944	8755.2	$4.5 \cdot 10^{-4}$
	9168	7334.4	$7.2 \cdot 10^{-4}$
	12000	9600	$7.6 \cdot 10^{-5}$
1^{st} harmonic unbalance	9504	158.4	$2.0 \cdot 10^{-4}$
	10944	182.4	$1.6 \cdot 10^{-4}$
	9168	152.8	$1.7 \cdot 10^{-4}$
	12000	200.0	$8.8 \cdot 10^{-4}$

Table 6.4: Comparison ERP values among different excitation, Model A

Obviously, it is meaningful to compare even the acceleration response at virtual accelerometers. Due to the large number of available virtual accelerometers, the contrast is performed only considering the most significant nodes. In particular, concerning the TE of both gear set, the greatest response, as highlighted in the previous pages, is recorded at nodes 2086, 28903, 12770 and 34220, whilst, considering the electromagnetic excitation, the most relevant is by far the node 28763. The unbalance, regardless of the considered node, shows an extremely smaller response. To execute a more effective analogy, please refer to Figure 6.33.

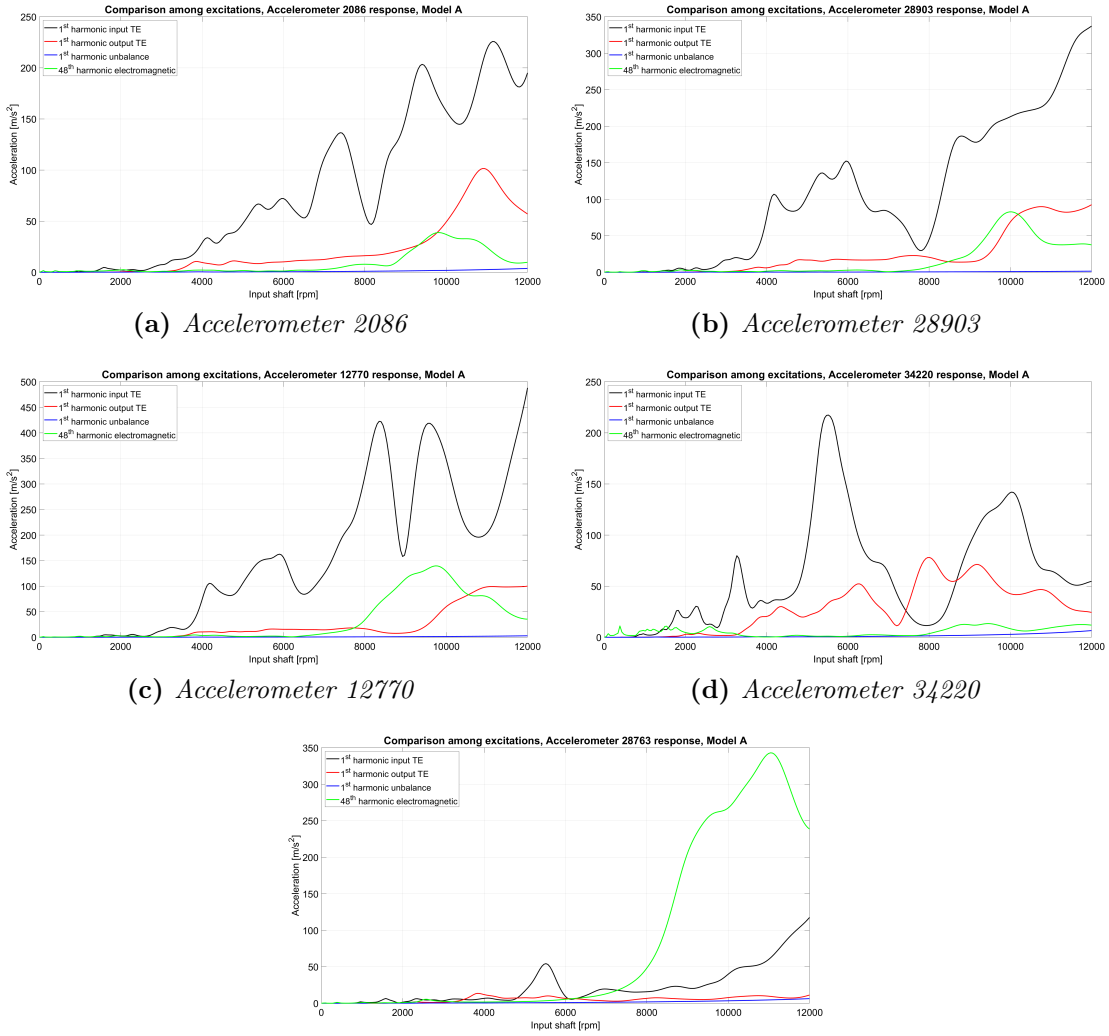

(a) *Accelerometer 2086*

(b) *Accelerometer 28903*

(c) *Accelerometer 12770*

(d) *Accelerometer 34220*

(e) *Accelerometer 28763*

Figure 6.33: Comparison among excitations, accelerometers response, Model A

In all considered accelerometers, with the exception of node 28763, it is clear the dominance of the response caused by the input gear set; furthermore, generally the output gear set and the electromagnetic excitation induce pretty comparable acceleration.
On the other hand, the electromagnetic excitation is dominant only concerning node 28763.
Besides, the unbalance excitation is totally negligible in all cases.
Then, to compare the structure borne noise, the housing mounts responses are compared in Figures 6.34-6.36.

In Table 6.5, three peaks are reported, one for each excitation (except for the unbalance, since it causes a negligible response with respect to others).
The three peaks are pretty close one to each other in terms of rotational speed of input shaft, but it appears evident that the input TE causes the highest response at the differential mount, while the output gear set and the electromagnetic excitation lead to comparable values.
The considered peaks are the following:

- Peak at 9408 rpm: speed of the most relevant peak considering 1^{st} harmonic input TE.

- Peak at 10896 rpm: speed of the most relevant peak considering 1^{st} harmonic output TE.

- Peak at 10080 rpm: speed of the most relevant peak considering 48^{th} harmonic electromagnetic.

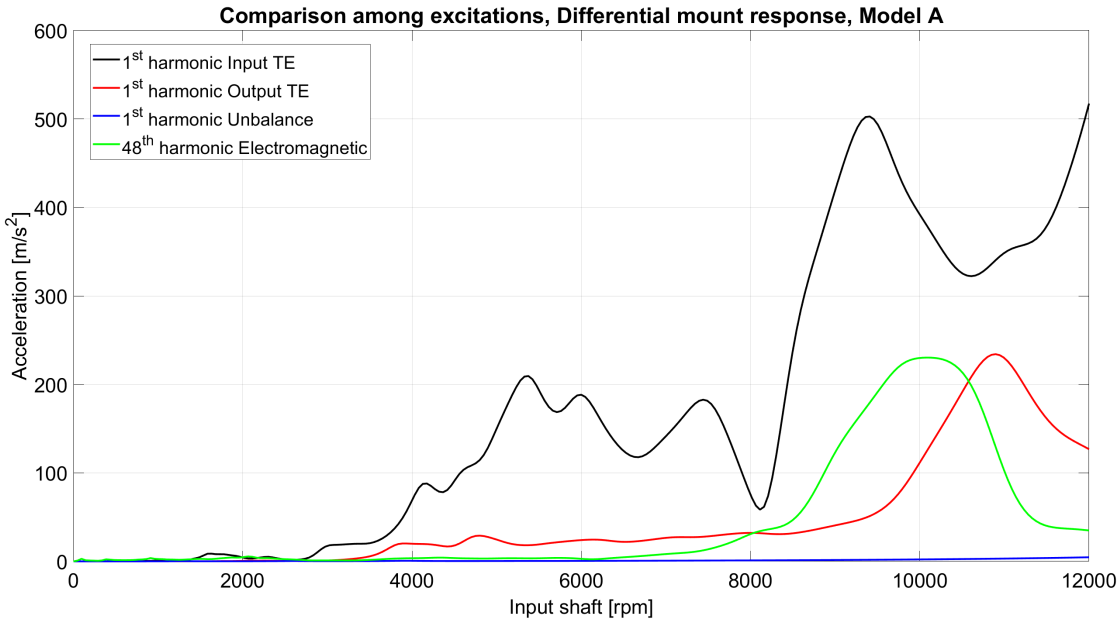

Figure 6.34: Comparison among excitations, differential mount response, Model A

Excitation	Speed (rpm)	Frequency (Hz)	Value (m/s^2)
1^{st} harmonic input TE	9408	3449.6	502.8
	10896	3995.2	340.4
	10080	3696	380.0
1^{st} harmonic output TE	9408	1432.9	51.1
	10896	1659.6	234.1
	10080	1535.3	124.1
N_{slots} harmonic electromagnetic	9408	7526.4	179.2
	10896	8716.8	129.4
	10080	8064	230.3
1^{st} harmonic unbalance	9408	156.8	1.8
	10896	181.6	3.0
	10080	168.0	2.3

Table 6.5: Comparison differential mount response among different excitation, Model A

With reference to the damper mount, the difference between the response to the input TE and the other excitations is even more significant, especially at high rotational speeds. At the maximum speed, the response to the TE of input gear set reaches a peak of 1281.9 m/s^2.
To perform a comparison of peak values, three peaks were selected:

- Peak at 8592 rpm: speed of the most relevant peak considering 1^{st} harmonic input TE.
- Peak at 10752 rpm: speed of the most relevant peak considering 1^{st} harmonic output TE.
- Peak at 9600 rpm: speed of the most relevant peak considering 48^{th} harmonic electromagnetic.

Excitation	Speed (rpm)	Frequency (Hz)	Value (m/s^2)
1^{st} harmonic input TE	8592	3150.4	449.2
	9600	3520	279.8
	10752	3942.4	724.8
1^{st} harmonic output TE	8592	1308.6	12.3
	9600	1462.2	27.8
	10752	1637.6	93.8
N_{slots} harmonic electromagnetic	8592	6873.6	90.4
	9600	7680	243.9
	10752	8601.6	148.0
1^{st} harmonic unbalance	8592	143.2	1.1
	9600	160.0	1.4
	10752	179.2	1.9

Table 6.6: Comparison damper mount response among different excitation, Model A

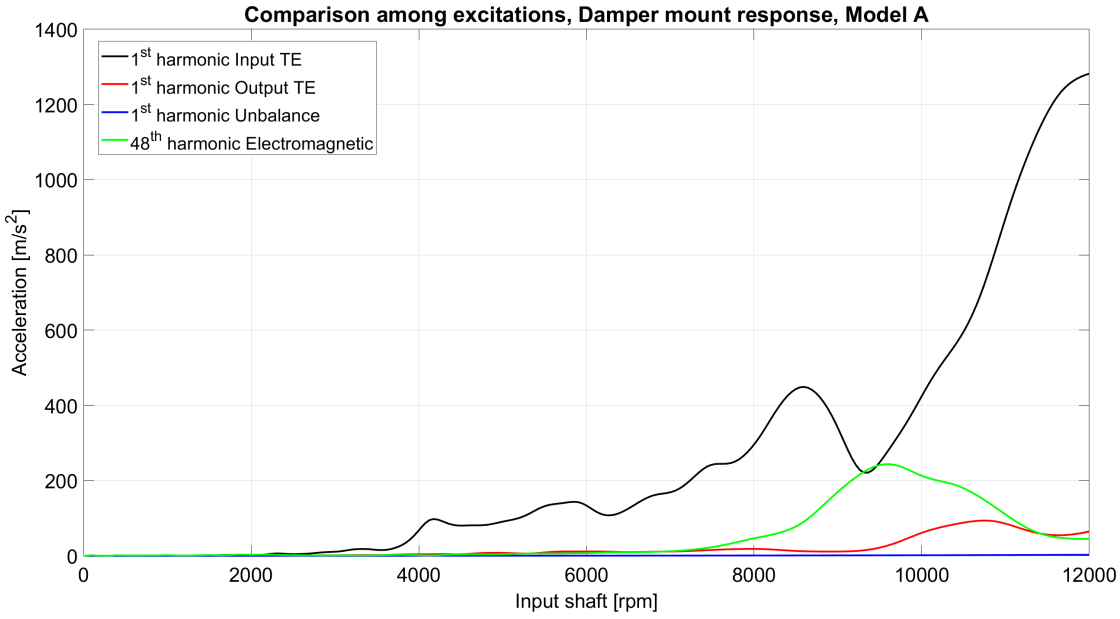

Figure 6.35: Comparison among excitations, damper mount response, Model A

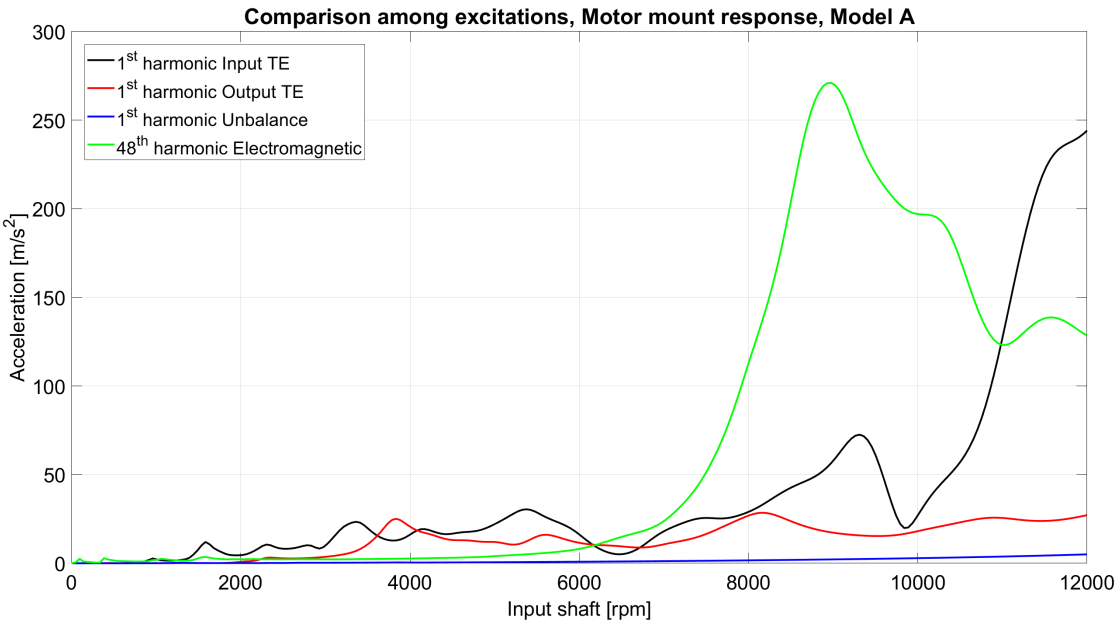

Figure 6.36: Comparison among excitations, motor mount response, Model A

Concerning the motor mount, three rotational speeds have been investigated more in details:

- Peak at 9312 rpm: speed of a relevant peak considering 1^{st} harmonic input TE.
- Peak at 12000 rpm: speed of the highest value of the response to 1^{st} harmonic input TE.
- Peak at 8976 rpm: speed of the most relevant peak considering 48^{th} harmonic electromagnetic.

Excitation	Speed (rpm)	Frequency (Hz)	Value (m/s^2)
1^{st} harmonic input TE	8976	3291.2	56.5
	9312	3414.4	72.5
	12000	4400	244.1
1^{st} harmonic output TE	8976	1367.1	17.4
	9312	1481.2	15.7
	12000	1827.7	27.2
N_{slots} harmonic electromagnetic	8976	7180.8	271.0
	9312	7449.6	238.6
	12000	9600	128.4
1^{st} harmonic unbalance	8976	149.6	2.2
	9312	155.2	2.4
	12000	200.0	5.0

Table 6.7: Comparison motor mount response among different excitation, Model A

Considering the motor mount, the 48^{th} of the electromagnetic excitation causes the highest response, while the output gear set TE causes a pretty flat response, without relevant peaks.
Investigating at the above tables, 6.4-6.7, it is noticeable how the peaks reached considering the 1^{st} harmonic of the input TE are in a pretty critical frequency range, i.e. about 3000 and 4000 Hz. The normal audiogram, reported in Figure 1.1, clearly shows that these values of frequency (about 3 and 4 kHz) are the ones to which the human's ear is particularly sensitive. This means that this produced noise can be really annoying. On the other hand, the unbalance causes noise at low frequency, which Figure 1.1 indicates as not that disturbing: the human's ear is less sensitive at low frequency.
Looking at comparison plots, it appears clear that the unbalance excitation leads to way smaller responses with respect to transmission error and electromagnetic excitation. Moreover, considering Model A, the 1^{st} harmonic of the TE of the input gear set is the excitation which causes the highest response in terms of vibration and noise. However, even the 48^{th} harmonic of electromagnetic excitations lead to not negligible responses. Therefore, it is possible to act both on the transmission error and on the electromagnetic excitations in order to enhance the NVH performance. First of all, a sensitivity analysis is carried out focusing more on the transmission system excitation (i.e. TE), and only later more considerations concerning the electromagnetic excitations will be provided.

Hence, in order to try to optimize the NVH performance caused by excitation originated by the transmission system, it is important to investigate the Models B and C.

6.4 Model B, spur gears with profile shift

Please keep in mind the moving from Model A to B, the only difference is that in Model B the profile shifting is added, but the gears are still spur gears.
Obviously, no major changes concerning the response to unbalance and electromagnetic excitations can be noted: the results completely overlap (for the sake of brevity the plots are not reported here). Moreover, also considering as excitation the 1^{st} harmonic of the transmission error of the input gear set, no differences between the two models can be noted.
On the other hand, only taking into account the output gear set, modest changes can be noted moving from Model A to B, as shown in Figures 6.39, 6.40.

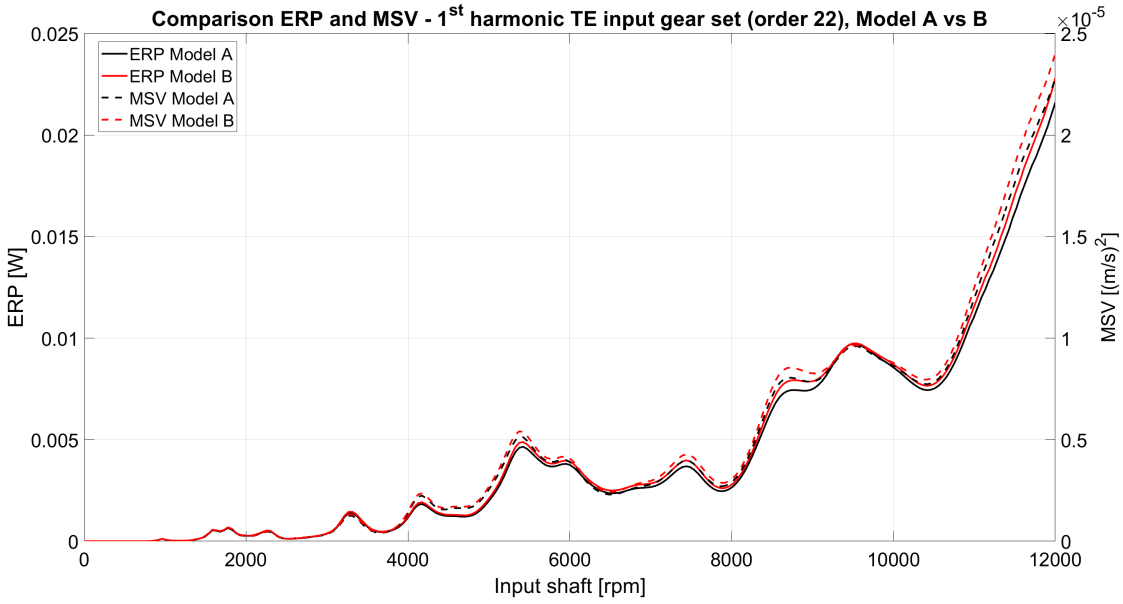

Figure 6.37: Comparison Model A vs B, ERP and MSV, 1^{st} harmonic TE input gear set

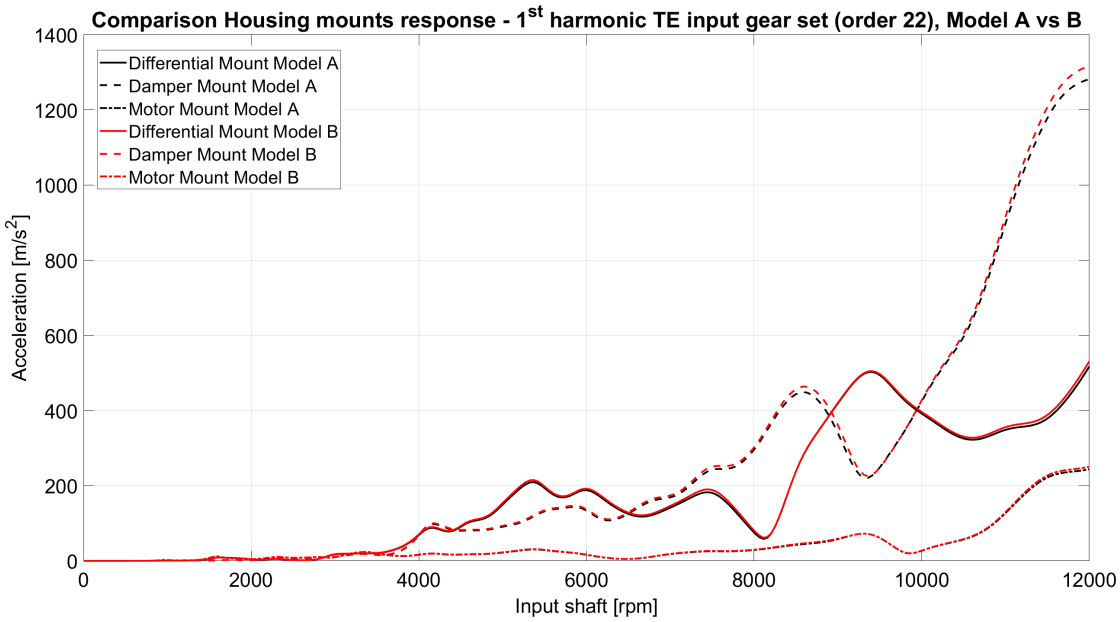

Figure 6.38: Comparison Model A vs B, housing mounts response, 1^{st} harmonic TE input gear set

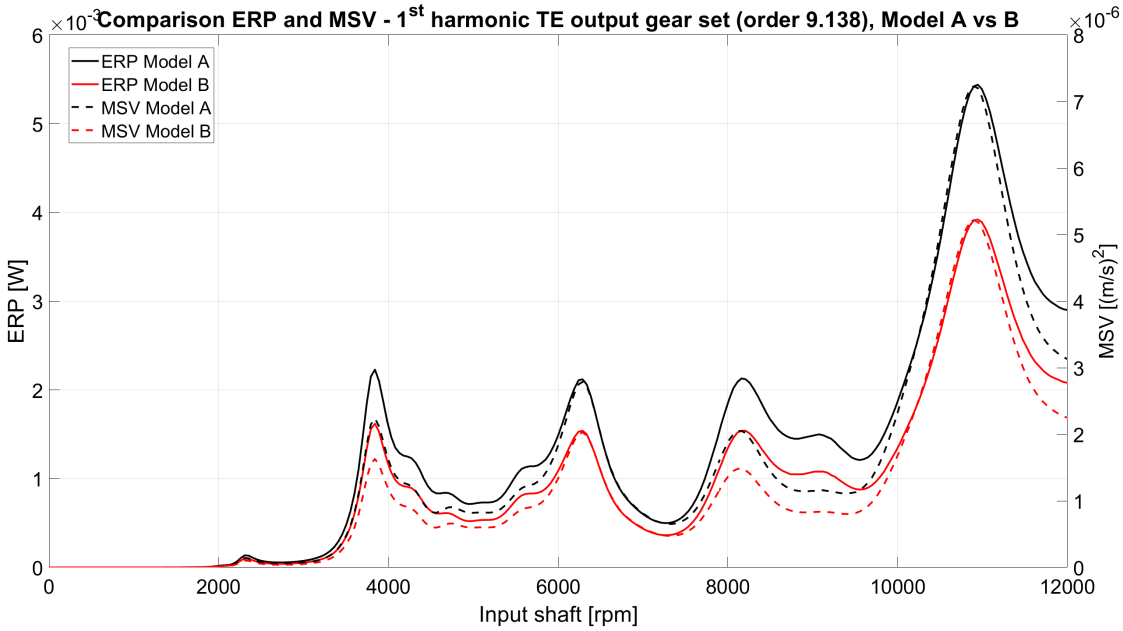

Figure 6.39: Comparison Model A vs B, ERP and MSV, 1^{st} harmonic TE output gear set

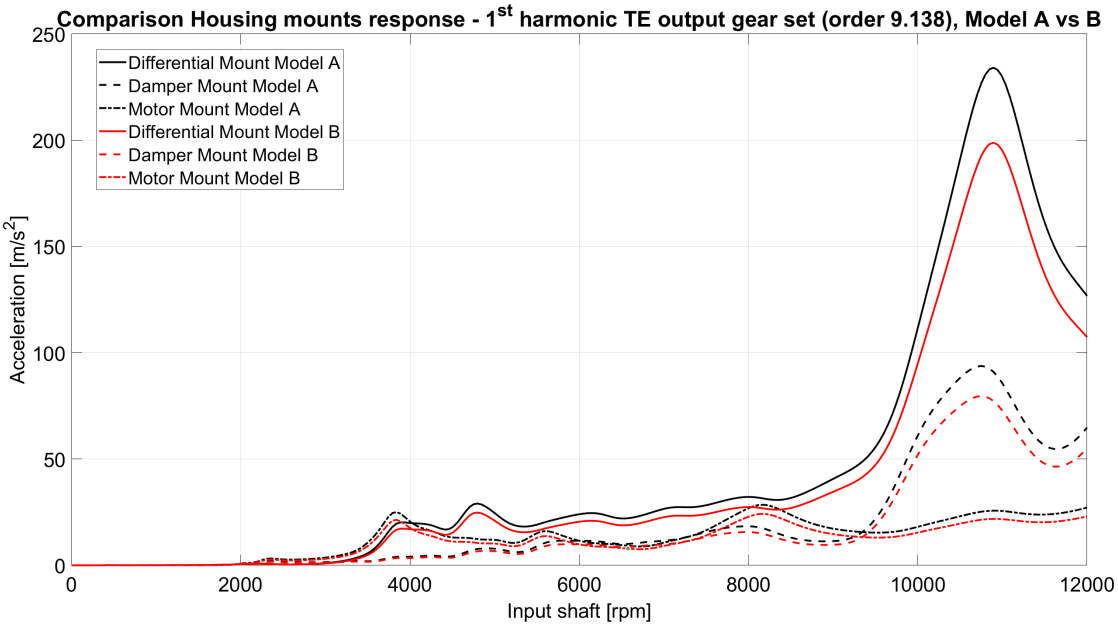

Figure 6.40: Comparison Model A vs B, housing mounts response, 1^{st} harmonic TE output gear set

As can be noted, only minor changes can be noted in the response, considering ERP, MSV or the housing mounts response. In particular, considering the TE of the input gear set, the responses almost overlap, while considering the output gear set a slight enhancement in the performance is noted moving from Model A to B. Exactly the same considerations can be done also considering the accelerometers response: the two models completely overlap considering input TE, while a modest reduction is noted as regards output TE.
However, to notice a considerable improvement, it is necessary to move to helical gears, as it will be proved in the following pages.

6.5 Model C, helical gears with profile shift

Doing a comparison between the Model B (spur gears with profile shift) and C (helical gears with profile shift), since the only difference between the two models concerns the gears, no changes can be noted considering as excitation the 48^{th} electromagnetic forces.
However, considering the unbalance as excitation, a slight difference can be noted, especially in the housing mounts response: a new peak is visible at $\approx$ 10200 rpm, as depicted in Figure 6.41. This new peak probably is caused by the presence of axial forces originated by the helix angle, which were absent in previous models.

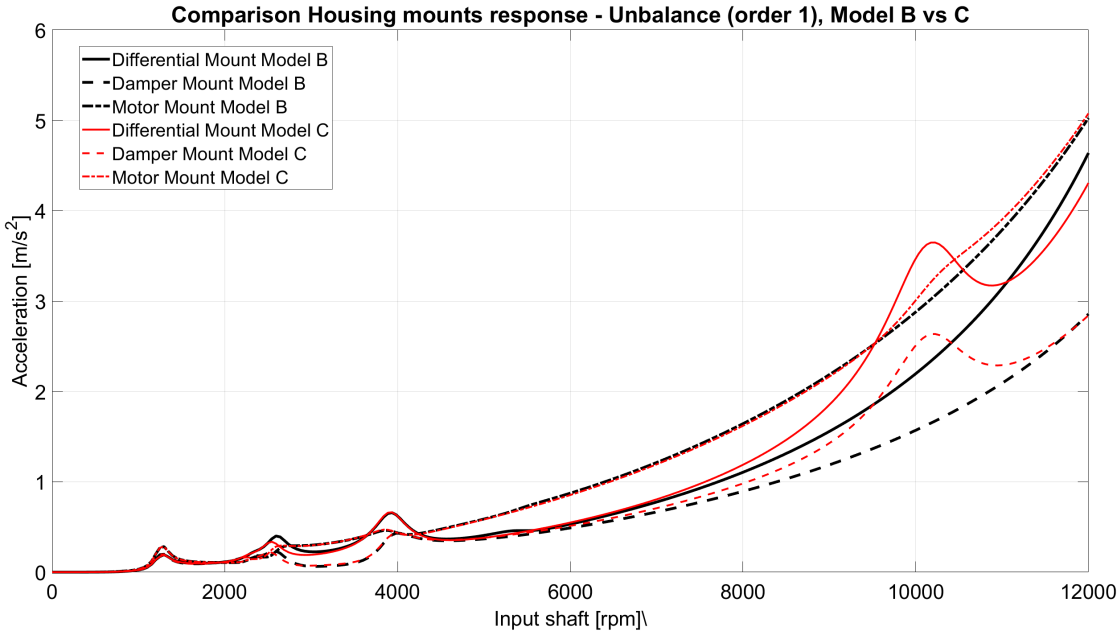

Figure 6.41: Comparison Model B vs C, housing mounts response, 1^{st} harmonic unbalance

However, the difference is really slight, and the values of the response are very small in both models.
It is way more interesting to investigate the differences in the responses due to the 1^{st} harmonic of the TE, considering both input and output gear set, Figures 6.42-6.47.
Looking at the plots, a very remarkable enhancement of the NVH performance can be noted moving to helical gears, considering both the airborne noise and the structure borne one. The improvement is really evident and it confirms the better performance of the helical gears with respect to spur ones.

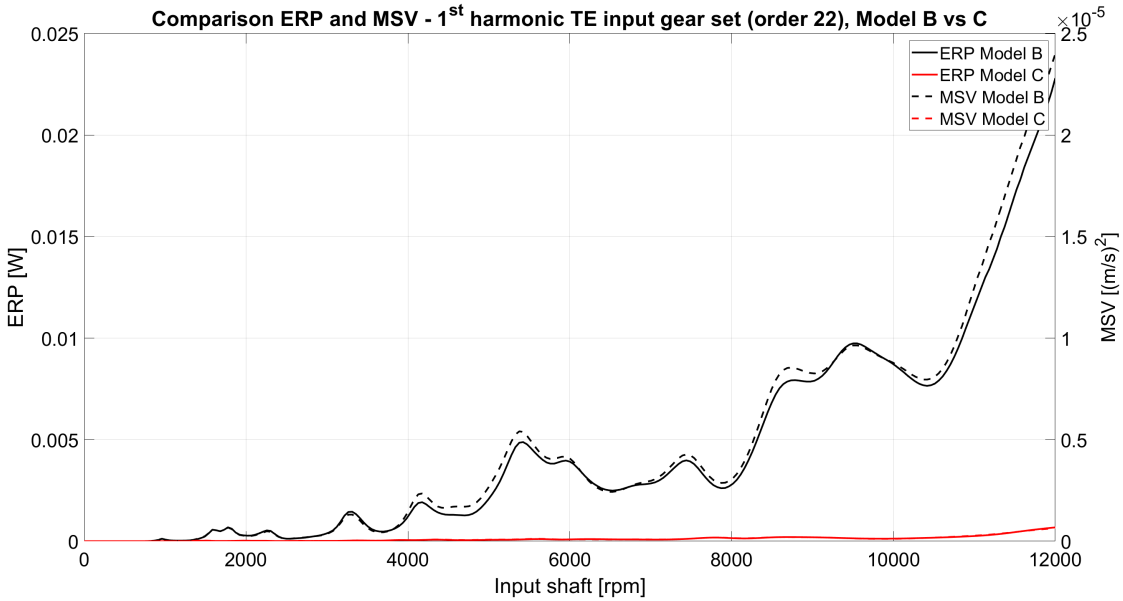

Figure 6.42: Comparison Model B vs C, ERP and MSV, 1^{st} harmonic TE input gear set

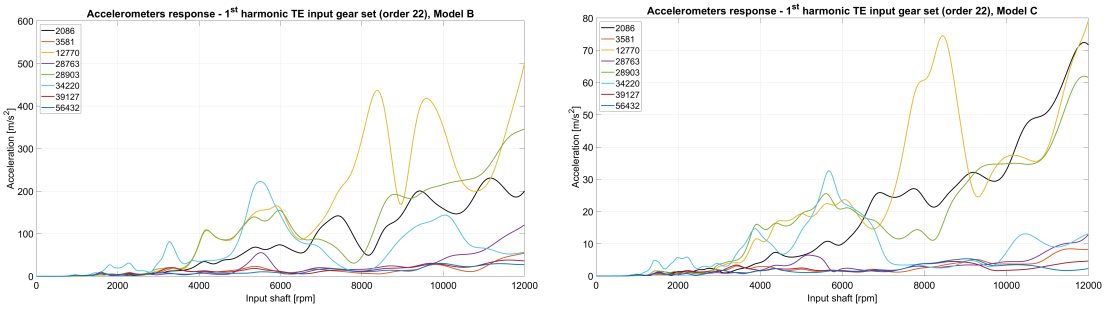

(a) *Model B* **(b)** *Model C*

Figure 6.43: Comparison Model B vs C, accelerometers response, 1^{st} harmonic TE input gear set

It is clear the improvement obtained in Model C: the highest peak of Model B is above 400 m/s^2, while in Model C it does not reach 80 m/s^2. In both models the nodes in which the recorded acceleration is greater are 2086, 12770 and 28903. The trend is pretty similar in both models, with the acceleration that increases as the shaft speed increase. However, in Model B, two peaks were present as regards node 12770, on the other hand, in Model C just one (at ≈ 8500 *rpm*). Moreover, both models show a not negligible peak just below 6000 *rpm*.

Moreover, considering the housing mounts, the improvement obtained considering Model C is evident: the response is way lower and almost negligible with respect to Model B.

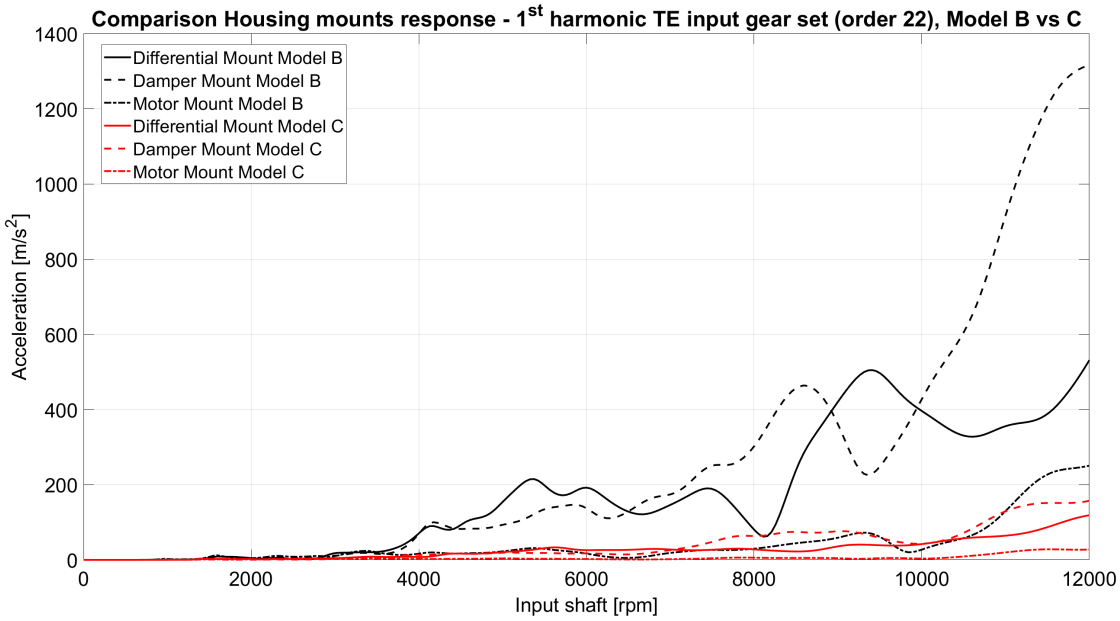

Figure 6.44: Comparison Model B vs C, housing mounts response, 1^{st} harmonic TE input gear set

Even considering the output gear set, similar outcomes are obtained: Model C (helical gears with profile shift) shows a remarkable improvement with respect to B (spur gears with profile shift), highlighting a considerably lower response, both in terms of ERP/MSV and of accelerations.

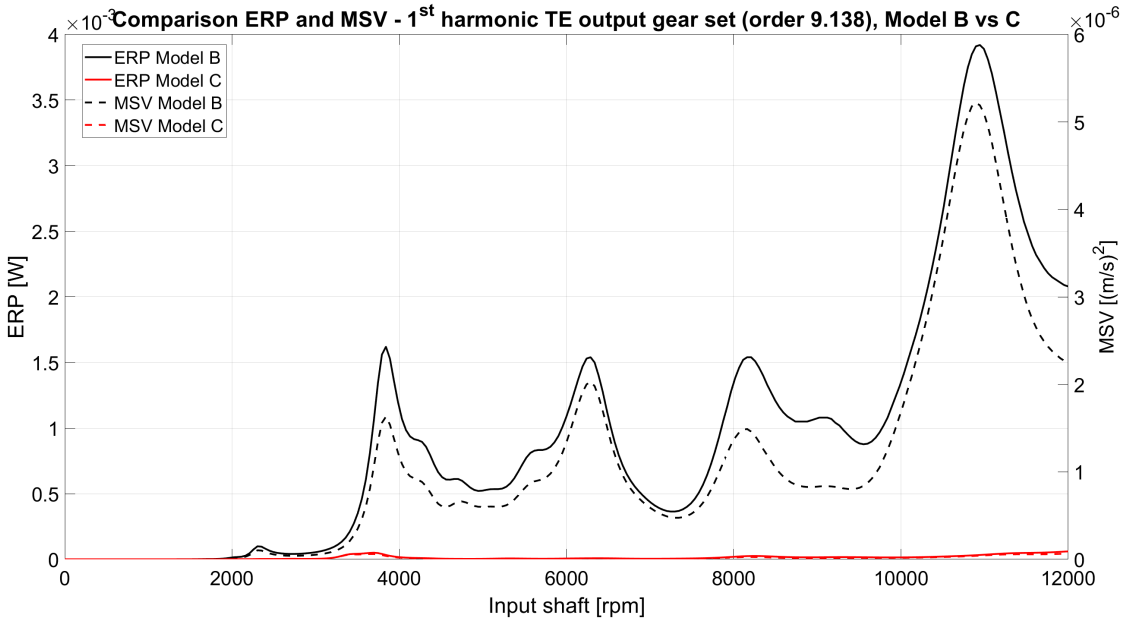

Figure 6.45: Comparison Model B vs C, ERP and MSV, 1^{st} harmonic TE output gear set

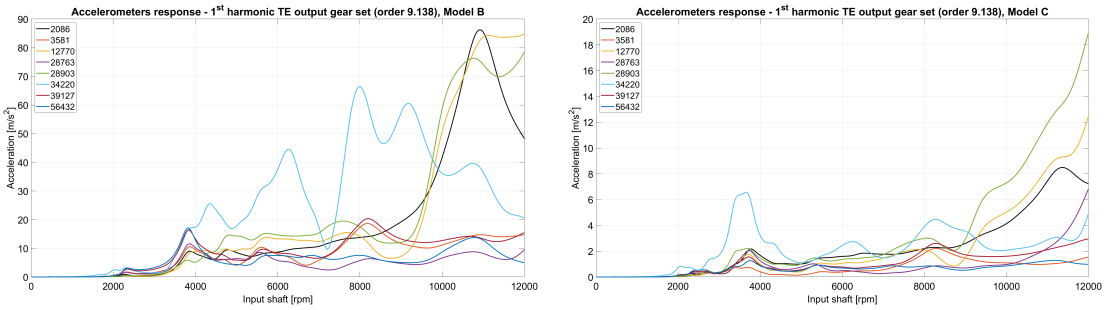

(a) *Model B* **(b)** *Model C*

Figure 6.46: Comparison Model B vs C, accelerometers response, 1^{st} harmonic TE output gear set

The reduction of response of Model C at virtual acceleromters is evident. Moreover, in Model B relevant peaks are ≈ 11000 rpm are visible, while they almost disappear in Model C. A clear peak of node 34220 is noted below 4000 rpm, but the amplitude is quite limited (just above 6 m/s^2). Considering all nodes, the magnitude of the acceleration is way smaller in Model C (the maximum does not reach 20 m/s^2).

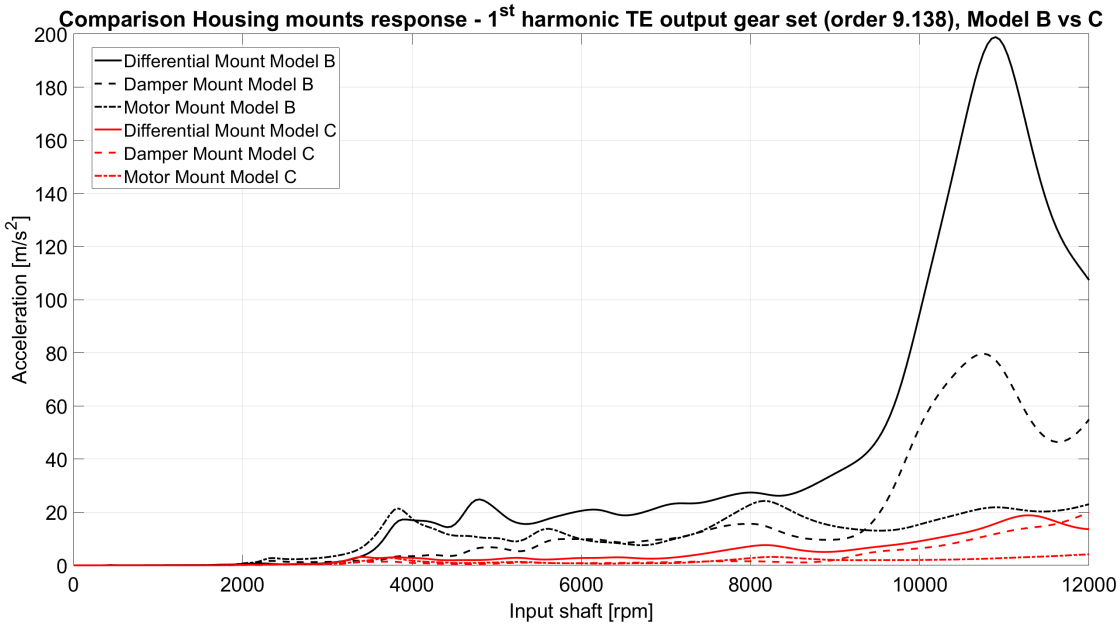

Figure 6.47: Comparison Model B vs C, housing mounts response, 1^{st} harmonic TE output gear set

At this point, having obtained a remarkable reduction of the vibration response of the gearbox caused by the 1^{st} harmonic of the TE, it can be interesting to perform again a comparison among the responses due to each kind of excitation.

6.5.1 Comparison among excitations

To perform again a comparison among the different kind of excitations can be really helpful to really perceive the improvements obtained considering the Model C.

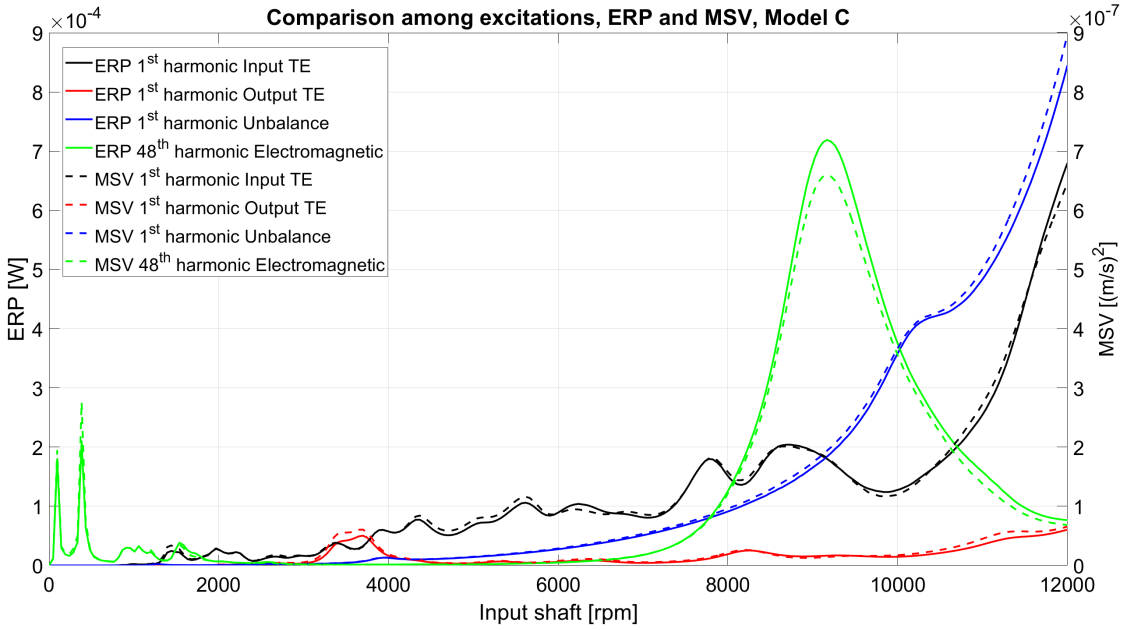

Figure 6.48: Comparison among excitations, ERP and MSV, Model C

It can be very interesting to analyse the ODS (Operating Deflection Shapes) at the main peaks, in order to really understand the deformations of the model. Looking at Figure 6.48, there are three peaks that are particularly relevant, and they are all caused by the 48^{th} harmonic of the electromagnetic excitations. In particular, the three peaks are located at 80 Hz, 320 Hz, 7320 Hz (remember that to move from rpm to Hz is necessary to multiply the value in rpm by the order of the harmonic, 48 in this case, and then divide by 60). The ODS are reported in Figures 6.49-6.51.

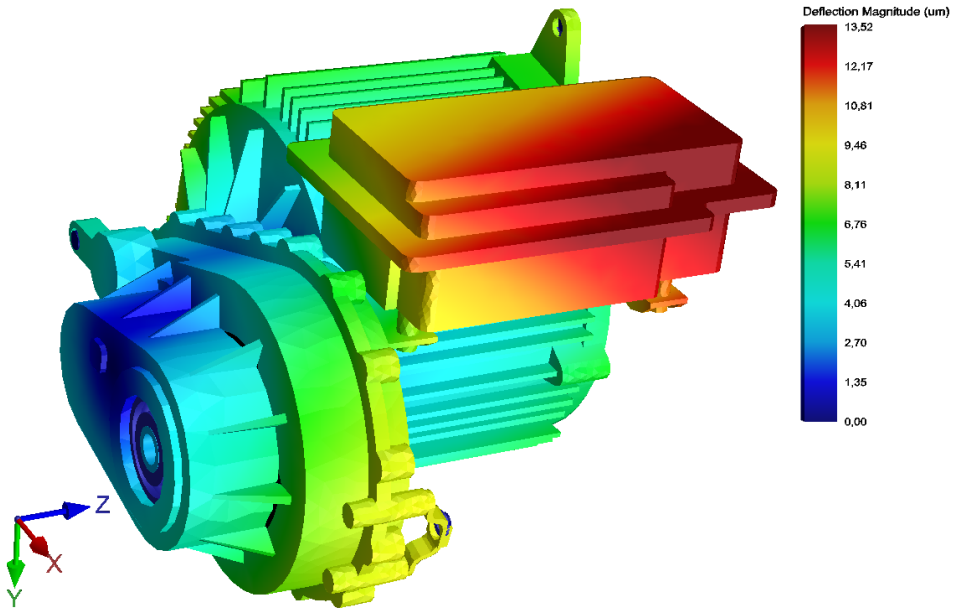

Figure 6.49: ODS at 80 Hz, Model C

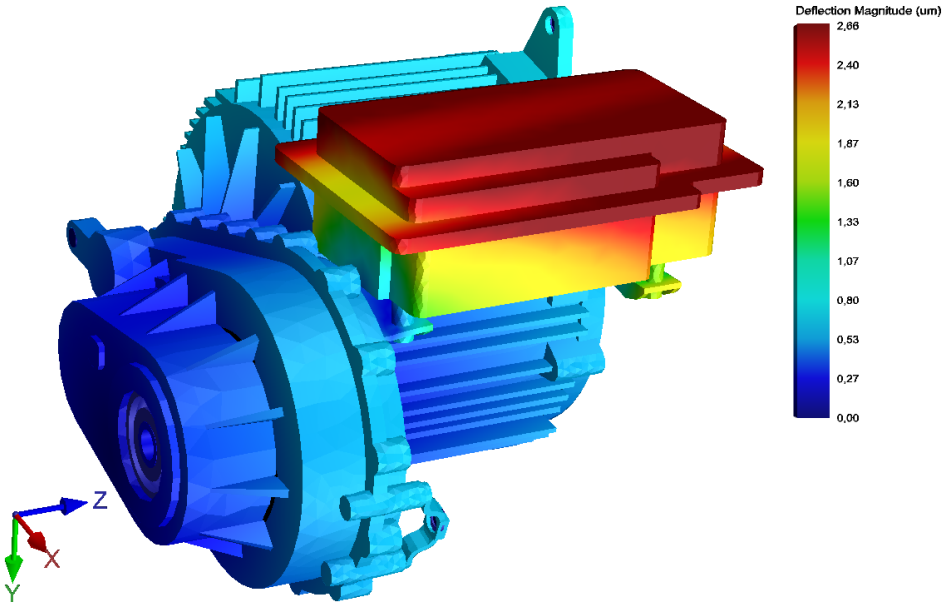

Figure 6.50: ODS at 320 Hz, Model C

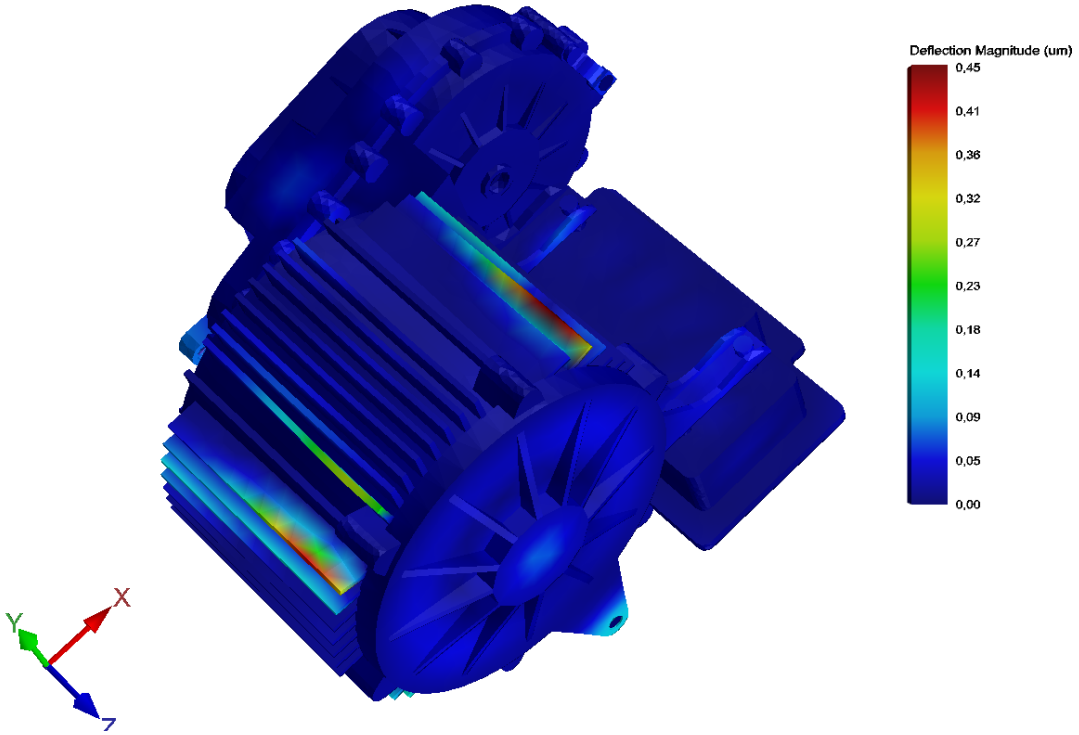

Figure 6.51: ODS at 7320 Hz, Model C

Analysing the peaks at 80 and 320 Hz, it appears evident that the deflection of the system is localized especially on the inverter case, while the rest of the system is not subjected to a too remarkable deformation.
On the other hand, looking at the highest peak in overall, the one at 7320 Hz, an important deflection of just some specific parts, similar to wings, of the housing are denoted. These deflections cause a very high equivalent radiated power, since a deflection of that point lead to a remarkable air movement, resulting in high values of sound propagated.
Obviously, is important to analyse also the accelerometers response. Exactly as in case of Model A (spur gears), the selected accelerometers for the comparison are the ones that show the highest response, i.e. 28903, 12770, 2086, 34220, 28763 (the last one is the one in which the response due to 48^{th} harmonic of electromagnetic excitation is the highest).

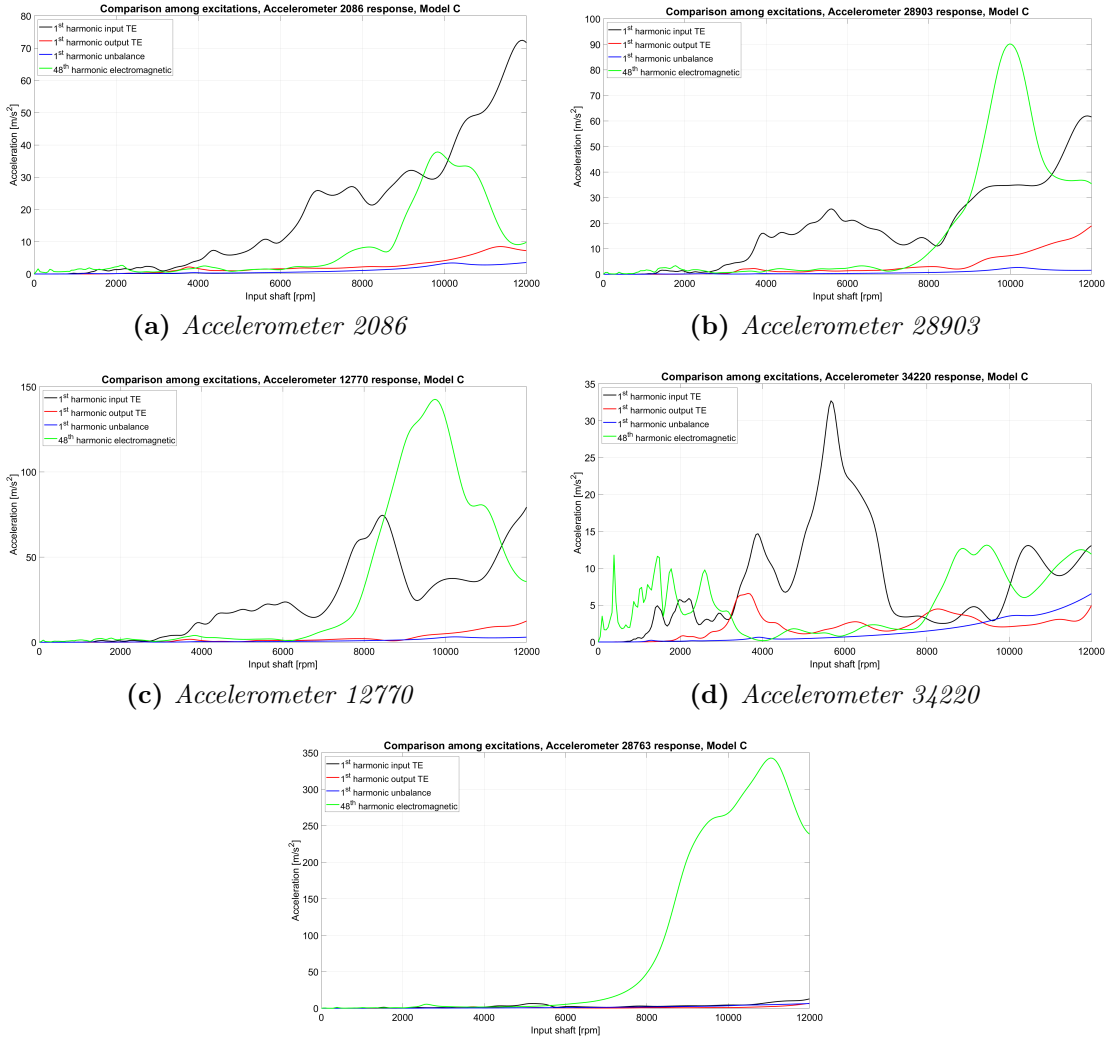

(a) *Accelerometer 2086*

(b) *Accelerometer 28903*

(c) *Accelerometer 12770*

(d) *Accelerometer 34220*

(e) *Accelerometer 28763*

Figure 6.52: Comparison among excitations, accelerometers response, Model C

The first observation is that, investigating Figure 6.52, the output TE and the unbalance provoke negligible accelerations with respect to input gear set and electromagnetic excitation. On the other hand, the 1^{st} harmonic of the input TE and the 48^{th} of the electromagnetic excitation lead to similar amplitudes of acceleration, with the exception of node 28763, in which is evident the predominance of the electromagnetic excitation.
Further analysing the responses caused by the 1^{st} harmonic of the input TE, from Figure 6.52, two peaks clearly stand out among the others: peak at 2080 Hz considering accelerometer 34220 and at 3080 Hz regarding accelerometer 12770.

Hence, it can be interesting to visualize the ODS of these two velocities.

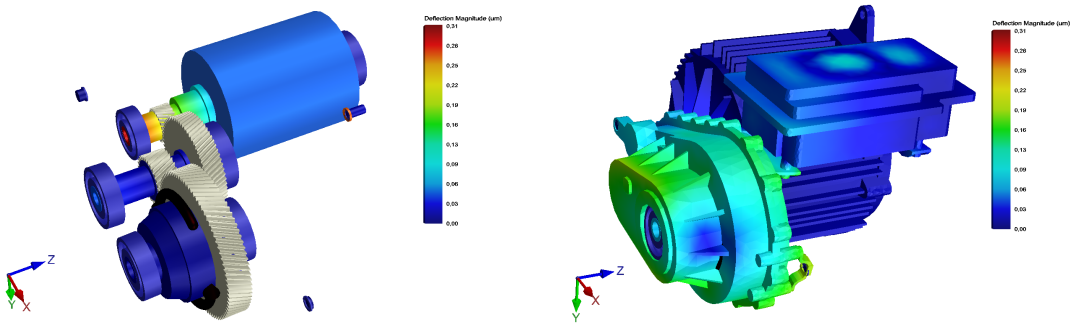

(a) *Without housing* **(b)** *With housing*

Figure 6.53: ODS at 2080 Hz, Model C

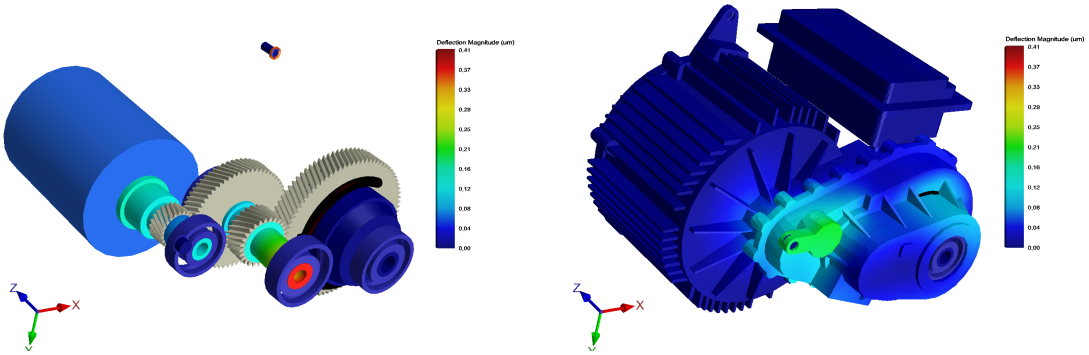

(a) *Without housing* **(b)** *With housing*

Figure 6.54: ODS at 3080 Hz, Model C

Looking at both above ODS with housing, a deflection can be noted in correspondence of the transmission system. Of course, the highest deflection on the housing, at 3080 Hz is recorded close to node 12770, while at 2080 Hz a remarkable deflection is noted also above the inverter case, close to node 34220.
However, it is way more interesting to analyse them without the housing, in order to be able to appreciate the maximum deflection of shafts.
At 2080 Hz, the main deflection is of the input shaft, and it is a kind of oscillation around z axis, whilst, at 3080 Hz, the main deflection is of the intermediate shaft: an oscillation in the xz plane, around y axis, like a bending deflection.
Then, to compare the structure borne noise, the housing mounts responses are compared in Figures 6.55-6.57.

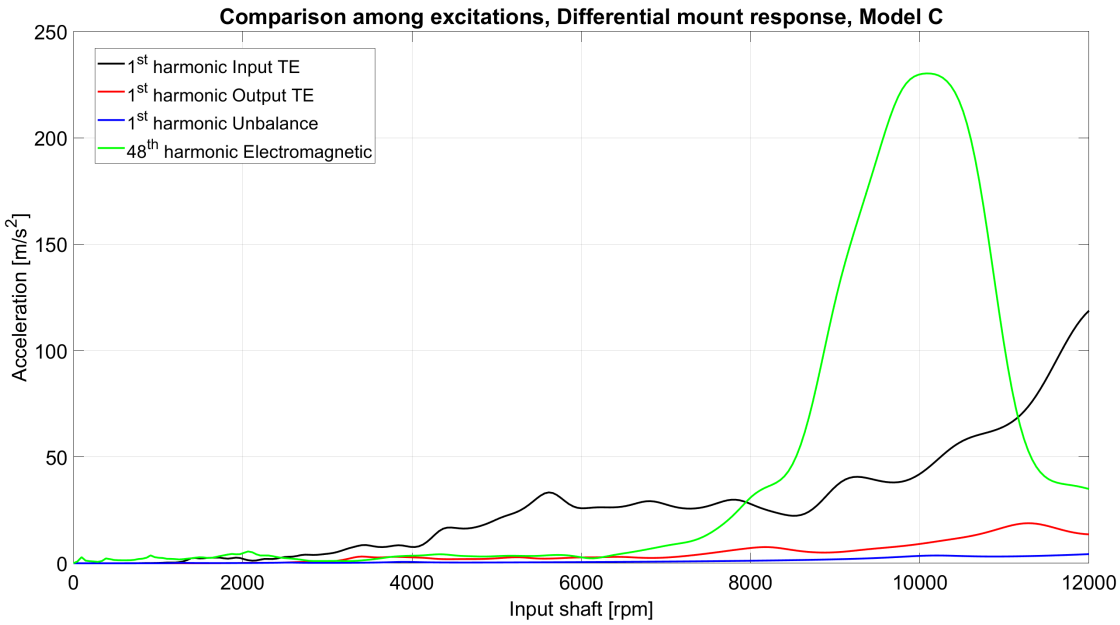

Figure 6.55: Comparison among excitations, differential mount response, Model C

The considered peaks are:

- Peak at 10080 rpm: most relevant peak considering 48^{th} harmonic of electromagnetic excitation
- Peak at 9216 rpm: local peak concerning 1^{st} harmonic of input TE
- Peak at 11280 rpm: most relevant peak considering 1^{st} harmonic of output TE

As far as the input TE is considered, it has been chosen to investigate a local peak at 9216 rpm and not the highest value at 12000 rpm, since the maximum speed is a very rare situation, therefore not so crucial.

Excitation	Speed (rpm)	Frequency (Hz)	Value (m/s^2)
1^{st} harmonic input TE	10080	3696	44.3
	9216	3379.2	40.5
	11280	4136	73.6
1^{st} harmonic output TE	10080	1535.3	9.5
	9216	1403.7	5.9
	11280	1718	18.8
N_{slots} harmonic electromagnetic	10080	8064	230.3
	9216	7372.8	154.7
	11280	9024	53.0
1^{st} harmonic unbalance	10080	168	3.6
	9216	153.6	2.1
	11280	188	3.4

Table 6.8: Comparison differential mount response among different excitation, Model C

Again, even in Model C the input TE causes high noises at particularly critical frequencies, according to Figure 1.1: the peaks are indeed at about 3000 and 4000 Hz. This, as will be highlighted in next pages, is valid for all housing mounts. Considering the damper mount, the relevant peaks are:

- Peak at 9600 rpm: most relevant peak considering 48^{th} harmonic of electromagnetic excitation
- Peak at 9072 rpm: local peak concerning 1^{st} harmonic of input TE
- Peak at 12000 rpm: most relevant peak considering 1^{st} harmonic of output TE

In this case the peak at 12000 rpm is considered, since the output gear set causes a almost negligible response along all speed range, increasing its value just at very high rotational speeds.

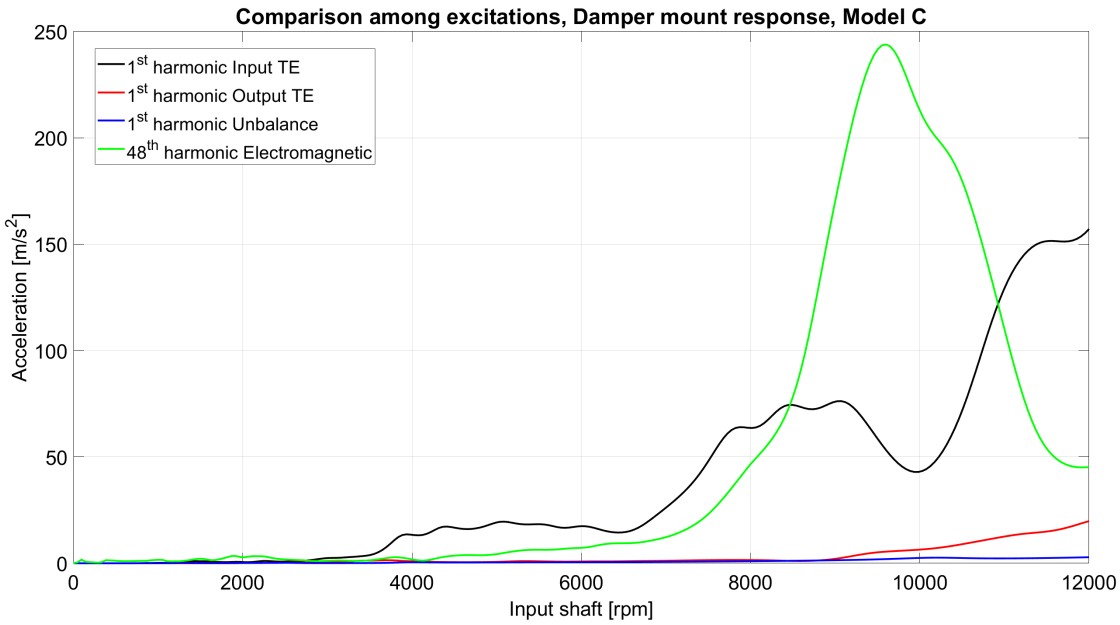

Figure 6.56: Comparison among excitations, damper mount response, Model C

Excitation	Speed (rpm)	Frequency (Hz)	Value (m/s^2)
1^{st} harmonic input TE	9600	3520	53.3
	9072	3326.4	76.2
	12000	4400	157.1
1^{st} harmonic output TE	9600	1462.2	5.5
	9072	1381.7	2.5
	12000	1827.7	19.8
N_{slots} harmonic electromagnetic	9600	7680	243.9
	9072	7257.6	183.9
	12000	9600	45.2
1^{st} harmonic unbalance	9600	160	2.0
	9072	151.2	1.5
	12000	200	2.8

Table 6.9: Comparison damper mount response among different excitation, Model C

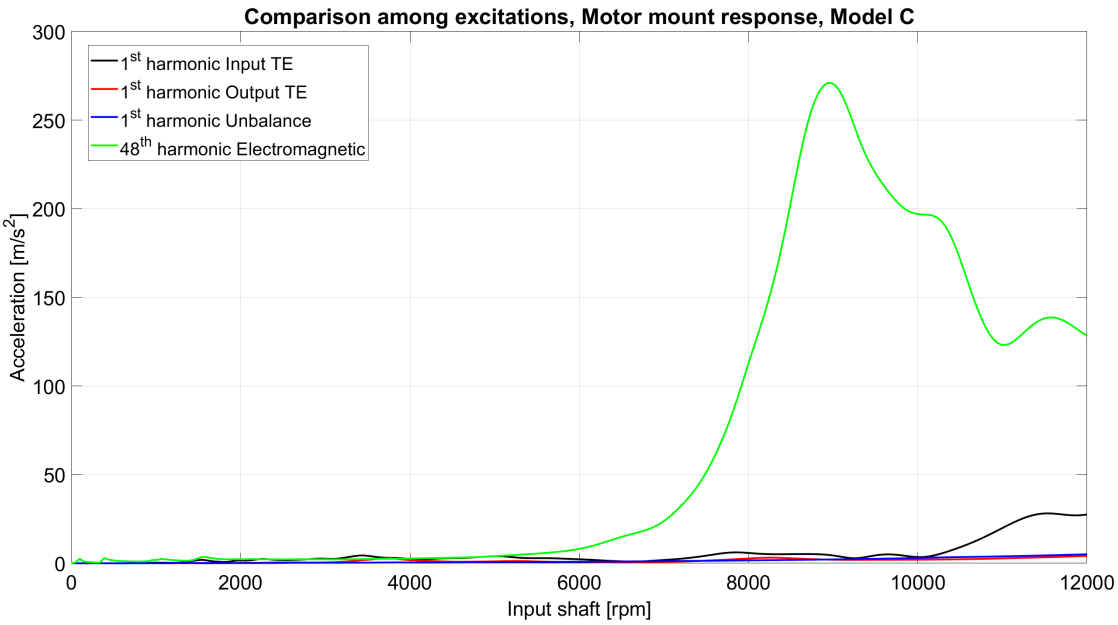

Figure 6.57: Comparison among excitations, motor mount response, Model C

As far as the motor mount is considered, just two peaks are relevant:

- Peak at 8976 rpm: most relevant peak considering 48^{th} harmonic of electromagnetic excitation
- Peak at 11520 rpm: local peak concerning 1^{st} harmonic of input TE

Excitation	Speed (rpm)	Frequency (Hz)	Value (m/s^2)
1^{st} harmonic input TE	8976 11520	3291.2 4224	4.5 28.1
1^{st} harmonic output TE	8976 11520	1373.9 1763.2	2.0 3.4
N_{slots} harmonic electromagnetic	8976 11520	7180.8 9216	271.0 138.4
1^{st} harmonic unbalance	8976 11520	149.6 192	2.1 4.4

Table 6.10: Comparison motor mount response among different excitation, Model C

Analysing the ODS of the most relevant peaks, caused by the 48^{th} harmonic of electromagnetic excitation, of all accelerometers and all housing mounts, it appears clear that the deflections show always the same behaviour. The highest deflection is always seen in the external wings of the housing, in correspondence of the electric motor. Therefore, to avoid redundancy, only one ODS is reported below. It has been selected, as representative of all other cases, the ODS at 7680 Hz, i.e. the peak related to the damper mount response.
The deflection of those wings, as already explained, cause an huge air movement, leading to remarkable noise radiated.

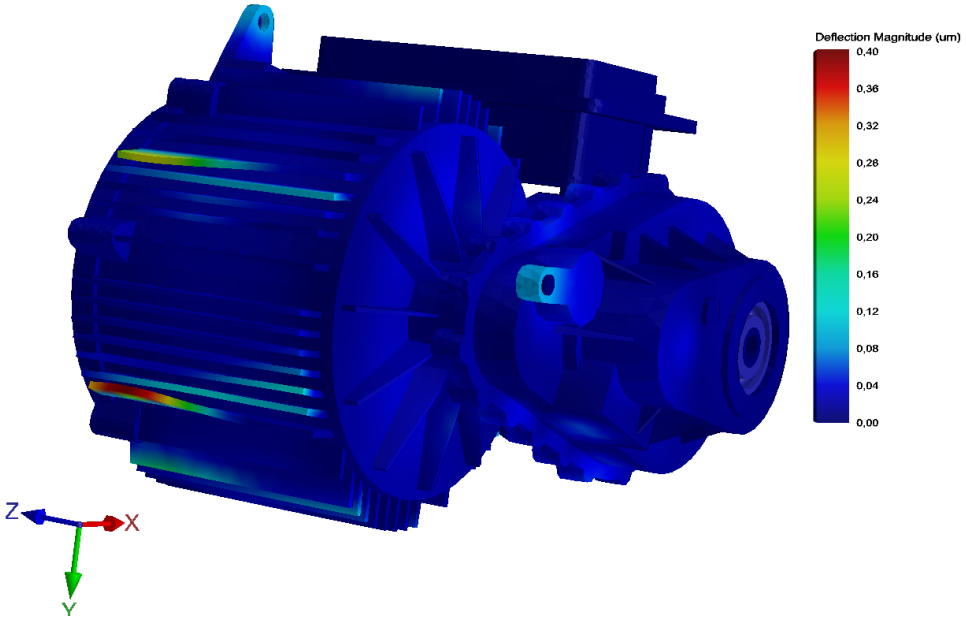

Figure 6.58: ODS at 7680 Hz, Model C

Investigating the above plots, considering now helical gears, a remarkable reduction of the dynamic response of the powertrain to transmission system excitation can be noted. Indeed, considering Model C (helical gears with profile shift), it is possible to say that the most critical source is now the electromagnetic one. However, the response due to the 1^{st} harmonic of the TE, especially of the input gear set, is still not negligible.
Therefore, it will follow now an even more detailed sensitivity analysis concerning the transmission system, introducing the microgeometry modifications explained in Section 4.2.7.
Finally, as already anticipated, the housing mounts response could also be analysed in terms of force, and not only accelerations, as displayed in Figure 6.59.

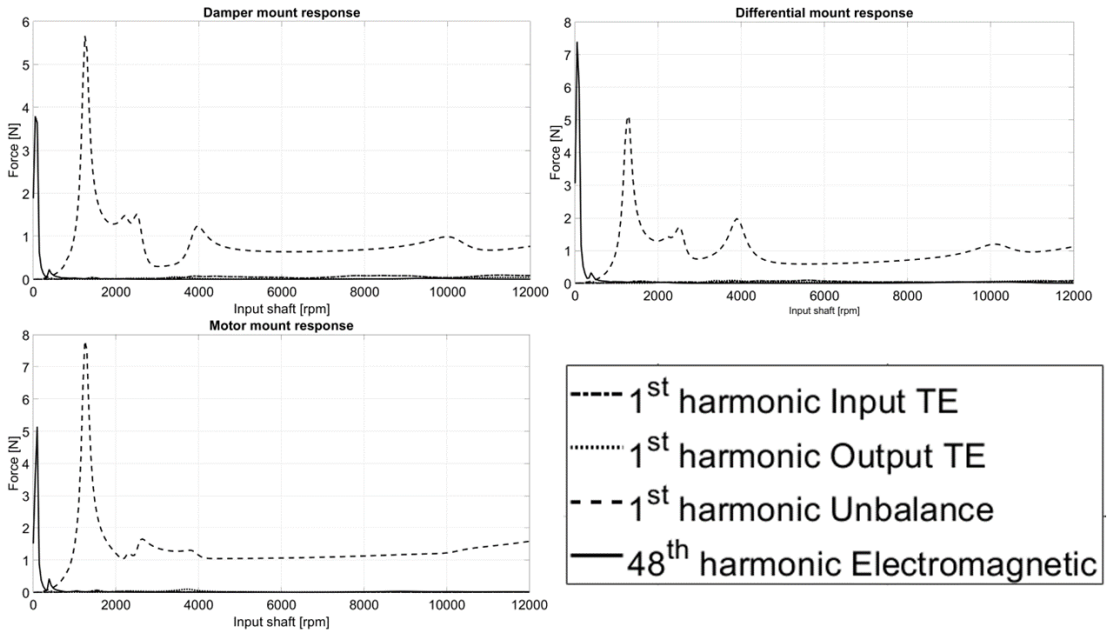

Figure 6.59: Housing mounts force response, Model C

Only knowing the transmissibility, it will be then possible to compute the actual values of forces transmitted to the rest of the vehicle. It can be noted that the values of forces are really small,in particular as regards the forces caused by transmission errors, of both gear sets. On the other hand, the unbalance and the electromagnetic excitation lea to highest response, especially at very low values of shaft speed. Only a small force due to the unbalance is present along the whole speed range.

6.5.2 Waterfall analysis

Waterfall plots are important results to be analysed in a dynamic analysis. In this thesis it has been chosen to show the Waterfall plots only related to Model C (helical gears with profile shift), to avoid redundancy of results. Indeed, models with spur gears (A and B) are not that representative of the system, since very high vibrations are due to poor transmission system design. Model C, even if it has no microgeometry modifications, on the other hand, represents pretty well the system.
Waterfall plots allow to represent in a single graph the input shaft rotational speed, in *rpm*, the frequency, in *Hz*, and the amplitude of the response, in this case acceleration at housing mounts, in m/s^2.
Waterfall plots are powerful since it is possible to represent in the same graph different orders of harmonics coming from different source of excitation.
Hence, it can be exploited to understand which excitation is the one which causes

highest response at a certain shaft rotational speed. Please notice that the following results are only related to housing mounts response, however even other responses, for instance at virtual accelerometers on the gearbox, if required, can be plotted.

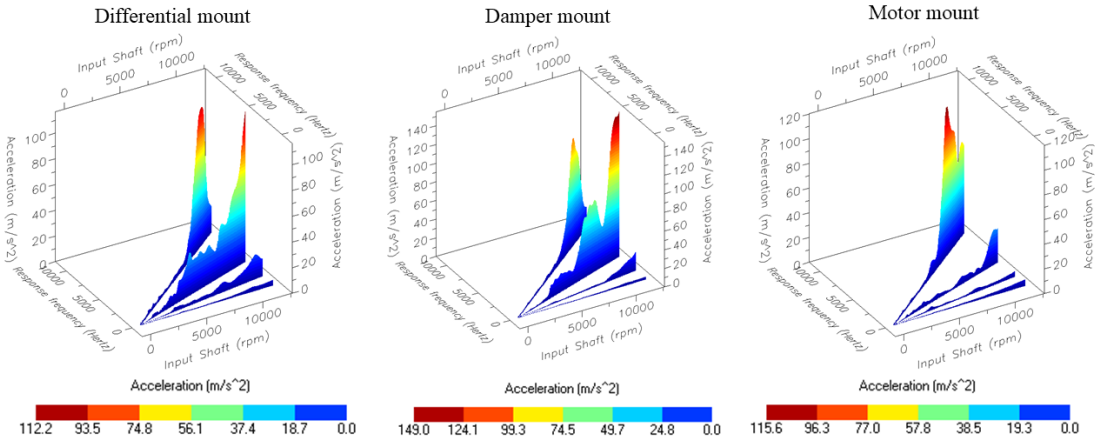

Figure 6.60: Waterfall plot, comparison among excitations, Model C

In Figure 6.60, four sources of excitation are represented. Moving counterclockwise, 1^{st} harmonic of unbalance, 1^{st} harmonic of output TE, 1^{st} harmonic of input TE, 48^{th} harmonic of electromagnetic excitation. It appears evident, as already analysed in Section 6.5.1, that the output TE and the unbalance lead to negligible results with respect to input TE and electromagnetic excitations. Moreover, it is also shown that 48^{th} harmonic of the electromagnetic excitation, of course, covers a wider frequency range.
In Waterfall plots, the harmonic components are depicted as radial lines, while the resonances, i.e. the natural frequency, are represented as horizontal (in rpm-Hz plane) straight lines.
It can be interesting to plot on the same graph the Waterfall and the natural frequency to analyse if there is a correspondence between the peak of the Waterfall and a natural frequency of the system. The correspondence of a peak of the response with a structural resonance of the system can bring to very high vibration ampltidues.
Let's do this considering as excitation source the 48^{th} harmonic of the electromagnetic excitation.

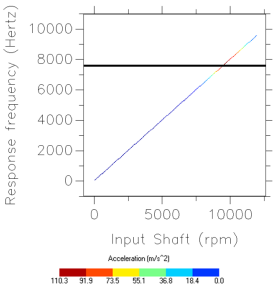

(a) *Waterfall plot, 48^{th} harmonic electromagnetic*

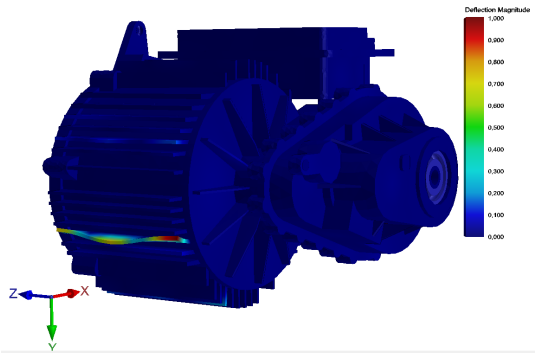

(b) *Modeshape 7689.8 Hz*

Figure 6.61: Waterfall and corresponding modeshape, damper mount, Model C

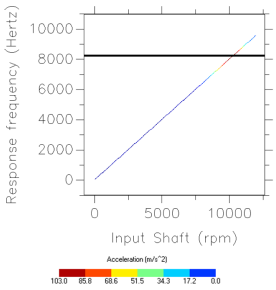

(a) *Waterfall plot, 48^{th} harmonic electromagnetic*

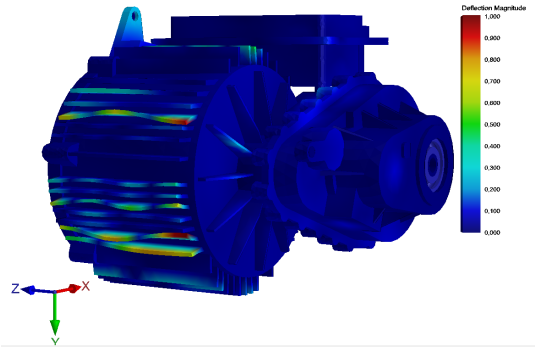

(b) *Modeshape 8235.9 Hz*

Figure 6.62: Waterfall and corresponding modeshape, differential mount, Model C

A possible solution to try to mitigate the vibration of the housing is to try to make the windings of the housing more rigid, or, changing the geometry, for instance adding some ribs, to try to increase the values of the resonance frequency above the working range.

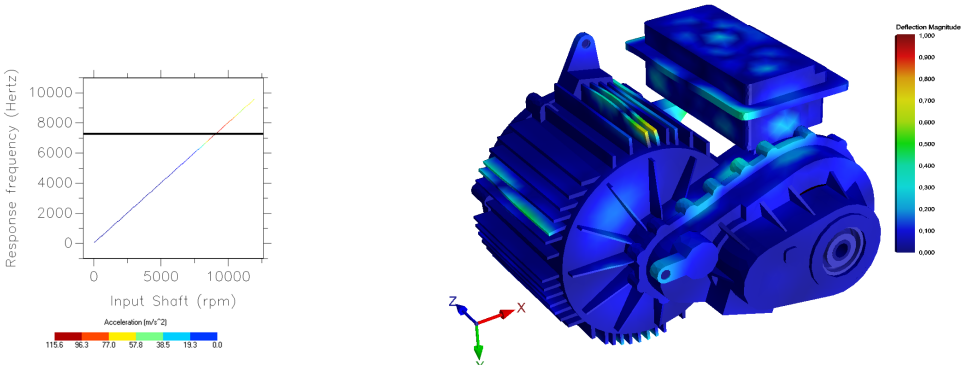

(a) *Waterfall plot, 48^{th} harmonic electromagnetic*

(b) *Modeshape 7689.8 Hz*

Figure 6.63: Waterfall and corresponding modeshape, motor mount, Model C

In correspondence of each peak of each mount, a natural frequency can be noted. The values and mode numbers are reported in Table 6.11.

Housing mount	Mode number	Frequency (Hz)
Damper	220	7689.8
Differential	247	8235.9
Motor	189	7209.0

Table 6.11: Natural frequencies at Waterfall peaks, 48^{th} electromagnetic excitation, Model C

Let's now consider the 1^{st} harmonic input TE. First of all, being the order of the harmonic 22, it can be noted that the frequency range is narrower.
Considering the damper mount, the reported natural frequency is not exactly related to the highest peak (i.e. at 12000 rpm), since 12000 rpm (4440 Hz) is a very extreme condition. It was thought that a relative peak at 3067.1 Hz is more interesting to be analysed.

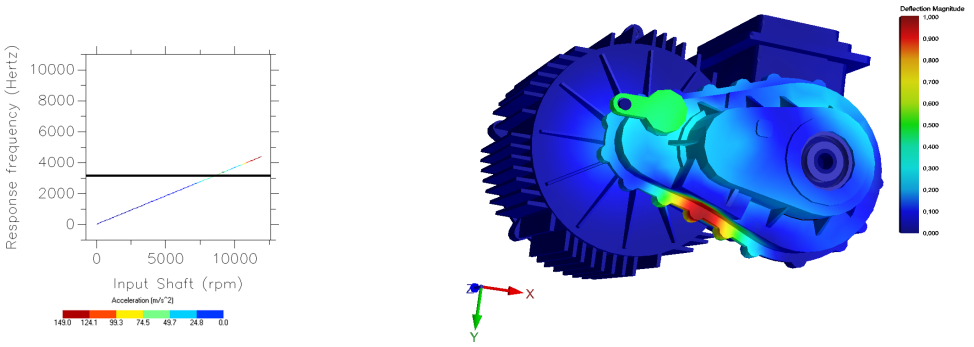

(a) *Waterfall plot, 1^{st} harmonic input TE* **(b)** *Modeshape 3067.1 Hz*

Figure 6.64: Waterfall and corresponding modeshape, damper mount, Model C

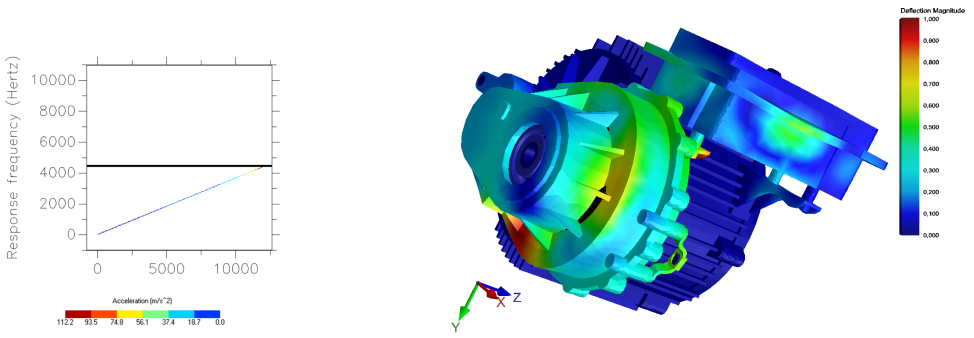

(a) *Waterfall plot, 1^{st} harmonic input TE* **(b)** *Modeshape 4329.1 Hz*

Figure 6.65: Waterfall and corresponding modeshape, differential mount, Model C

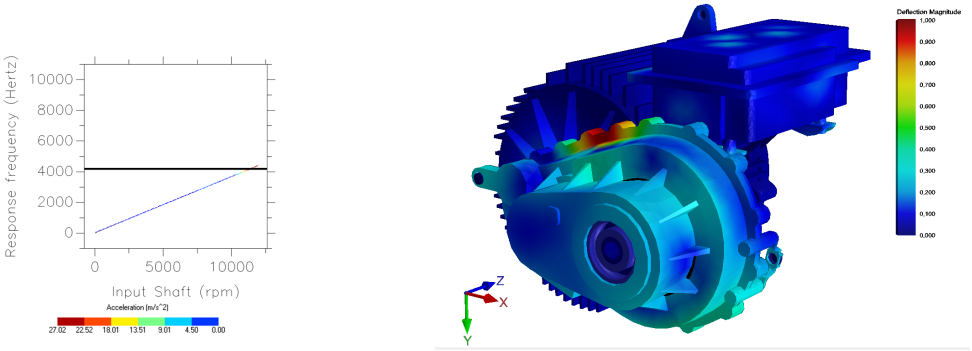

(a) *Waterfall plot, 1^{st} harmonic input TE* **(b)** *Modeshape 4235.1 Hz*

Figure 6.66: Waterfall and corresponding modeshape, motor mount, Model C

In correspondence of each peak of each mount, a natural frequency can be noted. These natural frequencies are relevant since they are in the critical range explained by Figure 1.1, in particular:

Housing mount	Mode number	Frequency (Hz)
Damper	57	3067.1
Differential	84	4329.1
Motor	82	4235.1

Table 6.12: Natural frequencies at Waterfall peaks, 1^{st} input TE, Model C

Finally, the same considerations can be done even for the 1^{st} harmonic output TE. For the same reasons of before, concerning the motor mount a relative peak is reported. Considering the output gear set, lower frequency are excited.

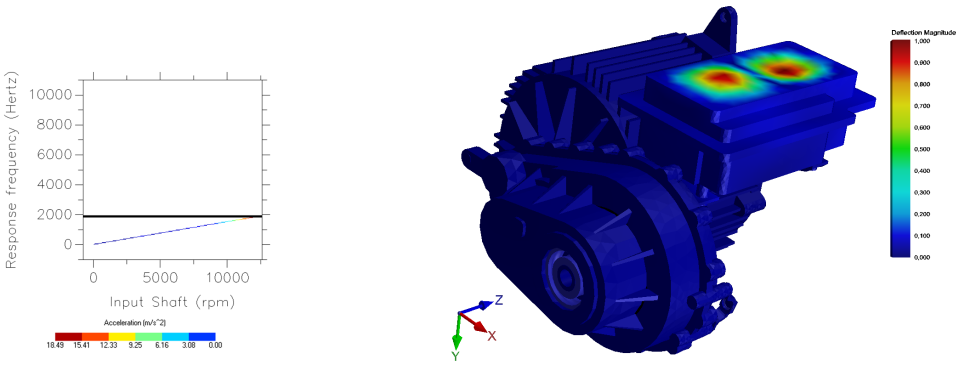

(a) *Waterfall plot, 1^{st} harmonic output TE* **(b)** *Modeshape 1829.3 Hz*

Figure 6.67: Waterfall and corresponding modeshape, damper mount, Model C

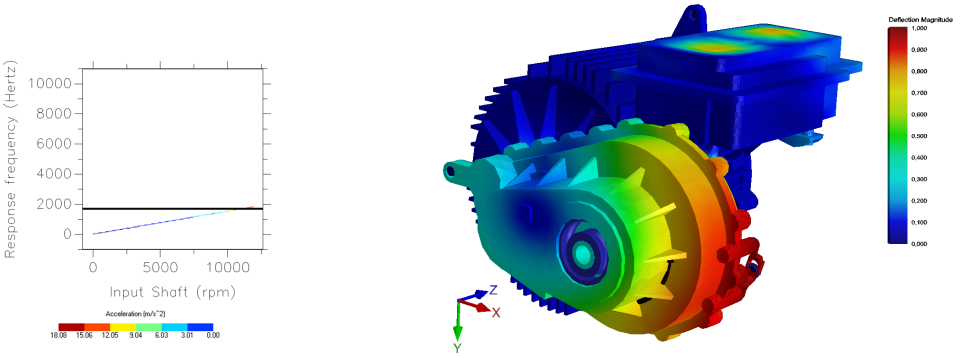

(a) *Waterfall plot, 1^{st} harmonic output TE* **(b)** *Modeshape 1723.2 Hz*

Figure 6.68: Waterfall and corresponding modeshape, differential mount, Model C

Looking at Figures 6.67-6.69, a possible solution to reduce the vibration on the inverter case is for sure to make the inverter case more rigid.

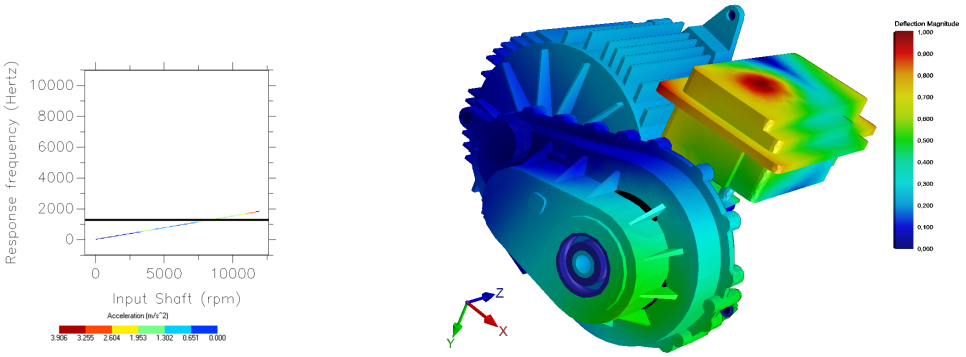

(a) *Waterfall plot, 1^{st} harmonic output TE* **(b)** *Modeshape 1252.4 Hz*

Figure 6.69: Waterfall and corresponding modeshape, motor mount, Model C

In correspondence of each peak of each mount, a natural frequency can be noted, in particular:

Housing mount	Mode number	Frequency (Hz)
Damper	37	1829.3
Differential	36	1723.2
Motor	32	1252.4

Table 6.13: Natural frequencies at Waterfall peaks, 1^{st} output TE, Model C

Furthermore, Waterfall plots can also be used in order to compare several harmonic orders of a single excitation to understand which one is the most critical. Considering the input TE, a comparison among the first three harmonics (order 22, 44, 66) is reported in Figure 6.70. It is proved how the first one is by far the one which causes the highest response in all housing mounts, so the behaviour is the expected one.

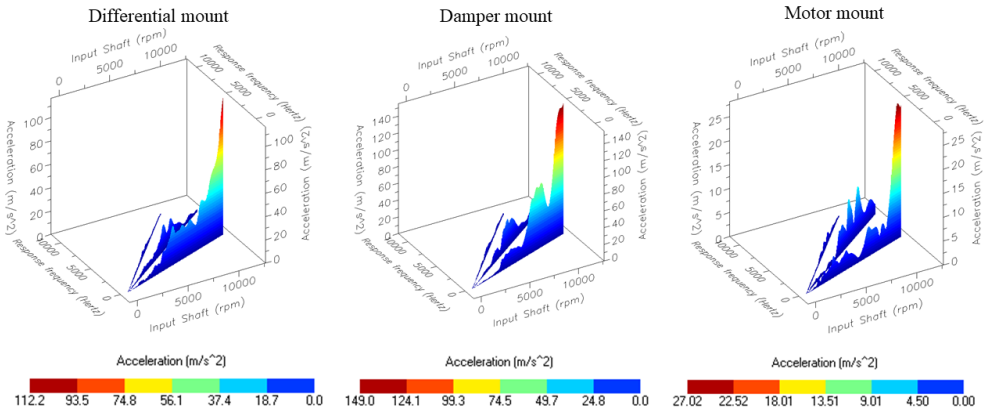

Figure 6.70: Waterfall plot, comparison harmonic orders, 1^{st} harmonic input TE, Model C

Now let's focus on the output TE: in Figure 6.71 the first three harmonics are reported, in counterclockwise order.
Investigating Figure 6.71, it is noted that the second harmonic, i.e. order 18.277, actually causes an higher response than the first harmonic, order 9.138. It can be seen that the difference between the first two harmonics is quite slight in all mounts, with the exception of the differential one. However, in any case, the response caused by the output TE is way smaller with respect to other sources of excitation. Hence, even if the comparison in Section 6.5.1 was done considering the 2^{nd} harmonic of the output TE, and not the 1^{st}, the outcome would not have changed: the highest response is by far caused by the 1^{st} harmonic of input TE and the 48^{th} of electromagnetic excitation. Indeed, remember that the goal of the analysis of Section 6.5.1 was just on understanding which excitation causes the highest response and therefore on selecting which optimization perform to reduce the NVH problems.

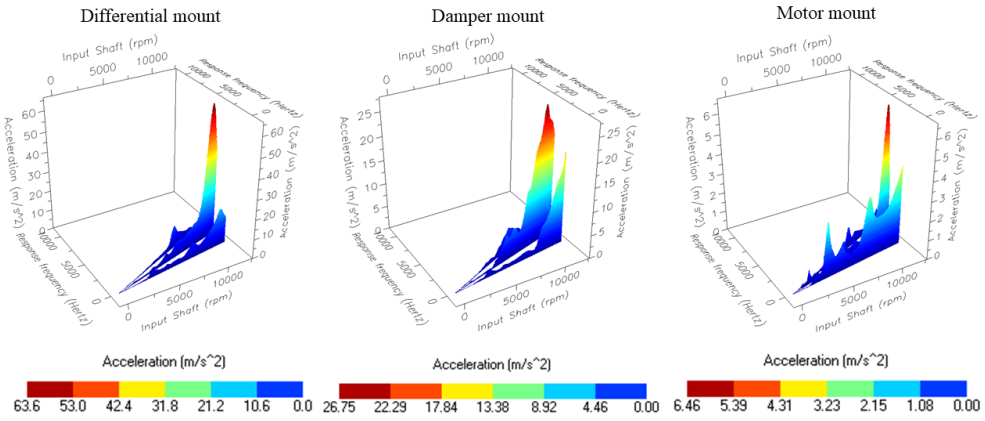

Figure 6.71: Waterfall plot, comparison harmonic orders, 1^{st} harmonic output TE, Model C

Lastly, Figure 6.72, which reports, counterclockwise, the 24^{th} and the 48^{th} harmonic of electromagnetic excitation, confirms that the most critical order is the 48^{th}.

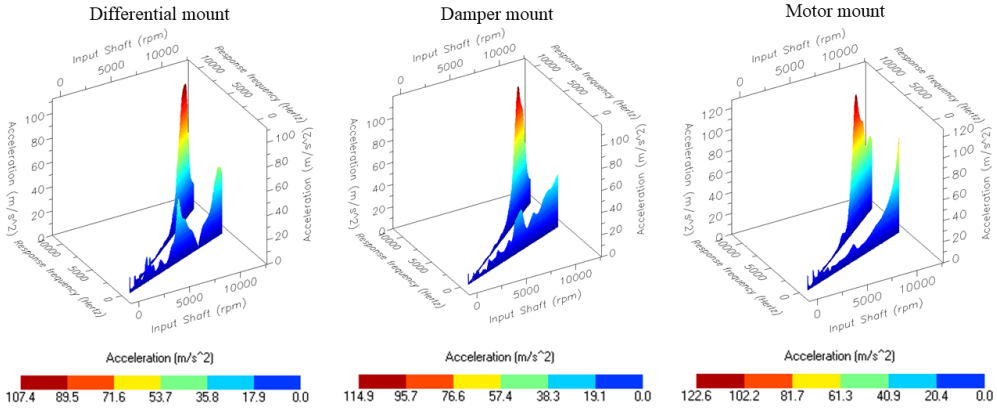

Figure 6.72: Waterfall plot, comparison harmonic orders, 48^{th} harmonic electromagnetic, Model C

6.5.3 Modal analysis

It has been chosen to perform the modal analysis just on Model C (helical gears with profile shift) since is it selected as representative of the model. Models with spur gears (A and B) provide too high responses, and on models with microgeometry modifications, the modal analysis is not reported to avoid redundancy.
First of all, it is interesting to investigate the rigid body motions of the system.

Mode Number	Frequency (Hz)	Description
1	0.74	Rigid torsion around z
2	13.4	Axial rigid translation along z
3	20.4	Radial rigid translation
4	21.4	Radial rigid translation
5	37.7	Rigid torsion around y
6	42.4	Rigid torsion around x

Table 6.14: Rigid body motions, Model C

The rigid body motions are reported in Figures 6.73-6.78. The figures report two instants of time, in order to show the deformation and better understand the rigid body motion, and some arrows help in the understanding of the motion.

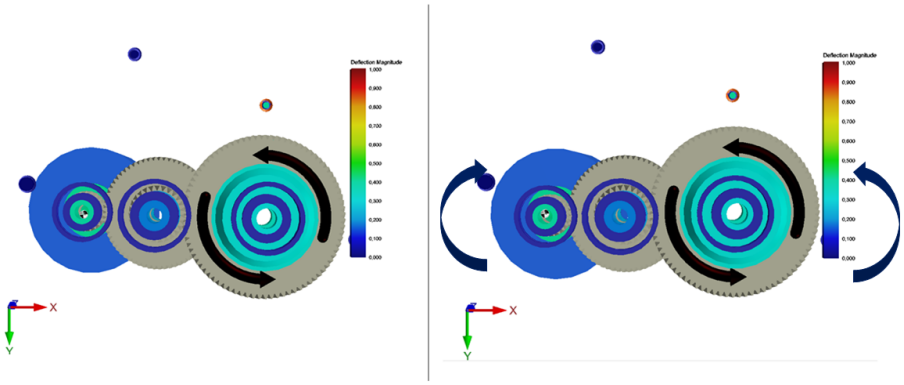

Figure 6.73: Mode 1, Rigid torsion around z, Model C

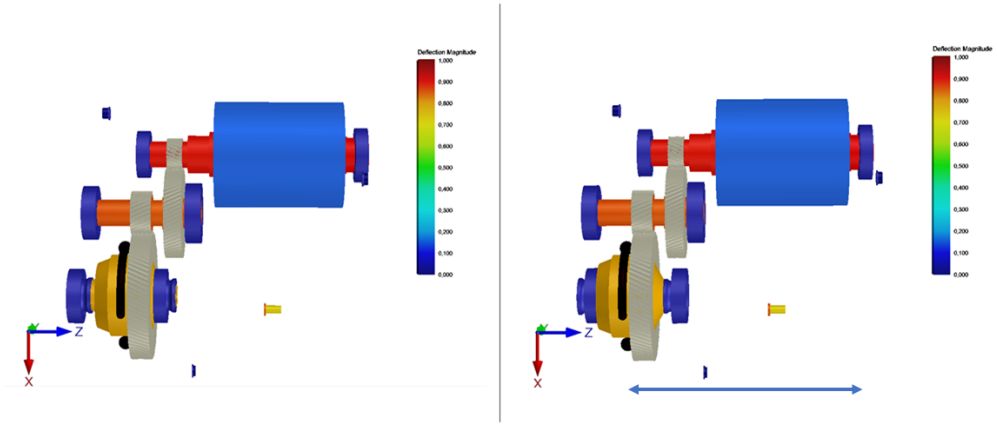

Figure 6.74: Mode 2, Axial rigid translation along z, Model C

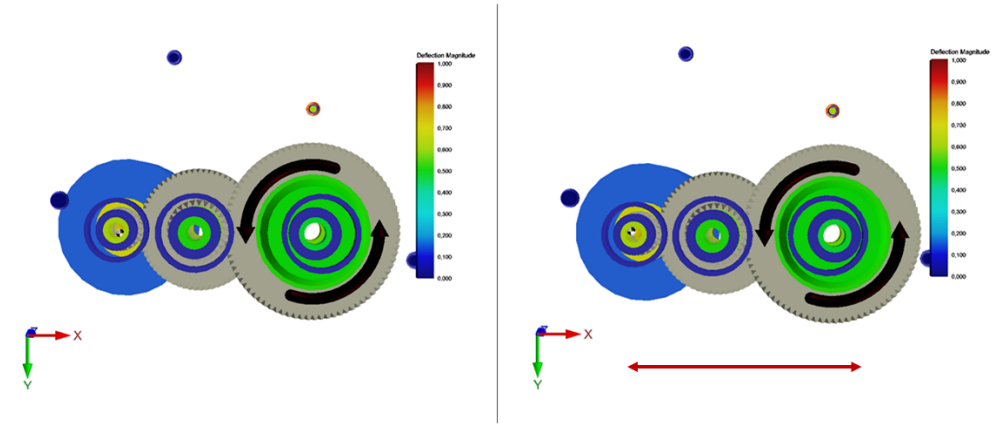

Figure 6.75: Mode 3, Radial rigid translation, Model C

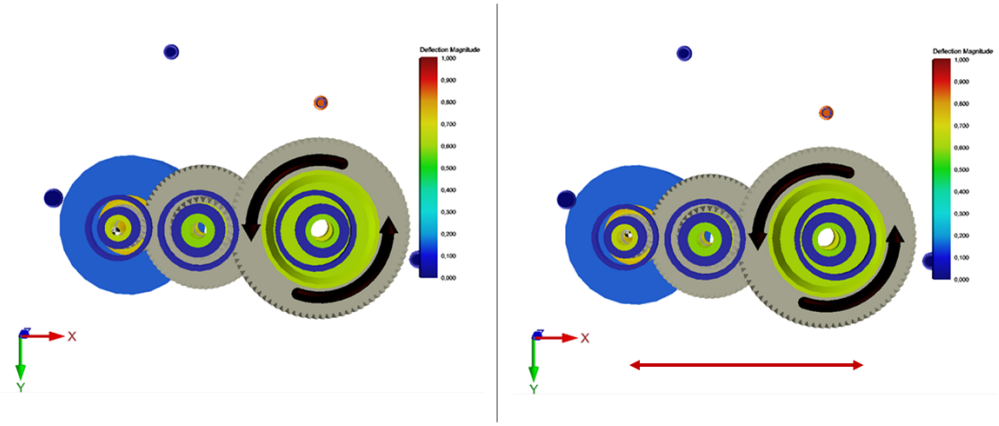

Figure 6.76: Mode 4, Radial rigid translation, Model C

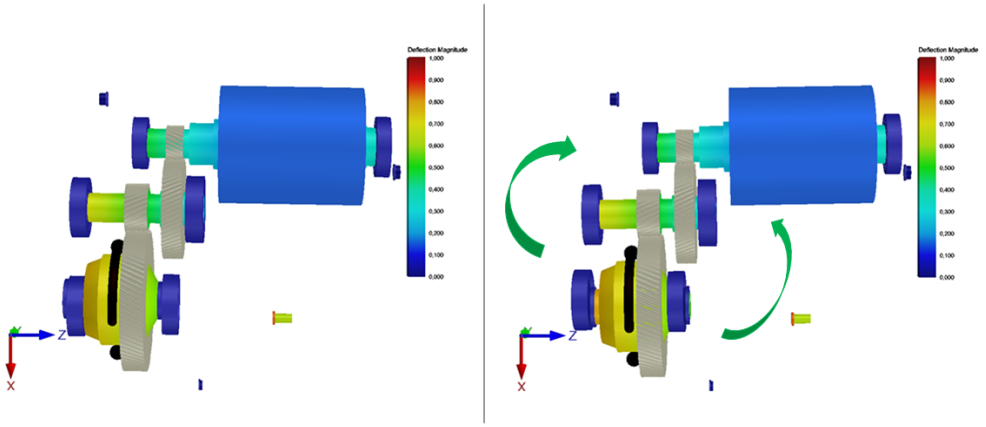

Figure 6.77: Mode 5, Rigid torsion around y, Model C

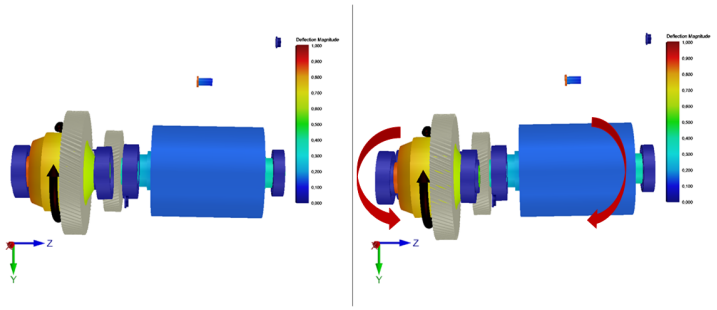

Figure 6.78: Mode 6, Rigid torsion around x, Model C

Moreover, it is possible to represent, on the same plot of the response, also the response to just some selected modes. This is important to have a visualization of the modal participation factor: indeed it allows to understand which are the most relevant modes that causes the peaks in the response. To avoid redundancy, this kind of analysis is performed only on Model C (helical gears with profile shift). Only the load case NVH is considered, taking into account the acceleration response at housing mounts. In the following plots, dashed plots are built considering just some relevant modes. The crucial aspect is that, only representing the response of some modes, it is possible to represent pretty well the behaviour of the whole plot in the frequency range. In fact, the two plots (the continuous line and the dashed one) almost overlap in each graph in the most important points, i.e. the peaks.

Excitation	Housing Mount	Mode number
1^{st} harmonic input TE	Differential	$40 \div 42$, $60 \div 65$, 84
	Damper	$61 \div 63$, $82 \div 87$
	Motor	$54 \div 56$, $82 \div 83$
1^{st} harmonic output TE	Differential	$14 \div 17$, $29 \div 32$, 36
	Damper	$15 \div 16$, 38
	Motor	$15 \div 16$, 32, 38
N_{slots} harmonic electromagnetic	Differential	$229 \div 252$
	Damper	$216 \div 231$
	Motor	$126 \div 245$

Table 6.15: Considered modes

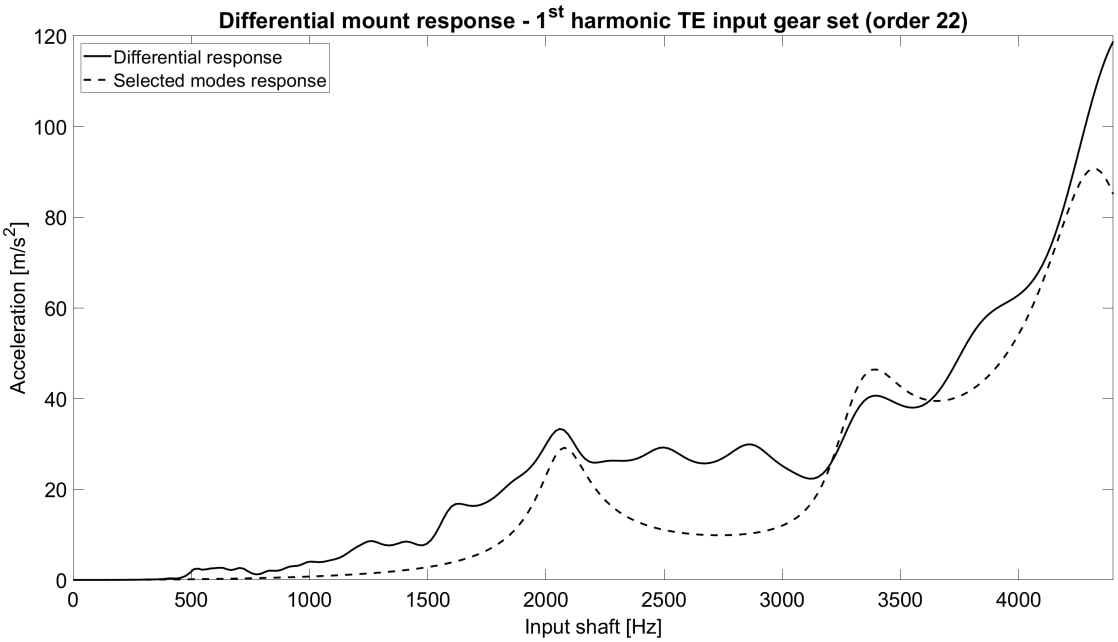

Figure 6.79: Differential mount, 1^{st} Harmonic input TE, Model C

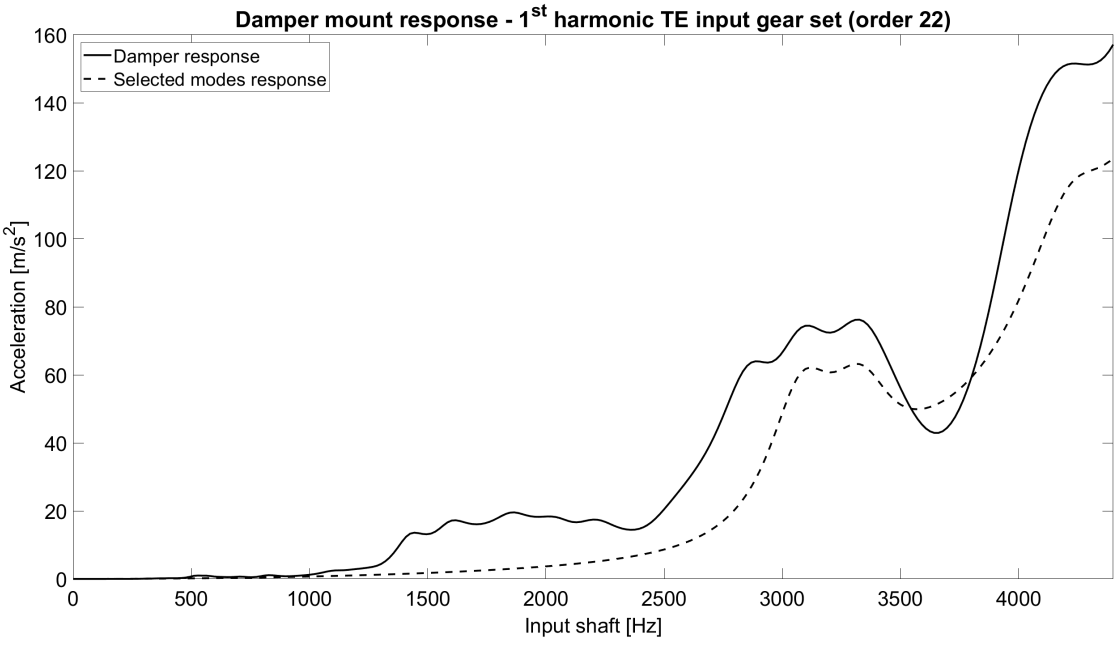

Figure 6.80: Damper mount, 1^{st} Harmonic input TE, Model C

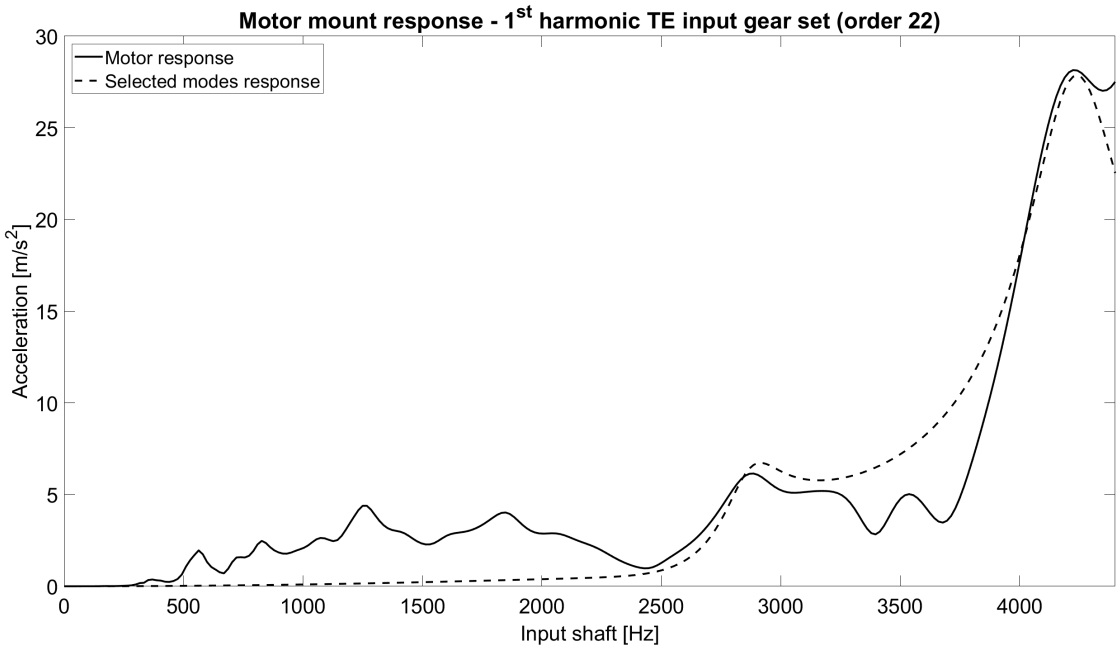

Figure 6.81: Motor mount, 1^{st} Harmonic input TE, Model C

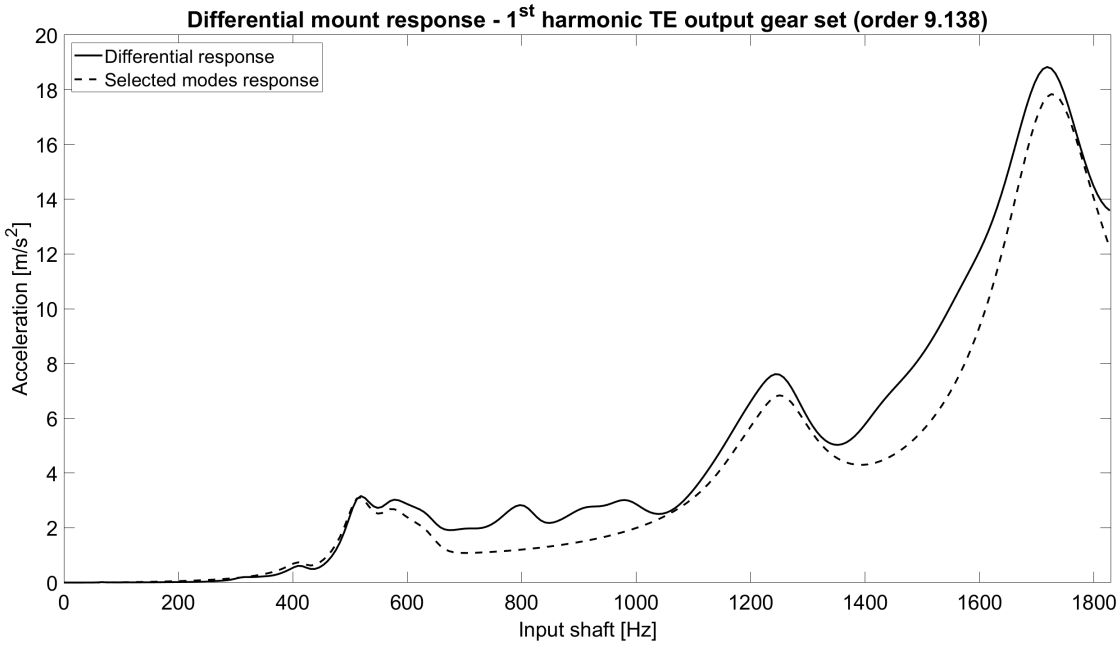

Figure 6.82: Differential mount, 1^{st} Harmonic output TE, Model C

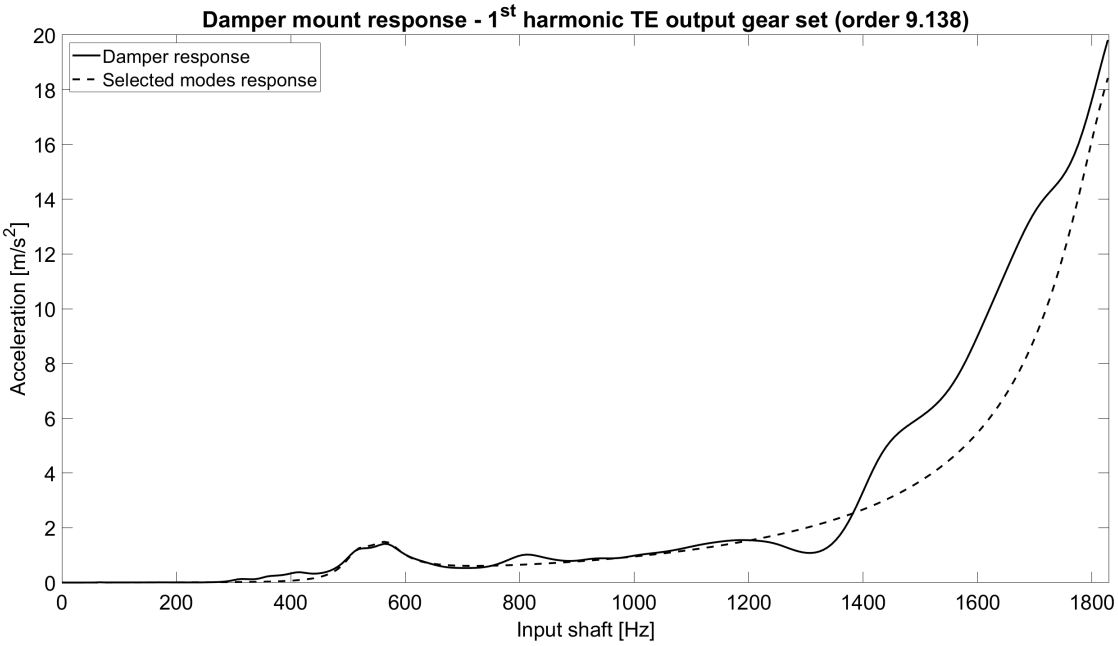

Figure 6.83: Damper mount, 1^{st} Harmonic output TE, Model C

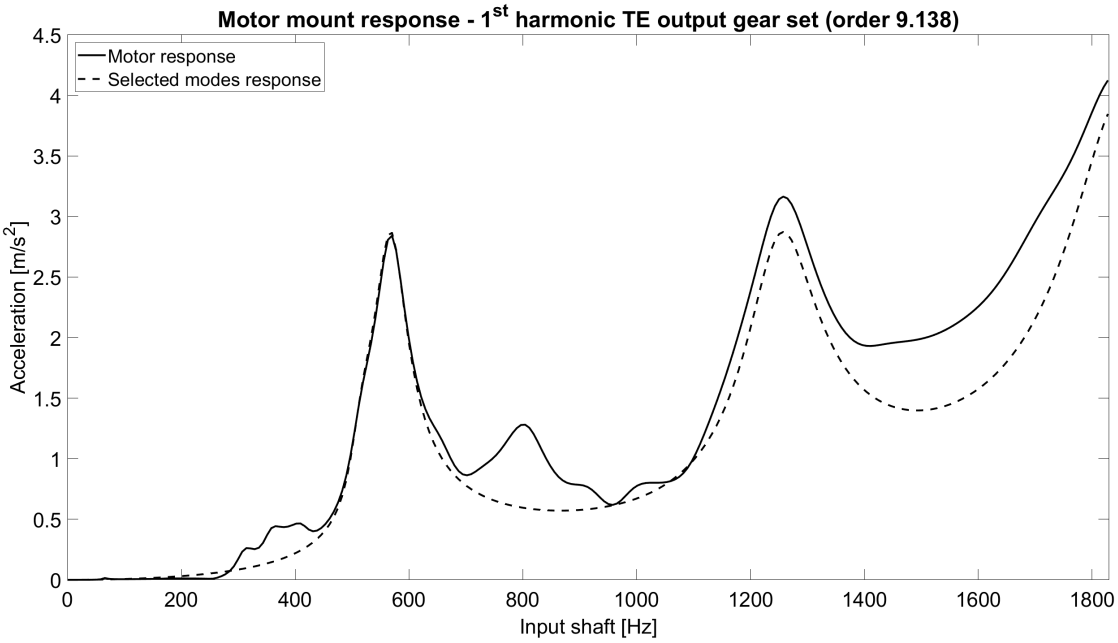

Figure 6.84: Motor mount, 1^{st} Harmonic output TE, Model C

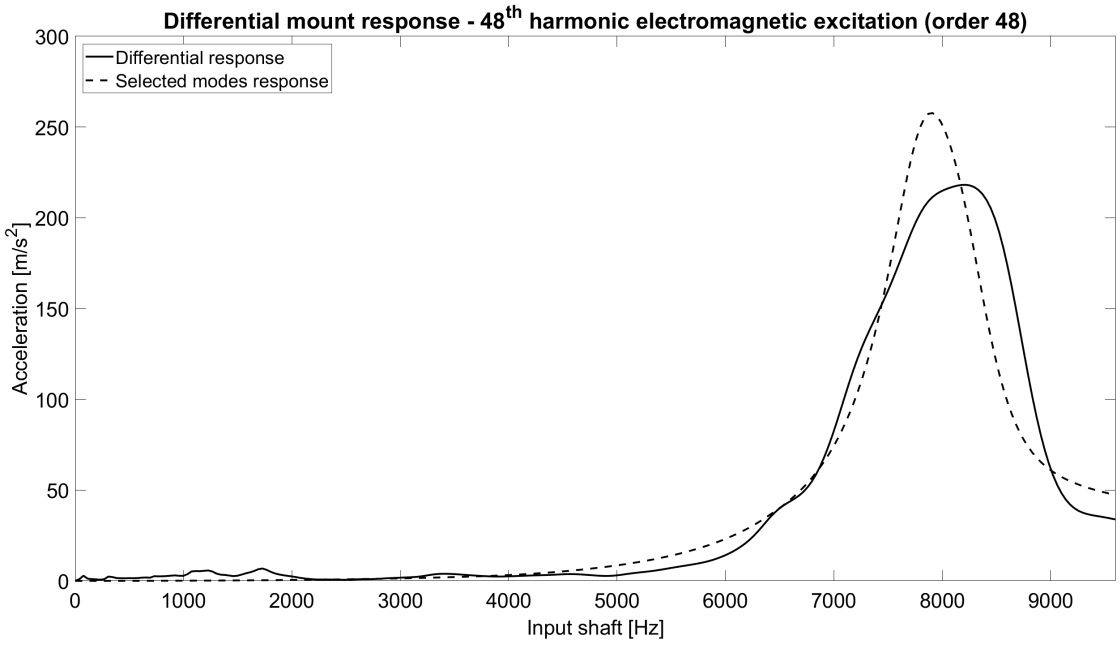

Figure 6.85: Differential mount, 48^{th} Harmonic electromagnetic excitation, Model C

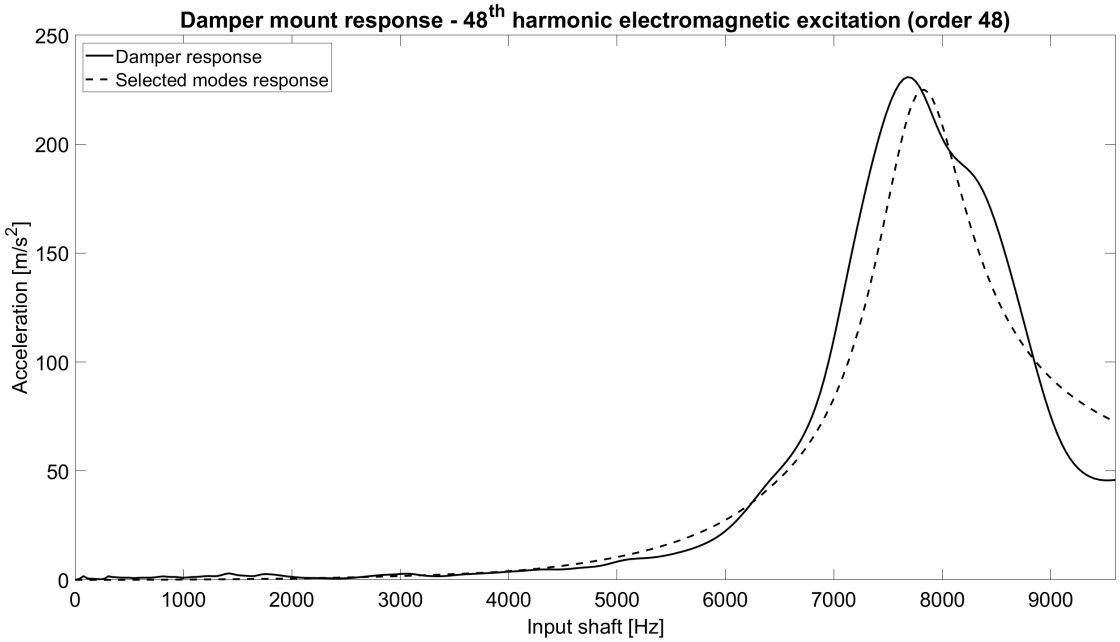

Figure 6.86: Damper mount, 48^{th} Harmonic electromagnetic excitation, Model C

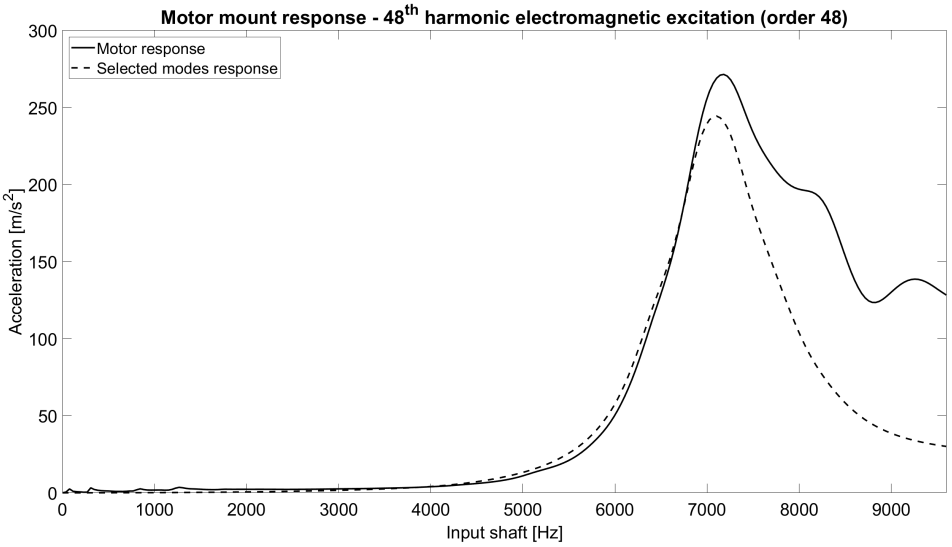

Figure 6.87: Motor mount, 48^{th} Harmonic electromagnetic excitation, Model C

6.5.4 Damping analysis

In this thesis, for all NVH analyses so far, and also for the ones that will follow in the next sections, a constant modal damping equals to 5% has been considered. However, Romax gives the possibilities to consider even different damping models, such as the Rayleigh method.
Starting from the equation of motion:

$$m\ddot{x} + c\dot{x} + kx = F$$

Rayleigh allows to approximate the damping c by considering two factors, α and β:

$$c = \alpha k + \beta m$$

Rewriting the equation of motion in terms of natural frequency ω_n and damping ratio xi:

$$\ddot{x} + 2\xi\omega_n\dot{x} + \omega_n^2 x = F/m$$

with $\omega_n^2 = k/m$, $\xi = c/2m\omega_n$. Finally, due to Rayleigh, the damping ratio becomes:

$$\xi = \frac{\alpha}{2\omega_n} + \frac{\beta\omega_n}{2}$$

Romax suggests two default values of the coefficients:

$$\alpha = 600\,s \;;\; \beta = 6.0 \cdot 10^{-6}\,s^{-1}$$

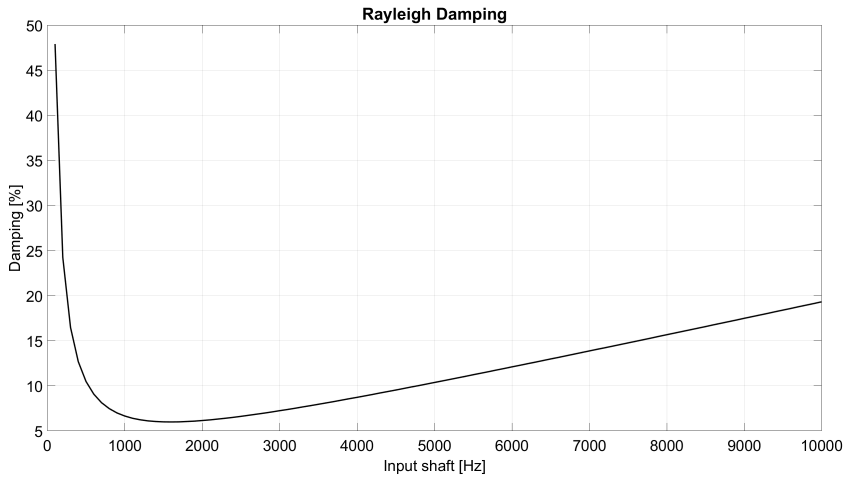

Figure 6.88: Rayleigh damping

Considering the above Rayleigh parameters, it is possible to see that the damping is high at extremely low frequency values, then it reaches a minimum at $\approx 1500\,Hz$, then it increases as the frequency further increases.
Considering for instance the housing mounts response to the 48^{th} harmonic of the electromagnetic response, the peaks are in the range $7000 \div 8500\,Hz$. In this frequency range the Rayleigh damping is about 15%: it is hence expected a strong reduction of the response moving from the constant modal damping of 5% to the Rayleigh one, as certified by Figure 6.89.

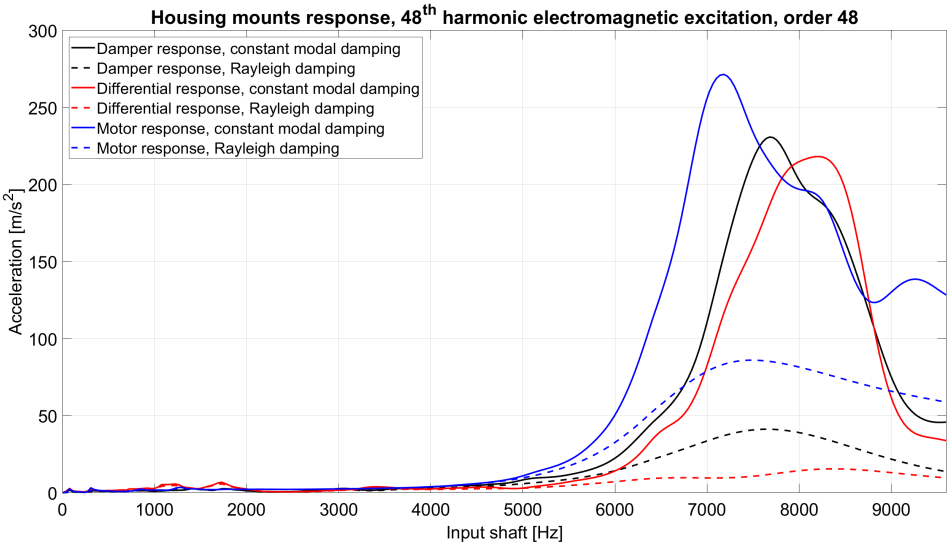

Figure 6.89: Comparison constant modal damping vs Rayleigh damping, 48^{th} harmonic electromagnetic excitation

6.6 Models with optimized microgeometry

In this section, the NVH analyses regarding the models with microgeometry modifications, explained in Section 4.2.7, are carried out.
The first step to perform is to analyse the amplitudes of the harmonics of the TE of both gear sets.

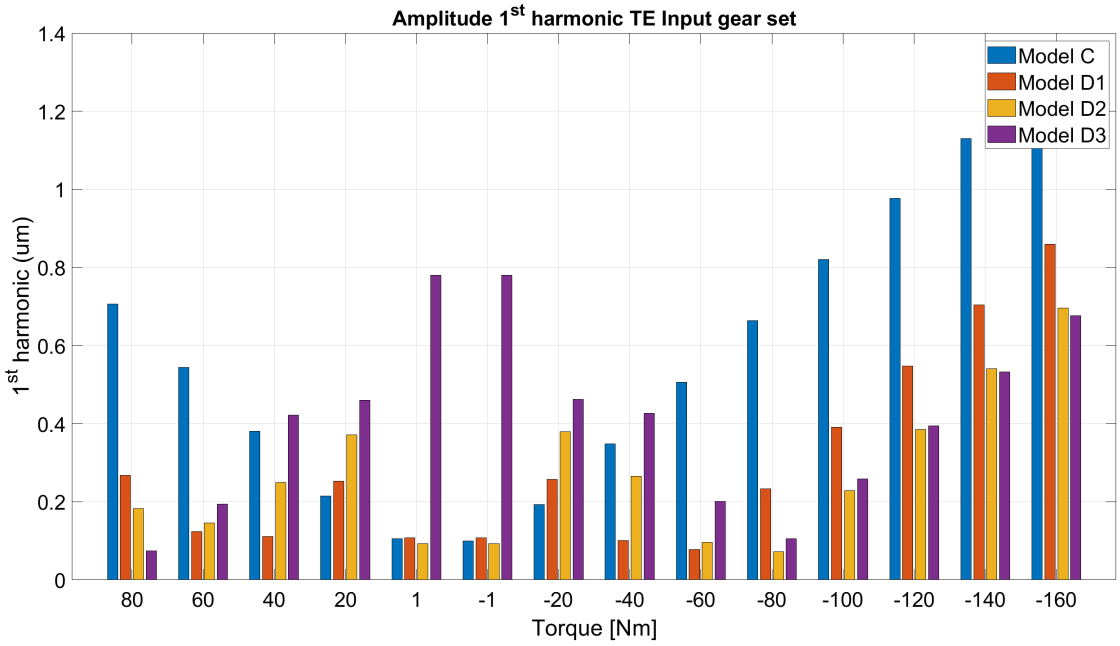

Figure 6.90: Amplitudes of 1^{st} harmonic TE, order 22, Input gear set, Models C, D1, D2, D3

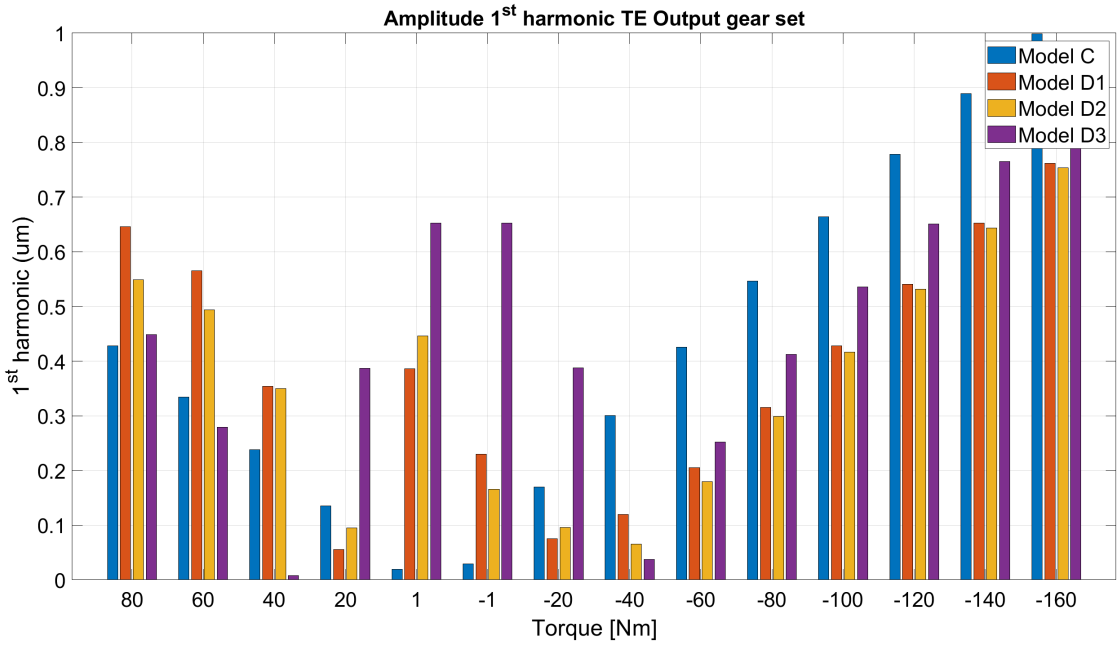

Figure 6.91: Amplitudes of 1^{st} harmonic TE, order 9.138, Output gear set, Models C, D1, D2, D3

As expected from Section 4.2.7, considering the first three optimization attempts, the desired results are not achieved. Indeed, a reduction of the amplitude of the 1^{st} harmonic of the TE of both gear set is not obtained in the crucial load cases (remember Table 6.2). A reduction of the values is obtained just at high values of torque, both on drive and coast conditions: however these cases are not really of interest for the NVH analysis.

On the contrary, considering Model D4, the requested results are obtained:

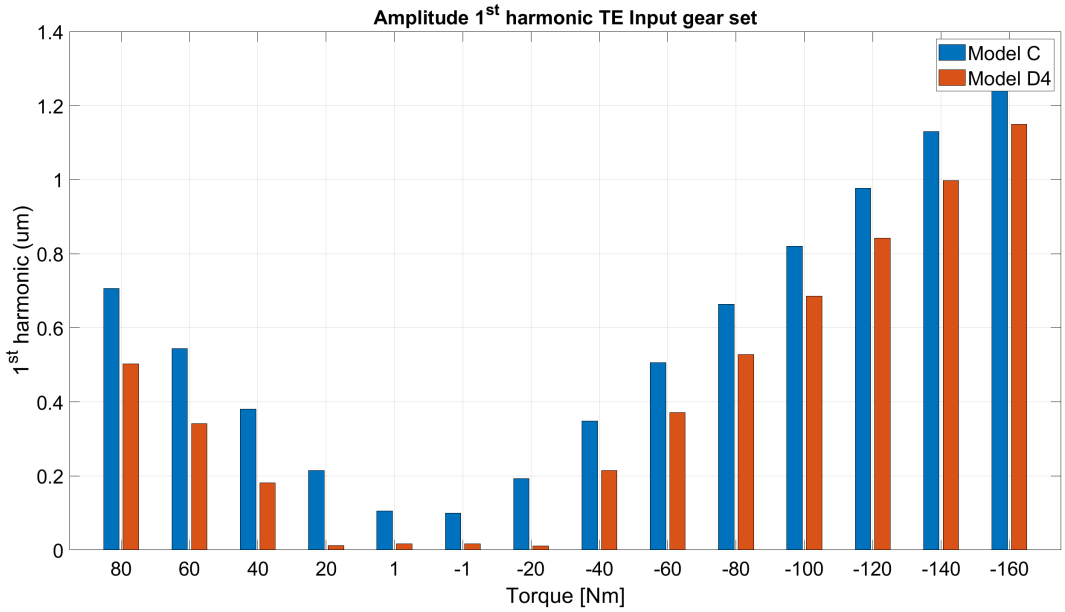

Figure 6.92: Amplitudes of 1^{st} harmonic TE, order 22, Input gear set, Models C, D4

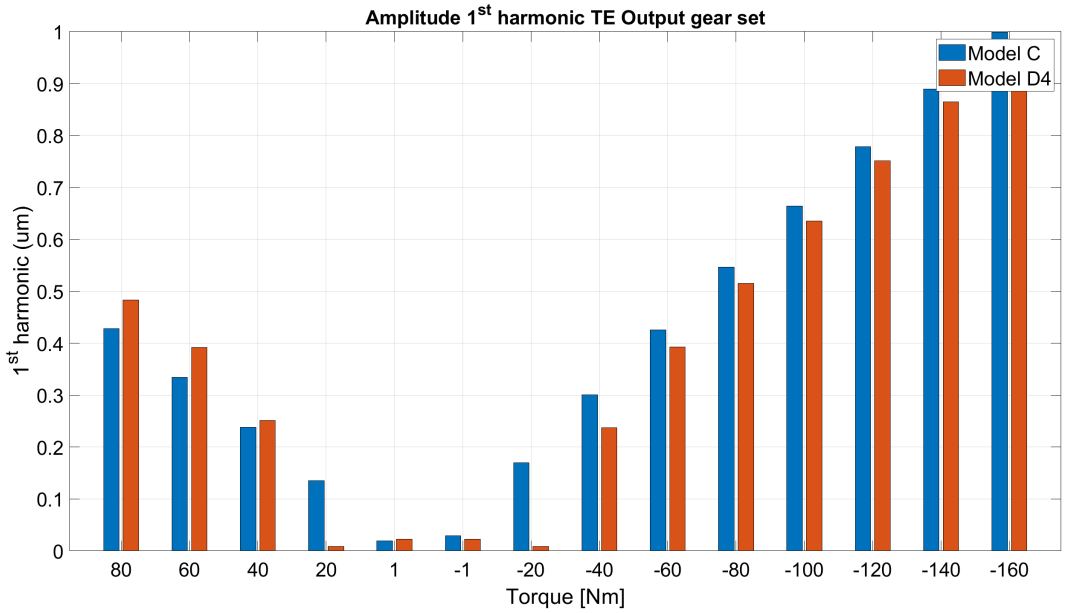

Figure 6.93: Amplitudes of 1^{st} harmonic TE, order 9.138, Output gear set, Models C, D4

The above plots covers the whole torque range of the motor, however the improvements are verified even for the desired load cases:

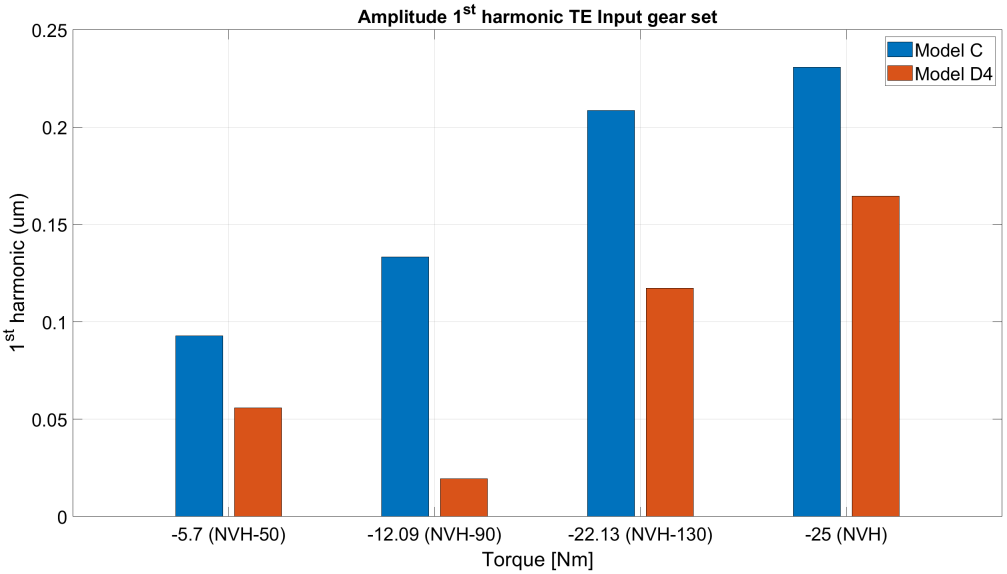

Figure 6.94: Amplitudes of 1^{st} harmonic TE, order 22, Input gear set, Models C, D4, NVH load cases

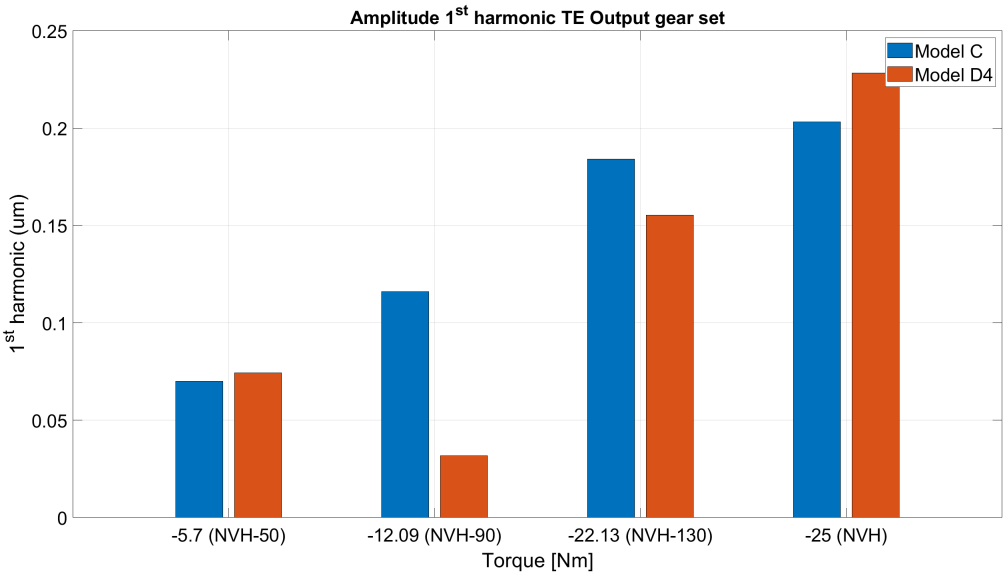

Figure 6.95: Amplitudes of 1^{st} harmonic TE, order 9.138, Output gear set, Models C, D4, NVH load cases

Let's now analyse the different dynamic results of these models, considering the load case *NVH*. Obviously, only the response due to the transmission error are taken into account now, since they are the only which are changing among the models. The responses to unbalance and to electromagnetic excitations are totally overlapping.

6.6.1 Excitation: 1^{st} Harmonic transmission error input gear set, Order 22

As already done, the first relevant result is the plot of the dynamic transmission error:

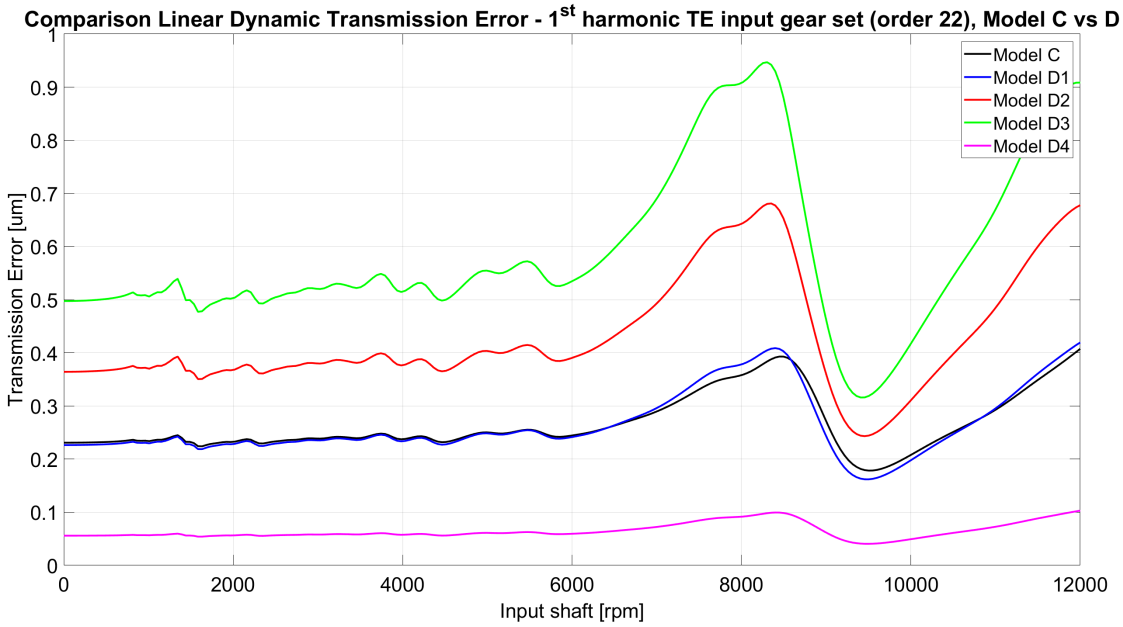

Figure 6.96: Linear Dynamic TE, 1^{st} harmonic TE, Input gear set, Comparison Model C vs D

It appears evident the strong improvement that is achievable considering Model D4.
Moreover, considering the ERP and MSV plots, the values of Model D4 are way lower, at least one order of magnitude, with respect to all other models: this certifies the goodness of Model D4.
On the other hand, the Model D3 leads to very poor NVH performance. This is not surprising, since that model has been built in order to just optimize the contact patch, without caring about dynamic characteristics (Section 4.2.7).

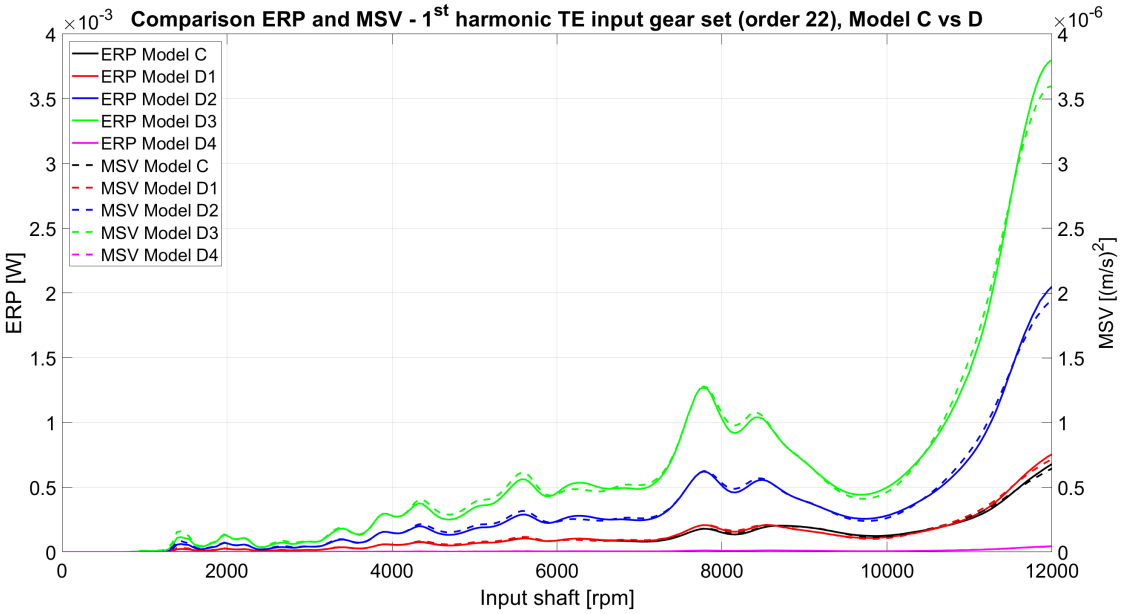

Figure 6.97: ERP and MSV, 1^{st} harmonic TE, Input gear set, Comparison Model C vs D

Excitation	Speed (rpm)	Frequency (Hz)	Value (W)
Model C	7776	2851.2	$1.8 \cdot 10^{-4}$
	12000	4400	$6.8 \cdot 10^{-4}$
Model D1	7776	2851.2	$2.1 \cdot 10^{-4}$
	12000	4400	$7.6 \cdot 10^{-4}$
Model D2	7776	2851.2	$6.2 \cdot 10^{-4}$
	12000	4400	$2.0 \cdot 10^{-3}$
Model D3	7776	2851.2	$1.3 \cdot 10^{-3}$
	12000	4400	$3.8 \cdot 10^{-3}$
Model D4	7776	2851.2	$1.2 \cdot 10^{-5}$
	12000	4400	$4.5 \cdot 10^{-5}$

Table 6.16: Comparison of ERP peaks among the different models, 1^{st} harmonic TE input gear set

Then, other relevant results concern the response at the housing mounts, which are reported in Figures 6.98-6.100.

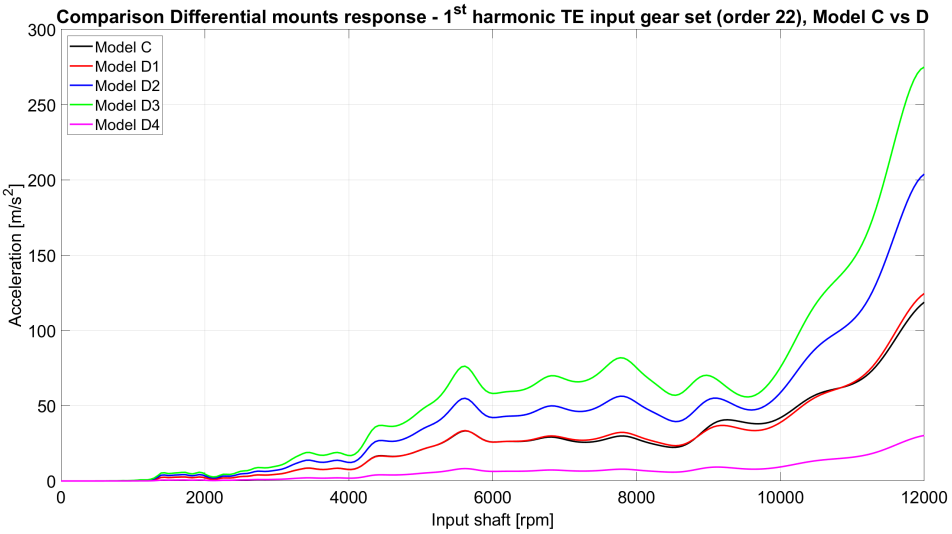

Figure 6.98: Differential mount response, 1^{st} harmonic TE, Input gear set, Comparison Model C vs D

Excitation	Speed (rpm)	Frequency (Hz)	Value (m/s^2)
Model C	5616	2059.2	33.3
	7776	2851.2	29.9
	12000	4400	118.8
Model D1	5616	2059.2	33.4
	7776	2851.2	32.3
	12000	4400	124.5
Model D2	5616	2059.2	54.9
	7776	2851.2	56.3
	12000	4400	203.8
Model D3	5616	2059.2	76.2
	7776	2851.2	81.9
	12000	4400	274.9
Model D4	5616	2059.2	8.2
	7776	2851.2	7.8
	12000	4400	30.2

Table 6.17: Comparison acceleration peaks at differential mount among the different models, 1^{st} harmonic TE input gear set

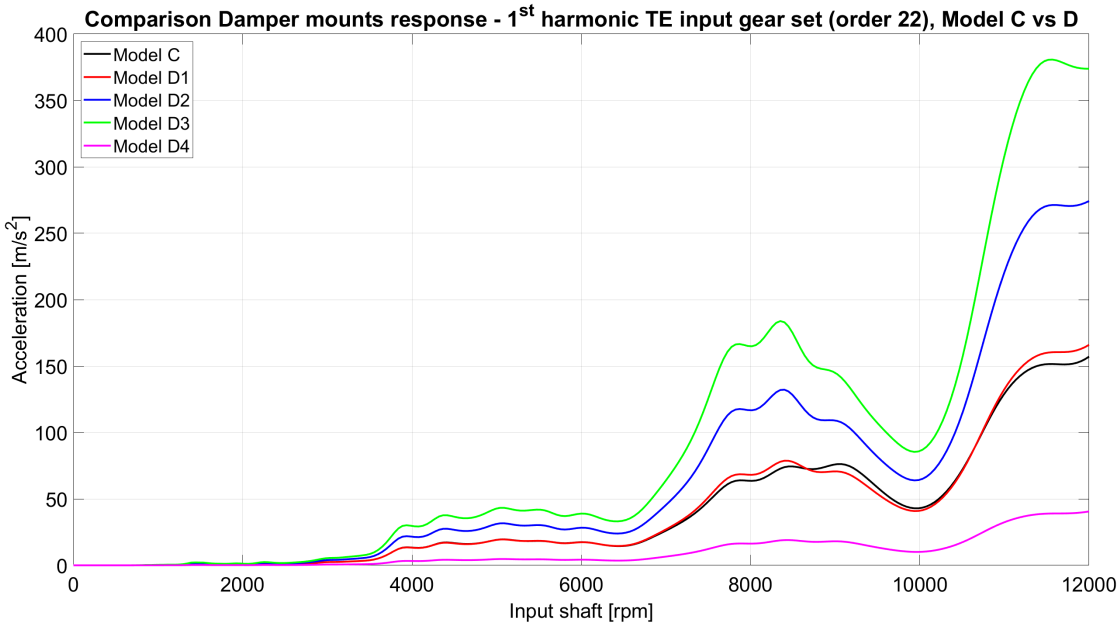

Figure 6.99: Damper mount response, 1^{st} harmonic TE, Input gear set, Comparison Model C vs D

Excitation	Speed (rpm)	Frequency (Hz)	Value (m/s^2)
Model C	8352 11520	3062.4 4224	72.8 151.5
Model D1	8352 11520	3062.4 4224	78.0 160.2
Model D2	8352 11520	3062.4 4224	132.0 270.9
Model D3	8352 11520	3062.4 4224	183.9 380.6
Model D4	8352 11520	3062.4 4224	18.8 39.0

Table 6.18: Comparison acceleration peaks at damper mount among the different models, 1^{st} harmonic TE input gear set

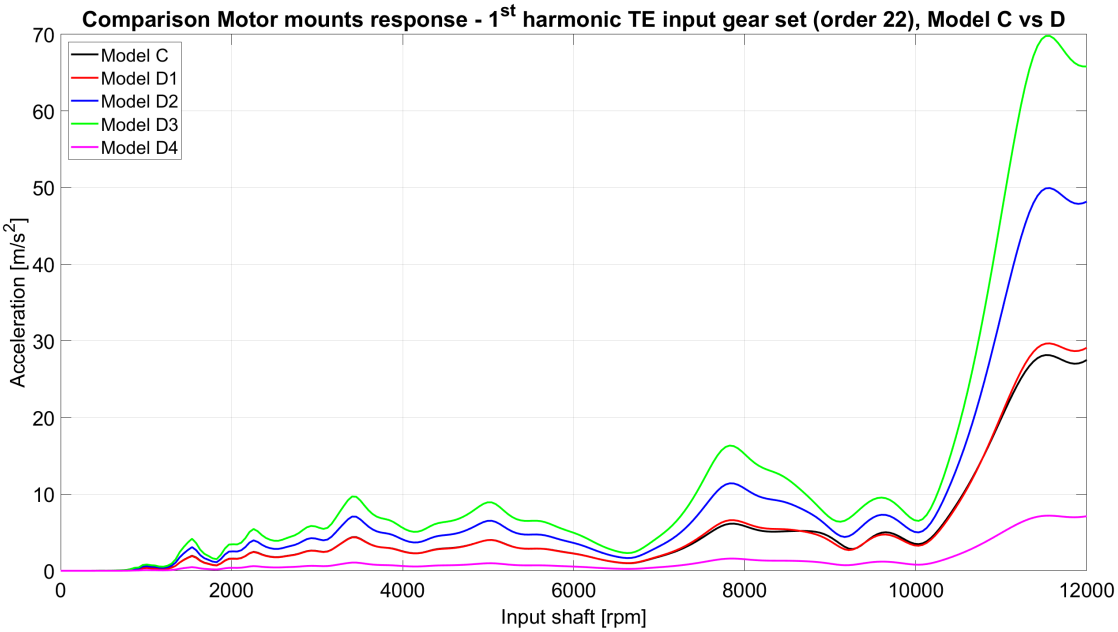

Figure 6.100: Motor mount response, 1^{st} harmonic TE, Input gear set, Comparison Model C vs D

Excitation	Speed (rpm)	Frequency (Hz)	Value (m/s^2)
Model C	7824	2868.8	6.1
	11520	4224	28.1
Model D1	7824	2868.8	6.6
	11520	4224	29.6
Model D2	7824	2868.8	11.4
	11520	4224	49.9
Model D3	7824	2868.8	16.3
	11520	4224	69.8
Model D4	7824	2868.8	1.6
	11520	4224	7.2

Table 6.19: Comparison acceleration peaks at motor mount among the different models, 1^{st} harmonic TE input gear set

Considering all housing mounts, the Model D4 is the one that ensures the best NVH performance. The reduction of the recorded acceleration is remarkable in all considered mounts. Looking also at peak values, the responses of Model D4 is at least one order of magnitude smaller with respect to other models. Microgeometry D1 leads to almost overlapping results with respect to C (no microgeometry), while D2 is slightly worse. Finally, as expected, D3 provides the worst performance, being totally inappropriate for NVH optimization.
Moreover, even regarding the accelerometer response the enhancement achieved considering Model D4 is confirmed, as indicated by Figure 6.101.

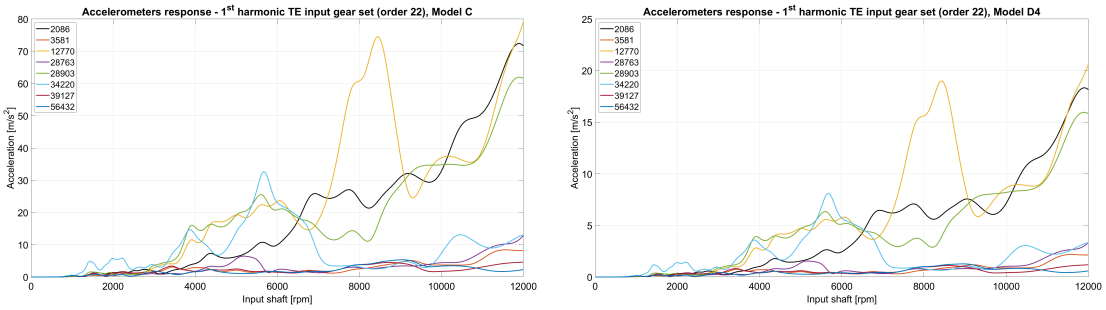

(a) *Model C* **(b)** *Model D4*

Figure 6.101: Comparison Model C vs D4, accelerometers response, 1^{st} harmonic TE input gear set

The two models provide responses that have the same behaviour, but the difference in amplitude is evident. The largest peak, considering Model C (no microgeometry) reaches almost 80 m/s^2, while as far as the Model D4 (with microgeometry) is examined, the peak is lowered to 20 m/s^2.
All the above considerations are done considering just the 1^{st} harmonic of input TE, in the following pages the output gear set is taken into account, too.

6.6.2 Excitation: 1^{st} Harmonic transmission error output gear set, Order 9.138

Figure 6.102: Linear Dynamic TE, 1^{st} harmonic TE, Output gear set, Comparison Model C vs D

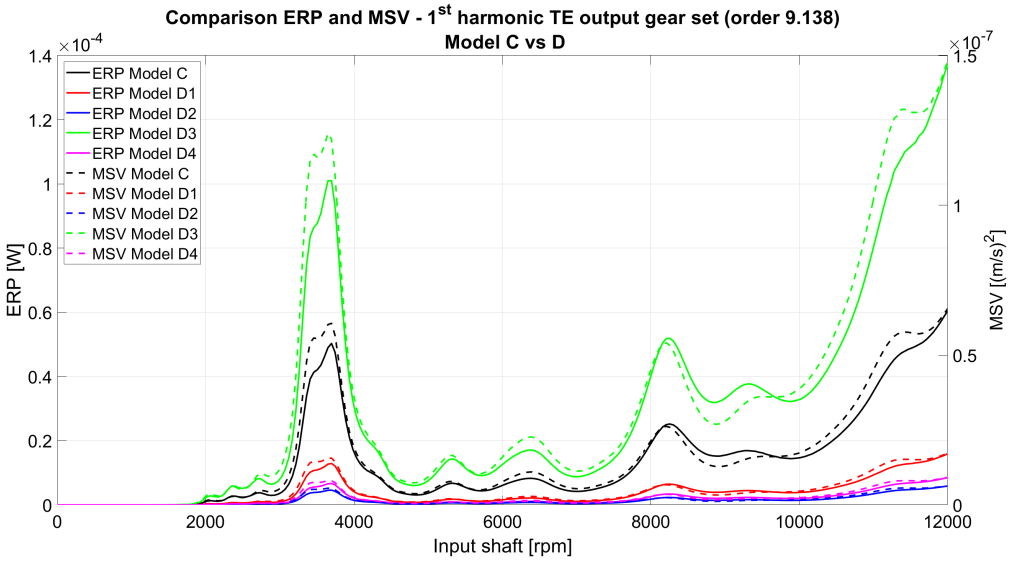

Figure 6.103: ERP and MSV, 1^{st} harmonic TE, Output gear set, Comparison Model C vs D

Excitation	Speed (rpm)	Frequency (Hz)	Value (W)
Model C	3696	562.93	$5.0 \cdot 10^{-5}$
	8256	1257.4	$2.5 \cdot 10^{-5}$
	12000	1827.7	$6.0 \cdot 10^{-5}$
Model D1	3696	562.93	$1.3 \cdot 10^{-5}$
	8256	1257.4	$6.5 \cdot 10^{-6}$
	12000	1827.7	$1.6 \cdot 10^{-5}$
Model D2	3696	562.93	$4.6 \cdot 10^{-6}$
	8256	1257.4	$2.3 \cdot 10^{-6}$
	12000	1827.7	$5.9 \cdot 10^{-6}$
Model D3	3696	562.93	$1.0 \cdot 10^{-4}$
	8256	1257.4	$5.2 \cdot 10^{-5}$
	12000	1827.7	$1.4 \cdot 10^{-4}$
Model D4	3696	562.93	$6.7 \cdot 10^{-6}$
	8256	1257.4	$3.4 \cdot 10^{-6}$
	12000	1827.7	$8.5 \cdot 10^{-6}$

Table 6.20: Comparison of ERP peaks among the different models, 1^{st} harmonic TE output gear set

Looking at Figure 6.103 and at Table 6.20, it can be noted that all the modified models, with the exception of Model D3, lead to strong reduction of both the ERP and the MSV.

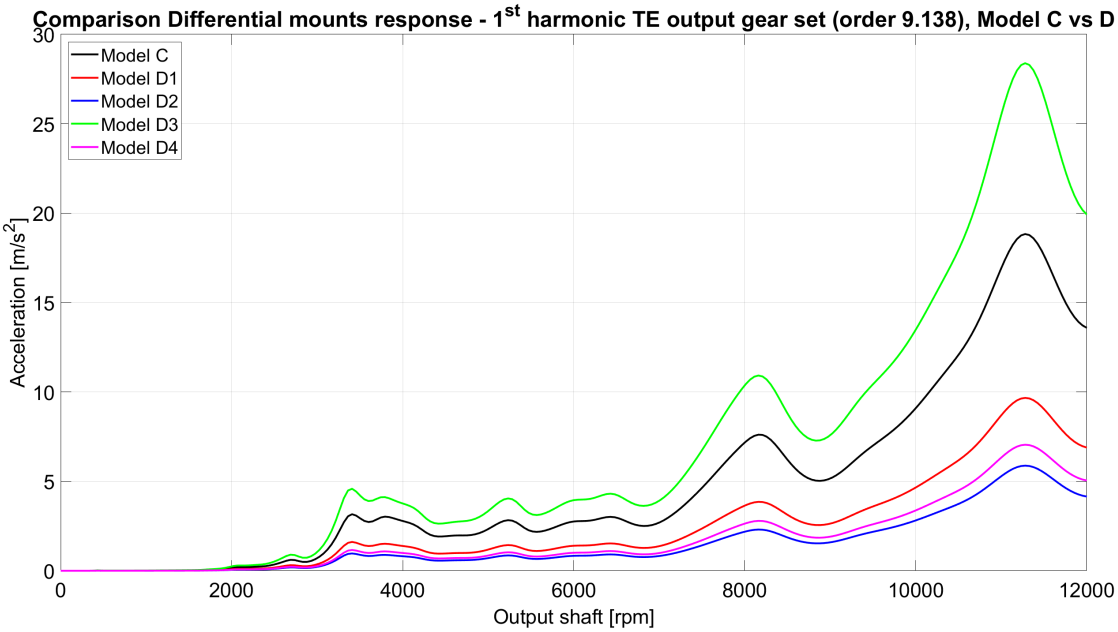

Figure 6.104: Differential mount response, 1^{st} harmonic TE, Output gear set, Comparison Model C vs D

Excitation	Speed (rpm)	Frequency (Hz)	Value (m/s^2)
Model C	8160	1242.8	7.6
	11280	1718.0	18.8
Model D1	8160	1242.8	3.9
	11280	1718.0	9.7
Model D2	8160	1242.8	2.3
	11280	1718.0	5.9
Model D3	8160	1242.8	10.9
	11280	1718.0	28.4
Model D4	8160	1242.8	2.8
	11280	1718.0	7.0

Table 6.21: Comparison acceleration peaks at differential mount among the different models, 1^{st} harmonic TE output gear set

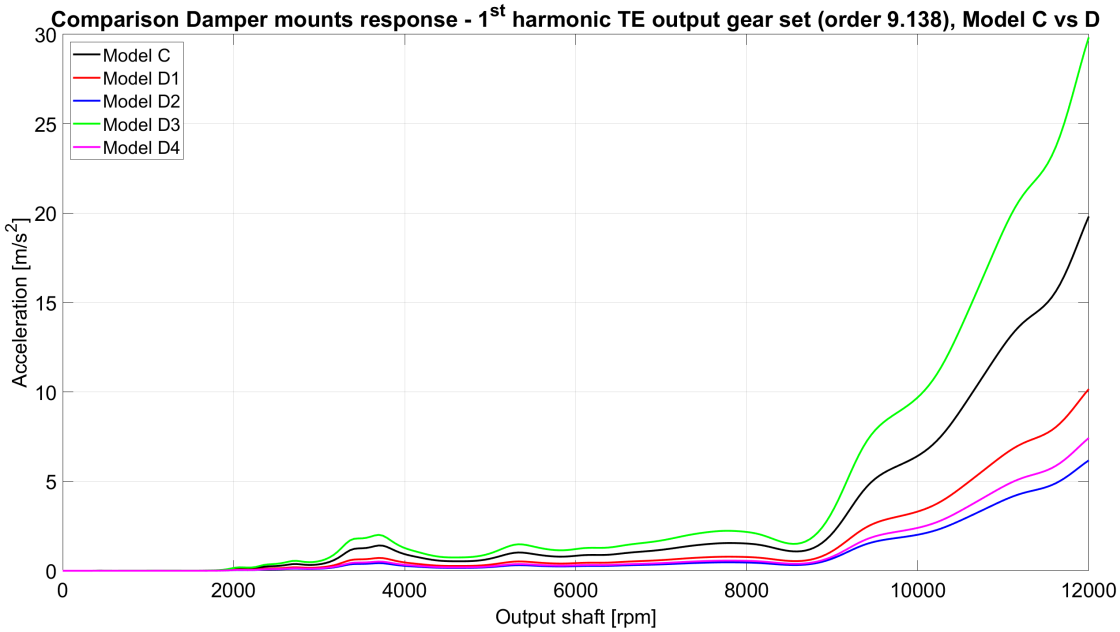

Figure 6.105: Damper mount response, 1^{st} harmonic TE, Output gear set, Comparison Model C vs D

Excitation	Speed (rpm)	Frequency (Hz)	Value (m/s^2)
Model C	12000	1827.7	19.8
Model D1	12000	1827.7	10.2
Model D2	12000	1827.7	6.2
Model D3	12000	1827.7	29.8
Model D4	12000	1827.7	7.4

Table 6.22: Comparison acceleration peaks at damper mount among the different models, 1^{st} harmonic TE output gear set

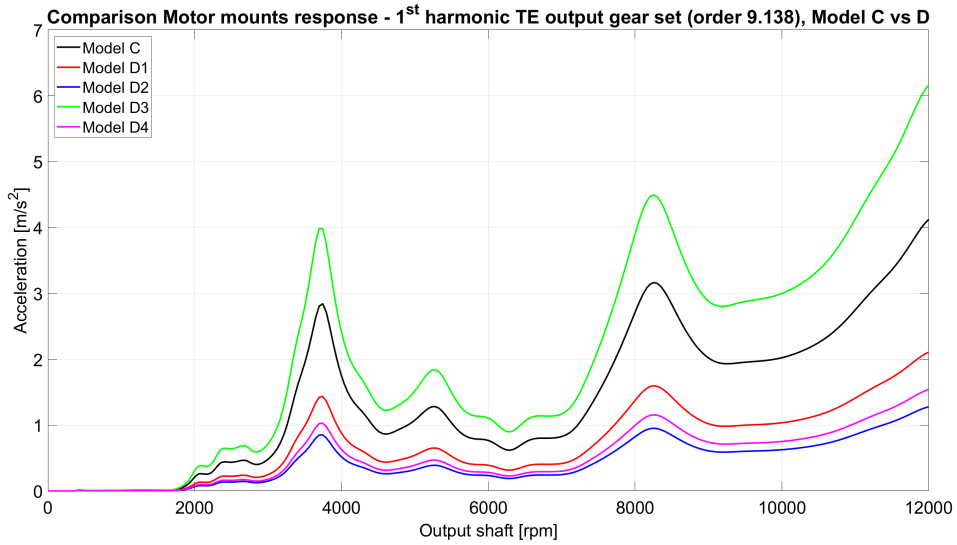

Figure 6.106: Motor mount response, 1^{st} harmonic TE, Output gear set, Comparison Model C vs D

Excitation	Speed (rpm)	Frequency (Hz)	Value (m/s^2)
Model C	3744	570.2	2.8
	8256	1257.5	3.2
	12000	1827.7	4.1
Model D1	3744	570.2	1.4
	8256	1257.5	1.6
	12000	1827.7	2.1
Model D2	3744	570.2	0.9
	8256	1257.5	1.0
	12000	1827.7	1.3
Model D3	3744	570.2	4.0
	8256	1257.5	4.5
	12000	1827.7	6.2
Model D4	3744	570.2	1.0
	8256	1257.5	1.2
	12000	1827.7	1.5

Table 6.23: Comparison acceleration peaks at motor mount among the different models, 1^{st} harmonic TE output gear set

Investigating Figures 6.102-6.106, it appears clear the improvement of the NVH performance obtainable using the microgeometry modifications of Model D4.
The peaks reported in Tables 6.21-6.23 demonstrate that adopting the proper microgeometry modifications, as it has been done in Model D4, it is possible to even more than halve the response at any housing mount, with respect to Model C (i.e. without microgeometry modifications).
However, among all models, Model D2 leads to even better results than Model D4. Anyway, Model D4 permits to have a remarkable reduction of the response with respect to Model C, too. The difference between Model D2 and D4 is actually slight. A brief deepening will be provided by Figures 6.116-6.119.
However, remember that only the load case *NVH* has been considered so far, hence the above considerations are not enough to state that Model D4 is worse than D2 concerning the 1^{st} harmonic of the output TE. Indeed, in the following section, all the relevant load cases are investigated, and the supremacy Model D4 is demonstrated.
Furthermore, even a comparison of the accelerometers response between Model C and D4 can be interesting, as highlighted in Figure 6.107. The improvement obtained moving to D4 is evident since the magnitude of the response is more than halved with respect to C.

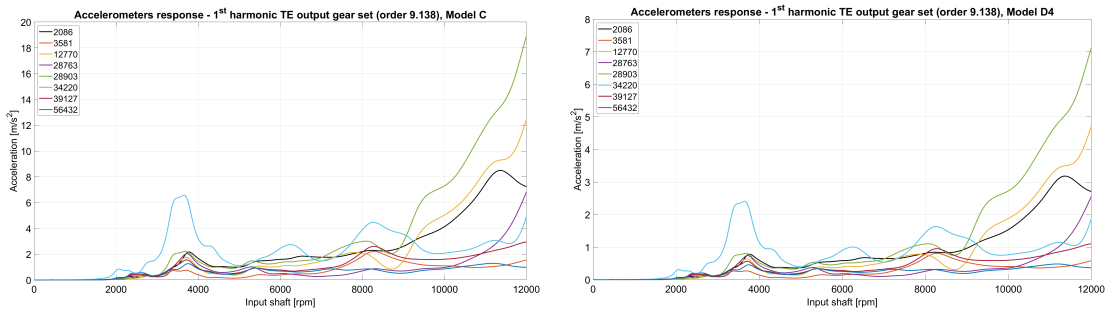

(a) *Model C* **(b)** *Model D4*

Figure 6.107: Comparison Model C vs D4, accelerometers response, 1^{st} harmonic TE output gear set

6.6.3 Comparison among load cases

As explained in Section 6.1, many load cases can be interesting for NVH analyses. Just for the sake of clarity let's report again the table which indicates all load cases.

Load case name	Vehicle speed [km/h]	P [kW]	T [Nm]	n [rpm]
NVH-50	50	2.41	5.70	4046.79
NVH	62	13.09	25	5000
NVH-90	90	9.22	12.09	7283.54
NVH-130	130	24.3	22.13	10520.27

Table 6.24: Analyzed load cases

A comparison of the principal results can be performed, investigating the difference between Model C (helical gears, with profile shift but without microgeometry modifications) and Model D4. To do the comparison, the Model D4 has been selected since it is the one with microgeometry modifications that lead to the best results.
First of all, comparing the ERP and MSV response due to the 1^{st} harmonic of the input TE, Figure 6.108, it is evident the better performance of the Model D4 in almost every load case. Only considering *NVH-50*, Model D4 shows a slightly higher response. Furthermore, it is safe to say that Model D4 is particularly optimized for the load cases *NVH* and *NVH-130*.

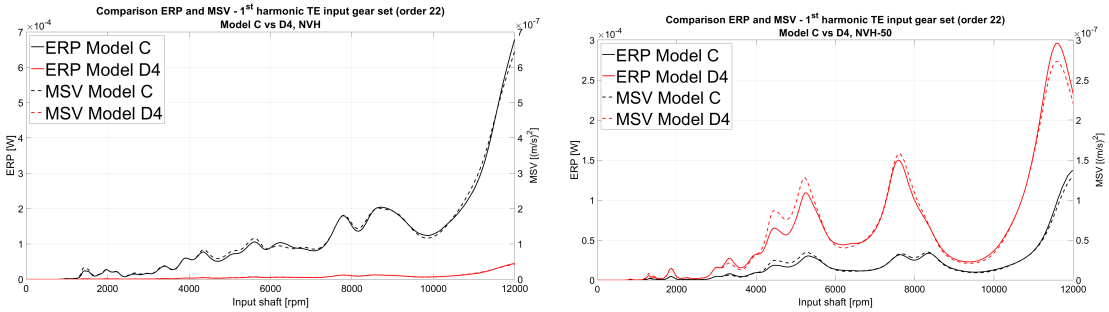

(a) *Load case NVH*

(b) *Load case NVH-50*

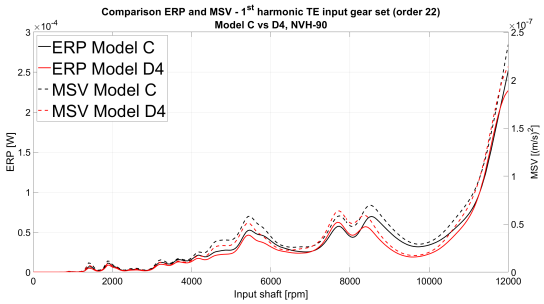

(c) *Load case NVH-90*

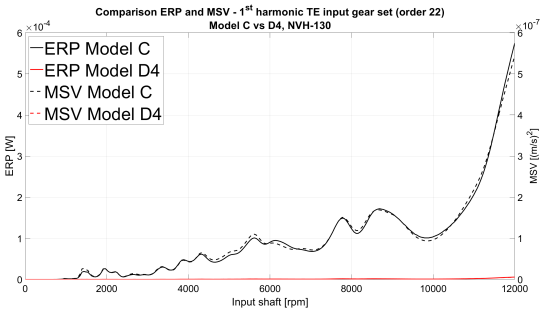

(d) *Load case NVH-130*

Figure 6.108: Comparison ERP and MSV, all load cases, 1^{st} harmonic input TE, Model C vs Model D4

Considering the housing mounts response, the trend is confirmed: Model D4 provides remarkable reduction of response considering load cases *NVH* and *NVH-130*. Again, taking into account *NVH-50*, Model C actually leads to better results. Furthermore, considering all load cases, the motor mount is the one that records the smallest response in the whole shaft speed range.
All mounts show a generally growing trend as the shaft speed increases. In particular, the values of the motor mount are almost negligible up to $\approx$ 10000 rpm.

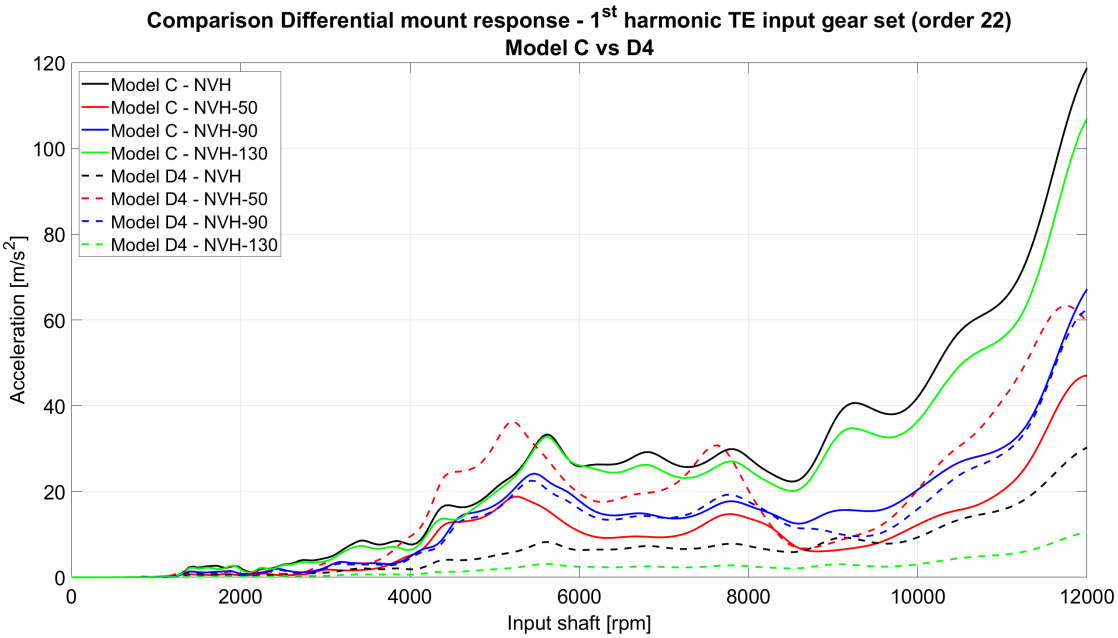

Figure 6.109: Differential mount response, all load cases, 1^{st} harmonic input TE, Comparison Model C vs D4

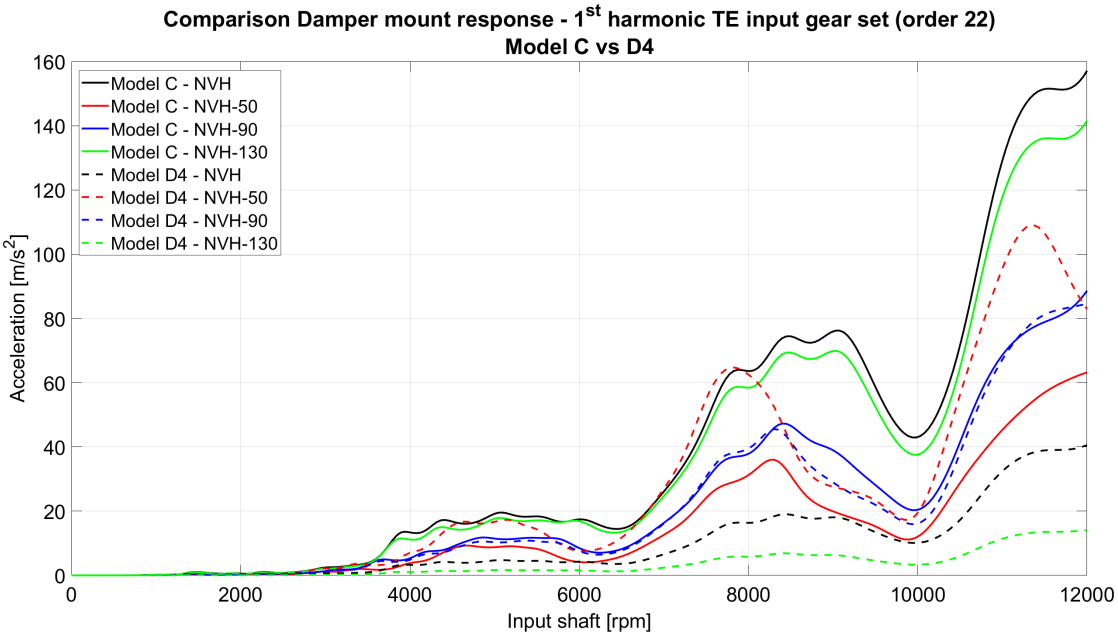

Figure 6.110: Damper mount response, all load cases, 1^{st} harmonic input TE, Comparison Model C vs D4

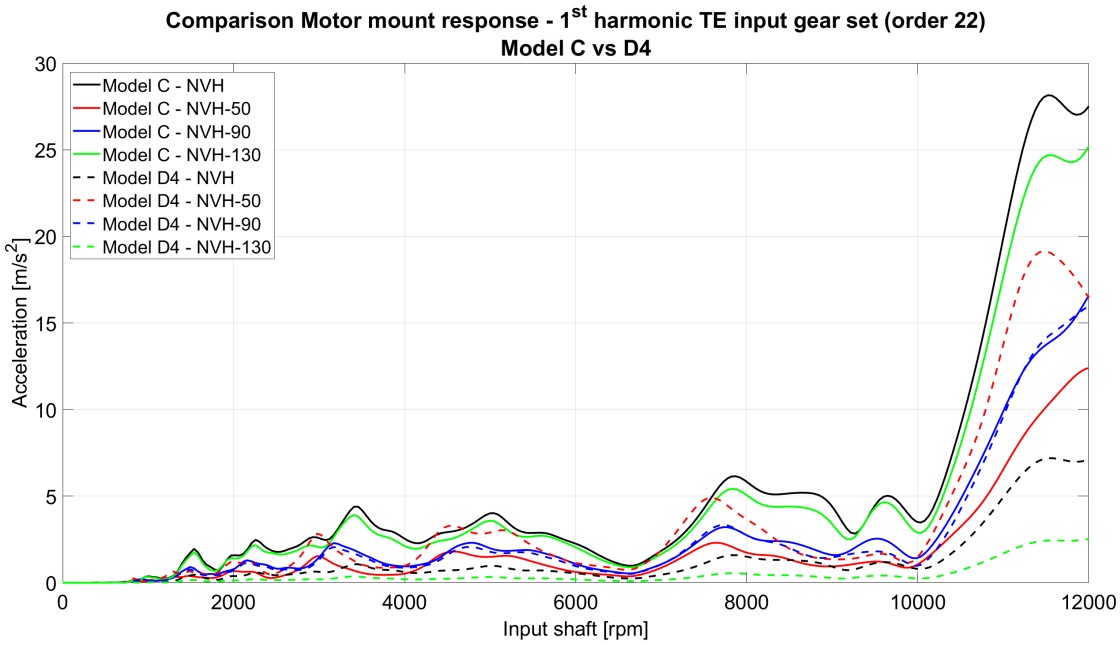

Figure 6.111: Motor mount response, all load cases, 1^{st} harmonic input TE, Comparison Model C vs D4

Furthermore, considering the 1^{st} harmonic of TE of the output gear set, Model D4 permits to reduce the response only considering *NVH* and *NVH-130*, exactly as considering TE of the input gear set, while inspecting *NVH-90* a slight worsening can be noted. Finally, *NVH-50* shows significantly better results adopting Model C.

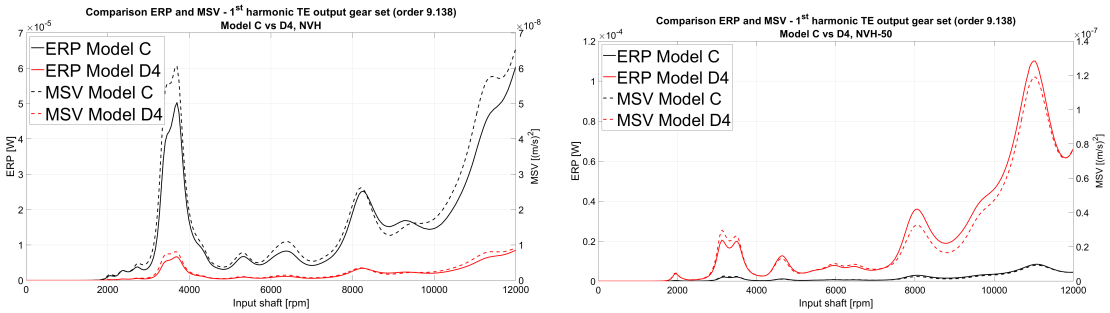

(a) *Load case NVH*

(b) *Load case NVH-50*

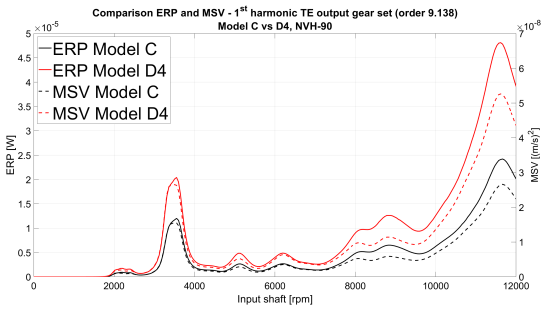

(c) *Load case NVH-90*

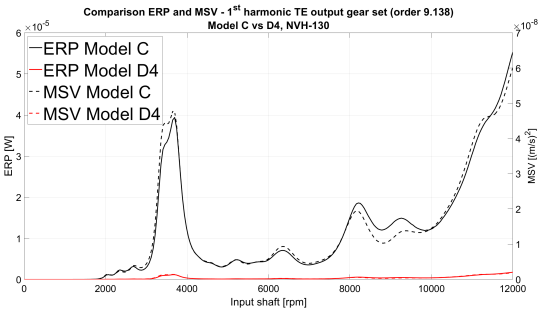

(d) *Load case NVH-130*

Figure 6.112: Comparison ERP and MSV, all load cases, 1^{st} harmonic output TE, Model C vs Model D4

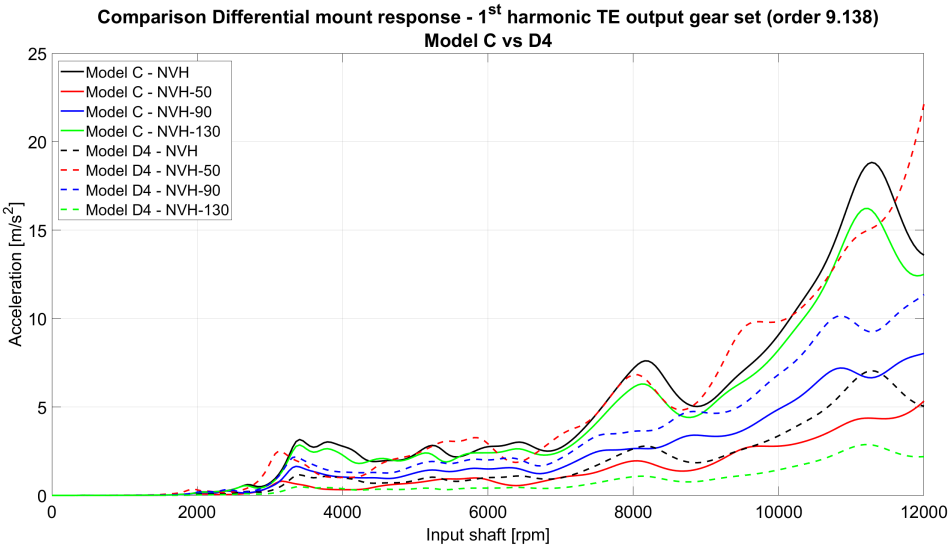

Figure 6.113: Differential mount response, all load cases, 1^{st} harmonic output TE, Comparison Model C vs D4

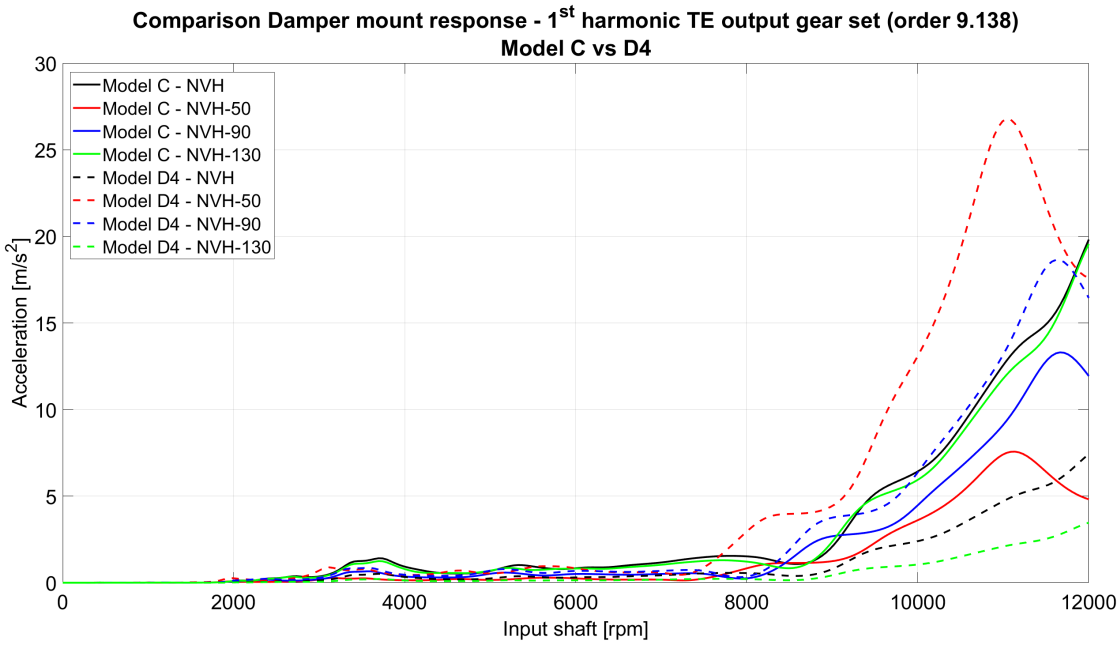

Figure 6.114: Damper mount response, all load cases, 1^{st} harmonic output TE, Comparison Model C vs D4

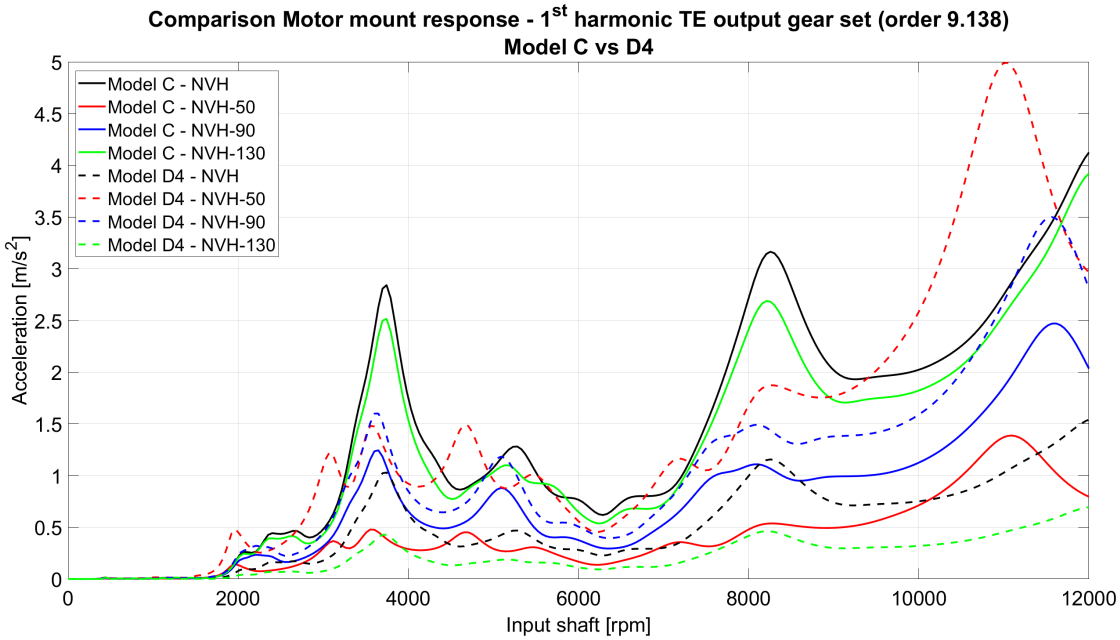

Figure 6.115: Motor mount response, all load cases, 1^{st} harmonic output TE, Comparison Model C vs D4

The above results certify the difficulty of selecting the correct microgeometry parameters. Even using the optimization tool provided by Romax, only having a good experience is possible to achieve the desired results.
Moreover, a certain optimization can perfectly suit for a certain load case, while it can be terrible for another one. Indeed, since in this case study many load cases are of NVH interest, it is very challenging to properly optimize all of them. However, Model D4 allows to achieve pretty good results in overall.
The following plots represent a comparison of Model D2 and D4, considering output TE as excitation. The pictures certify that Model D4 shows better results overall: only considering *NVH*, Model D2 is actually better than D4. However, comparing all relevant NVH load cases, it is pretty visible the superiority of Model D4 over D2.

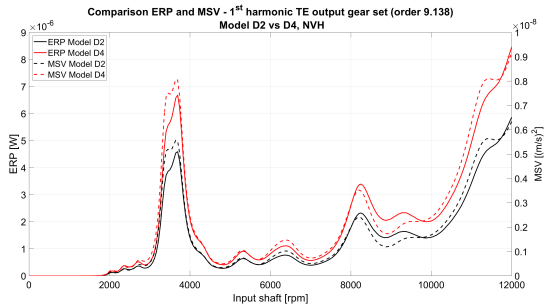

(a) *Load case NVH*

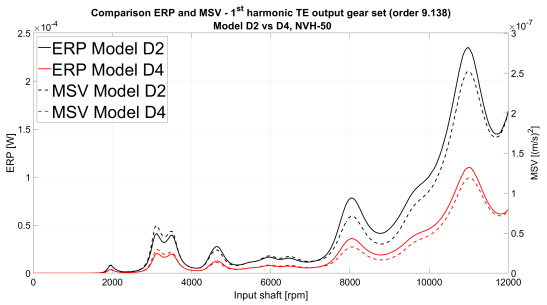

(b) *Load case NVH-50*

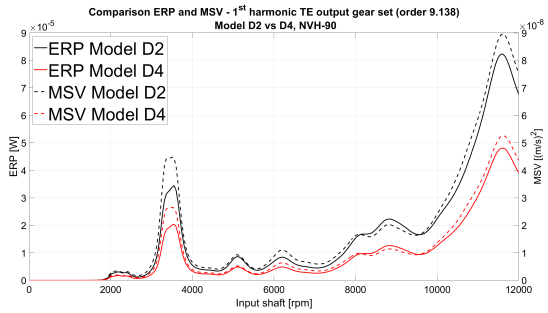

(c) *Load case NVH-90*

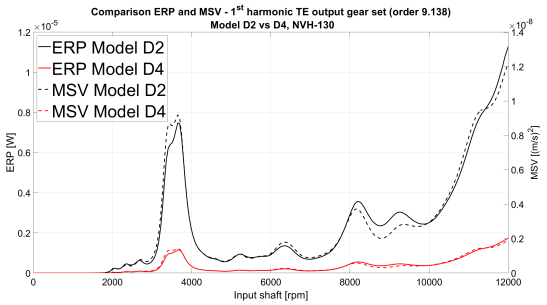

(d) *Load case NVH-130*

Figure 6.116: Comparison ERP and MSV, all load cases, 1^{st} harmonic output TE, Model D2 vs Model D4

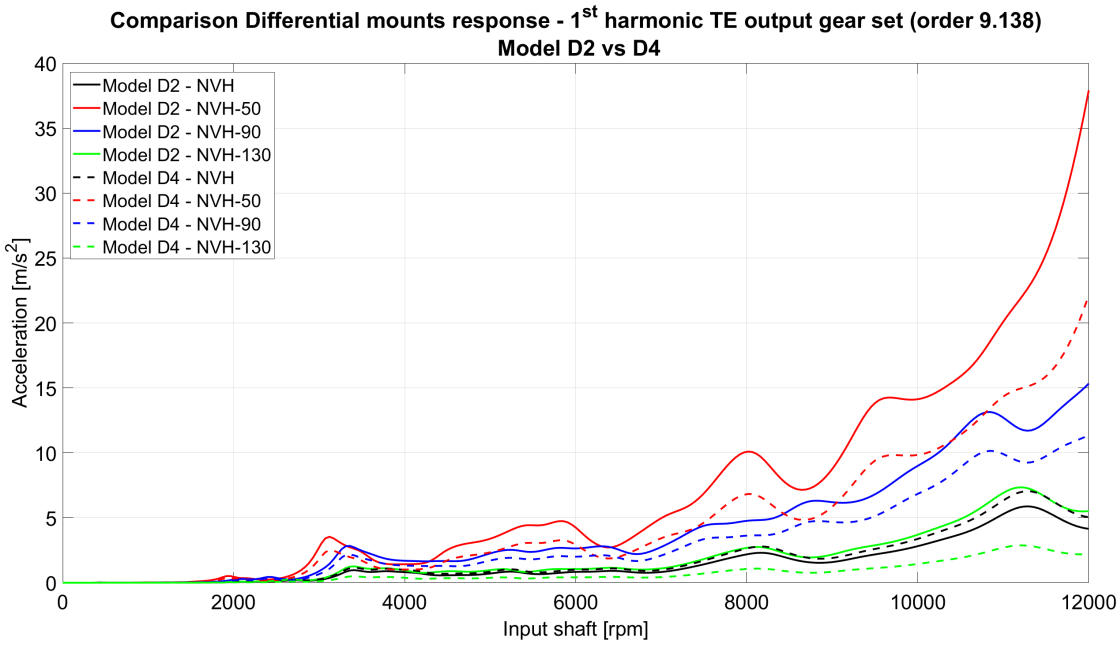

Figure 6.117: Differential mount response, all load cases, 1^{st} harmonic output TE, Comparison Model D2 vs D4

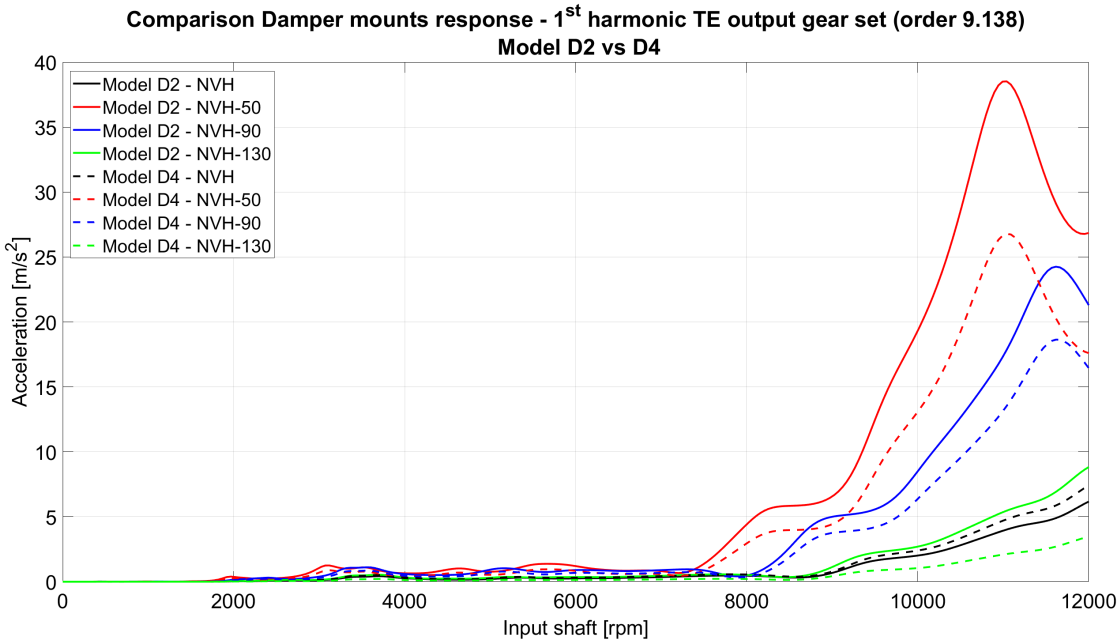

Figure 6.118: Damper mount response, all load cases, 1^{st} harmonic output TE, Comparison Model D2 vs D4

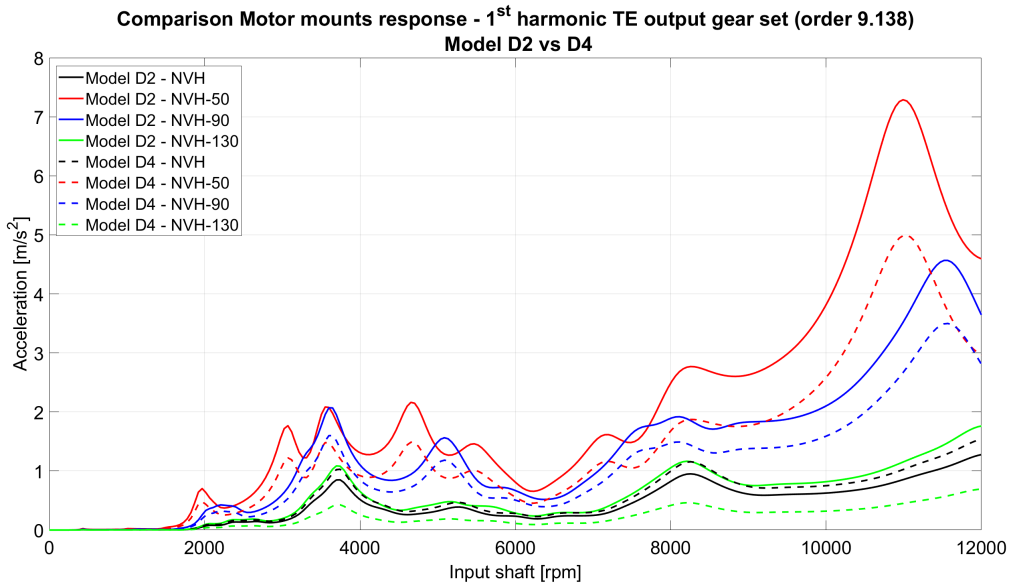

Figure 6.119: Motor mount response, all load cases, 1^{st} harmonic output TE, Comparison Model D2 vs D4

6.6.4 Comparison among exctitations, Model D4

Having proved that the Model D4 allows to achieve a certain enhancement of the NVH performances, it is now important to compare again the response to the different kind of excitations.

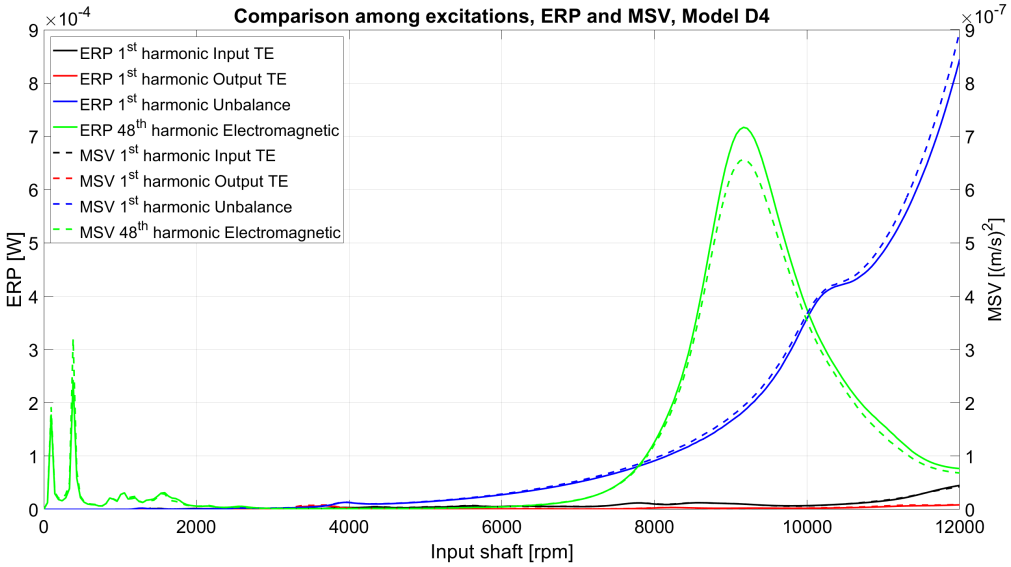

Figure 6.120: Comparison among excitations, ERP and MSV, Model D4

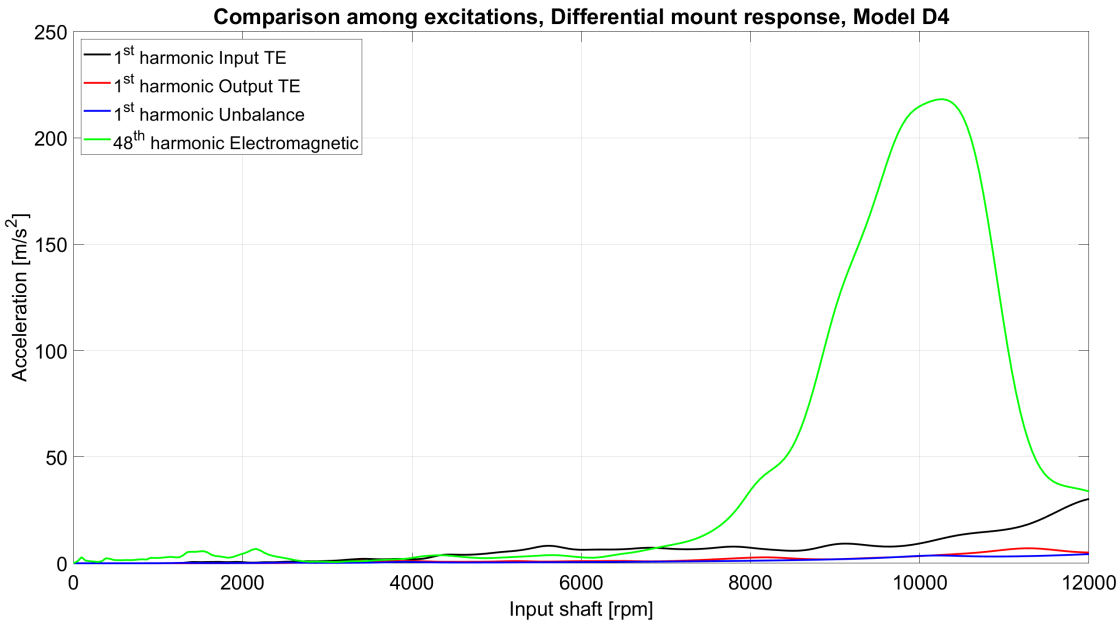

Figure 6.121: Comparison among excitations, differential mount response, Model D4

Excitation	Speed (rpm)	Frequency (Hz)	Value (m/s^2)
1^{st} harmonic input TE	10272	3766.4	11.7
1^{st} harmonic output TE	10272	1564.5	4.0
N_{slots} harmonic electromagnetic	10272	8217.6	218.2
1^{st} harmonic unbalance	10272	171.2	3.6

Table 6.25: Comparison differential mount response among different excitation, Model D4

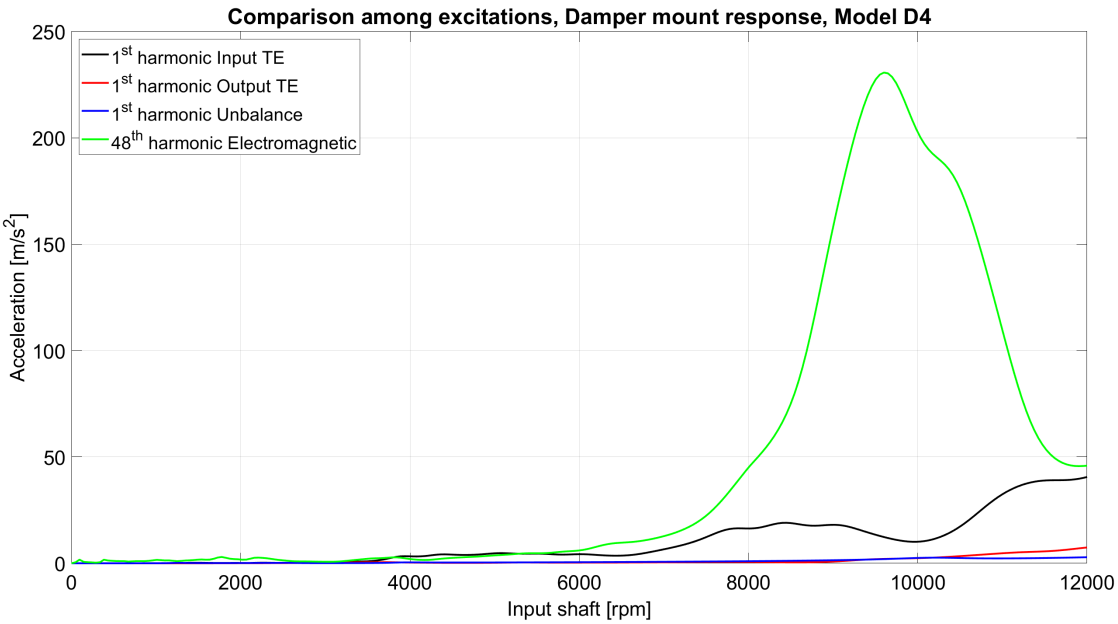

Figure 6.122: Comparison among excitations, damper mount response, Model D4

Excitation	Speed (rpm)	Frequency (Hz)	Value (m/s^2)
1^{st} harmonic input TE	9600	3520	12.3
1^{st} harmonic output TE	9600	1462.2	2.0
N_{slots} harmonic electromagnetic	9600	7680	230.7
1^{st} harmonic unbalance	9600	160	2.0

Table 6.26: Comparison damper mount response among different excitation, Model D4

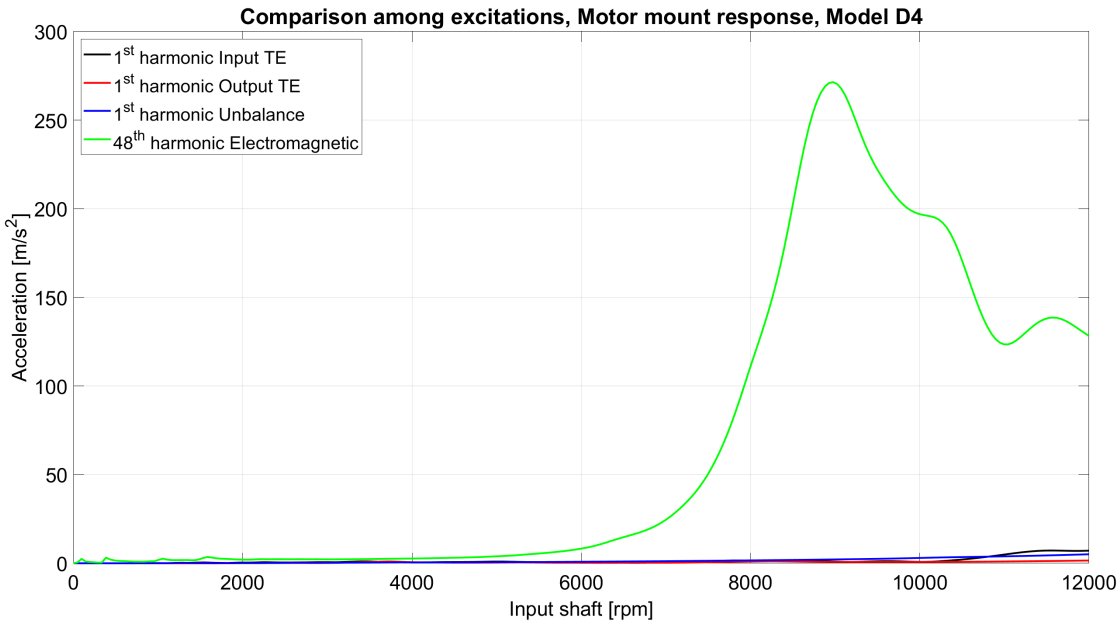

Figure 6.123: Comparison among excitations, motor mount response, Model D4

Excitation	Speed (rpm)	Frequency (Hz)	Value (m/s^2)
1^{st} harmonic input TE	8976	3291.2	1.0
1^{st} harmonic output TE	8976	1367.1	0.7
N_{slots} harmonic electromagnetic	8976	7180.8	271.4
1^{st} harmonic unbalance	8976	149.6	2.1

Table 6.27: Comparison motor mount response among different excitation, Model D4

From Figures 6.120-6.123, and from Tables 6.25-6.27, which report the value of the most relevant peak of each case, it is clear the benefits brought by Model D4. Indeed, the acceleration at the housing mounts caused by the gear sets is almost negligible: the response is caused almost entirely by the 48^{th} harmonic of the electromagnetic excitation.
As already explained, as regards the housing mounts, another useful result is represented by the force response. Comparing the results of Model C and D4, it is further proved the goodness of Model D4, highlighted by a remarkable reduction of the force response at each mount. In any case, at each mount the evaluated force is pretty low along all speed range.

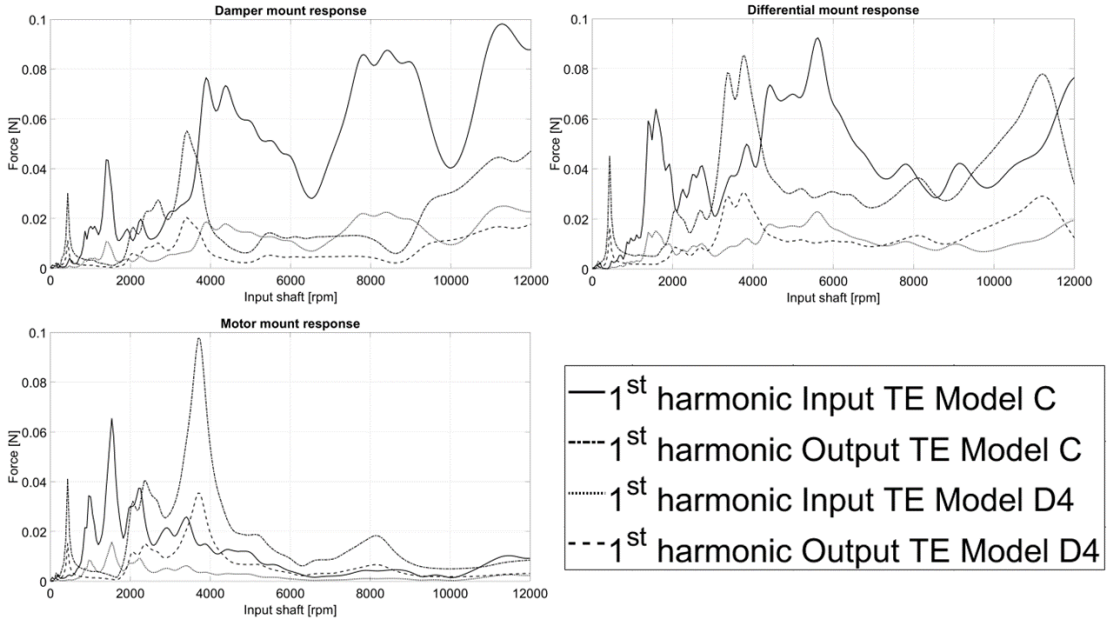

Figure 6.124: Housing mounts force response, Model C vs D4

Therefore, at this point it can be interesting to try to perform a sensitivity analysis regarding the excitations coming from the electric motor, which is done in Chapter 7. But, before that, a deepening on the acoustic can be done.

6.7 Acoustic analyses

Through the acoustic analysis, it is possible to predict the radiated noise from the powertrain, gaining important information about the directivity of the sound, too. The first crucial step is to define the so called *shrinkwrap mesh*, which is defined by [22] as an interface between the vibrations generated by the powertrain structure and the air acoustic domain.
The radiated sound is evaluated through 40 virtual microphones positioned on a sphere around the housing, according to standard ISO 3744. The achievable results are in terms of directivity, pressure (calculated at each microphone) and power (computed as sum of the power of all microphones) of the sound radiated.

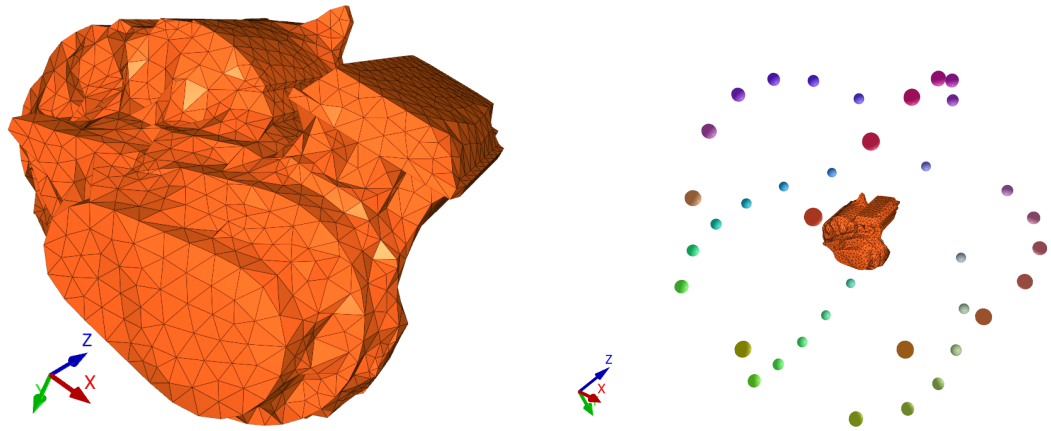

(a) *Shrinkwrap mesh* **(b)** *Position of microphones*

Figure 6.125: Shrinkwrap mesh and microphones placed according to ISO 3744

Acoustic analysis is very heavy from computational viewpoint, and with the available work station, the maximum frequency range which can be analysed is $0 \div 4400\ Hz$. This range is enough to completely investigate the results of all considered excitation sources, with the exception of the 48^{th} harmonic of the electromagnetic excitation. Indeed, recalling the maximum speed of the motor of 12000 rpm, and reminding the formula which allows to move from rpm to Hz

$$frequency\ (Hz) = speed\ (rpm) \cdot \frac{harmonic\,order}{60}$$

the maximum frequency of each excitation is:

Excitation	Order	Maximum frequency (Hz)
1^{st} harmonic unbalance	1	200
1^{st} harmonic input TE	22	4400
1^{st} harmonic output TE	9.138	1827.7
N_{slots} harmonic electromagnetic excitation	48	9600

Table 6.28: Maximum frequency of each excitation

Let's analyse the load case *NVH*, considering just the models with helical gears, since they are more representative of the system. A comparison between the Model C (without microgeometry), and D4 (the one with the best microgeometry, from NVH viewpoint) will be carried out in the following pages.

6.7.1 Model C, helical gears with profile shift

As anticipated, the software offers the possibility to compute the radiated sound power by summing the contributions of all microphones around the gearbox: it is possible to make a comparison among the different excitation sources considered. The plot is in dB scale, with a reference of $10^{-12}\,W$. Unfortunately, considering the 48^{th} harmonic of electromagnetic excitation, the whole range of speed can not be covered: analysing just $4400\,Hz$, the maximum speed reached by that excitation, given the harmonic order 48, is just $5500\,rpm$.
The electromagnetic excitation is the one which causes high power at the lowest rotational speed of the motor, while the unbalance starts to emit power only at higher values of speed.
Among all excitations, the 1^{st} harmonic of the input gear set is clearly the one which leads to the highest values of noise power, along almost the whole speed range. The unbalance generates remarkable noise power only at very high rotational speed, while as long as the speed of the motor is low the power emitted is pretty low, too. Moreover, another important consideration is that the unbalance causes noise at a maximum frequency of 200 Hz. As indicated by the normal audiogram, Figure 1.1, this is not a very annoying frequency level for human's ear.

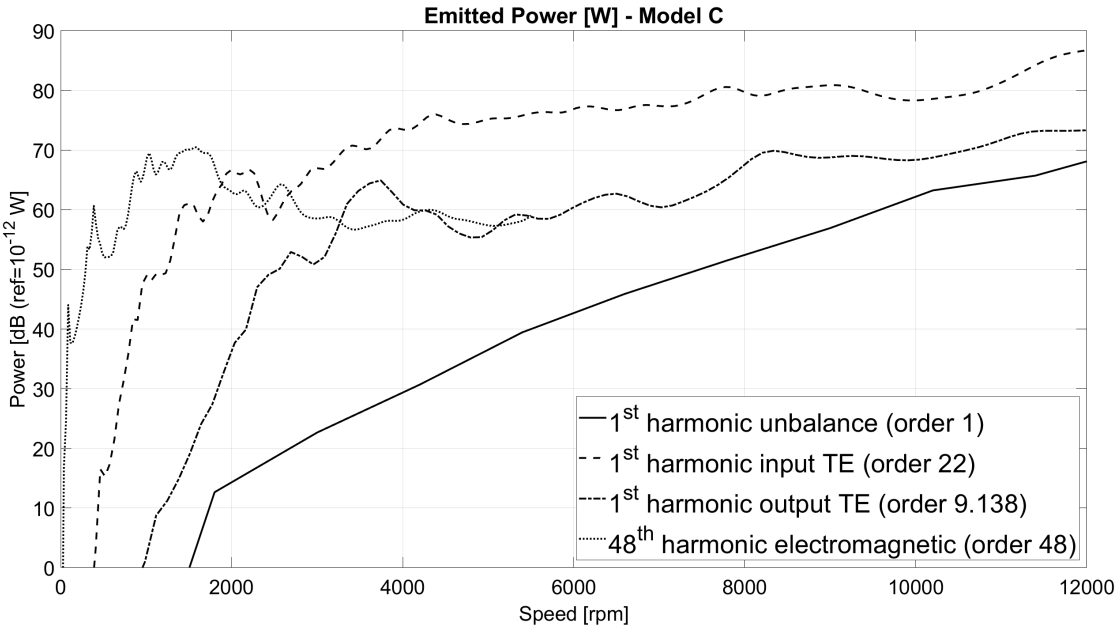

Figure 6.126: Power (W) vs Speed (rpm), Model C

Another plot which allows to effectively compare all excitation orders is the Waterfall, Figure 6.127. It shows the whole speed and frequency ranges, representing on the same plot all excitation orders considered. The results can be shown as

both power or pressure; in particular, in case of pressure, the values are the root mean square of the pressure amplitudes at all microphones.

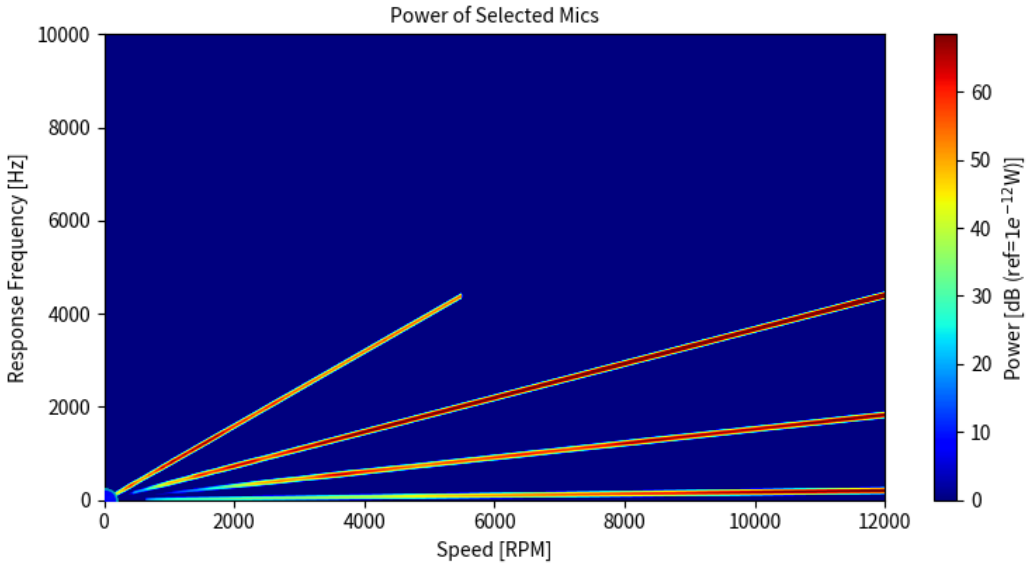

Figure 6.127: Waterfall plot, Model C

First of all, thanks to Figure 6.127, it appears evident the differences in the frequency ranges covered by each excitation, as indicated also by Table 6.28.
Waterfall plot is another way to observe that, to obtain a certain power, a remarkably lower shaft speed is needed considering as excitation the 48^{th} electromagnetic harmonic. On the other hand, the unbalance causes high power only at very high rotational speed.
To analyse the directivity of the radiated sound, it is possible to investigate the sound pressure recorded by each microphone around the gearbox. In the following plots, the microphones are represented as balls animated by both size and color: this means that the bigger the size and the reddish the color, then the higher is the pressure recorded. Please notice that the virtual microphones are just 40, as represented by Figure 6.125, however, to have a better representation, Romax allows to display more microphones, doing an interpolation.
For each excitation, two plots are represented: one showing the velocity on the housing surface, i.e. surface vibration velocity distribution, and one focusing on the pressure recorded by microphones.
It is possible to show the recording to just one excitation, and not all together, at a certain speed. For instance, to analyse a pretty relevant case, the rotational speed chosen is $5000\,rpm$, i.e. load case *NVH*.
To investigate the directivity of the radiated airborne noise is very important

to properly design the system. In fact, knowing in which direction the sound propagates more can really be helpful in design phase, to know where to properly act to reduce the propagation of noise.
Considering the unbalance, Figure 6.128, the maximum velocity on the housing is recorded on the side of the electric motor, about direction -x, while on the transmission system side the velocity is the smallest. For sure, an higher housing velocity leads to high pressure measured by microphones. Indeed, the highest pressure is recorded exactly on the region in front of the motor, about -x direction.

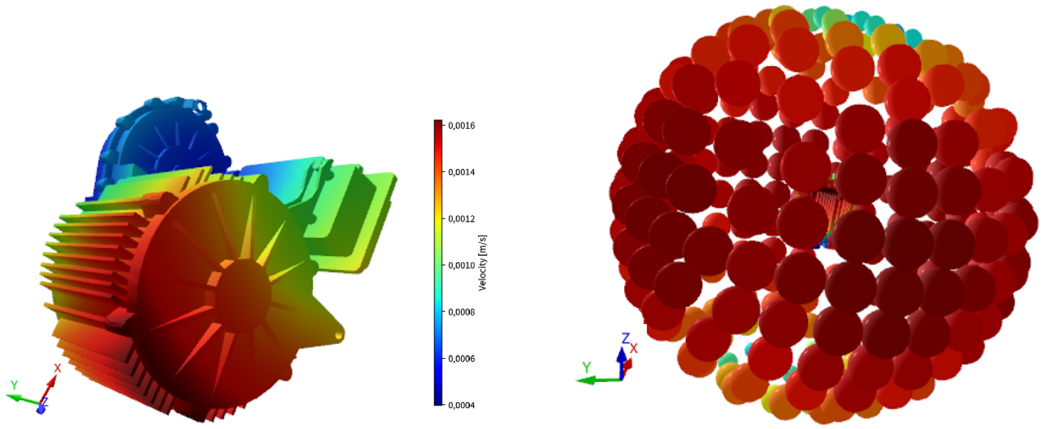

(a) *Velocity on housing* **(b)** *Microphones*

Figure 6.128: Acoustic results, 1^{st} harmonic unbalance, order 1, Model C,

Concerning the output TE, Figure 6.129, it appears evident how the highest velocity is noted close to the differential shaft, and hence close to the output wheel. As a consequence, the highest pressure is measured by microphones placed exactly in the region around the output wheel, about +x direction. On the other hand, on the electric motor side, the velocity, and therefore the pressure is the lowest.

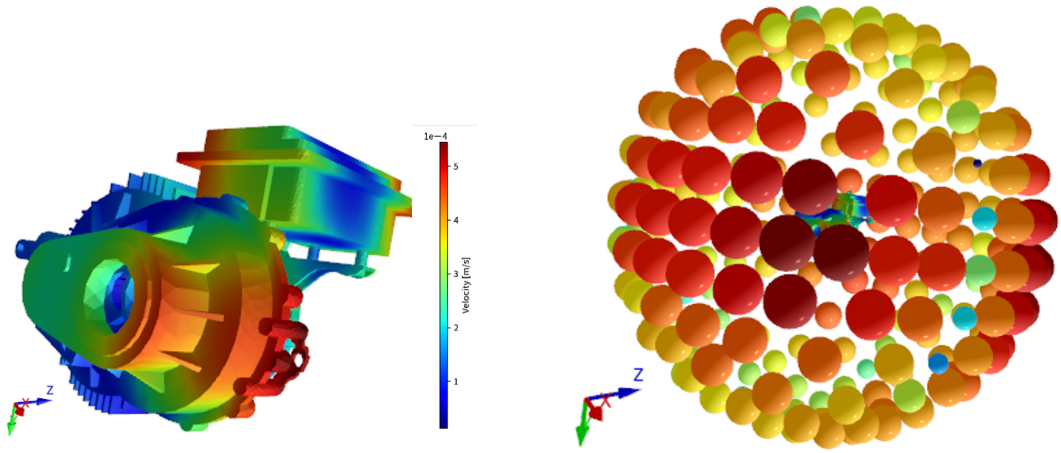

(a) *Velocity on housing* **(b)** *Microphones*

Figure 6.129: Acoustic results, 1^{st} harmonic output TE, order 9.138, Model C

Investigating the input TE response, Figure 6.130, the highest housing velocity, and hence the highest pressure, is recorded on the transmission system side, in particular close to the input pinion, about -z direction. On the other hand, the minimum values are visible on the electric motor side, about *-x direction*.

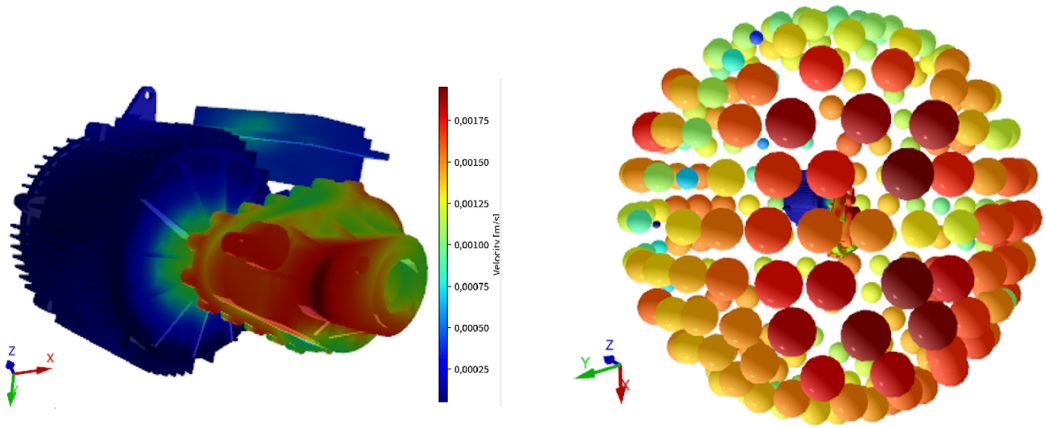

(a) *Velocity on housing* **(b)** *Microphones*

Figure 6.130: Acoustic results, 1^{st} harmonic input TE, order 22, Model C

Finally, considering the electromagnetic excitation, Figure 6.131, the highest results, both in terms of velocities and of pressure, are recorded all around the electric motor. The region of maximum pressure is constituted by kind of a ring

all around the electric motor. The minimum values are instead registered on the transmission system side.

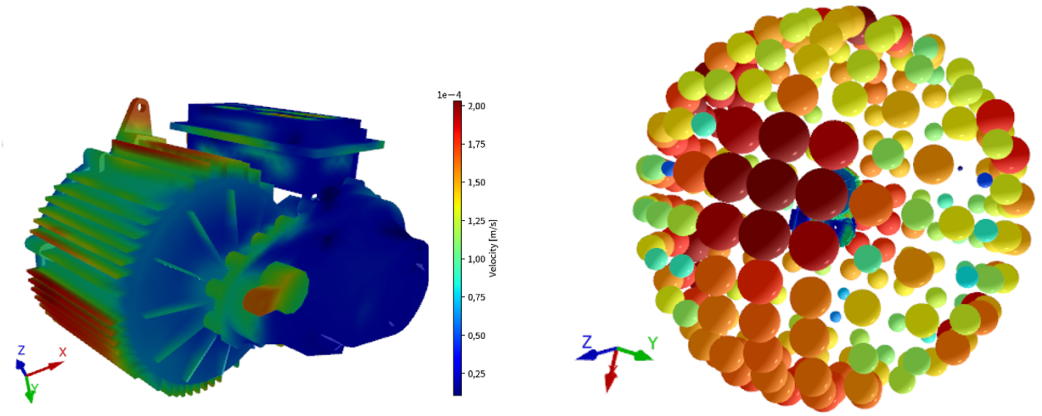

(a) *Velocity on housing* **(b)** *Microphones*

Figure 6.131: Acoustic results, 48^{th} harmonic electromagnetic, order 48, Model C

6.7.2 Model D4, helical gears with profile shift and micro-geometry optimizations

Considering now the Model D4, which is the one with the best microgeometry parameters from NVH viewpoint, some important differences with Model C can be highlighted.

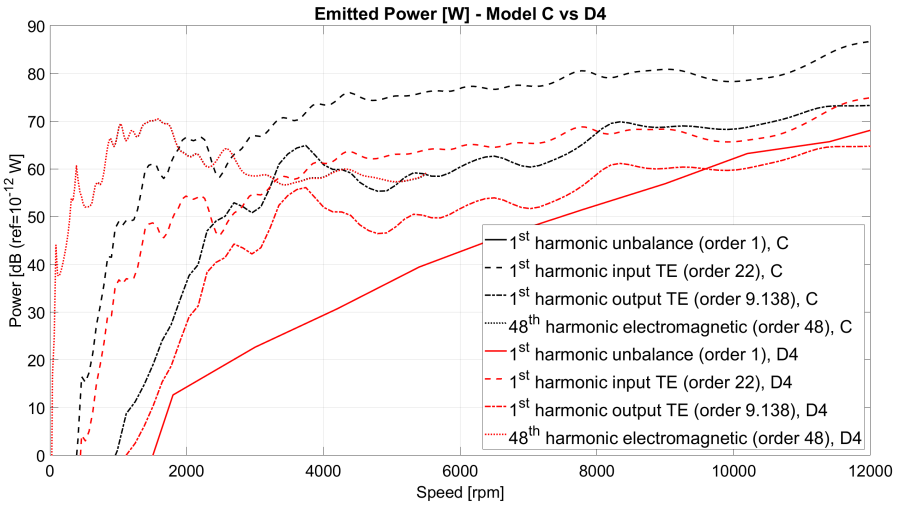

Figure 6.132: Power (W) vs Speed (rpm), comparison Model C vs D4

Surely, comparing the two models, no differences can be noted considering just the electromagnetic and the unbalance excitations. On the other hand, important differences are evident considering both input and output TE.
A remarkable reduction of the emitted power can be noted moving to Model D4, considering both the input and the output gear sets.
This outcome further certify the goodness of Model D4, since a noteworthy improvement of the NVH performance, focusing on airborne noise, is obtained.
These enhancement of the performance is maybe even more evident looking at the plot in linear scale, Figure 6.133.

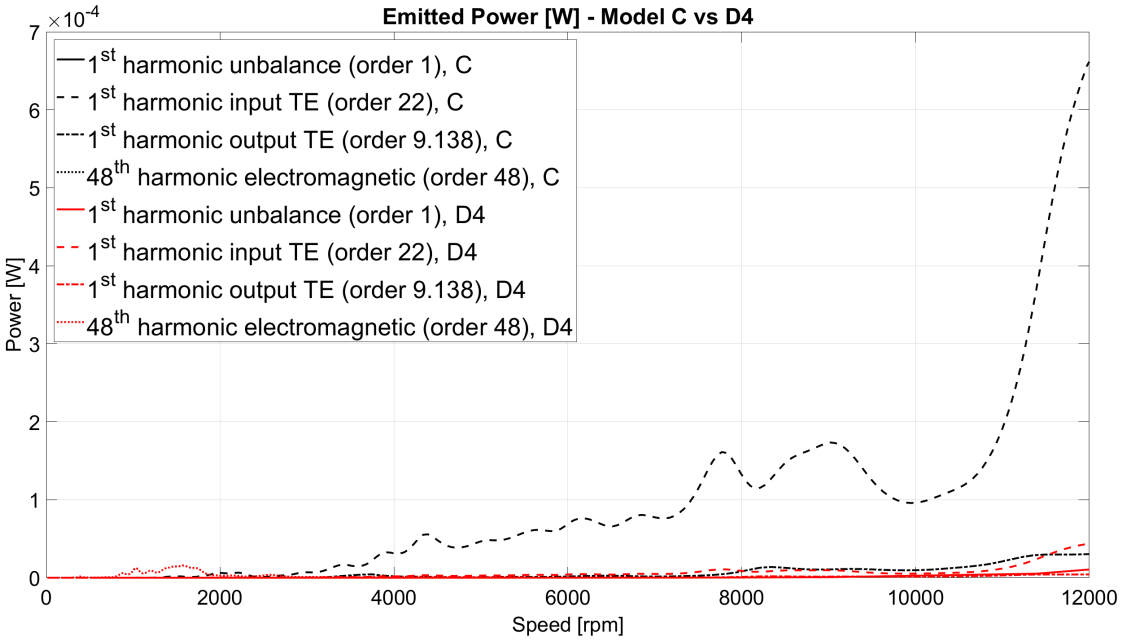

Figure 6.133: Power (W) vs Speed (rpm), comparison Model C vs D4, linear scale

The results concerning the directivity of the sound are not repeated again for Model D, since they are qualitatively exactly the same with respect to Model C. Indeed, the directions in which the noise propagates more are equivalent.
However, even if the behaviour is the same, it is interesting to compare the values of the peaks of the velocity on the housing. In fact, as expected, in Model C higher peaks are recorded with respect to Model D4 for which concerns the input and output TE excitation. The results are reported in Table 6.29.
Since the difference between Model C and D4 regard just the transmission system, it is not surprising that no major differences are noted considering unbalance and electromagnetic excitation.

Excitation	Order	Model C	Model D4
Unbalance	1	$1.6 \cdot 10^{-3}$	$1.6 \cdot 10^{-3}$
Output TE	9.138	$5.5 \cdot 10^{-4}$	$2.0 \cdot 10^{-4}$
Input TE	22	$2.0 \cdot 10^{-3}$	$5.0 \cdot 10^{-4}$
Electromagnetic	48	$2.0 \cdot 10^{-4}$	$2.0 \cdot 10^{-4}$

Table 6.29: Comparison among peaks of velocity on housing, Model C vs D4

Chapter 7

NVH analyses, electric motors from SyR-e

In this last section of the NVH analyses, a comparison between two different electric motors is performed. The former is a surface permanent magnet (SPM) motor with 6 slots and 4 poles, the latter is a internal permanent magnet (IPM) with 48 slots and 4 poles, with cross sections reported in Figure 7.1. These two motors have been deeply studied by [45], [44]. Both motors have a maximum speed of $12000\,rpm$. The IPM 48-4 has a base speed of $3500\,rpm$, while the SPM 6-4 has a base speed of $\approx 4000\,rpm$. They both are liquid cooled. Both motors are able to provide a $50\,kW$ continuous power at $12000\,rpm$ maximum speed.

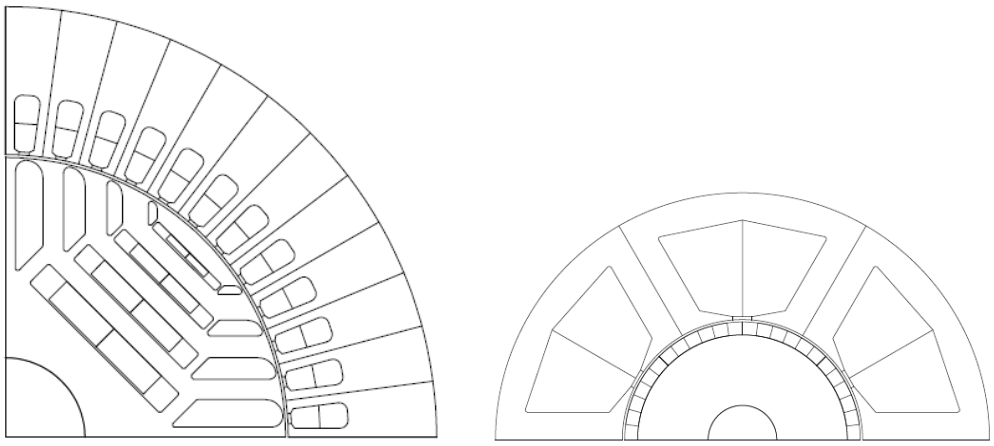

(a) *IPM 48-4* **(b)** *SPM 6-4*

Figure 7.1: Cross sections of the considered motors

The most relevant properties of the two motors are reported in Table 7.1.

Parameter	IPM 48-4	SPM 6-4
Number of slots	48	6
Number of poles	4	4
Rotor outer diameter (mm)	140.20	103.00
Stator outer diameter (mm)	216.00	216.00
Stator inner diameter (mm)	141.80	105.00
Active length (mm)	170.00	170.00
Slot height (mm)	14.24	42.26
Slot width (at air gap) (mm)	4.91	37.43

Table 7.1: Parameters of the electric motors

The two motors differ a lot one to each other. The most important parameter which changes is the number of slots per pole per phase, indicated by the letter q. The motor SPM 6-4 has a value equals to $q = 6/4/3 = 0.5$, while the IPM 48-4 has $q = 6/4/3 = 4$.
Moreover, as indicated in Chapter 1, from the literature, [14], it is known that the lowest mode number of radial force harmonics is equal to GCD(2p,Ns). [14] claims that the radial force harmonics with the lowest mode number cause large vibration at low frequency. Moreover, [14], state that motors with fractional q have lower mode number with respect to motors with integer q, generally. Indeed, in this case:

- SPM 6-4: GCD(2p,Ns)=GCD(4,6)=2
- IPM 48-4: GCD(2p,Ns)=GCD(4,48)=4

Furthermore, in Chapter 1, it has been indicated that some studies from literature, [10] and [16], state that the combinations that provoke the lowest noises and vibrations are the ones that have $N_s = 6kp$, with $k \in \mathbb{N}^*$ (as the motor IPM 48-4). Hence, due to the above considerations, it is expected to have better NVH performance considering the IPM 48-4 motor, rather than the SPM 6-4, as analysed by [48], too. The electromagnetic excitation have been calculated for both motors exploiting a dedicated software, i.e. SyR-e [43], with the cooperation of DENERG. Considering the load case *NVH*, the radial and tangential forces and the torque ripple have been defined for two operating speed: 5000 rpm (i.e. speed of the load case) and 12000 rpm (i.e. maximum speed of the motor). The excitations obtained by SyR-e [43] are waveforms reporting the magnitude of the force or of the torque against the mechanical angle θ. They are reported for both motors, and considering the two just exposed operating speeds, in Figures 7.2-7.5.
The different periodicity between the waveforms of the two motors is given by the

different number of slots. Comparing the waveforms of the two motors, it appears evident how the excitations of the SPM 6-4 have generally higher amplitude with respect to the ones of the IPM 48-4.

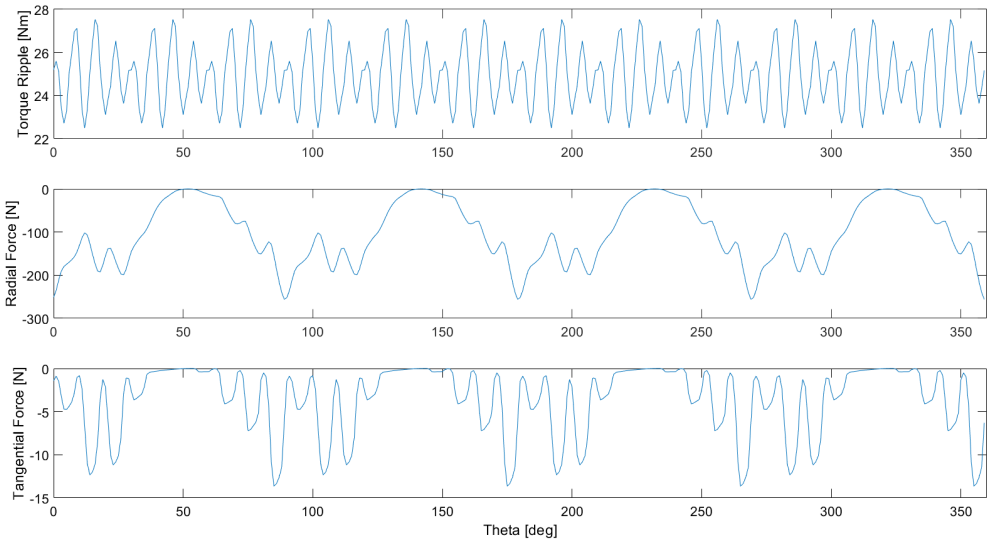

Figure 7.2: Waveforms excitations IPM 48-4, 5000 rpm

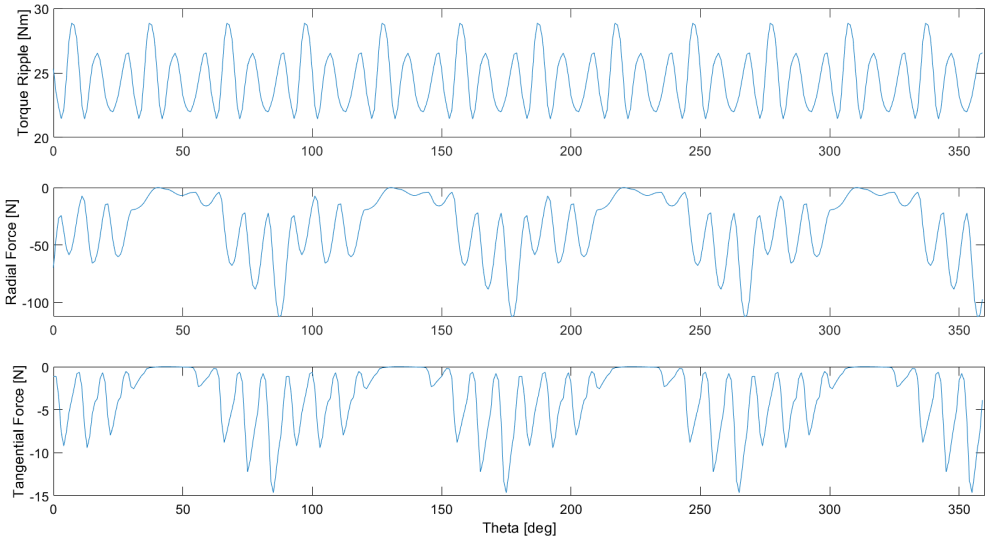

Figure 7.3: Waveforms excitations IPM 48-4, 12000 rpm

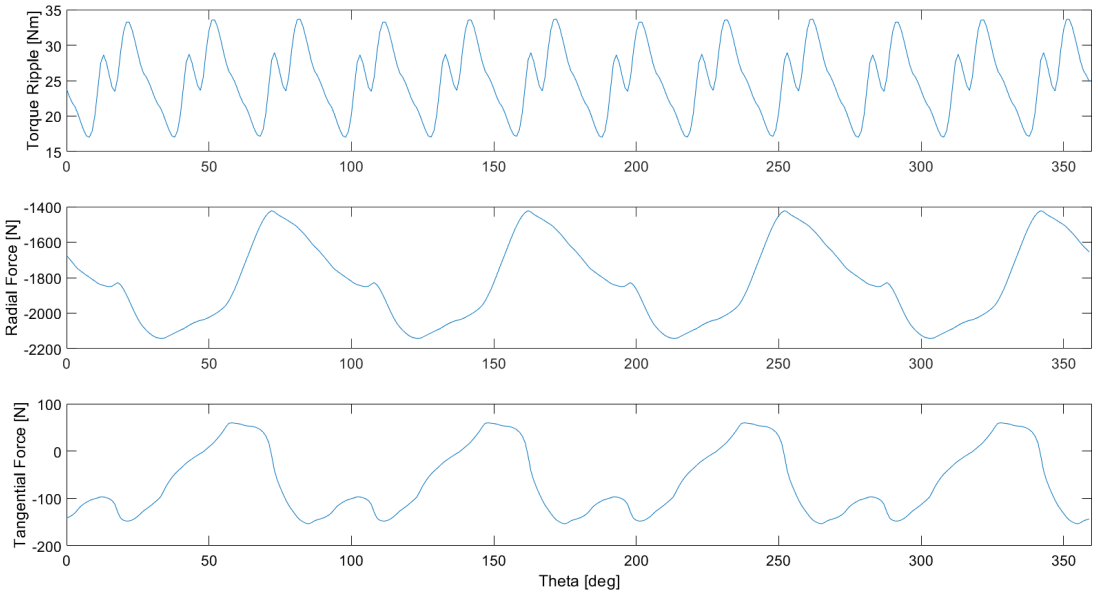

Figure 7.4: Waveforms excitations SPM 6-4, 5000 rpm

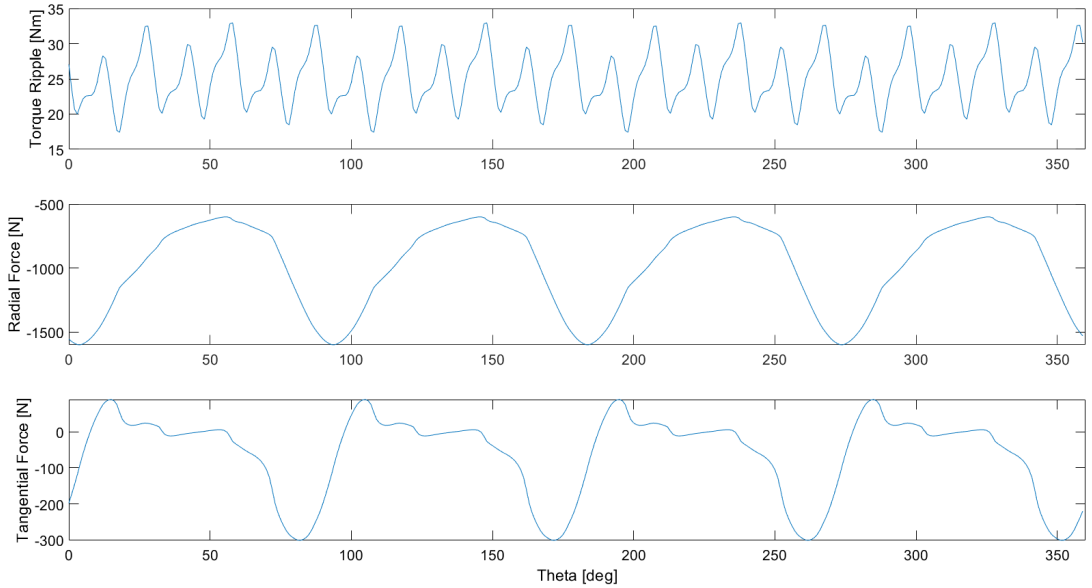

Figure 7.5: Waveforms excitations SPM 6-4, 12000 rpm

Then, from the waveforms, it is possible to obtain the amplitudes of the most important harmonics, which are plotted in Figures 7.6-7.8. Romax is capable of perform this passage by itself.

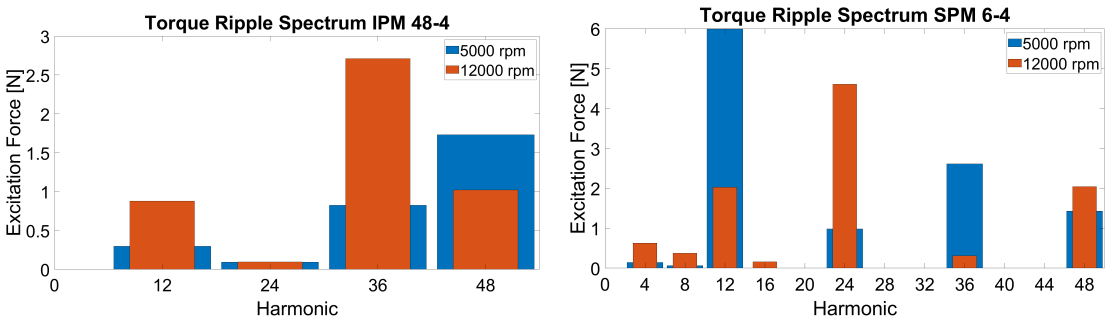

(a) *IPM 48-4* **(b)** *SPM 6-4*

Figure 7.6: Torque ripple spectrum

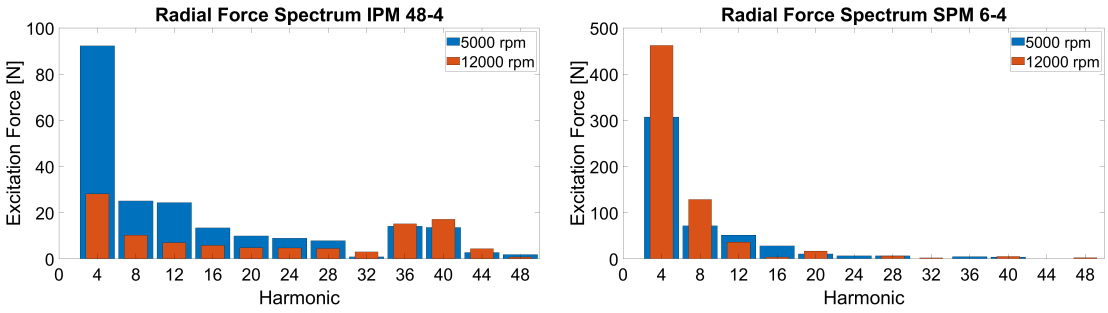

(a) *IPM 48-4* **(b)** *SPM 6-4*

Figure 7.7: Radial force spectrum

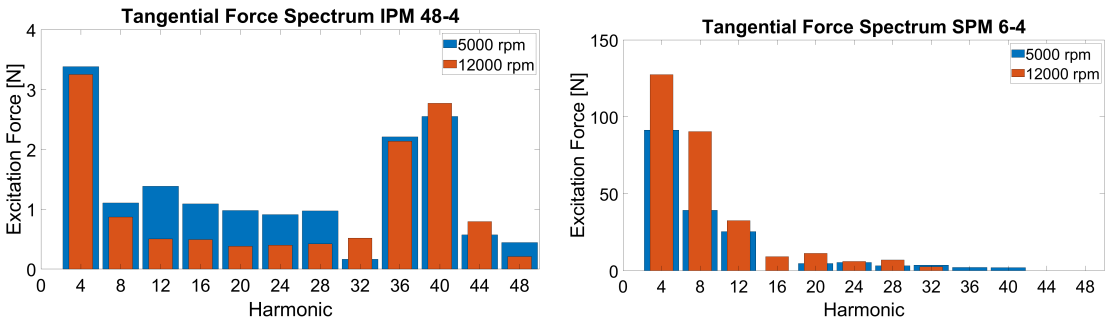

(a) *IPM 48-4* **(b)** *SPM 6-4*

Figure 7.8: Tangential force spectrum

From the spectra, it is possible to notice that, as regards the torque ripple, the order which has the highest amplitude (considering 5000 rpm, blue plots in above

figures) is the 48^{th} for the IPM 48-4, while it is the 12^{th} for the SPM 6-4. This outcome, especially considering the IPM 48-4, which has integer q (i.e. $q = 4$): a motor with integer value of q usually has as critical harmonic the one corresponding to the number of slots, i.e. 48. On the other hand, it is not that easy to define in advance the critical harmonic for motors with fractional q, as the SPM 6-4 (i.e. $q = 0.5$). Additionally, considering as operating speed 12000 rpm (orange plots in the above figures), it is more complex, since it is the flux weakening condition, hence it is impossible to establish in advance the most critical orders.
Thanks to SyR-e [43], and a FEMM software, it is possible even to understand the distribution of the magnetic flux density of the two motors. Notice that at $12000\,rpm$ the motors are in flux weakening condition.

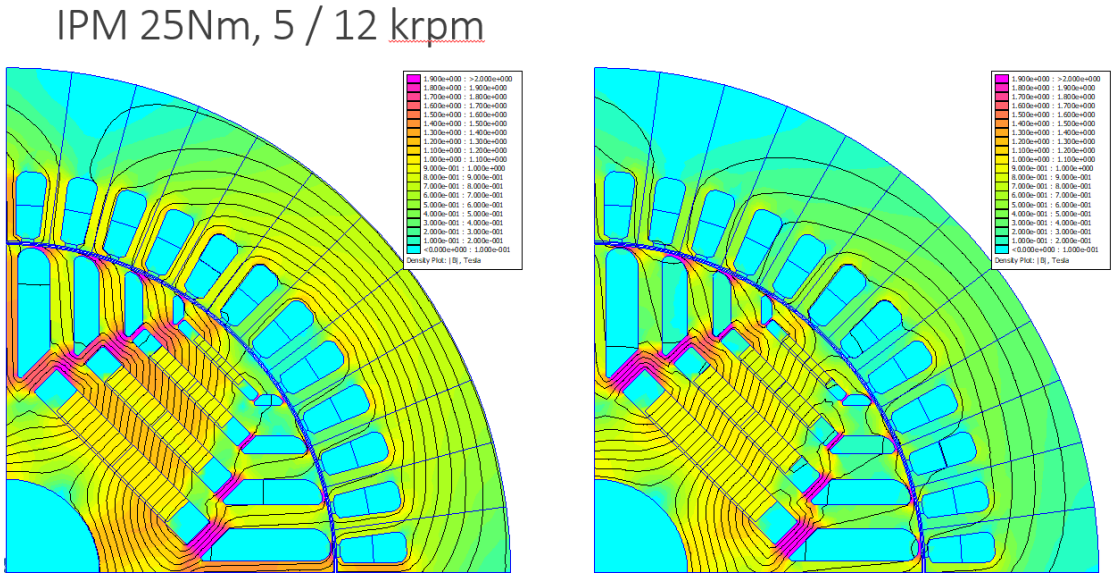

Figure 7.9: Magnetic flux density, IPM 48-4

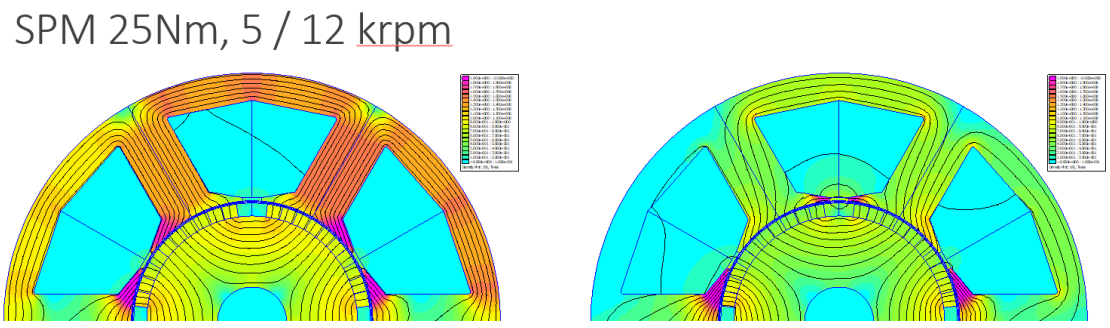

Figure 7.10: Magnetic flux density, SPM 6-4

In both motors, it is noticeable that in flux weakening condition the magnetic flux density is way higher in the rotor rather than on the stator. This means that the stator will influence less the excitations. This further prove that it should not surprise that the orders of the critical harmonic can change moving from *standard* condition (i.e. below the base speed) to flux weakening.
To perform a more effective comparison between the two motors, the most critical electromagnetic excitations are considered. As regards the SPM 6-4 motor, the most critical order is verified to be the 12^{th}, while for the IPM 48-4 is the 48^{th}. These are the orders which cause the breathing mode of the stator, particularly crucial for the vibration analysis. The response to the other excitations is not reported here since not that important differences between the two motors can be highlighted. By far, the most remarkable comparison concerns the electromagnetic sources.
For all plots that follow, the Model D4 has been considered, taking into account the load case *NVH*. To avoid redundancy, results of the other load cases are not reported here below, but it has been checked that the behaviour is exactly the same.
The first interesting graph to be analysed is the one reporting the ERP and the MSV, Figure 7.11.

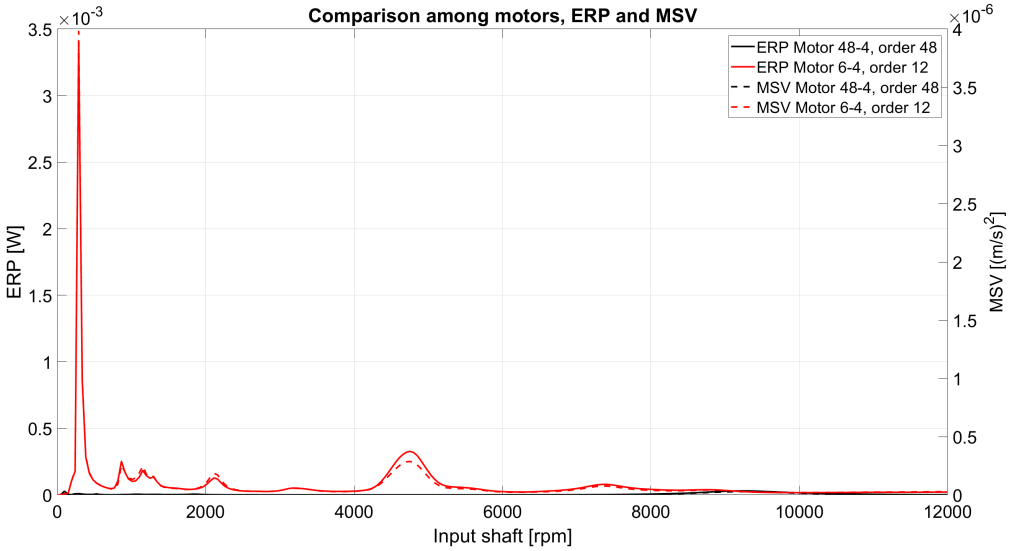

Figure 7.11: Comparison ERP and MSV, SPM 6-4 vs IPM 48-4

From Figure 7.11, as expected, it is clearly noticeable the difference of the equivalent power radiated from the two motors. In the plot, the response of the IPM 48-4 is almost impossible to detect: it is two order of magnitude smaller than the ERP of the SPM 6-4. This difference is evident for the whole speed range.

Then, the comparison can be extended also to the housing mounts response, Figure 7.12.

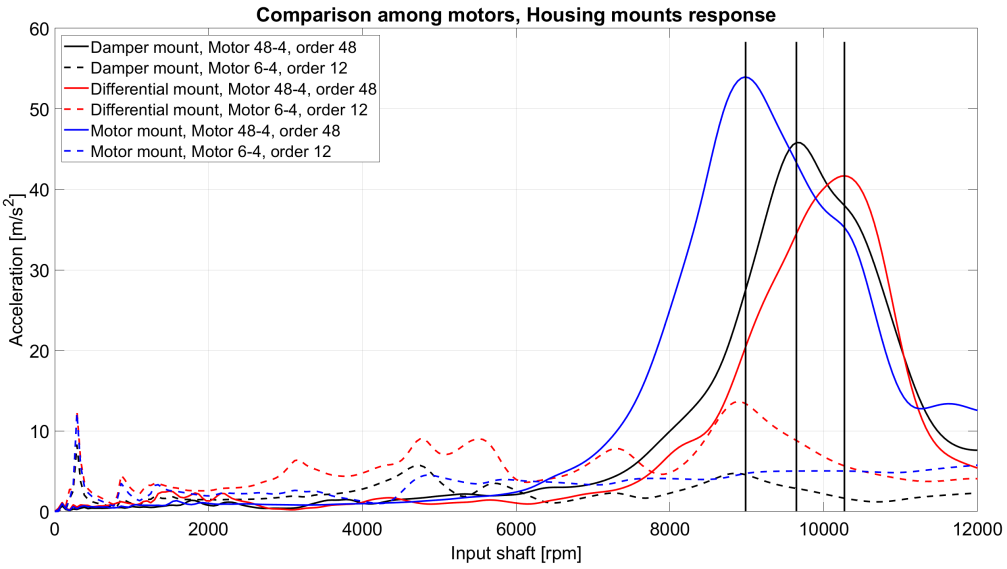

Figure 7.12: Comparison housing mounts response, SPM 6-4 vs IPM 48-4

Figure 7.12 shows that at low speed, below the base speed of the motor, the SPM 6-4 causes higher response than the IPM 48-4. In particular, the response provoked by the IPM 48-4 is almost negligible at low speed. On the other hand, at high rotational speed, i.e. flux weakening condition, the motor IPM 48-4 leads to way higher response. This can not be that surprising: indeed, in flux weakening conditions is almost impossible to predict the behaviour of the motor. Moreover, the peaks of the IPM 48-4 can be justified also by the overlapping with a resonance of the system: each peak almost perfectly corresponds to a natural frequency, indeed, represented by vertical lines in Figure 7.12. The values of the natural frequency are reported in Table 7.2. Please keep in mind the conversion between the *Hz* to the *rpm* domain (i.e. frequency [Hz] = (shaft speed [rpm] · order of harmonic)/60).

Housing mount	Peak (Hz)	Natural Frequency (Hz)	Mode Number
Differential	8217.6	8212.8	245
Damper	7718.4	7716.1	223
Motor	7180.8	7188.1	188

Table 7.2: Peaks and natural frequencies

Chapter 8

Efficiency analyses

To investigate the efficiency of the powertrain, there is a dedicated module in Romax, called Energy.
Through this software, it is possible to evaluate both the mechanical and the electrical efficiency, considering several losses, defined by [22]:

- Gear meshes: due to the mesh of each gear set, it is the drag on the gear from mesh rolling and sliding losses, which depends on rolling and sliding velocities, respectively.
- Gear blanks: oil drag losses, it is the drag on the gear from windage and churning losses. The windage losses are increased due to the fact that, as the gear rotates, the lubricant is thrown, as drops, by gear teeth due to the centrifugal force. The drops will remain within the housing, leading to an increase of windage losses, as explained by [49]. On the other hand, the churning losses are caused by the entrapment of the lubricant within the gear mesh, as [49] indicates.
- Bearings: bearing drag considers load dependent drag and viscous friction.
- Electric machine

To properly perform an efficiency analysis, first of all it is required to define a gearbox lubricant, since it strongly affects the drag on all components. Many lubricants are at disposal from the software, in this example it has been selected to use ISO VG 32 mineral, with an ISO 4406 contamination code -/17/14. Moreover, it is necessary also to set a certain lubricant level within the system. From supporting material [22], a level of 67 mm is used, this is defined from the gearbox origin (center of rotation of shafts) along the gravity vector (along y axis). Therefore, to increase the value of oil level means actually to decrease the amount of oil within the gearbox, hence less portion of the gears are immersed in the lubricant.

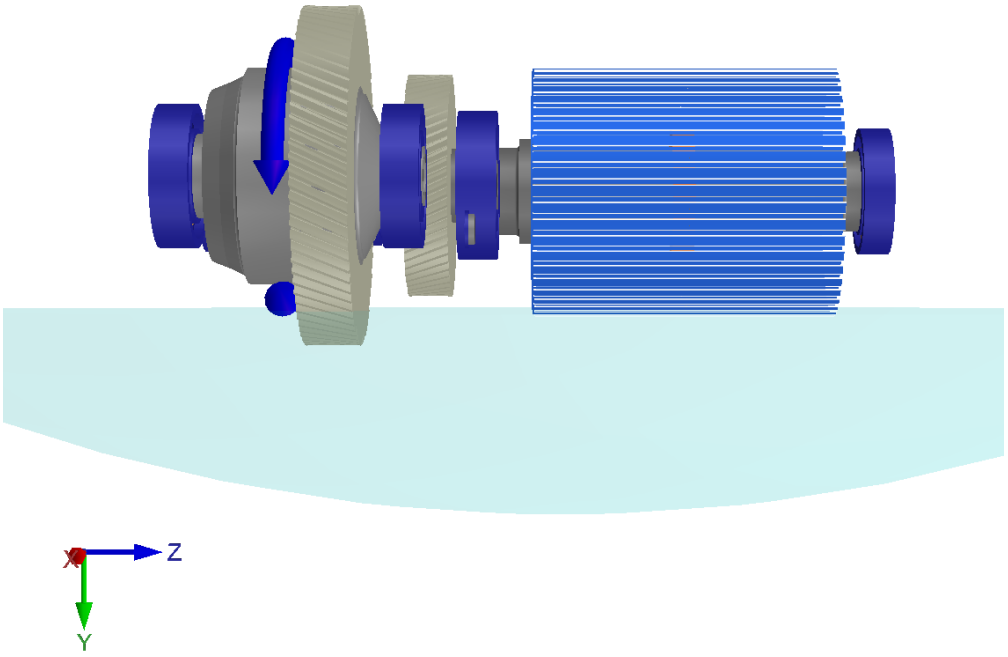

Figure 8.1: Oil level 67 mm

Kinematic viscosity (mm^2/s)	40° 100°	32.00 5.06
Dynamic viscosity (mm^2/s)	40° 100°	27.18 4.29

Table 8.1: Lubricant ISO VG 32 Mineral Data

To consider the losses on each component, Romax offers the possibility to take into account several standards, for instance, for the following analyses it has been selected a German standard, ISO 14179-2 (DE).

Bearings loss model	ISO 14179-2 (DE)
Gear drag - Gear loss model	ISO 14179-2 (DE)
Gear mesh - Helical mesh loss model	Microgeometry based - ISO 14179-2 (DE)

Table 8.2: Loss models

Notice that, considering the gear meshes, the software offers the opportunity to consider the microgeometry modifications to compute the forces and sliding velocities required by the standards.
To contemplate the electric efficiency, it is requested to have an efficiency map of the electric machine.
An example of efficiency map of the electric machine is provided by supporting material [22], and it is reported in the following figure:

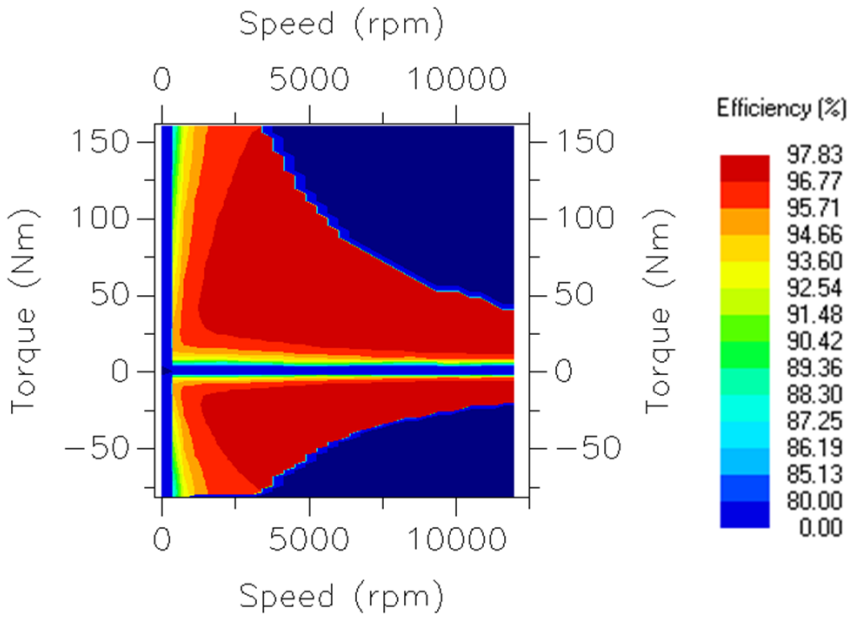

Figure 8.2: Electric machine efficiency map

Considering the efficiency map which can be defined in Romax, is mandatory to consider positive speed for both drive and coast, while the torque is positive for drive and negative for coast.
Romax gives the possibility to perform the efficiency analysis of a specific load case. In the following pages the load case *NVH*, maybe the one of most interest along this thesis, is investigated.
The operating temperature is a crucial parameter to be considered, in the load case *NVH*, the temperature is $70°C$.
A comparison among all models is given below, considering all possible power losses.

8.1 Component losses

8.1.1 Electric machine

Considering the losses in the electric machine, they are not affected by which model is considered, since the differences among models concern just the gear sets. Considering the load case *NVH*, the input electrical power is 13.386 kW, while the power at the rotor is just 13.090 kW. Therefore, the efficiency of the electric machine is equal to 97.79%. As expected, the efficiency of the electric motor is pretty high.

Comparison between electric motors

Furthermore, it is possible also to compare the efficiencies of the two electric motors analysed and explained in Section 7. The data derive from simulation performed in SyR-e [43].

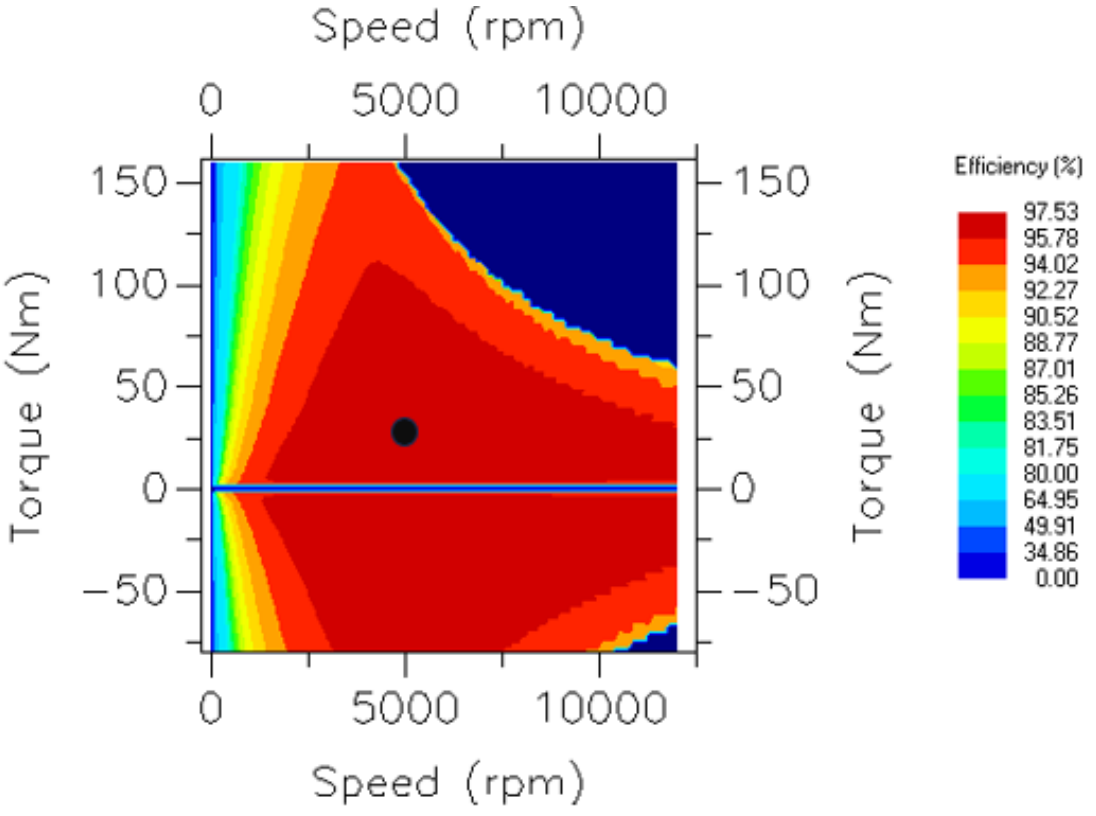

Figure 8.3: Efficiency map, IPM 48-4

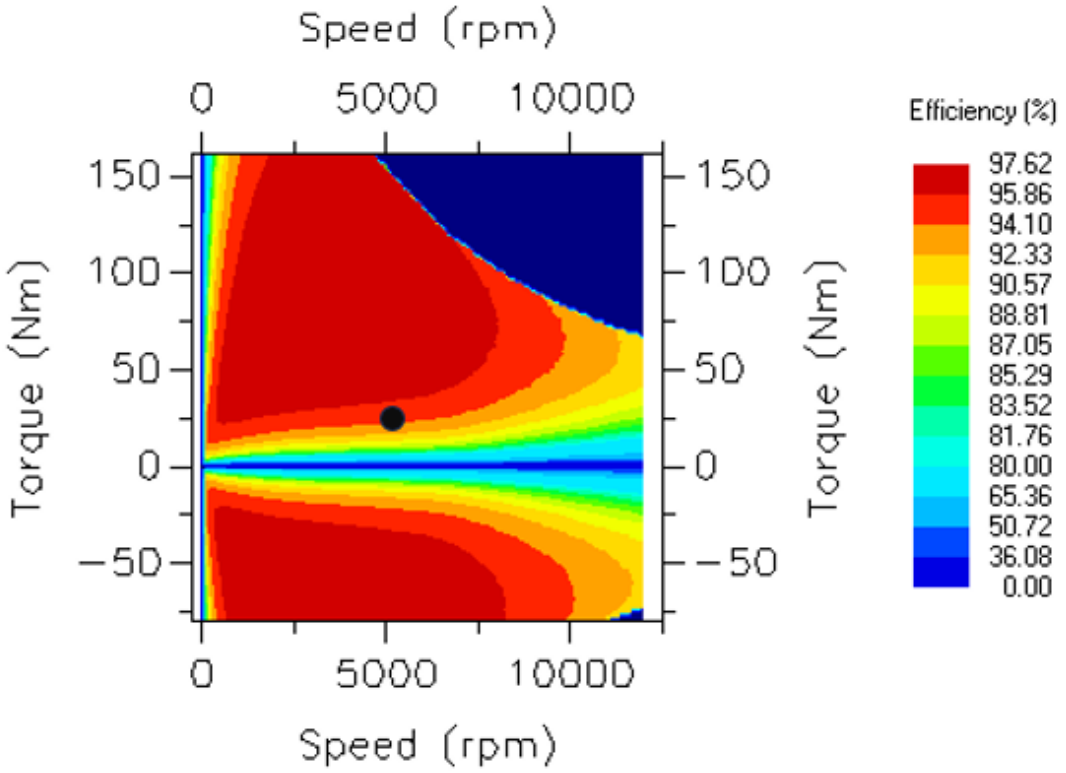

Figure 8.4: Efficiency map, SPM 6-4

The comparison is done considering again the load case *NVH*, and,in that specific load case, it results in a better efficiency of the IPM 48-4 motor, as highlighted by Table 8.3 (the black dots in Figures 8.3 and 8.4 highlight the NVH load case). However, considering the whole map, the comparison is not that easy. Indeed, at high speed and low torque, the IPM 48-4 has a better efficiency than the SPM 6-4. On the other hand, at low speed but high torque, the SPM 6-4 have a better efficiency.

Motor	Torque	Speed	Elect. P_{in}	Electrical P_{out}	Electrical efficiency
IPM 48-4	25 Nm	5000 rpm	13.455 kW	13.090 kW	97.29 %
SPM 6-4	25 Nm	5000 rpm	13.815 kW	13.090 kW	94.75 %

Table 8.3: Comparison efficiency, IPM 48-4 vs SPM 6-4

8.1.2 Gears

As already anticipated, two main losses are possible to be computed concerning the gears: gear blank and gear meshes losses.

Model	Gear Blanks	Power loss (kW)	Drag torque (Nm)
Model A	Input pinion	0	0
	Input wheel	0	0
	Output pinion	0	0
	Output wheel	$1.6517 \cdot 10^{-3}$	$2.8650 \cdot 10^{-2}$
Model B	Input pinion	0	0
	Input wheel	0	0
	Output pinion	0	0
	Output wheel	$1.6517 \cdot 10^{-3}$	$2.8650 \cdot 10^{-2}$
Model C	Input pinion	0	0
	Input wheel	0	0
	Output pinion	0	0
	Output wheel	$1.6516 \cdot 10^{-3}$	$2.8648 \cdot 10^{-2}$
Models D1-D4	Input pinion	0	0
	Input wheel	0	0
	Output pinion	0	0
	Output wheel	$1.6516 \cdot 10^{-3}$	$2.8648 \cdot 10^{-2}$

Table 8.4: Gear blanks losses

Looking at Table 8.4, very low values of losses are detected. Moreover, only the output wheel is affected by this kind of losses. This is due to the lubricant level, defined in Figure 8.1. Indeed, only the output wheel is immersed in the lubricant. Furthermore, gear blanks losses are almost the same for all considered models, in fact the models with modified microgeometry are reported in the same row of Table 8.4, since the values are exactly the same. This is expected since they depend mostly on the rotational speed of gears, the viscosity of the lubricant, the operating temperature (all parameters which do not depend on the model). Moreover, being the rotational speed of the differential shaft low, it is expected to have low values of gear blank losses.

Model	Gear Set	Power loss (kW)	Efficiency (%)
Model A	Input gear set	0.113	99.14
	Output gear set	0.123	99.06
Model B	Input gear set	0.113	99.14
	Output gear set	0.129	99.02
Model C	Input gear set	0.131	99.00
	Output gear set	0.138	98.94
Model D1	Input gear set	$8.525 \cdot 10^{-2}$	99.35
	Output gear set	0.105	99.20
Model D2	Input gear set	$7.638 \cdot 10^{-2}$	99.42
	Output gear set	$9.147 \cdot 10^{-2}$	99.30
Model D3	Input gear set	$9.816 \cdot 10^{-2}$	99.25
	Output gear set	0.109	99.16
Model D4	Input gear set	0.127	99.03
	Output gear set	0.131	99.00

Table 8.5: Gear meshes losses

Investigating gear meshes losses, in all cases very high values of efficiency are obtained. It is possible to notice that generally spur gears have a slightly better efficiency than helical ones, if no microgeometry is taken into account. This is caused by the sliding contact between teeth, leading to axial forces and heat generation in case of helical gears.
By adding microgeometry modifications it is possible to increase the gear meshes efficiency: moving from Model C to Model D2 an increase of almost half percentage point can be denoted. These modifications lead even to a better efficiency of the helical gears with respect to spur ones. However, in Model D4 the aim of the microgeometry optimization was totally dedicated to the reduction of the NVH response, and therefore the efficiency is less important. Anyway, even in Model D4 a slight increase of the efficiency can be noted with respect to Model C.
Even if very high values of efficiency are recorded regarding gear meshes losses, it appears evident the higher impact that the gear meshes losses have with respect to gear blanks.

8.1.3 Bearings

Looking at bearings, Table 8.6, in all models the values of losses are very modest. Moreover, a slight increase of the losses moving from models with spur gears to the helical ones can be noted. Moreover, all models which consider microgeometry modifications of course provoke the same bearing losses.

Model	Bearing	Power loss (kW)	Drag Torque (Nm)
Model A	Input shaft LH	$1.881 \cdot 10^{-2}$	$3.592 \cdot 10^{-2}$
	Input shaft RH	$2.330 \cdot 10^{-2}$	$4.451 \cdot 10^{-2}$
	Interm. shaft LH	$7.020 \cdot 10^{-3}$	$3.961 \cdot 10^{-2}$
	Interm. shaft RH	$1.099 \cdot 10^{-2}$	$6.201 \cdot 10^{-2}$
	Diff. shaft LH	$9.864 \cdot 10^{-4}$	$1.711 \cdot 10^{-2}$
	Diff. shaft RH	$2.315 \cdot 10^{-3}$	$3.703 \cdot 10^{-2}$
Model B	Input shaft LH	$1.880 \cdot 10^{-2}$	$3.591 \cdot 10^{-2}$
	Input shaft RH	$2.330 \cdot 10^{-2}$	$4.451 \cdot 10^{-2}$
	Interm. shaft LH	$7.020 \cdot 10^{-3}$	$3.961 \cdot 10^{-2}$
	Interm. shaft RH	$1.099 \cdot 10^{-2}$	$6.201 \cdot 10^{-2}$
	Diff. shaft LH	$9.864 \cdot 10^{-4}$	$1.711 \cdot 10^{-2}$
	Diff. shaft RH	$2.135 \cdot 10^{-3}$	$3.703 \cdot 10^{-2}$
Model C	Input shaft LH	$2.170 \cdot 10^{-2}$	$4.144 \cdot 10^{-2}$
	Input shaft RH	$2.317 \cdot 10^{-2}$	$4.426 \cdot 10^{-2}$
	Interm. shaft LH	$8.232 \cdot 10^{-3}$	$4.645 \cdot 10^{-2}$
	Interm. shaft RH	$1.070 \cdot 10^{-2}$	$6.040 \cdot 10^{-2}$
	Diff. shaft LH	$1.047 \cdot 10^{-3}$	$1.816 \cdot 10^{-2}$
	Diff. shaft RH	$3.859 \cdot 10^{-3}$	$6.693 \cdot 10^{-2}$
Models D1-D4	Input shaft LH	$2.170 \cdot 10^{-2}$	$4.144 \cdot 10^{-2}$
	Input shaft RH	$2.317 \cdot 10^{-2}$	$4.426 \cdot 10^{-2}$
	Interm. shaft LH	$8.232 \cdot 10^{-3}$	$4.645 \cdot 10^{-2}$
	Interm. shaft RH	$1.070 \cdot 10^{-2}$	$6.040 \cdot 10^{-2}$
	Diff. shaft LH	$1.047 \cdot 10^{-3}$	$1.816 \cdot 10^{-2}$
	Diff. shaft RH	$3.859 \cdot 10^{-3}$	$6.693 \cdot 10^{-2}$

Table 8.6: Bearing losses

8.1.4 Total efficiency

Finally, considering both electrical and mechanical losses, it is possible to compute the total efficiency of the system in this specific load case (*NVH*).
In Table 8.7, the term total mechanical losses represents the sum of gear blanks, gear meshes and bearing losses.

Model	A	B	C	
Electrical power IN (kW)	13.386	13.386	13.386	
Electrical efficiency (%)	97.79	97.79	97.79	
Total mech. power IN (kW)	13.09	13.09	13.09	
Total mech. power loss (kW)	0.301	0.307	0.340	
Total mech. power OUT (kW)	12.789	12.783	12.750	
Total mech. efficiency (%)	97.70	97.66	97.40	
Total efficiency (%)	95.54	95.50	95.25	
Model	D1	D2	D3	D4
Electrical power IN (kW)	13.386	13.386	13.386	13.386
Electrical efficiency (%)	97.79	97.79	97.79	97.79
Total mech. power IN (kW)	13.09	13.09	13.09	13.09
Total mech. power loss (kW)	0.260	0.238	0.278	0.329
Total mech. power OUT (kW)	12.829	12.852	12.812	12.761
Total mech. efficiency (%)	98.01	98.18	97.88	97.49
Total efficiency (%)	95.84	96.01	95.71	95.34

Table 8.7: Load case efficiency summary

As previously explained, the spur gears have a higher efficiency than helical, leading to a higher total mechanical efficiency (and hence even total efficiency) of Models A and B with respect to Models C. However, by adapting microgeometry modifications, it is possible to improve the efficiency of the gears, leading to an enhancement of mechanical efficiency of almost one percentage point comparing Model C and D2, and about 0.5 percentage point moving from Model B to D2.
On the other hand, considering the mechanical efficiency of Model D4, even if it is improved with respect to the model with helical gears but without microgeometry modifications (Model C), its value is lower than the one related spur gears. This further proves the difficulties of select the proper microgeometry modifications, since each configuration can bring benefits to a particular aspect (e.g. NVH) without significantly improving others (e.g. efficiency). Hence, it is fundamental to set and decide precisely the aim of the optimization in order to select the parameters that

better suit the objective.

8.2 Power loss distribution

Another interesting result is the power loss distribution of all mechanical components of the model, varying either the torque or the speed, in a certain range. For instance, the region around the speed and torque values of the considered load case can be investigated. Hence, two distributions are represented in Figures 8.5-8.12, considering a range of $\pm 25\%$ with respect to load case values.

- Speed range: $-3750 \div -6250$ (rpm)
- Torque range: $-18.75 \div -31.25$ (Nm)

The distribution of just Model D4 are reported below. However, all models show exactly the same behaviour.
Notice that in all plots, considering either the speed or the torque range, the absolute value of the x axis is increasing from right to left.

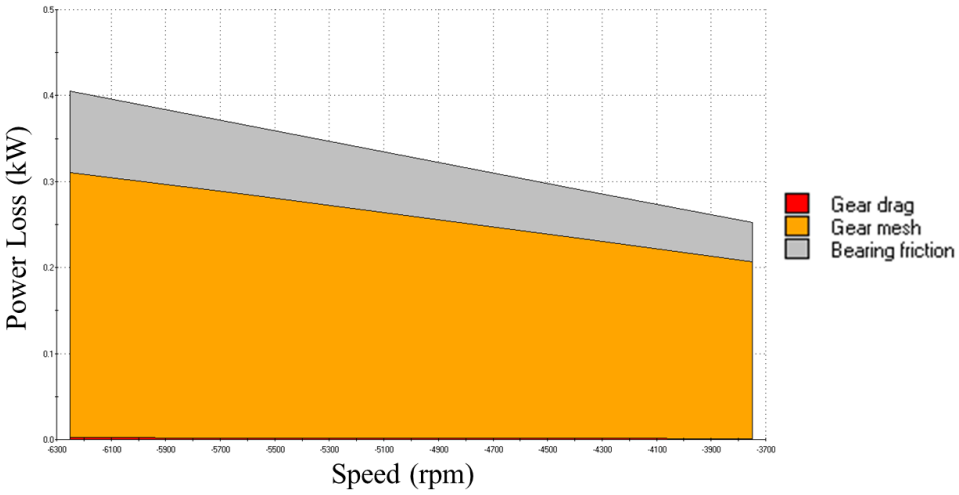

Figure 8.5: Power losses distribution, System, speed range

Looking at the losses of the whole system, Figure 8.5, it is noticed that the largest amount of losses are caused by the gear mesh; the bearing friction gives also an important contribution to overall losses, while the gear drag is negligible. Moreover, for all losses the trend is to increase as the absolute value of speed increases.

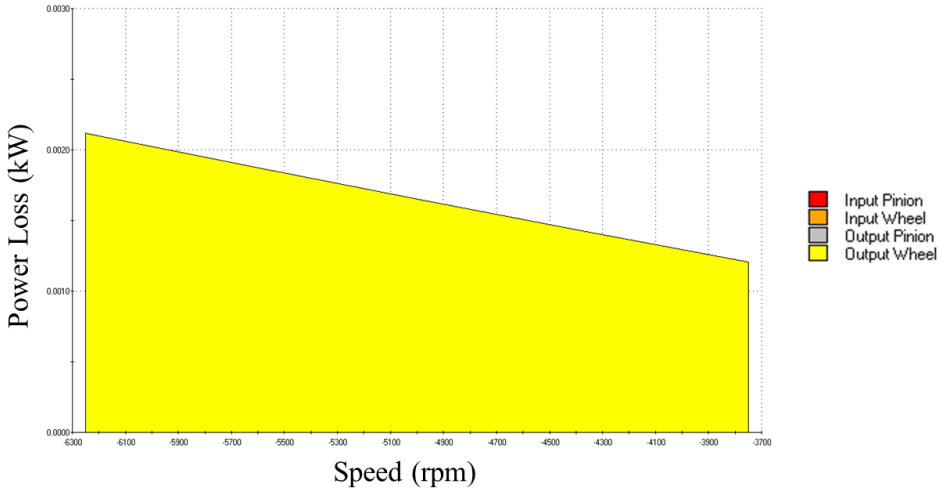

Figure 8.6: Power losses distribution, Gear drag, speed range

Figure 8.6 indicates that the gear drag is caused exclusively by the output wheel, and it increments with the absolute value of speed.

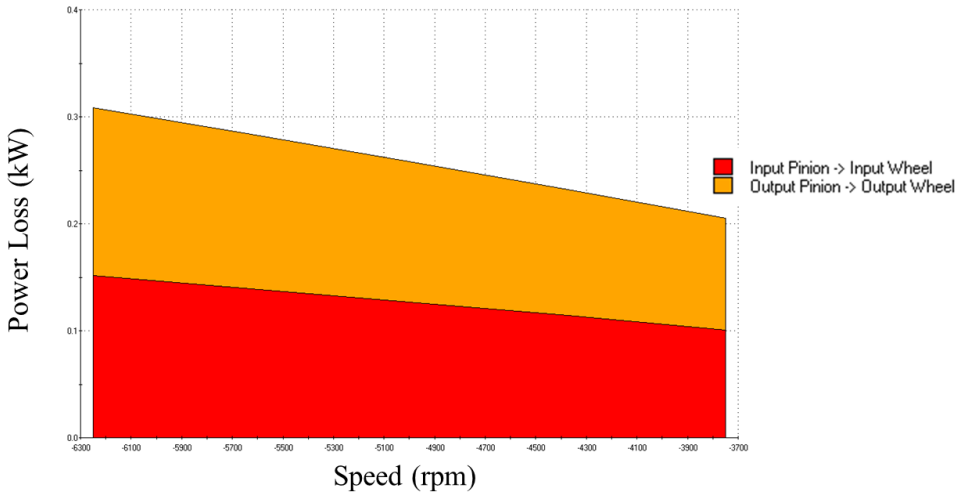

Figure 8.7: Power losses distribution, Gear mesh, speed range

Analysing gear mesh power losses distribution, Figure 8.7, it can be noted that both gear sets provide almost the same contribution to power losses.

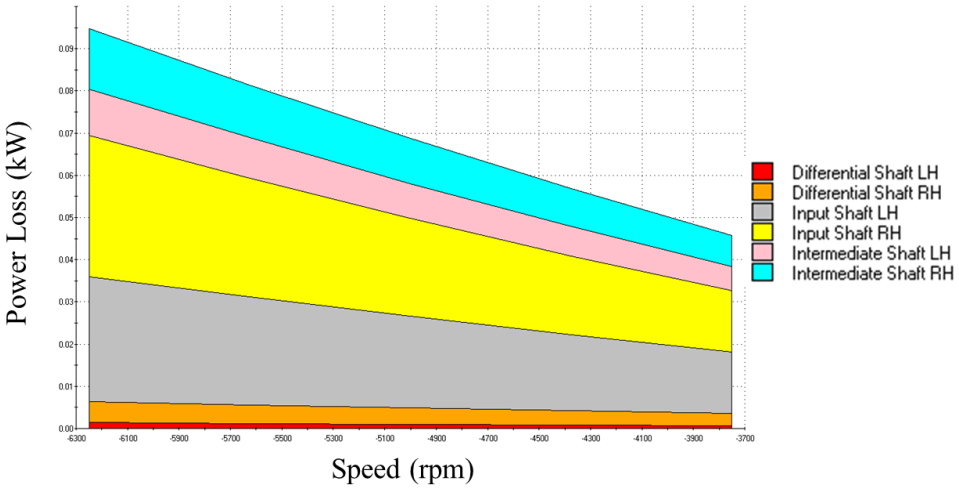

Figure 8.8: Power losses distribution, Bearings, speed range

Investigating bearing losses, the major contribution is given by the ones of the input shaft.

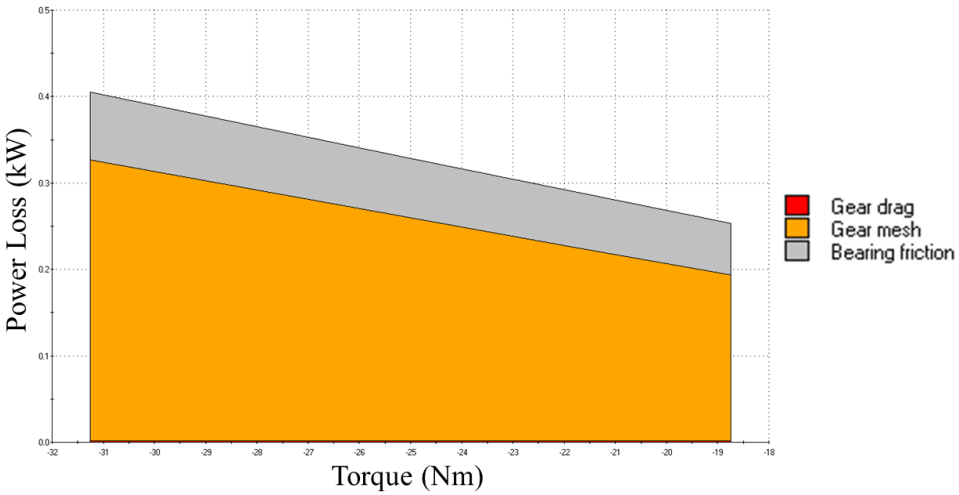

Figure 8.9: Power losses distribution, System, torque range

Then, the same plots can be also displayed varying the torque rather than the rotational speed (Figure 8.10-8.12).

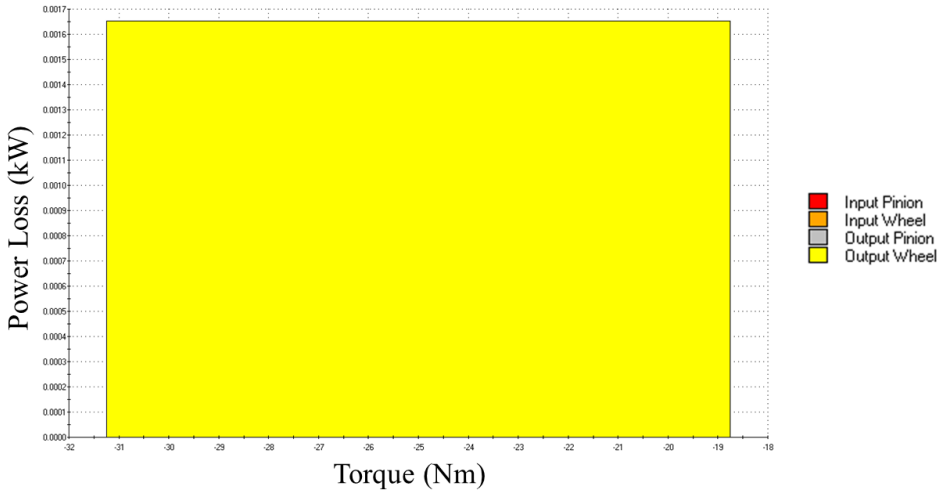

Figure 8.10: Power losses distribution, Gear drag, torque range

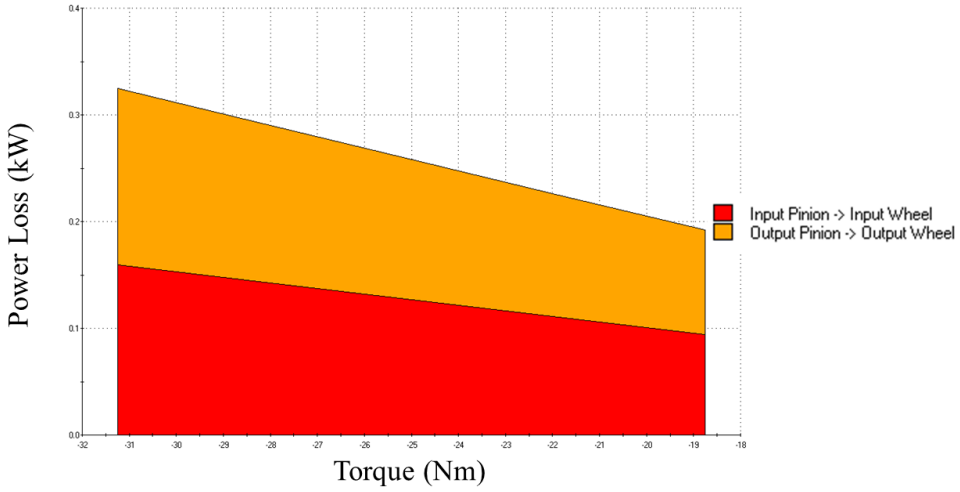

Figure 8.11: Power losses distribution, Gear mesh, torque range

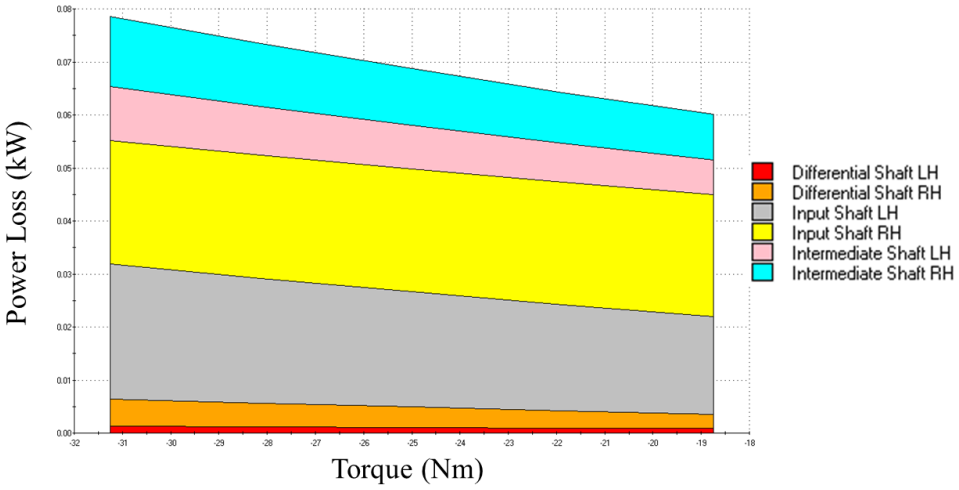

Figure 8.12: Power losses distribution, Bearings, torque range

Comparing the plots in the torque range with the ones in the speed range, the same behaviour is highlighted for almost all plots. The only one which differs is the one related to gear drag. Indeed, varying the torque the gear drag does not change.

8.3 Efficiency maps

Efficiency maps are important since they allow to investigate the effect of two variables simultaneously on the overall mechanical efficiency of the gearbox. Two plots are proposed here below, the former analyzes the effects of varying torque and speed (ranging from 75% to 125% of the load case values), while in the latter the impact of oil level and temperature is investigated.
It can be seen by Figure 8.13 that the mechanical efficiency is the highest when the absolute values of both torque and the speed increase. Of course, on the other hand, as torque and speed decrease, in terms of absolute values, the efficiency decreases as well.
Focusing on Figure 8.14, the investigated ranges are $75\% \div 125\%$ regarding the oil level (reference value: 67 mm), $50\% \div 150\%$ concerning the temperature (reference value: $70°C$).
It appears evident the increase of the efficiency as both temperature and oil level increase. Please keep in mind the sign convention of the y axis. Indeed, to increase the oil level actually means to reduce the amount of oil within the gearbox.

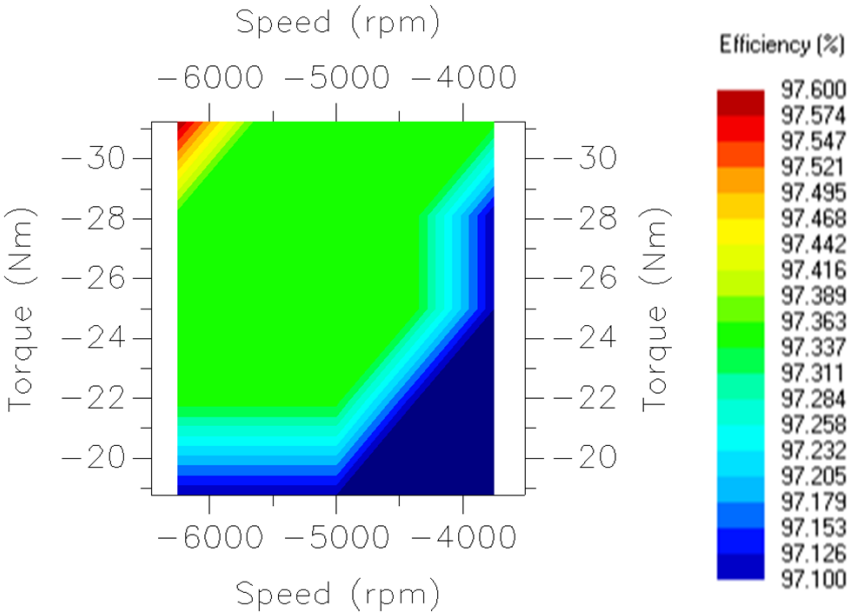

Figure 8.13: Efficiency map, torque vs speed

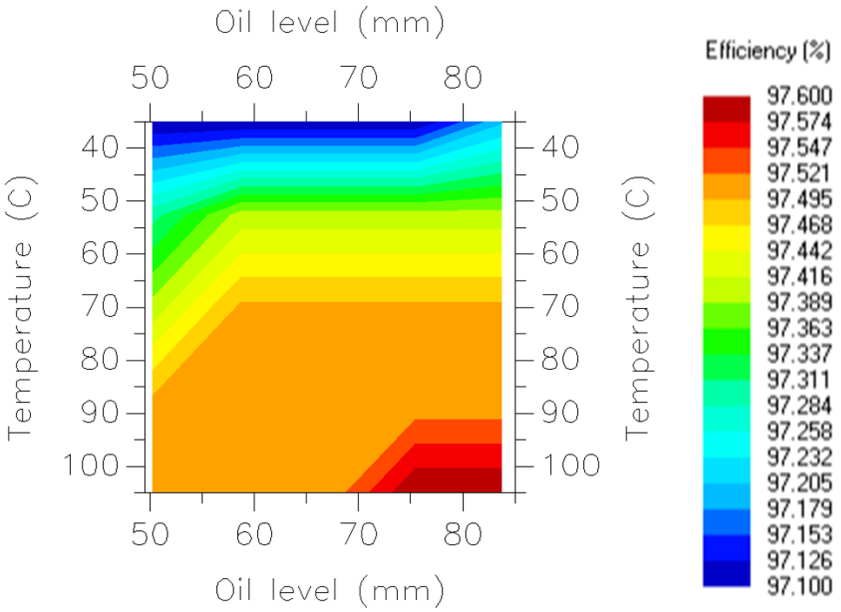

Figure 8.14: Efficiency map, temperature vs oil level

Chapter 9

Conclusions and future developments

The aim of this thesis is to propose a method to completely design an electric powertrain exploiting a commercial software, focusing especially on the NVH aspects.
Before deepening the dynamic analysis, the static analysis has been completed.
Different models have been studied, modifying parameters related to the transmission system, considering both macro and micro geometry modifications of both gear sets constituting the model.
Static analysis starts by evaluating the life of all components of the gearbox. The first fundamental outcome is the prove of the benefits brought by the introduction of the helix angle. Indeed, the comparison among the models with no helix angle (Models A and B) and the model with a certain helix angle in both gear sets (Model C) clearly affirms the goodness of the last model: a remarkable improvement of the life of gears, and therefore a reduction of their damage, is noted.
Moreover, moving to helical gears, it is possible to improve the contact patches, too: this is another fundamental aspect of static analysis.
Lastly, another critical result coming from the static analysis is the transmission error (TE), considering both its peak to peak value and also its harmonic content. This parameter, indeed, represent a crucial source of excitation of the transmission system, causing noise and vibrations.
Introducing the helix angle, a strong reduction of the peak to peak value of the TE is obtained, but an even greater improvement of the static performances of gears can be obtained only by introducing microgeometry modifications.
An optimization tool directly available in the software has been exploited to find out the best possible parameters. After many attempts, Model D4 has been selected as the best (especially from NVH viewpoint), since it provides an extraordinary reduction of the peak to peak TE.

The following step require to move to the NVH analysis. These analyses are performed considering some particularly relevant load cases, in which the vehicle proceeds at constant speed for a certain time, therefore any unwanted noise can be exceptionally annoying.
Three sources of excitations are considered:

- Rotor unbalance
- Electromagnetic forces
- Transmission error

Several responses have been investigated, to evaluate both the airborne noise and the structure borne one. In particular, the former has been estimated by considering the equivalent radiated power (ERP), the mean square velocity (MSV) and the acceleration response at virtual accelerometers placed all over the gearbox; the latter is evaluated considering the acceleration measured at some specific points: the housing mounts, which represent the connection between the gearbox and the vehicle.
Different sensitivity analyses have been performed, modifying both parameters related to the transmission system and to the electric motor.
First of all, considering the two models with spur gears, which differs only by the presence or not of the profile shifting, it appears clear that the most critical excitation, i.e. the one which provoke the worst NVH outcome, is the first harmonic of the TE, especially of the input gear set.
Then, moving to helical gears, a strong reduction of the response to the first harmonic of the TE is appreciated. With Model C (helical gears, profile shift but no microgeometry) a condition in which both the transmission system and the electric motors are similarly critical is reached. To further the optimization, as anticipated, it is necessary to implement microgeometry modifications. With Model D4 (helical gears, profile shift and microgeometry modifications) in particular is possible to strongly reduce the amplitudes of the harmonics of the TE, leading to an incredibly lower response to the first harmonic of the TE, of both input and output gear sets.
Lastly, a sensitivity analysis is performed also on electric motors. Two different solutions are compared: an IPM 48-4 motor and a SPM 6-4 one are considered. The latter has a fractional value of slots per pole per phase, hence a worst NVH behaviour is expected with respect to the IPM 48-4. This expectation is confirmed by the analyses performed, especially considering the working points of the motor before the flux weakening condition.
Then, even results directly related to the acoustics are obtainable by the software. These are helpful to understand better the directivity of the sound around the gearbox, and also to further demonstrate the effectiveness of the improvements

brought by the microgeometry optimization.
Finally, the last chapter is dedicated to the efficiency analysis. Looking at the losses of each mechanical component of the gearbox, it has been demonstrated that the biggest power loss is caused mostly by the gear mesh and partially by bearings, while the gear drag is less relevant. Then, it has been proved that by increasing the absolute values of torque and speed, and increasing the working temperature or the lubricant level, it is possible to even enhance the efficiency. Moreover, the benefits of the proper microgeometry on the efficiency are highlighted in this chapter.
Considering the electric motor, pretty high values of efficiency are noted. Doing a comparison between the IPM 48-4 and the SPM 6-4, a better efficiency is noted in the first one.
This thesis is a first step to better understand how to use this commercial software to design an electric powertrain, focusing especially on NVH performance. Future steps could require moving beyond just the simulation world: it would be very interesting to correlate the simulation results to experimental ones coming from prototype. Additionally, further optimization of the microgeometry can also be done, but more experience from the designer is required. Indeed, microgeometry modifications are really difficult to be selected, even by exploiting the optimization tool of the software. Moreover, it is fundamental to clearly understand which is the main goal of the microgeometry modifications: indeed, trying to optimize one aspect can lead to a worsening of another one.
Moreover, additional analyses could include an optimization of the housing geometry, to improve the NVH performance.
Further optimization of the electric motor can be considered, too. For instance deepening different geometries, different combinations of number of poles and slots, and even considering skewed rotors. Moreover, it would be interesting to consider also the switching noise generated by inverter operation.

Bibliography

[1] Romano Borchiellini. *Advanced engineering thermodynamics/Numerical modelling*. Notes of the course. Politecnico di Torino (cit. on p. 4).

[2] Giancarlo Genta. *Vibration dynamics and control*. New York : Springer, 2009 (cit. on pp. 5, 6, 168).

[3] Christoph Steffens; Christopher Lechner; Marius Lauen; Hrishikesh Suresh. «Challenges for Vehicle NVH and Acoustics Due to Electric Mobility». In: *ATZ Worldw* 125 (Jan. 2023), pp. 38–43 (cit. on pp. 7, 9).

[4] Christoph Steffens; Michael Kauth; Hrishikesh Suresh. «NVH Development of Electric Powertrains - Implementation from a Vehicle Perspective». In: *ATZ Worldw* 124 (2022), pp. 16–21 (cit. on p. 8).

[5] Gianmario Pellegrino. *Electrical machines*. Notes of the course. Politecnico di Torino (cit. on pp. 10, 13, 14, 17–19, 39).

[6] K. T. Chau. *Electric vehicle machines and drives : Design, analysis and application*. John Wiley & Sons, Incorporated, 2015 (cit. on pp. 11, 12, 15, 16, 19).

[7] Malcolm J. Crocker. *Handbook of Noise and Vibration Control*. John Wiley & Sons, Incorporated, 2007 (cit. on pp. 22, 24, 34, 36, 38).

[8] Z. Q. Zhu; D. Howe. «Influence of Design Parameters on Cogging Torque in Permanent Magnet Machines». In: *IEEE Transactions on Energy Conversion* 15 (2000), pp. 407–412 (cit. on p. 26).

[9] Jibin Zou; Hua Lan; Yongxiang Xu; Bo Zhao. «Analysis of Global and Local Force Harmonics and Their Effects on Vibration in Permanent Magnet Synchronous Machines». In: *IEEE Transactions on Energy Conversion* 32.4 (Dec. 2017), pp. 1523–1532 (cit. on pp. 26–28).

[10] Tao Sun; Ji-Min Kim; Geun-Ho Lee; Jung-Pyo Hong; Myung-Ryul Choi. «Effect of Pole and Slot Combination on Noise and Vibration in Permanent Magnet Synchronous Motor». In: *IEEE Transactions on Magnetics* 47.5 (May 2011), pp. 1038–1041 (cit. on pp. 26, 30, 272).

[11] Mostafa Valavi; Arne Nysveen; Robert Nilssen; Robert D. Lorenz; Terje Rølvåg. «Influence of Pole and Slot Combinations on Magnetic Forces and Vibration in Low-Speed PM Wind Generators». In: *IEEE Transactions on Magnetics* 50.5 (May 2014), pp. 1–11 (cit. on pp. 26, 28).

[12] Weidong Zhu; Steve Pekarek; Babak Fahimi; Bradley J. Deken. «Investigation of Force Generation in a Permanent Magnet Synchronous Machine». In: *IEEE Transactions on Magnetics* 22.3 (Sept. 2007), pp. 557–565 (cit. on pp. 26, 28).

[13] Bertrand Cassoret; Jean-Philippe Lecointe; Jean-François Brudny. *Power electronics and motor drives*. Ed. by Bogdan M. Wilamowski; J. David Irwin. Second. The Industrial Electronics Handbook. CRC Press Taylor & Francis Group (cit. on p. 28).

[14] Haodong Yang; Yangsheng Chen. «Influence of Radial Force Harmonics With Low Mode Number on Electromagnetic Vibration of PMSM». In: *IEEE Transactions on Energy Conversion* 29.1 (Mar. 2014), pp. 38–45 (cit. on pp. 28, 29, 272).

[15] Yuichi Yokoi; Tsuyoshi Higuchi; Yasuhiro Miyamoto. «General formulation of winding factor for fractional-slot concentrated winding design». In: *IET Electric Power Applications* 10.4 (2016), pp. 231–239 (cit. on p. 29).

[16] Guillaume Verez; Georges Barakat; Yacine Amara; Ghaleb Hoblos. «Impact of Pole and Slot Combination on Vibrations and Noise of Electromagnetic Origins in Permanent Magnet Synchronous Motors». In: *IEEE Transactions on Magnetics* 51.3 (Mar. 2015), pp. 1–4 (cit. on pp. 30, 272).

[17] Heesoo Kim. «Effects of unbalanced magnetic pull on rotordynamics of electric machines». PhD thesis. Lappeenranta, Finland: Lappeenranta-Lahti University of Technology LUT, 2021 (cit. on p. 31).

[18] Dimitri Torregrossa; Damien Paire; François Peyraut; Babak Fahimi; Abdellatif Miraoui. «Active Mitigation of Electromagnetic Vibration Radiated by PMSM in Fractional-Horsepower Drives by Optimal Choice of the Carrier Frequency». In: *IEEE Transactions on Industrial Electronics* 59.3 (Mar. 2012), pp. 1346–1354 (cit. on p. 31).

[19] Ioannis P. Tsoumas; Hans Tischmacher. «Influence of the Inverter's Modulation Technique on the Audible Noise of Electric Motors». In: *IEEE Transactions on Industry Applications* 50 (1) (2014), pp. 269–278 (cit. on pp. 32, 33).

[20] Fu Lin; Shu-Guang Zuo; Wen-Zhe Deng; Shuang-Long Wu. «Reduction of vibration and acoustic noise in permanent magnet synchronous motor by optimizing magnetic forces». In: *Journal of Sound and Vibration* 429 (2018), pp. 193–205 (cit. on pp. 39, 40).

[21] W. Liu. *Hybrid electric vehicle system modeling and control*. John Wiley & Sons, Incorporated, 2017 (cit. on p. 40).

[22] Hexagon AB. *Romax 2022.1 Tutorial packs*. Tutorials. Hexagon (cit. on pp. 41–43, 45, 46, 54, 56–59, 65, 85, 126, 130–132, 141, 158, 159, 164, 168, 169, 171, 177, 178, 262, 279, 281).

[23] Manuel Haas; Jan Bräunig; Eric Hensel. «Acoustical improvement of a train gearbox based on gear microgeometry and housing geometry optimization». In: (May 2017) (cit. on p. 42).

[24] *Gear backlash*. URL: https://khkgears.net/new/gear_knowledge/gear_technical_reference/gear_backlash.html (cit. on pp. 55, 62).

[25] *Gears - Cylindrical involute gears and gear pairs - Concepts and geometry*. ISO 21771:2007. ISO (cit. on pp. 59, 60).

[26] *Cylindrical gears for general and heavy engineering — Standard basic rack tooth profile*. ISO 53:1998. ISO (cit. on pp. 60, 61).

[27] KHK Gears - Stock Gear Manufacturer. *KHK Gears*. URL: https://khkgears.net (cit. on p. 63).

[28] Horsburgh Scott. *Gear terminology*. URL: http://www.horsburgh-scott.ca/resources/gear-terminology.php (cit. on p. 63).

[29] Eugenio Brusa. *Machine Design*. Notes of the course. Politecnico di Torino (cit. on pp. 63, 67).

[30] *Electric vehicle database*. URL: https://www.ev-database.org/uk (cit. on p. 71).

[31] ultimateSPECS. *Schede tecniche auto, consumo di carburante e dimensioni*. URL: https://www.ultimatespecs.com/it (cit. on p. 71).

[32] Crolla D; Mashadi B; Mashhadi B. *Vehicle Powertrain Systems : Integration and Optimization*. John Wiley & Sons, Incorporated, 2012 (cit. on p. 73).

[33] *REGULATION (EU) 2020/740 OF THE EUROPEAN PARLIAMENT AND OF THE COUNCIL of 25 May 2020*. L 177/1. Official Journal of the European Union (cit. on pp. 73, 75).

[34] MEAD info. *Comparison of Gear Efficiencies - Spur, Helical, Bevel, Worm, Hypoid, Cycloid*. URL: https://www.meadinfo.org/2008/11/gear-efficiency-spur-helical-bevel-worm.html (cit. on p. 76).

[35] Max Power Gears. *KNOW WHICH GEAR IS MORE EFFICIENT?* URL: https://maxpowergears.com/know-gear-efficient/ (cit. on p. 76).

[36] KHK Gears - Stock Gear Manufacturer. *HELICAL GEARS*. URL: https://khkgears.net/new/helical_gears.html (cit. on p. 76).

[37] Enrico Galvagno. *Motor vehicle mechanics*. Notes of the course. Politecnico di Torino (cit. on p. 80).

[38] G. De Donno. «Definition and Vibration Monitoring of the Endurance Test for an e-Axle». MA thesis. Torino, Italia: Politecnico di Torino, 2023 (cit. on pp. 86, 87).

[39] Christian Brecher; Christoph Löpenhaus; Marius Schroers. «Analysis of Excitation Behavior of Two-Stage Gearbox Based Upon Validated Simulation Model». In: *GEAR TECHNOLOGY* (2017) (cit. on p. 91).

[40] *Rolling bearings — Methods for calculating the modified reference rating life for universally loaded bearings*. ISO/TS 16281:2008. ISO (cit. on p. 104).

[41] *Rolling bearings — Static load ratings*. BS ISO 76:2006+A1:2017. ISO (cit. on p. 104).

[42] *Calculation of load capacity of spur and helical gears*. ISO 6336-1:2019. ISO (cit. on p. 108).

[43] G. Pellegrino S.Ferrari and et al. *SyR-e: Synchronous reluctance (machines) - evolution*. URL: `https://github.com/SyR-e/syre%20public` (cit. on pp. 158, 159, 171, 272, 276, 282).

[44] Gianmario Pellegrino; Alfredo Vagati; Paolo Guglielmi; Barbara Boazzo. «Performance Comparison Between Surface-Mounted and Interior PM Motor Drives for Electric Vehicle Application». In: *IEEE Transactions on Industrial Electronics* 59.2 (Feb. 2012) (cit. on pp. 158, 271).

[45] Chao Lu; Simone Ferrari; Gianmario Pellegrino. «Two Design Procedures for PM Synchronous Machines for Electric Powertrains». In: *IEEE Transactions on transportation electrification* 3 (2017), pp. 98–107 (cit. on pp. 158, 271).

[46] *Mechanical vibration — Balance quality requirements for rotors in a constant (rigid) state*. ISO 1940-1:2003(E). ISO (cit. on p. 168).

[47] A. Hofmann; F. Qi; T. Lange; R. W. De Doncker. «The breathing mode-shape 0: Is it the main acoustic issue in the PMSMs of today's electric vehicles?» In: *2014 17th International Conference on Electrical Machines and Systems (ICEMS)* (2014), pp. 3067–3073 (cit. on p. 169).

[48] Y.S. Chen; Z.Q. Zhu; D. Howe. «Vibration of PM Brushless Machines Having a Fractional Number of Slots Per Pole». In: *IEEE Transactions on Magnetics* 42.10 (2006), pp. 3395–3397 (cit. on p. 272).

[49] Petra Heingartner; David Mba. «Determining Power Losses in the Helical Gear Mesh». In: *GEAR TECHNOLOGY* (2005) (cit. on p. 279).

[50] Dejan V. Matijevic; Vladimir M. Popovic. «Overview of Modern Contributions in Vehicle Noise and Vibration Refinement with Special Emphasis on Diagnostics». In: *FME Transactions* 45 (3) (Jan. 2017), pp. 448–458.

[51] J.A. Mosquera-Sánchez; M. Sarrazin; K. Janssens; L.P.R. de Oliveira; W. Desmet. «Multiple target sound quality balance for hybrid electric powertrain noise». In: *Mechanical Systems and Signal Processing* 99 (2018), pp. 478–503.

[52] Mengyuan Zeng; Bohuan Tan; Fei Ding; Bangji Zhang; Hongtao Zhou; Yuanchang Chen. «An experimental investigation of resonance sources and vibration transmission for a pure electric bus». In: *Proceedings of the Institution of Mechanical Engineers, Part D: Journal of Automobile Engineering* 234 (4) (Mar. 2020), pp. 950–962.

[53] Robert Holehouse; Annabel Shahaj; Melanie Michon; Barry James. «Integrated approach to NVH analysis in electric vehicle drivetrains». In: *The Journal of Engineering* 2019 (17) (2019), pp. 3842–3847.

[54] Hua X; Thomas A; Shultis K. «Recent progress in battery electric vehicle noise, vibration, and harshness». In: *Science Progress* 104 (1) (2021).

[55] Yuan Fang; Huicui Chen; Tong Zhang. «Contribution of acoustic harmonics to sound quality of pure electric powertrains». In: *IET Electric Power Applications* 12 (6) (2018), pp. 808–814.

[56] Yechen Qin; Xiaolin Tang; Tong Jia; Ziwen Duan; Jieming Zhang; Yinong Li; Ling Zheng. «Noise and vibration suppression in hybrid electric vehicles: State of the art and challenges». In: *Renewable and Sustainable Energy Reviews* 124 (2020).

[57] R. Sannino. «NVH analysis of electric motors for hybrid and electric powertrains». MA thesis. Torino, Italia: Politecnico di Torino, 2022.

[58] S. Giacobbe. «Impiego di tecniche multibody per la predizione della radiazione acustica e del comfort interno di veicoli per l'autotrazione». PhD thesis. Napoli, Italia: Università degli studi di Napoli Federico II, 2012.

[59] The Engineers Post. *Types of Motors used in EV | Single, Dual, Three & Four Motor Configuration in EV*. URL: `https://www.youtube.com/watch?v=6H5vtu5_SF4`.

[60] Alain Cassat; Christophe Espanet; Ralph Coleman; Luc Burdet; Emmanuel Leleu; Dimitri Torregrossa; Jérémie M'Boua; Abdellatif Miraoui. «A Practical Solution to Mitigate Vibrations in Industrial PM Motors Having Concentric Windings». In: *IEEE Transactions on Industry Applications* 48 (5) (2012), pp. 1526–1538.

[61] Subhadeep Bhattacharya; Diego Mascarella; Geza Joos; Gerry Moschopoulos. «A discrete random PWM technique for acoustic noise reduction in electric traction drives». In: *2015 IEEE Energy Conversion Congress and Exposition (ECCE)* (2015), pp. 6811–6817.

[62] M.E. Braun; S.J. Walsh; J.L. Horner; R. Chuter. «Noise source characteristics in the ISO 362 vehicle pass-by noise test: Literature review». In: *Applied Acoustics* 74 (11) (2013), pp. 1241–1265.

[63] Pietro Asinari; Eliodoro Chiavazzo; Matteo Fasano. *Selected lectures on engineering thermodynamics*. Lecture notes of the course Advanced engineering thermodynamics/Numerical modelling. Politecnico di Torino, Mar. 2021.

[64] Munjal M.L. *Noise And Vibration Control*. World Scientific Publishing Company, 2013.

[65] Fu Lin; Shuguang Zuo; Wenzhe Deng; Shuanglong Wu. «Modeling and Analysis of Electromagnetic Force, Vibration, and Noise in Permanent-Magnet Synchronous Motor Considering Current Harmonics». In: *IEEE Transactions on Industrial Electronics* 63.12 (Dec. 2016), pp. 7455–7466.

[66] Jean Le Besnerais; Vincent Lanfranchi; Michel Hecquet; Pascal Brochet. «Characterization and Reduction of Audible Magnetic Noise Due to PWM Supply in Induction Machines». In: *IEEE Transactions on Industrial Electronics* 57.4 (Apr. 2010), pp. 1288–1295.

[67] EOMYS. *What is PWM (Pulse-Width Modulation)?* URL: https://e-nvh.eomys.com/what-is-pwm-pulse-width-modulation/.

[68] EOMYS. *What is the effect of current harmonics?* URL: https://e-nvh.eomys.com/what-are-current-harmonics/.

[69] EOMYS. *What is switching noise?* URL: https://e-nvh.eomys.com/what-are-pwm-force-harmonics-pwm-electromagnetic-excitations/.

[70] EOMYS. *Noise mitigation techniques of electrical machines*. URL: https://e-nvh.eomys.com/noise-mitigation-techniques-of-electrical-machines/.

[71] *automobile catalog*. URL: https://www.automobile-catalog.com/#gsc.tab=0.